PREFACE

The work presented in this thesis has been carried out at SIMLab, Department of Structural Engineering, NTNU, Norway, during my Ph.D.-study which started in January 2008 and ended with the submission of this thesis in December 2011. My supervisors have been Professor Tore Børvik and Professor Odd Sture Hopperstad.

The Ph.D.-study is a natural continuation of my Master's thesis work carried out at the Department of Physics, NTNU, in cooperation with SIMLab. The Master's thesis work was finished in July 2004 and the thesis was titeled "*Accurate measurements of out-of-plane deformations using structured light and close-range photogrammetry*". Here, tools for digital-image analysis were developed and applied to measure the full-field, out-of-plane deformations of plates subjected to quasi-static penetration.

In the Ph.D.-work presented herein, the structured-light technique has been further improved and used to measure the out-of-plane deformations of plates subjected to low-velocity impact. The main part of this thesis work has however concerned the development of a Digital Image Correlation (DIC) code and the application of this on various mechanical experiments. Additional functionalities to handle cracked specimens are also developed and tested. The work on DIC has mainly concerned two-dimensional problems (2D-DIC). However, with the camera-calibration tools developed for the structured-light technique, 3D-DIC has also been made available throughout this work.

The main motivation for this study arises from the desire to gain knowledge on digital image analysis techniques, which has become increasingly important in the work carried out at mechanical laboratories in the later years. It is appreciated that a number of commercial codes for image analysis in mechanical problems are available. However, it is believed that keeping local knowledge on such measurement tools may represent a benefit for mechanical laboratories such as SIMLab, especially when complex and non-standard mechanical tests are carried out.

Egil Fagerholt

Trondheim, December 16th 2011

ABSTRACT

This thesis contains a study on using numerical post-processing of recorded digital images from mechanical experiments to obtain continuous measurements of both displacement and strain fields of a particular specimen surface. Both two-dimensional and three-dimensional field data are measured. Two different measurement techniques have been applied in this study, i.e. structured light (projected fringes) and Digital Image Correlation (DIC). By using the technique of structured light combined with a calibrated camera model, continuous three-dimensional full-field out-of-plane deformations of plates subjected to impact have been measured. However, this technique does not allow for measurements of strain fields in the test specimen. By applying DIC on plane specimens, two-dimensional in-plane displacement and strain fields may be measured. A DIC code for analysis of mechanically recorded image series has been developed in this Ph.D.-work, and the DIC functionality has been further improved to be suitable for plane specimens experiencing crack growth. Effort has been made to increase the accuracy and robustness of the DIC algorithm in measuring such cracked specimens, and the discontinuous displacement fields of propagating cracks have been successfully captured. The developed DIC functionalities have mainly been tested for two-dimensional problems. However, the presented functionalities are extendable to three-dimensional problems. In this study, three-dimensional DIC analyses have been carried out to investigate the necking of mechanical specimens during loading.

A main part of the Ph.D.-work has concerned the development and testing of the image-analysis code. Particularly, increasing the computational speed of the code has been a challenging and time-consuming task.

The thesis starts with a synopsis, giving an introduction and the organization of the research work, together with a brief summary of the main findings and conclusions. The synopsis also includes a brief introduction to the image-analysis techniques of interest and an overview of the development of a 2D-DIC code for analysis of images recorded in mechanical experiments. Following the synopsis, four independent papers are presented.

Paper I presents a study where the technique of structured light has been applied to measure the continuous out-of-plane deformations of aluminium plates subjected to low-

velocity impact. The principles of the measurement technique are presented in detail as well as the results from an experimental test series. The experimental measurements have further been used to validate numerical and analytical models.

Paper II presents an experimental and numerical investigation of fracture in a cast aluminium alloy using a modified Arcan test setup. Two-dimensional DIC has been applied to measure displacement and strain fields in the specimens and further used to validate finite element simulations where the fracture parameters were assumed to follow a modified weakest-link Weibull distribution. Comparison of strain fields and crack paths between the experimental and numerical studies was emphasized.

Paper III presents a study where two-dimensional DIC, incorporating a mesh of elements suitable for node-splitting, has been applied to investigate fracture in small-scale SENT tests of a pipeline steel. The node-splitting approach proved valuable to measure fracture-mechanics parameters such as crack path, crack length, CTOD and CMOD as well as capturing the discontinuous displacement and strain fields of the cracked SENT specimen. The results from the DIC analyses were compared with traditional clip-gauge measurements. In addition, an assessment of the measurement uncertainties in two-dimensional versus three-dimensional DIC in the presence of specimen necking is included in the paper.

Paper IV contains an evaluation of mesh adaption techniques, as well as a crack-path optimization procedure in DIC, by analyzing synthetic image series of a specimen with a single propagating crack. A node-splitting approach is applied, together with an approach based on overlapping meshes. Using this latter approach, a crack-path mask is applied, which lets a random crack path to be defined at pixel level. The synthetic images are generated from finite element simulations, and the known displacement fields are used as a validation tool for the DIC analyses.

ACKNOWLEDGEMENTS

My supervisors during this Ph.D.-study have been Professor Tore Børvik and Professor Odd Sture Hopperstad at SIMLab, Department of Structural Engineering, NTNU. Their continuous support, guidance and encouragement throughout this work are highly appreciated.

The experimental work in this study has been carried out at the laboratories at Department of Structural Engineering, NTNU. The assistance of the laboratory staff is acknowledged, in particular Mr. Trond Auestad who has provided support in most of the experimental tests. Also, Dr. Frode Grytten, Dr. Cato Dørum, Mr. Hans Lange and Dr. Erling Østby at SINTEF have contributed to this thesis, and their contributions are highly appreciated.

I wish to thank Mr. Bernt Førre and late Professor Hans M. Pedersen at the Department of Physics, NTNU for introducing me to the field of optical measurements during my Master's thesis work.

Thanks to my fellow Ph.D.-students at the Department of Structural Engineering and my colleagues at SIMLab for an inspiring and friendly working environment.

Finally, I would like to thank my family for their encouragement and support during my Ph.D.-work.

The thesis was made possible thanks to the sponsor of this project, Structural Impact Laboratory (SIMLab), Centre for Research-based Innovation (CRI), Department of Structural Engineering at NTNU.

CONTENT

Part I

E. Fagerholt, F. Grytten, B.E. Gihleengen, M. Langseth and T. Børvik.
Continuous out-of-plane deformation measurements of AA5083-H116 plates subjected to low-velocity impact loading. International Journal of Mechanical Sciences, Volume 52, Issue 5, Pages 689-705, 2010.

Part II

E. Fagerholt, C. Dørum, T. Børvik, H.I. Laukli and O.S. Hopperstad.
Experimental and numerical investigation of fracture in a cast aluminium alloy. International Journal of Solids and Structures, Volume 47, Issue 24, Pages 3352-3365, 2010.

Part III

E. Fagerholt, E. Østby, T. Børvik and O.S. Hopperstad.
Investigation of fracture in small-scale SENT tests of a welded X80 pipeline steel using Digital Image Correlation with node splitting. Submitted for possible journal publication.

Part IV

E. Fagerholt, T. Børvik and O.S. Hopperstad.
Measuring discontinuous displacement fields in cracked specimens using Digital Image Correlation with mesh adaptation and crack-path optimization. Submitted for possible journal publication.

SYNOPSIS

1. Introduction

This thesis is titled “Field measurements in mechanical testing using close-range photogrammetry and digital image analysis”. The term “photogrammetry” refers to a range of techniques applied to capture geometric properties of an observed target from photographic images. The essential part in close-range photogrammetry is the determination of a proper camera model, i.e. a mathematical transformation between the three-dimensional target coordinates (X, Y, Z) and the corresponding two-dimensional image coordinates (u, v). The term “digital image analysis” refers to the process of numerical analysis of digital images in a computer code. In this study, the image analysis regards both the detection and tracking of artifacts in series of recorded images from mechanical experiments. Field measurements of displacements and strains are obtained by combining photogrammetry techniques with the post-processing analyses of recorded image series.

Mechanical problems involving impact and/or fracture are considered as complex problems both from an experimental, analytical and numerical point of view. Numerical techniques, such as the finite element method (FEM), have become increasingly powerful during the last decades and FEM is today accepted as a general computation tool within most branches of industry. A major benefit of the numerical tools is that they provide the possibility to investigate complicated problems in full detail. However, care should be taken when conclusions are made on numerical simulations solely. In general, knowledge on mechanical problems should come from a combination of experiments and numerical simulations based on appropriate material models.

The gap between mechanical experiments and numerical simulations can be bridged by measurements. A significant number of optical measurement techniques has during the years been applied to mechanical problems, obtaining non-contact, full-field and high-quality

measurements of properties such as displacements, geometries, strains, vibrations, etc. Optical measurement techniques may provide a vast amount of data, which may be advantageous when numerical models should be validated. Traditional optical techniques include among others Moirè methods, holographic interferometry, projected fringes, photoelasticity, and caustics [1][2]. Common for these optical methods is that they provide significant measurement sensitivity and for some of the methods, sensitivities in the order of the wave length for visible light may be obtained. However, because the methods exploit different kinds of optical effects (interference, holography, etc), more or less comprehensive optical setups are needed.

The considerable development of digital cameras in later years when it comes to resolution, recording rate and data storage has cleared the way for sophisticated numerical post-processing of images recorded in a mechanical experiment, increasing the range of measurements which is possible to extract from optical methods. Digital Image Correlation (DIC) [3][4] is such a post-processing technique and has become a widely used measurement tool in mechanical laboratories. In contrast to the traditional optical measurement techniques, DIC does not necessarily require a comprehensive experimental setup, which may be one of the reasons for its rising popularity in mechanical testing.

In 1986, Sutton et al. [5] presented the numerical approach employing Newton-Raphson methods for optimization of two-dimensional displacements in a test specimen, which founded the basis of the two-dimensional DIC method as it is used today. It is noted that this method has during the years been given different names in the literature, such as digital speckle interferometry (DSCM), texture correlation, computer-aided speckle interferometry (CASI) and electronic speckle photography (ESP) [4]. However, in this study the mostly used term, DIC, is adopted.

A significant number of problems have been addressed using the DIC method in solid mechanics problems, measuring two-dimensional displacement and strain fields in a wide range of materials. Using a two-camera (binocular) stereovision system together with DIC (3D-DIC), displacements and strains in three dimensions have also been obtained [6]. A further extension of the technique is the digital volume correlation technique (DVC), where the internal deformation of specimens is calculated from three-dimensional X-ray tomography recordings [7].

In 2006 Besnard et al. [8] proposed a new numerical formulation of the DIC approach, where the problem was formulated as a finite-element (FE) decomposition. Here, nodal

displacements were optimized in a mesh of elements. This provided a natural interface with finite-element numerical modeling of material behavior. A number of research papers have been published where the FE-based DIC approach has been further improved and applied to study different mechanical problems [9][10]. A particular advantage of the FE formulation of DIC is the possibility of applying numerical tools especially designed for FE methods in the development of the DIC algorithms. Rèthorè et al. [12][13] showed how the enrichment of nodal degrees of freedom as formulated in the extended finite element method (X-FEM) [15] could be adopted in DIC to model cracks in the test specimen (X-DIC). The X-DIC approach has also been applied on volume problems using x-ray tomography [14]. Lately, the DIC formulation has also been further extended by the development of integrated approaches for material model calibration [16][17]. Here, the measured displacement fields are used as input to analytical or numerical models for optimization of material model parameters.

Analyzing images to obtain field measurements in mechanical experiments is a computational expensive process. Because of the development of digital cameras with higher spatial resolution as well as digitization and frame rates, the field data can be measured with increasing resolution and accuracy. However, stress is put on the computer processing systems to be able to analyze image series within a sensible time frame. Heterogeneous programming, applying both serial and parallel code, may be a way to decrease processing time by spreading the computational tasks to different computational platforms.

In this study the traditional optical technique of structured light (projected fringes) has been applied to measure the out-of-plane deformations of plates subjected to low-velocity impact. This technique includes the calibration of a full camera model and numerical post-processing of recorded images to obtain three-dimensional measurements of the surface topography of the plate. Further, a DIC code, based on the formulation of Besnard et al. [8], has been developed and applied to measure two-dimensional and three-dimensional displacement and strain fields in various mechanical tests. The DIC code has been optimized on computational speed. Functionalities for handling of cracked specimens and measurement of discontinuous displacement fields are implemented. Some of the main achievements of this study are given in four papers, which in this thesis are presented as four independent parts following the synopsis.

2. Objectives and scope

The overall objective of this study has been to develop and evaluate image analysis techniques for field measurements in mechanical experiments, providing measurement data suitable for validation of both numerical simulations and analytical studies on the mechanical behavior of materials. The scope is limited to the analysis of grayscale digital images recorded from white-light cameras. The main objective has been to develop functionality, implementing code and carry out measurements on image series recorded from mechanical experiments. Both two- and three-dimensional problems have been considered. Also, both images of specimens with and without cracks are considered. The main objectives in this study are listed below:

- Measure continuous full-field out-of-plane deformation fields of plates subjected to impact using the technique of projected fringes.
- Develop and evaluate a DIC code for displacement and strain measurements in mechanical specimens.
- Optimize the DIC code when it comes to computational speed.
- Develop and evaluate algorithms for handling cracked specimens in DIC.
- Apply the developed DIC functionality on a set of mechanical experiments.
- Validate the DIC code against FE simulations

The research in this project will be limited to the optical methods of structured light and DIC, with main focus on the latter. The "finite-element" formulation of DIC, presented by Besnard et al. [8], will be used as basis for further development of the algorithms. It should be noted that both the subset-based DIC approach as proposed by Sutton et al. [5] and the "finite-element" formulation of DIC have advantages and disadvantages when it comes to practical applications in mechanical testing. Keeping similar formulations in experimental measurements (DIC) as in numerical modeling (FEM) was here emphasized, and led to the choice of the FE formulation of DIC. In general, the research project is limited to obtain fast and accurate algorithms for post-processing of images using the above-mentioned optical techniques and apply the algorithms to a set of relevant mechanical tests. Only macroscopic effects will be measured in the mechanical tests. Results will be obtained by analysis of

photographic (white-light) cameras. Thus, only surface effects of the mechanical specimens will be available from the measurements.

3. Research strategy

The work in the research project will be accomplished by carrying out mechanical experiments and developing an appropriate code for digital image analysis. Design and setup of optical measurement equipment in experiments will be emphasized as well as the implementation of numerical analysis algorithms. Resolution and uncertainties of the measurement techniques will be evaluated. Both methods and experimental data suitable for material-model calibration and numerical-model validation will be provided in this study. **Figure 1** shows a graphical representation of the research strategies that will be relevant for this study. In the strategy shown in **Figure 1**(a), images are recorded from a mechanical experiment. The results from the image analysis will be used to extract valuable information from mechanical tests and to validate numerical models. Further, the image analysis techniques may be validated from other measurement techniques applied during the experiment (e.g. extensometers and clip gauges). It should however be noted that the numerical-model validation process is not covered in this study, merely the generation of measurement data. In **Figure 1**(b) a numerical (FE) model of a specific mechanical problem is used to generate synthetic image series. After analyzing the synthetic images, the image analysis technique is validated by comparing the results with the data from the numerical model.

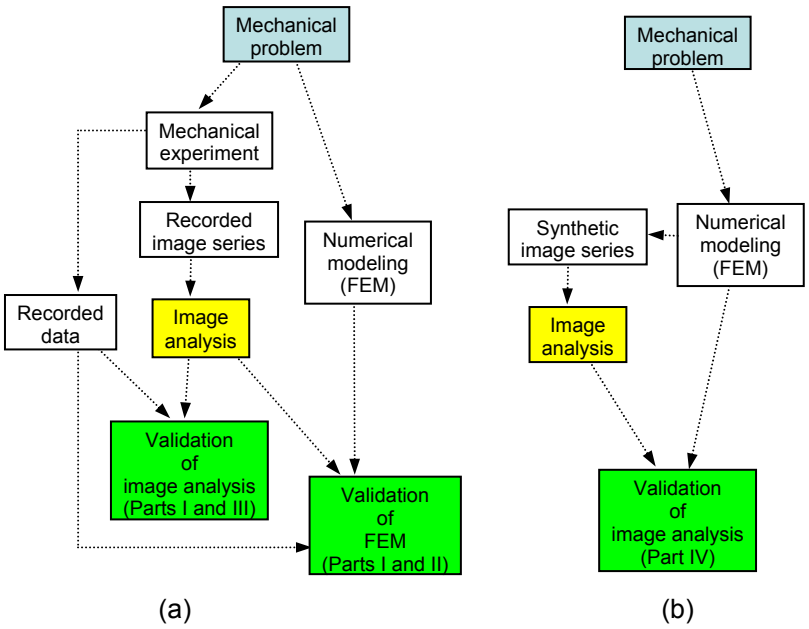

Figure 1. Research strategy for the different parts in this thesis. (a) A flow chart showing the analysis of image series recorded from a mechanical experiment. The chart shows the validation of both the image analysis (presented in Parts I and III) and the numerical modeling (presented in Parts I and II). (b) The flow chart for analysis of synthetic images generated from a FE model with validation of the image analysis (presented in Part IV).

4. Organization and summary of the thesis work

This Ph.D.-study is organized as a part of a larger project called Fracture and Crack Propagation (F&CP) at the Centre for Research based Innovation (CRI), Structural Impact Laboratory (SIMLab), Department of Structural Engineering, Norwegian University of Science and Technology (NTNU). In the F&CP research programme, the main objective is to develop validated models for fracture and crack propagation in ductile materials including rolled and extruded aluminium alloys, high-strength steels, cast aluminium and polymers.

This thesis consists of a synopsis and four independently published or submitted journal papers, referred to as parts (Part I, II, III and IV). The synopsis is intended to give an introduction to the basic concepts and an overview of the techniques developed throughout this study, as well as linking the parts together. The different parts are presented at the end of the synopsis and they are completely referred to in **Table 1**. The parts are numbered and presented in the succession as they have been written. In addition to the four parts included in the thesis, three journal papers (listed in **Table 2**) have been published with contribution from this Ph.D.-work.

Table 3 shows an outline of the main activities in this work and their corresponding parts.

Table 1: Journal papers included in the thesis

Part #	*Reference*
I	E. Fagerholt, F. Grytten, B.E. Gihleengen, M. Langseth and T. Børvik. *Continuous out-of-plane deformation measurements of AA5083-H116 plates subjected to low-velocity impact loading*. International Journal of Mechanical Sciences, Volume 52, Issue 5, Pages 689-705, 2010.
II	E. Fagerholt, C. Dørum, T. Børvik, H.I. Laukli and O.S. Hopperstad. *Experimental and numerical investigation of fracture in a cast aluminium alloy*. International Journal of Solids and Structures, Volume 47, Issue 24, Pages 3352-3365, 2010.
III	E. Fagerholt, E.Østby, T. Børvik and O.S Hopperstad. *Investigation of fracture in small-scale SENT tests of a welded X80 pipeline steel using Digital Image Correlation with node splitting.* Submitted for possible journal publication
IV	E. Fagerholt, T. Børvik and O.S. Hopperstad. *Measuring discontinuous displacement fields in cracked specimens using Digital Image Correlation with mesh adaptation and crack-path optimization.* Submitted for possible journal publication.

Table 2: Journal papers with contribution from the Ph.D.-work, but not included in the thesis

Part #	*Reference*
V	F. Grytten, E. Fagerholt, T. Auestad, B. Førre and T. Børvik. *Out-of-plane deformation measurements of an aluminium plate during quasi-static perforation using structured light and close-range photogrammetry*. International Journal of Solids and Structures, Volume 44, Issue 17, Pages 5752-5773, 2007.
VI	R.T. Moura, A.H. Clausen, E. Fagerholt, M. Alves and M. Langseth. *Impact on HDPE and PVC plates – Experimental tests and numerical simulations*. International Journal of Impact Engineering, Volume 37, Issue 6, Pages 580-598, 2010.
VII	G. Gruben, E. Fagerholt, O.S. Hopperstad and T. Børvik. *Fracture characteristics of a cold-rolled dual-phase steel*. European Journal of Mechanics – A/Solids, Volume 30, Issue 3, Pages 204-218, 2011.

Table 3. Outline of the published activities in the Ph.D.-work and the corresponding parts.

Research activity	*Part #*
Three-dimensional out-of-plane deformation measurements of plates subjected to impact or quasi-static loading using structured light.	I, V, VI
Two-dimensional displacement and strain-field measurements in mechanical tests using DIC.	II, III, IV, VII
Handling propagating cracks in two-dimensional DIC	III, IV

A short summary from each manuscript presented in this thesis (Parts I – IV) will be given in the following:

Part I:

Fagerholt E, Grytten F, Gihleengen BE, Langseth M and Børvik T. Continuous out-of-plane deformation measurements of AA5083-H116 plates subjected to low velocity impact loading. International Journal of Mechanical Sciences, Volume 52, Issue 5, Pages 689-705, 2010.

An optical system based on structured light and close-range photogrammetry has been developed and is in this study used to continuously measure the full-field out-of-plane deformation of aluminium plates subjected to low-velocity impact loading. During testing, square AA5083-H116 aluminium plates with thickness 5 mm were mounted in a circular frame and impacted by a 30 mm diameter blunt-nose projectile with velocities ranging from 7 to 11 m/s, while the out-of-plane deformations were measured at the opposite side. A fringe pattern was projected onto the rear target surface by a slide projector and the variation in the pattern during penetration was observed by a high-speed camera recording 10 000 images pr second. The recorded images were subsequently computer processed to provide full-field topography information of the target surface during deformation. Degradation of measurement data due to impact induced vibration has been evaluated and reduced to a minimum by isolating the optical system from the mechanical experiment. The out-of-plane deformation measurements were compared to non-linear finite element simulations, and the agreement between experimental and predicted results was in general found to be good.

Part II:

Fagerholt E, Dørum C, Børvik T, Laukli HI and Hopperstad OS. Experimental and numerical investigation of fracture in a cast aluminium alloy. International Journal of Solids and Structures, Volume 47, Issue 24, Pages 3352-3365, 2010.

This paper describes an experimental and numerical investigation on the fracture behaviour of a cast AlSi9MgMn aluminium alloy. In the experiments, a modified Arcan test set-up was used to study mixed-mode fracture. During testing, the tension load and the displacement of the actuator of the test machine were recorded, simultaneously as a high-resolution digital camera was used to record a speckle-patterned surface of the specimen. The recorded images were post-processed using an in-house digital image correlation (DIC) software to obtain information of the displacement and strain fields in the specimen during the test. In addition, some newly implemented features in the DIC software allowed us to detect and follow the crack propagation in the material. The numerical calculations were carried out with a user-defined material model implemented in an explicit finite element code. In the model, the material behaviour is described by the classical J_2 flow theory, while fracture was modelled by the Cockcroft-Latham criterion, assuming the fracture parameter to follow a modified weakest-link Weibull distribution. With the proposed probabilistic fracture modelling approach, the fracture parameter can be introduced as a random variable in the finite element simulations. Crack propagation was modelled by element erosion, and a non-local damage formulation was used to reduce mesh-size sensitivity. To reveal the effect of mesh density and meshing technique on the force-displacement curves and the crack propagation, several different meshes were used in the numerical simulations of the Arcan tests. The numerical results were finally compared to the experimental data and the agreement between the measured and predicted response was evaluated.

Part III:

Fagerholt E, Østby E, Børvik T and Hopperstad OS. Investigation of fracture in small-scale SENT tests of a welded X80 pipeline steel using Digital Image Correlation with node splitting. Submitted for possible journal publication.

Single Edge Notch Tension (SENT) tests have been carried out on a girth welded X80 pipeline steel using two different weld materials. The focus has been to obtain information on the effect of weld metal mismatch on fracture strength of the pipe. In addition to the traditional clip gauge CMOD/CTOD measurements, information has been obtained by applying Digital Image Correlation (DIC). The DIC mesh has been modified to allow for node splitting in order to capture the discontinuous displacement field of the propagating crack. Parameters such as crack path, crack length and crack opening have been successfully measured using this modification to the standard DIC analysis. The paper contains a description of the material and the experimental setup, as well as results from the experimental tests. Emphasis is laid on the DIC analysis and the additional information gained from this approach. Parallelization of the DIC algorithm and a discussion on the accuracies of 2D vs. 3D DIC analyses are also included in this paper.

Part IV:

Fagerholt E, Børvik T and Hopperstad OS. Measuring discontinuous displacement fields in cracked specimens using Digital Image Correlation with mesh adaptation and crack-path optimization. Submitted for possible journal publication.

This paper evaluates mesh adaptation techniques in two-dimensional Digital Image Correlation (2D-DIC) analyses of specimens with large deformations and a single propagating crack. The "finite element" formulation of DIC is chosen as basis for this study. The focus has been on the challenges caused by high-gradient and discontinuous displacement fields in the region of a propagating crack, and the aim has been to improve both the robustness and the accuracy of the correlation in such regions. Mesh adaptation based on node splitting and a novel overlapping-mesh technique have been implemented in a DIC code and used to capture the discontinuous displacement fields of cracked specimens. In addition, a procedure for optimization of the location of the crack path is presented. Synthetic image series with known displacement fields, generated from finite element simulations, have been analyzed to evaluate the performance of the presented techniques. Additionally, an experimental image series of a modified Arcan test has been analyzed using the proposed mesh adaptation and crack-path optimization. The paper contains a detailed description of the proposed techniques and results from the evaluation. It is found that both the node-splitting and overlapping-mesh techniques can be applied to successfully capture the discontinuous displacement field of a propagating crack. In the latter technique, the crack path is described down to pixel level. The crack-path optimization is capable of locating the crack path with sub-pixel accuracy, reducing correlation residuals and thus increasing the robustness of the DIC analysis. In addition, a certain filtering of pixels based on high correlation residual is found to increase the robustness of the correlation in areas affected by a propagating crack.

5. From digital images to field measurements

Photographic images can be seen as two-dimensional projections of the three-dimensional world, where the visible range of electromagnetic radiation (white-light) is captured. To analyze images on a computer, the images has to be digitized, and today most cameras are digital in nature. Digital images are in essence two-dimensional matrices, where each component, called pixel, is given a value representing a specific color. The color value may consist of a combination of different color types, e.g. red, green and blue in color images, or it may consist of a single value indicating the white-light intensity, i.e. a grayscale value. In this study, solely grayscale images are considered. The digitization of the continuous real world to digital matrices induces a limited spatial resolution. In addition, the digitization of the grayscale value also imposes a limitation and in this study images with 8-bit digitization are considered. This means that each pixel is given an integer intensity value ranging from 0 (black) to 255 (white). The spatial resolution of the image matrix, the grayscale resolution and the grayscale-value noise forms the limitations or boundaries within which measurements can be obtained. Thus, measurement uncertainties in image analysis can in general always be decreased by increasing the spatial resolution, increasing the grayscale resolution and/or decreasing the grayscale noise level.

In the following when discussing image analysis techniques, the term "image" will refer to a grayscale value field, e.g. $I(u,v)$, where the coordinates u (horizontal axis) and v (vertical axis) are the coordinates defined by the column and row indices of the image matrix, respectively. Grayscale values at decimal (sub-pixel) locations (u,v) in the field I are defined by a certain interpolation of nearby grayscale values in the image matrix, as will be described in Section 5.4. The term "pixel" will both be used to refer to a single component in the image matrix, but also as a measure of length, i.e. one pixel length is equal to one in the grayscale field $I(u,v)$ of a particular image.

Systematic errors in the image may impose deviations from the assumption of an image being an exact mathematical projection of the three-dimensional world. One cause of such systematic errors may be "non-simultaneous pixel recording" and is caused by cameras not being able to record all pixels at the exact same time. This is particularly important to consider when dynamic processes are recorded. Other causes of systematic errors are lens distortions, which are present to varying degrees in different camera lenses [18]. This will be

covered in more detail in the following subsection concerning the camera model. For modern and professional lenses, such distortion factors are reduced to a minimum. However, keeping control of such systematic error factors is of significant importance when accurate measurements are sought from digital images.

The following subsections will give brief descriptions of the basic concepts and the mathematical formulations applied in this study on digital image analysis.

5.1 Camera model

Because digital images are stored as matrices, the intuitive local image coordinate system (u,v) is defined such that u defines the column index and v defines the row index of the matrix. Thus, the positive u-axis is horizontal in a left-to-right direction, while the v-axis is vertical in a downwards direction. To relate the image coordinate system (u,v) (denoted in pixels), to the coordinate system (X,Y,Z) of the recorded target/specimen (denoted in millimeters), a mathematical transformation between the coordinate systems needs to be defined. This mathematical transformation is referred to as a "camera model". The mathematical derivation of the camera model presented here is based on the work of Heikkilä et al. [19][20]. A basic form of a camera model is called the "pinhole projection model" and is a mathematical projection of the target coordinates (X,Y,Z) onto the image plane (u,v) through a projection center (X_0,Y_0,Z_0). The optical axis is defined as a line that is normal to the image plane, going through the projection center. The pinhole projection model is illustrated in **Figure 2**. To mathematically describe the translation from target coordinates to image coordinates, an additional coordinate system (shown in **Figure 2**), i.e. the camera coordinate system, has to be defined. The camera coordinate system (x,y,z) is defined such that the origin is located in the projection center, and the z-axis is directed along the optical axis of the camera.

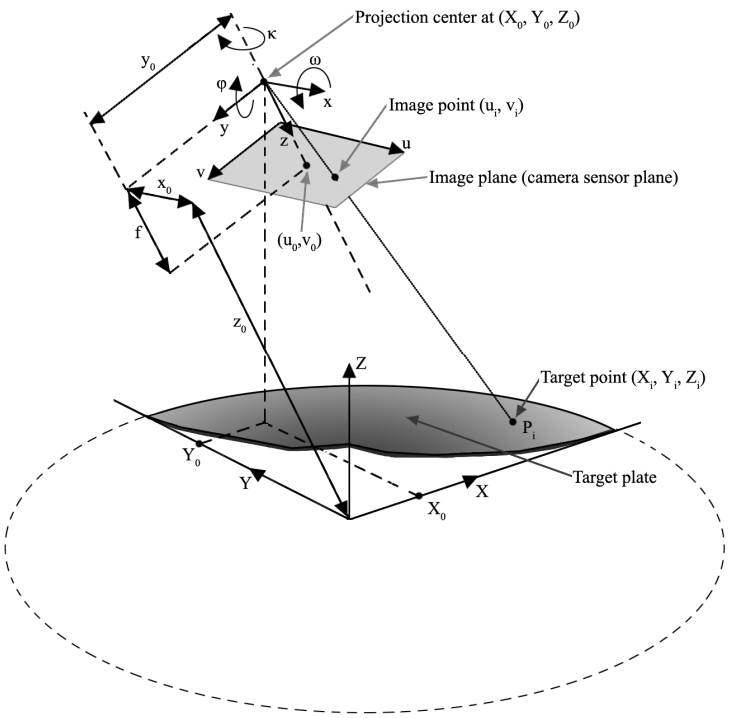

Figure 2. The pinhole projection model.

Assuming a target point P_i with coordinates (X_i, Y_i, Z_i), the transformation from target coordinates to camera coordinates is given by the following three-dimensional translations and rotations

$$\begin{bmatrix} x_i \\ y_i \\ z_i \end{bmatrix} = \mathbf{R} \cdot \begin{bmatrix} X_i \\ Y_i \\ Z_i \end{bmatrix} + \begin{bmatrix} x_0 \\ y_0 \\ z_0 \end{bmatrix} \tag{1}$$

where $\mathbf{R}$ is a 3×3 rotational matrix defined by the three rotation angles ω, φ and κ of the three camera coordinate axes x, y and z. $[x_i, y_i, z_i]^T$ is the location of the point P_i in the camera coordinate system, while $[x_0, y_0, z_0]^T$ is the location of the target coordinate system origin denoted in camera coordinates. Next, the camera coordinates are projected onto the camera sensor plane. The projection is described as

$$\begin{bmatrix} \tilde{u}_i \\ \tilde{v}_i \end{bmatrix} = \frac{f}{z_i} \begin{bmatrix} x_i \\ y_i \end{bmatrix} \tag{2}$$

where $[\tilde{u}_i, \tilde{v}_i]^T$ are the image coordinates (in millimetres) of the point P_i and f is the distance between the camera-coordinate origin (projection center) and the image plane along the z-axis, i.e. the effective focal length of the camera lens. The image coordinates are then transformed from millimeters to pixels (u_i, v_i) by

$$\begin{bmatrix} u_i \\ v_i \end{bmatrix} = \begin{bmatrix} D_u \tilde{u}_i \\ D_v \tilde{v}_i \end{bmatrix} + \begin{bmatrix} u_0 \\ v_0 \end{bmatrix} \tag{3}$$

where D_u and D_v are the proportional constants between millimetres and pixels and $[u_0, v_0]^T$ gives the translation (in pixel values). The point (u_0, v_0) is called the principal point and is defined as the location in the image where the optical axis crosses the image plane (see **Figure 2**).

Equations (1) – (3) describe a basic three-dimensional camera model, i.e. the pinhole projection model. The model can however be simplified if it is assumed that the recorded target surface is plane $(Z = 0)$ and that the optical axis is directed normally onto the target surface. In such cases the rotation matrix **R** is reduced to a unit matrix, and $z_i = z_0$ is constant for all points P_i on the target surface. Thus, Equations (1) – (3) is reduced to

$$\begin{bmatrix} u_i \\ v_i \end{bmatrix} = \frac{f}{z_0} \begin{bmatrix} D_u \cdot (X_i + x_0) \\ D_v \cdot (Y_i + y_0) \end{bmatrix} + \begin{bmatrix} u_0 \\ v_0 \end{bmatrix} = \begin{bmatrix} C_u X_i \\ C_v Y_i \end{bmatrix} + \begin{bmatrix} \hat{u}_0 \\ \hat{v}_0 \end{bmatrix} \tag{4}$$

where the image coordinates (u_i, v_i) are calculated by scaling and a translation of the target coordinates (X, Y). The scaling is given by the constants (C_u, C_v), while the translation is given by $(\hat{u}_0, \hat{v}_0)$. Further simplifications can be made by assuming the aspect ratio between the horizontal and vertical axes in the image to be equal to one, giving

$$\begin{bmatrix} u_i \\ v_i \end{bmatrix} = C \begin{bmatrix} X_i \\ Y_i \end{bmatrix} + \begin{bmatrix} \hat{u}_0 \\ \hat{v}_0 \end{bmatrix} \tag{5}$$

where $C = C_u = C_v$. Equation (5) represents the most basic form of a camera model which may be applied for plane specimens. However, the limitations of which it is based on must be appreciated to obtain valid measurements in a particular image analysis.

Equations (4) and (5) represent reduced camera models only suitable for planar specimens. In the following, the pinhole projection model in Equations (1) – (3) will be extended to account for particular types of lens distortions. Depending on the quality of the camera lenses used, systematic deviations from the pinhole projection model may be encountered to varying extents [18]. In professional lenses, these distortion factors are however reduced to a minimum. Two different lens-distortion factors are incorporated in this study, i.e. radial and tangential (decentering) distortion. Radial distortion may arise from asymmetrical lens systems [18] and the distortion parameters $\left(\delta\tilde{u}_i^r, \delta\tilde{v}_i^r\right)$ in u and v directions are here approximated by [19]

$$\begin{bmatrix} \delta\tilde{u}_i^r \\ \delta\tilde{v}_i^r \end{bmatrix} = \begin{bmatrix} \tilde{u}_i \cdot \left(k_1 r_i^2 + k_2 r_i^4 + ...\right) \\ \tilde{v}_i \cdot \left(k_1 r_i^2 + k_2 r_i^4 + ...\right) \end{bmatrix} \tag{6}$$

where $k_1, k_2, ..., k_n$ are the coefficients of radial distortion and $r_i = \sqrt{\tilde{u}_i^2 + \tilde{v}_i^2}$. Here it is assumed that the radial distortion is symmetric around the principal point (u_0, v_0). In this study, the two first terms of the radial distortion (given by k_1 and k_2) are adopted. The tangential distortion, on the other hand, may arise from misalignment of the camera lenses [18]. The tangential distortion parameters $(\delta\tilde{u}_i^t, \delta\tilde{v}_i^t)$ are here defined as [19]

$$\begin{bmatrix} \delta\tilde{u}_i^t \\ \delta\tilde{v}_i^t \end{bmatrix} = \begin{bmatrix} 2p_1\tilde{u}_i\tilde{v}_i + p_2 \cdot \left(r_i^2 + 2\tilde{u}_i^2\right) \\ p_1 \cdot \left(r_i^2 + 2\tilde{v}_i^2\right) + 2p_2\tilde{u}_i\tilde{v}_i \end{bmatrix} \tag{7}$$

where p_1 and p_2 are the coefficients defining the degree of tangential distortion. When the radial and tangential distortions are incorporated into the pinhole projection model, Equation (3) is extended to

$$\begin{bmatrix} u_i \\ v_i \end{bmatrix} = \begin{bmatrix} D_u \cdot \left(\tilde{u}_i + \delta\tilde{u}_i^r + \delta\tilde{u}_i^t\right) \\ D_v \cdot \left(\tilde{v}_i + \delta\tilde{v}_i^r + \delta\tilde{v}_i^t\right) \end{bmatrix} + \begin{bmatrix} u_0 \\ v_0 \end{bmatrix} \tag{8}$$

Qualitative effects of both radial and tangential distortions, with some chosen parameters of k_1, k_2, p_1 and p_2, are illustrated in **Figure 3**.

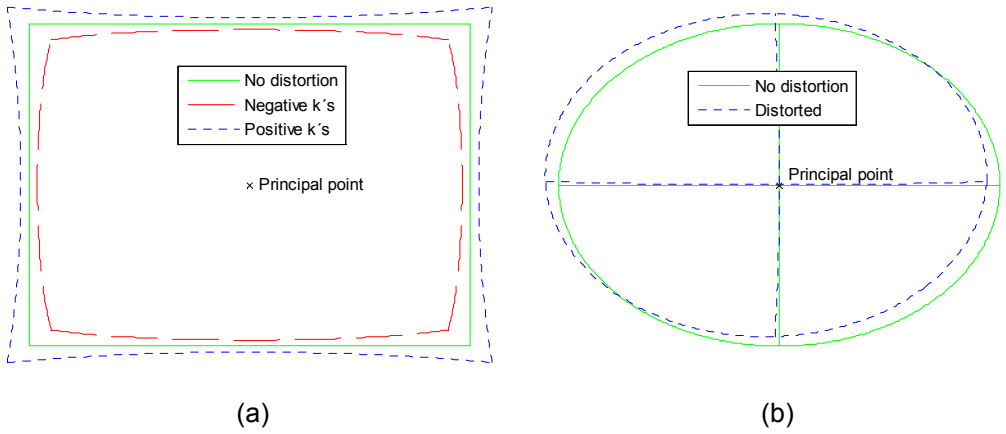

Figure 3. Examples of the effect of (a) radial distortion and (b) tangential distortion. The geometric shapes are plotted in the image plane (u, v) with and without the two types of lens distortion.

The full camera model defined by Equations (1), (2) and (8) consists of 15 parameters that need to be obtained in order to achieve a valid transformation of coordinates. The 15 parameters are the three rotation angles $(\omega, \varphi, \kappa)$, the target coordinate-system origin $(x_{0,} y_0, z_0)$, the effective focal length f, the scaling parameters (D_u, D_v), the principal point (u_0, v_0) and the radial- and tangential distortion parameters (k_1, k_2, p_1, p_2). The parameters are optimized in a calibration routine which will be described in the following section.

The scaling parameters (D_u, D_v) are often given by the camera specifications. Because the effective focal length f is inversely proportional to the scaling parameters in the camera model (see Equations (2) and (3)), the number of parameters to be optimized can be reduced by applying fixed scaling parameters (D_u, D_v) from the camera specifications. The benefit of this approach is that the effective focal length f may be optimized to a more physically correct value, and correspond to the focal length of the particular lens. However, the disadvantage is that the aspect ratio between the horizontal and vertical axes is fixed in the calibration. To include the aspect ratio, an additional scaling parameter s_v is introduced so that Equation (8) becomes

$$\begin{bmatrix} u_i \\ v_i \end{bmatrix} = \begin{bmatrix} D_u \left(\tilde{u}_i + \delta\tilde{u}_i^r + \delta\tilde{u}_i^t \right) \\ D_v s_v \left(\tilde{v}_i + \delta\tilde{v}_i^r + \delta\tilde{v}_i^t \right) \end{bmatrix} + \begin{bmatrix} u_0 \\ v_0 \end{bmatrix}. \tag{9}$$

Now the camera model consists of 14 parameters (ω, φ, κ, x_0, y_0, z_0, f, s_v, u_0, v_0, k_1, k_2, p_1, p_2) that need to be optimized, and two parameters (D_u, D_v) given by the specifications of the camera prior to the calibration.

5.2 Camera model calibration

Two different camera models have been incorporated in this study, i.e. the two-dimensional model in Equation (5) and the full three-dimensional model given by Equations (1), (2) and (9).

For the two-dimensional model in Equation (5), the scaling parameter C has to be established. This has been done by measuring known distances of the specimen in the recorded images. Zhang et al. [11] presented an approach for setting up cameras with the optical axis normal to the target surface in a 2D-DIC approach. Also, two-dimensional camera models applying lens distortions are found in the literature [21]. In this study, effort has been made to direct the optical axis of the camera normal to the specimen surfaces, but no optimization of the camera setup has been carried out.

For the three-dimensional camera model, a full camera calibration routine has been implemented based on the approach presented by Heikkilä [19]. The 14 parameters in this camera model are optimized by obtaining a set of corresponding target coordinates (X_i, Y_i, Z_i) and image coordinates (U_i, V_i). It is required that the target points (X_i, Y_i, Z_i) are non-coplanar. The objective function to be minimized in the calibration routine is expressed as

$$F = \sum_{i=1}^{N} \left[(U_i - u_i)^2 + (V_i - v_i)^2 \right] \tag{10}$$

where N is the number of calibration points and (u_i, v_i) are image coordinates calculated from the target coordinates (X_i, Y_i, Z_i) using the relevant camera model. The camera model parameters are optimized in a least squares algorithm. To help the optimization routine to converge to the correct solution, proper initial values for the 14 parameters must be provided. Initial values for nine of the 14 parameters (focal length, principal point, target-coordinate origin and rotation angles) are provided using a Direct Linear Transform (DLT) [22]. Initial

values for the four distortion parameters are set to zero, while the scaling parameter s_v is set to one.

The least squares algorithm determines the 14 parameters of the camera model in Equations (1), (2) and (9). Thus, the transformation from target coordinates (X,Y,Z) to image coordinates (u,v) is given. However, the inverse transformation from image coordinates to target coordinates (where one of the target coordinates is initially known) is also of interest. Problems arise when trying to inverse Equation (9). This results in fifth order polynomials which are not trivial to solve. To overcome this problem, Heikkilä [19] presented an approximate solution, where the undistorted image coordinates $(\tilde{u},\tilde{v})$ are calculated from the distorted image coordinates (u,v). This approximate solution is given by *

$$\tilde{u}_i = \frac{\tilde{u}'_i + \tilde{u}'_i\left(a_1 r_i^2 + a_2 r_i^4\right) + 2a_3\tilde{u}'_i\tilde{v}'_i + a_4\left(r_i^2 + 2\tilde{u}'^2_i\right)}{\left(a_5 r_i^2 + a_6\tilde{u}'_i + a_7\tilde{v}'_i + a_8\right)r_i^2 + 1} \tag{11}$$

$$\tilde{v}_i = \frac{\tilde{v}'_i + \tilde{v}'_i\left(a_1 r_i^2 + a_2 r_i^4\right) + a_3\left(r_i^2 + 2\tilde{v}'^2_i\right) + 2a_4\tilde{u}'_i\tilde{v}'_i}{\left(a_5 r_i^2 + a_6\tilde{u}'_i + a_7\tilde{v}'_i + a_8\right)r_i^2 + 1} \tag{12}$$

where $\tilde{u}'_i = (u_i - u_0)/D_u$, $\tilde{v}'_i = (v_i - v_0)/(s_v D_v)$ and $r_i = \sqrt{\tilde{u}'^2_i + \tilde{v}'^2_i}$.

To obtain the eight unknown parameters $(a_1, a_2, ..., a_8)$, calibration points covering the entire image area are required. A set of 2000 such calibration points is generated using the calibrated camera model in Equations (1), (2) and (9). The eight parameters are then optimized using a least squares fitting algorithm and Heikkilä [19] showed that this approach gives insignificant residuals even when high radial and tangential distortions were present. In this study, the full camera model was incorporated to measure three-dimensional out-of-plane deformation of plates, using the technique of structured light. This technique will be described in the following subsection.

* It is noted that a typo, given in Part I, has here been corrected in Equation (11).

5.3 Structured light

The technique of structured light, also called "projected fringes", is a technique suitable to measure the three-dimensional geometrical shape of specimens during loading. A schematic setup is illustrated in **Figure 4**. Here the technique is applied to measure the full-field out-of-plane deformation of a plate during impact. The inclination angles of the projector ω_p and the camera ω_c are indicated in the figure. It is noted that ω_c can be related to ω in the camera model described in Section 5.1 if the plate is located in the XY-plane.

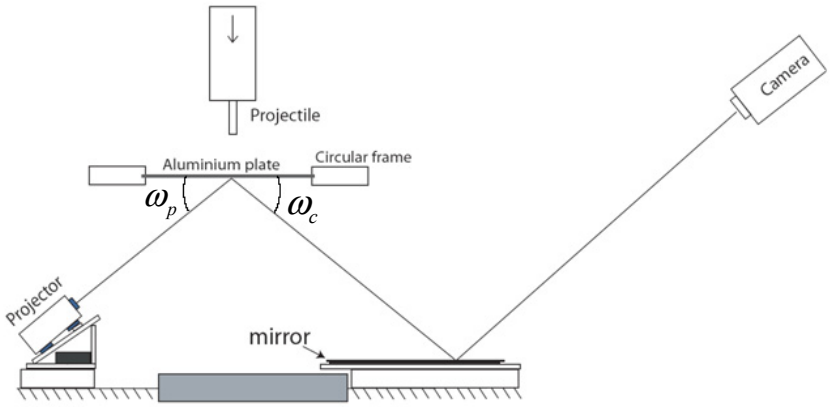

Figure 4. Schematic setup of the structured light technique used to measure out-of-plane deformation of a plate subjected to impact. The inclination angles of the projector ω_p and the camera ω_c are indicated in the figure.

A slide projector projects a binary (black-white) fringe pattern onto the plate surface, while a high-speed camera records the plate surface during the experiment. **Figure 5** shows examples of the recorded fringe patterns at the reference (no deformation) and at a deformed stage during impact.

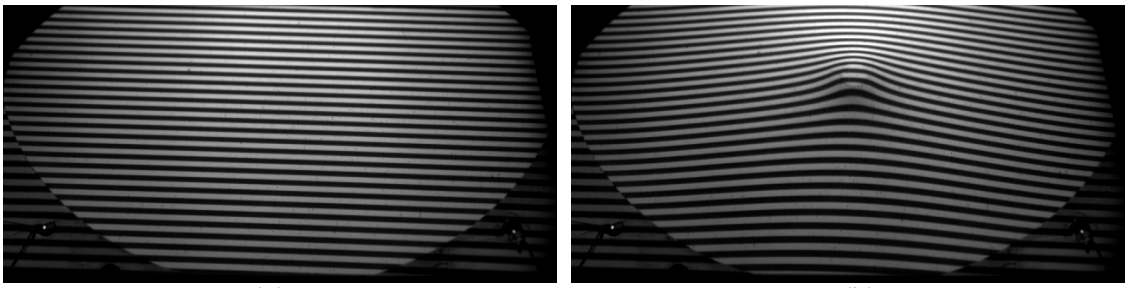

Figure 5. Examples of recorded images of a plate with projected fringe pattern at (a) reference (no deformation) and (b) during impact.

The appearance of the fringe pattern in the image coordinate system (u,v) is dependent on the topography of the plate as can be seen in **Figure 5**. The sensitivity of the measurement system is particularly dependent on the projector inclination angle ω_p (indicated in **Figure 4**). Reducing ω_p will increase the sensitivity in the out-of-plane deformation measurements, while it may be necessary to increase ω_p if large deformations are expected. For small ω_p, out-of-focus problems may arise. If the focal plane is situated normal to the optical axis of the projector, it may become impractical to project a sharp and focused pattern onto the plate. This was solved by adapting the Scheimpflug principle [23], tilting the slide inside the projector and thus, modifying the focal plane to be situated in the plane of the target plate.

To capture the topography of the plate, the three-dimensional camera model of the applied camera is firstly calibrated. Similarly, it may be possible to describe the projector with a "projector model", using the same formulation as for the camera, and calibrate this to mathematically describe the projection, i.e. the mathematical translation between target coordinates (X,Y,Z) and the projected image coordinates (u^p,v^p). In this study a traditional analog slide projector was used, and the "image" coordinates (u^p,v^p) in the projector were therefore not easily available. Thus, a different and more straight-forward calibration routine was chosen for the projector, as will be described below.

The formulation described in Section 5.2 was applied to calibrate the camera. A set of non-coplanar calibration points were obtained. This was done using a planar 10 mm thick glass plate with a glued-on "checker-board" pattern as calibration target. The calibration setup is illustrated in **Figure 6**. The calibration target is prearranged to lie in the XY-plane of the target coordinate system. The plate is then moved along the Z-axis while synchronized

recordings from the camera and the linear transducer is carried out. The linear transducer gives the recording of the Z-value of which the glass plate is located. A recorded image from the camera calibration is illustrated in **Figure 7**(a). Because the physical properties of the "checker-board" pattern are known, corresponding (X,Y) and (u,v) coordinates may be obtained by analyzing the recorded images and extracting the corners of all squares in the pattern. The corner-extraction algorithm by Harris et al. [32] was here used to locate the corners with sub-pixel accuracy in the recorded images. The calibration set of points with corresponding (X_i,Y_i,Z_i) and (u_i,v_i) coordinates is then used to calibrate the camera model using the formulation described in Section 5.2.

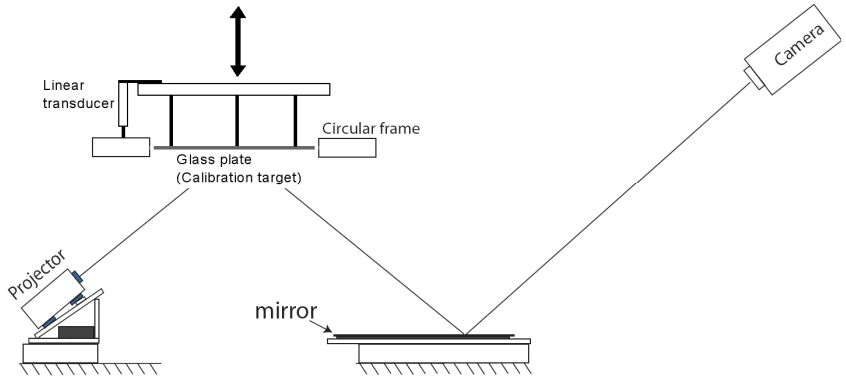

Figure 6. Calibration setup. This setup is used for calibration of both the camera and the projector. A glass plate, used as calibration target, is prearranged to lie in the XY-plane of the target coordinate system. It is then moved along the Z-axis. The camera records images which are synchronized with the readings from the linear transducer, giving the Z-value of the glass plate for a particular recorded image.

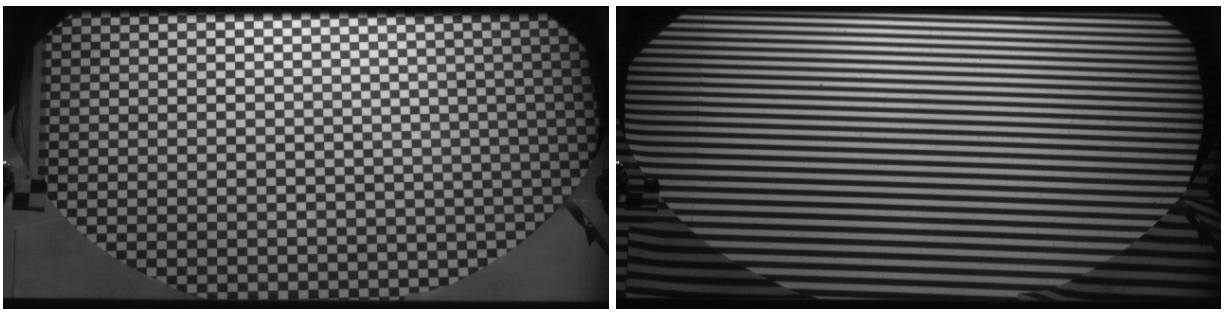

(a) (b)

Figure 7. Recorded patterns from (a) camera calibration and (b) projector calibration.

The setup for calibration of the projector is the same as the setup for the camera calibration and is illustrated in **Figure 6**. Now, a planar glass plate with a matt white surface is used as calibration target. The projector is set to project the same fringe pattern as will be used during the experiments. Similar to the camera calibration, the glass plate is prearranged to lie in the XY-plane of the target coordinate system. Then the plate is moved along the Z-axis while synchronized recordings of the camera and the linear transducer is carried out. The linear transducer obtains Z-values for a particular image and thus the appearance of the fringe pattern and its dependence on the Z-value is obtained. **Figure 7**(b) illustrates an example of a recorded image during the projector calibration.

The recorded fringe patterns from both the projector calibration (see **Figure 7**(b)) and the experiment (see **Figure 5**) require a certain fringe-pattern analysis algorithm. Because the chosen fringe pattern consists of black and white fringes (binary pattern), it was believed that the best possible accuracy was gained by locating the edges of the fringes, i.e. the maximum and minimum derivatives of the grayscale values along a particular column u. **Figure 8**(a) illustrates the recorded grayscale values along a column in the image shown in **Figure 5**(a). The grayscale values are plotted as function of the row number v. An image analysis algorithm was developed to first detect an edge in this signal, and then determine the interpolated sub-pixel location (in v) of the particular edge. **Figure 8**(b) illustrates a zoomed-in version of the grayscale signal in **Figure 8**(a), together with the extracted locations v_i of the edges.

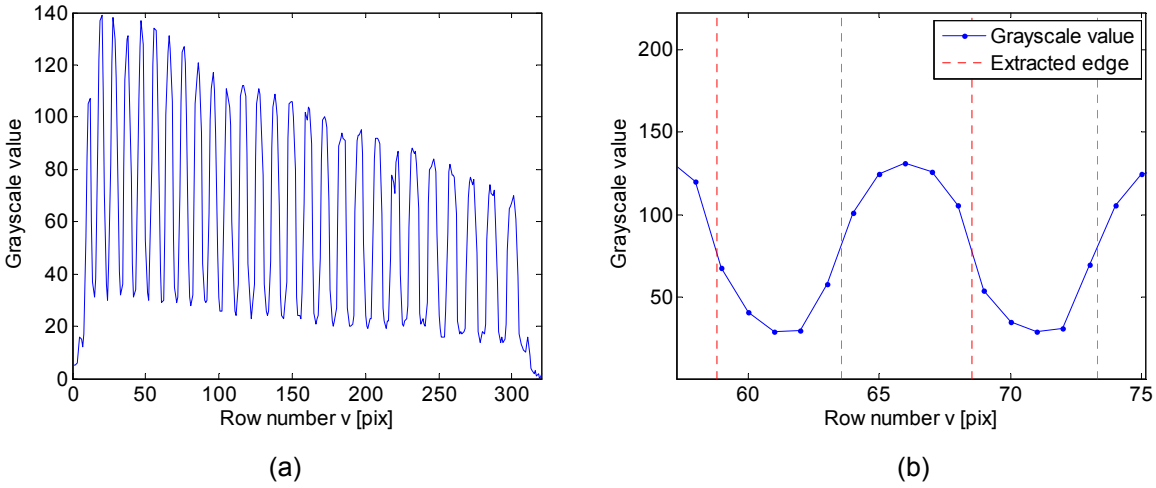

Figure 8. Grayscale values along a particular column $(u = 320)$ in the image (fringe pattern) shown in **Figure 7**(b). To the right (a), the grayscale values along the entire column are plotted. To the left (b), a zoomed-in version of the grayscale values together with the location of the extracted edges are shown.

The technique of structured light, presented in this subsection, has in this study been applied to measure the full-field out-of-plane deformations in plates subjected to low-velocity impact. A full presentation of the study on low-velocity impact of plates is given in Part I in this thesis.

The structured light technique provides accurate out-of-plane deformation measurements of a specimen, but is incapable of material-point tracking and thus incapable of measuring strain fields on the surface of a specimen. Because of this limitation, the focus in this Ph.D.-study was shifted towards the DIC technique, which may provide measurements of displacement and strain fields in both two and three dimensions. The principles of the DIC technique will be presented in the following subsection.

5.4 Digital Image Correlation (DIC)

In the previous subsection concerning the structured-light technique, two different image analysis algorithms have been applied, i.e. the corner-extraction (applied on checker board patterns) and the edge-extraction algorithms (applied on fringe patterns). These techniques are custom made for and thus limited to the detection and tracking of certain artifacts (corners and edges) in digital images. The technique presented in this subsection, called Digital Image Correlation (DIC), is in this context a general algorithm which concerns the tracking of random patterns in series of digital images.

In the DIC algorithm, an image of a specimen at a deformed stage (current configuration) is compared to an image of the specimen at a reference stage (reference configuration). The deformation of the specimen from the reference to the current stage, in the two-dimensional image coordinate system, may be described by a set of parameters. These parameters are then calculated in an optimization algorithm, minimizing the differences in grayscale values between the reference and the current image. The reference configuration may here either refer to a stage where the specimen has zero or non-zero deformation.

In this subsection concerning DIC, only two-dimensional coordinates in the image plane (denoted in pixels) will be referred to. Here, $\mathbf{X} = (X, Y)$ will refer to the image coordinates in the reference configuration, $\mathbf{x} = (x, y)$ will refer to the image coordinates in the current configuration, while $\mathbf{u} = (u, v)$ will refer to the translation in horizontal and vertical direction, such that $\mathbf{u} = \mathbf{x} - \mathbf{X}$.

The mathematical formulation of DIC, employing Newton-Raphson methods for optimization, was firstly developed by Sutton et al. [5]. Here the correlation is carried out on a small rectangular region of an image, i.e. a subset. The deformation of the subset is given by six parameters, i.e. the translation of the center point (u_c, v_c) as well as the first order displacement gradient $\left(\frac{\partial u}{\partial X}, \frac{\partial u}{\partial Y}, \frac{\partial v}{\partial X}, \frac{\partial v}{\partial Y}\right)$ within the subset. The deformation parameters for a subset in a current image I_c (at a deformed stage) are found by minimizing a certain correlation function F based on the difference in grayscale values between a reference image I_r and I_c. Thus, the correlation function F is used as the objective function in the Newton-Raphson optimization. Different correlation functions have been presented in the literature.

The sum-of-squares of the grayscale differences (SSD) within the subset is such a correlation function and is defined by

$$F = \sum_{i \in \Omega} \left(I_r(\mathbf{X}_i) - I_c(\mathbf{x}_i) \right)^2 \tag{13}$$

where i denotes a specific pixel and Ω denotes the set of pixels within the subset at the reference configuration. Other correlation functions include zero-shifting and normalization to reduce sensitivity to variations in the illumination of the specimen. An overview of the mostly used correlation functions can be found in e.g. [4].

The basic principle of the subset-based DIC approach is shown in **Figure 9**. Here the deformation of the subset from the reference stage to the current stage has been tracked in a series of 150 images. The subset size is 30×30 pixels. The figure shows the reference subset in the reference image I_r and the deformed subset in the current image I_c as well as the displacement (u_c, v_c) of the center point of the subset.

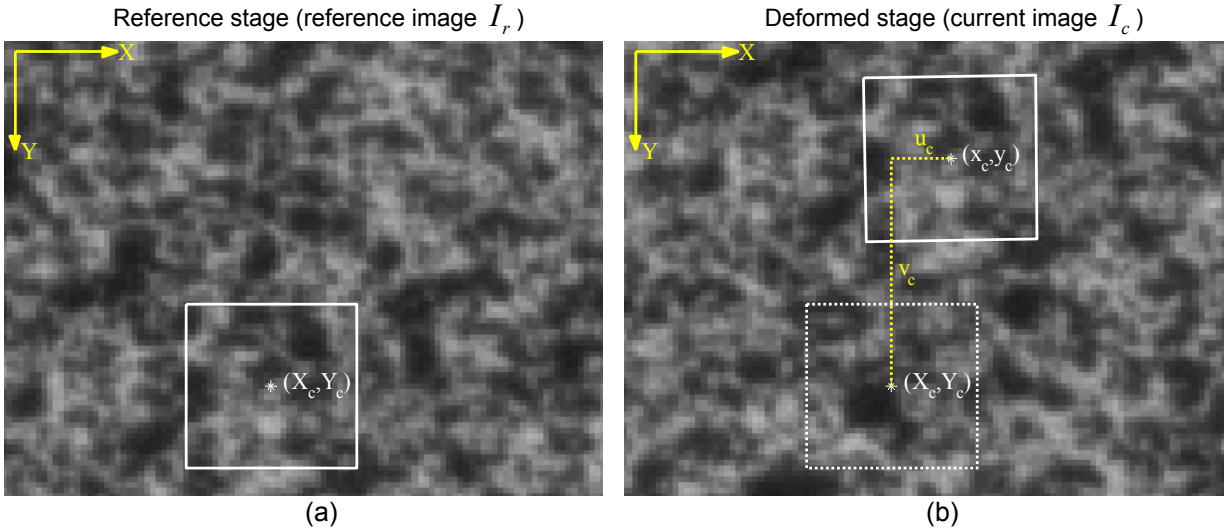

Figure 9. Principle of subset-based DIC. (a) The reference image I_r with a subset at reference stage. (b) The current image I_c showing the subset in both reference and current state. The displacement of the center point (u_c, v_c) is also indicated in the figure.

From the literature, it is evident that the success of the correlation is highly dependent on parameters such as the contrast and speckle size of the recorded grayscale pattern, the subset size, the subset shape function and the digitization level of the grayscale values [24][25]. In the example shown in **Figure 9**, a random speckle pattern has been applied by spray painting

the surface of the specimen with black and white paint. This procedure has also been applied in the mechanical experiments presented in this study (Parts II, III and IV).

Another important feature of the DIC algorithm is how the grayscale values are collected at sub-pixels locations. When calculating the correlation function F, the reference-configuration coordinates $\mathbf{X}_i$ may be chosen as integer values. However, sub-pixel accuracy of the displacement field $\mathbf{u}_i(\mathbf{X})$ demands sub-pixel look-ups of grayscale values in the current image $I_c(\mathbf{x}_i)$. The sub-pixel look-ups are carried out by interpolation of the nearby grayscale values. Systematic errors in the measured displacement may arise from the chosen interpolation function [26], and this is particularly evident for bilinear interpolation. Going from bi-linear interpolation to bi-cubic interpolation, these systematic errors are significantly reduced. A further increase in the order of the interpolation function, e.g. bi-quintic interpolation may further decrease the systematic errors [26], but the computational effort increases significantly with the order of interpolation. In this study the bi-cubic interpolation algorithm presented in [27] has been adopted. **Figure 10** shows examples of the bi-linear and bi-cubic sub-sampling of a 10×10 pixel region. Bi-linear interpolation of a single point requires 2×2 pixel look-ups of the raw pixel data, while bi-cubic interpolation requires 4×4 pixel look-ups. Examples of the pixel look-up regions for a single point are indicated in **Figure 10**.

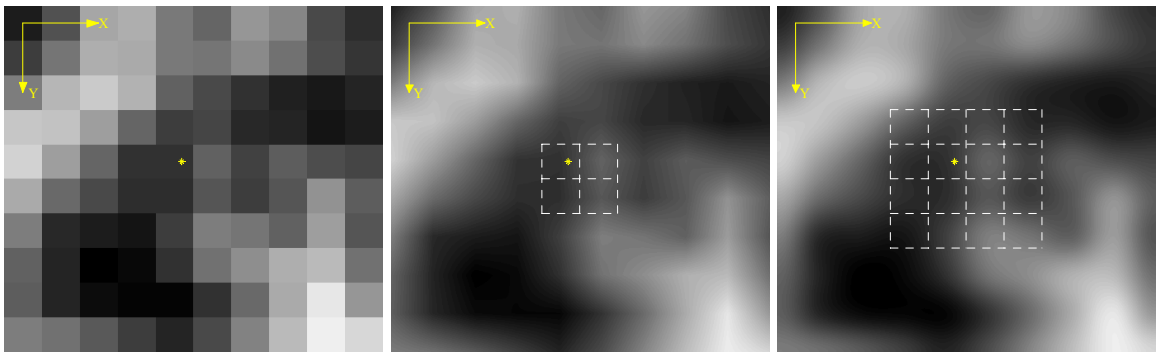

(a) (b) (c)

Figure 10. Interpolation of grayscale values. A raw 10×10 pixel region (a) is shown together with two different sub-pixel samplings of the region using (b) bi-linear and (c) bi-cubic interpolation of the grayscale values. The pixel look-up region (dashed lines) for a specific point (star) is also indicated for the bi-linear and the bi-cubic interpolation.

The subset-based DIC approach, using Newton-Raphson optimization, seems to be the most widely used DIC algorithm in the literature today. However, other formulations of DIC

exist. A particularly interesting formulation of DIC is the "finite-element" based DIC approach presented by Besnard et al. [8]. Here the correlation problem was formulated as a (global) finite-element decomposition on a mesh of Q4 elements. This formulation has also been adopted in this study. Instead of applying individual optimization of subsets, the correlation is carried out as a global optimization on a mesh of elements. Also, instead of optimizing the displacement of the center point and the displacement gradient of the subset, the nodal displacements in the mesh are optimized.

The principle of the "finite-element" based DIC is illustrated in **Figure 11**. Here a single Q4 element located within a mesh is shown. The Q4 element has four nodes (1-4) and the nodal degrees of freedom (u_n, v_n) are also indicated in the figure. The index n here denotes the internal node numbers of the particular element.

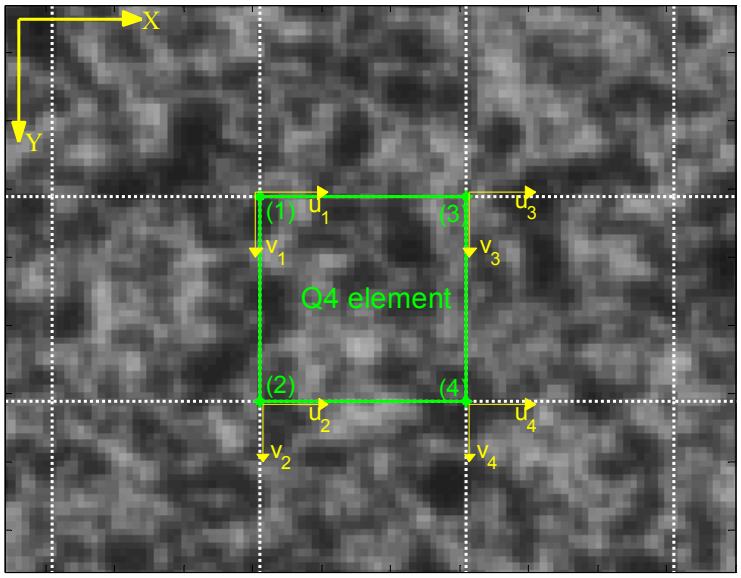

Figure 11. Principle of the "finite-element" based DIC. The nodes (1-4) and the degrees of freedom (u_n, v_n) of a particular Q4 element within a mesh is illustrated.

The major difference between the "finite-element" based DIC approach and the subset-based DIC approach, is that the displacement continuity across the boundaries of elements is preserved. Also, the number of parameters to be optimized for a single element differs between the two approaches. For a single Q4 element, eight parameters (4 nodes × 2 degrees of freedom) need to be optimized, while for a single linear subset, six parameters need to be optimized as described above. The redundant parameters for a Q4 element may in principle

impose increased measurement uncertainty compared to a linear subset. This is partly because each optimization parameter is subjected to measurement noise, and thus the number of optimization parameters should in general be kept on a minimum. For Q4 elements located within a mesh with neighboring elements connected to all nodes, only two extra optimization parameters (one node) per element are required, and the number of optimization parameters per element is therefore reduced compared to the subset approach. It is not clear from the literature whether the "finite-element" based DIC approach gives increased measurement accuracy compared to the subset-based DIC approach [4]. However, Zhang et al. [11] carried out a comparison of the two formulations of DIC and emphasized the benefit of applying the "finite-element" based DIC on complex specimen shapes. Also, keeping the same mesh in numerical modeling as in the "finite-element" DIC may provide benefits. However, the "finite-element" based formulation seems to have higher computational costs than the subset based formulation, as stated by Zhang et al. [11].

The full mathematical formulation of the "finite-element" based DIC from [8] will be presented in the following. The basic assumption is the "conservation of optical flow", i.e. that a particular current image $I_c(\mathbf{X}+\mathbf{u})$ is equal to the reference image $I_r(\mathbf{X})$, given a certain displacement field $\mathbf{u}(\mathbf{X})$. This displacement field may consist of an initially known part $\mathbf{u}'(\mathbf{X})$ and a small unknown part $\Delta\mathbf{u}(\mathbf{X})$, such that $\mathbf{u}(\mathbf{X})=\mathbf{u}'(\mathbf{X})+\Delta\mathbf{u}(\mathbf{X})$. The "conservation of optical flow" yields

$$I_c\left(\mathbf{X}+\mathbf{u}(\mathbf{X})\right)=I_r\left(\mathbf{X}\right). \tag{14}$$

By inserting the initially known coordinates in the current configuration $\mathbf{x}'=\mathbf{X}+\mathbf{u}'$, and the unknown incremental part of the displacement $\Delta\mathbf{u}$, this becomes

$$I_c(\mathbf{X}+\mathbf{u}'(\mathbf{X}))=I_c\left(\mathbf{x}'\right)=I_r\left(\mathbf{X}-\Delta\mathbf{u}(\mathbf{X})\right). \tag{15}$$

The incremental part of the displacement is here subtracted from the reference configuration coordinates $\mathbf{X}$ at the right-hand side of the equation, but it may alternatively be added to the current configuration coordinates $\mathbf{x}'$ at the left-hand side. By the choice made here, the reference configuration is used as basis for the following derivation. A first order Taylor expansion is carried out on the unknown part of the displacement field in Equation (15), where it is assumed that the reference image I_r is differentiable. This gives

$$I_c(\mathbf{x}') = I_r(\mathbf{X}) - \Delta\mathbf{u}(\mathbf{X}) \cdot \nabla I_r(\mathbf{X}) . \tag{16}$$

Now, the sum of squared differences in grayscale values (see Equation (13)) between the reference image I_r and current image I_c is integrated over a pixel region Ω, giving

$$F = \iint_{\Omega} \left[\Delta\mathbf{u}(\mathbf{X}) \cdot \nabla I_r(\mathbf{X}) + I_c(\mathbf{x}') - I_r(\mathbf{X}) \right]^2 d\mathbf{X} . \tag{17}$$

The displacement field increment $\Delta\mathbf{u}(\mathbf{X})$ is then decomposed over a set of elements. In the following derivation, the pixel region Ω^e corresponds to a particular element e. The decomposition of the displacement field increment within a particular element is described as

$$\Delta\mathbf{u}^e(\mathbf{X}) = \sum_{\alpha} \sum_{m} a_{\alpha m} N_m(\mathbf{X}) e_{\alpha} \tag{18}$$

where m is a local node index of the element and $N_m(\mathbf{X})$ is the shape function of the node m. The subscript α denotes a particular axis and $a_{\alpha m}$ is the degrees-of-freedom amplitude corresponding to the node m and the axis α. e_{α} is a unit vector along axis α. Inserting Equation (18) into Equation (17) gives

$$F = \iint_{\Omega^e} \left[\sum_{\alpha} \sum_{m} a_{\alpha m} N_m(\mathbf{X}) \nabla I_r(\mathbf{X}) \cdot e_{\alpha} + I_c(\mathbf{x}') - I_r(\mathbf{X}) \right]^2 d\mathbf{X} . \tag{19}$$

The expression is then differentiated by a and set to zero to find the minimum of F, viz

$$\frac{\partial F}{\partial a} = \iint_{\Omega^e} 2 \left[\sum_{\beta} \sum_{n} a_{\beta n} N_n(\mathbf{X}) \frac{\partial I_r(\mathbf{X})}{\partial X_{\beta}} + I_c(\mathbf{x}') - I_r(\mathbf{X}) \right] \cdot N_m(\mathbf{X}) \frac{\partial I_r(\mathbf{X})}{\partial X_{\alpha}} d\mathbf{X} = 0 . \tag{20}$$

The minimization of F leads to a linear system of equations

$$\sum_{\beta} \sum_{n} a_{\beta n} \iint_{\Omega^e} N_m(\mathbf{X}) N_n(\mathbf{X}) \cdot \frac{\partial I_r(\mathbf{X})}{\partial X_{\alpha}} \cdot \frac{\partial I_r(\mathbf{X})}{\partial X_{\beta}} d\mathbf{X} = \iint_{\Omega^e} \left[I_r(\mathbf{X}) - I_c(\mathbf{x}') \right] \cdot N_m(\mathbf{X}) \cdot \frac{\partial I_r(\mathbf{X})}{\partial X_{\alpha}} d\mathbf{X} \tag{21}$$

which can be written in the compact form

$$\mathbf{M}^e \mathbf{a}^e = \mathbf{b}^e \tag{22}$$

where $\mathbf{a}^e$ is a vector containing the unknown incremental nodal displacements. $\mathbf{M}^e$ is a matrix and $\mathbf{b}^e$ is a vector defined by the following expressions collected from Equation (21)

$$M^e_{\alpha m \beta n} = \sum_{\Omega^e} N_m(\mathbf{X}) N_n(\mathbf{X}) \frac{\partial I_r(\mathbf{X})}{\partial X_\alpha} \frac{\partial I_r(\mathbf{X})}{\partial X_\beta} \tag{23}$$

$$b^e_{\alpha m} = \sum_{\Omega^e} \left[I_r(\mathbf{X}) - I_c(\mathbf{x}') \right] N_m(\mathbf{X}) \frac{\partial I_r(\mathbf{X})}{\partial X_\alpha}. \tag{24}$$

Here, the integration operator in Equation (21) is replaced by a summation operator. The integration is thereby carried out as a summation over all pixels within the element region Ω^e in the reference configuration. The global equation for an entire mesh of elements is defined as

$$\mathbf{Ma} = \mathbf{b} \tag{25}$$

where the global $\mathbf{M}$ and $\mathbf{b}$ is built by the assembly of element contributions in $\mathbf{M}^e$ and $\mathbf{b}^e$. The global matrix $\mathbf{M}$ is symmetric and sparse, which should be exploited to make the building and solving process efficient. The global incremental nodal displacements in $\mathbf{a}$ are solved from Equation (25). This is a solution to the first order Taylor expansion, imposed in Equation (16). This particular problem is however generally non-linear. Thus, to obtain an accurate solution to the displacement field $\mathbf{u}(\mathbf{X})$ in a current image I_c, the process should be carried out in an iterative process, updating the "known" part of the displacement field $\mathbf{u}'(\mathbf{X})$ between each iteration.

A large variety of element types and shape functions N_m may be incorporated into Equations (23) and (24). In this study, isoparametric Q4 elements [33] are applied as default. Each element is mapped onto a unit square $[0,1]^2$ in a normalized coordinate system (ξ,η) giving the shape functions $N_1 = (1-\xi)(1-\eta)$, $N_2 = (1-\xi)\eta$, $N_3 = \xi(1-\eta)$ and $N_4 = \xi\eta$. The mapping from the normalized coordinate system (ξ,η) to the image coordinate system (X,Y) is now given by

$$\mathbf{X} = \sum_{m=1}^{4} N_m(\xi,\eta) \mathbf{X}_m \tag{26}$$

where $\mathbf{X}_m$ denote the location of the node with index m. This isoparametric approach removes the rectangular restriction of the Q4 element such that meshes with any convex quadrilateral element shape can be applied. The displacement $\mathbf{u}(\mathbf{X})$ at an arbitrary location inside an element is calculated as a weighted sum of the nodal displacements $\mathbf{u}_m$ where the weight factors are given by the shape functions $N_m(\mathbf{X})$, so that $\mathbf{u}(\mathbf{X}) = \sum_m N_m(\mathbf{X})\mathbf{u}_m$.

To further extract physical data from the image analysis, a camera model should be applied to convert the measurements in image coordinates to physical target coordinates as described in Sections 5.1 and 5.2. For the two-dimensional DIC analyses in this study, the camera model in Equation (5) has been adopted. For three-dimensional analyses, the camera model in Equation (9) was applied. Because the camera model in Equation (5) only contains a scaling and a translation of the image coordinates to obtain physical coordinates, the strain calculations has for the 2D analyses been carried out directly from the measured displacement field $\mathbf{u}(\mathbf{X})$. These strain calculations will be presented in the following.

The two-dimensional deformation gradient $\mathbf{F} = \mathbf{F}(\mathbf{X},t)$ are firstly calculated from the measured two-dimensional displacement field $\mathbf{u}(\mathbf{X})$ as

$$\mathbf{F} = \frac{\partial \mathbf{x}}{\partial \mathbf{X}} = \mathbf{1} + \frac{\partial \mathbf{u}}{\partial \mathbf{X}}. \tag{27}$$

The two-dimensional Green deformation tensor $\mathbf{C} = \mathbf{C}(\mathbf{X},t)$ are then calculated from the deformation gradient as

$$\mathbf{C} = \mathbf{F}^T\mathbf{F}. \tag{28}$$

The in-plane principal stretches $\mu_i = \mu_i(\mathbf{X},t)$, $i = 1,2$ are found by solving the eigenvalue problem for the Green deformation tensor

$$\left(\mu_i^2\mathbf{1} - \mathbf{C}\right)\cdot\mathbf{n}_i = \mathbf{0}, \tag{29}$$

where $\mathbf{n}_i$ are the principal directions of the Green deformation tensor. It should here be noted that because of the two-dimensional nature of the DIC measurements, the third principal direction $\mathbf{n}_3$ is assumed to be normal to the surface of the specimen, i.e. the shear strains

through the thickness of the specimen are assumed negligible. The in-plane logarithmic principal strains $\varepsilon_i = \varepsilon_i(\mathbf{X},t)$, $i = 1,2$ are then calculated as

$$\varepsilon_i = \ln(\mu_i), \; i = 1,2 \tag{30}$$

For the experimental tests presented in this thesis, negligible elastic strains and plastic incompressibility has been further assumed. Thus, the logarithmic principal strain in the thickness (out-of-plane) direction $\mathbf{n}_3$, has been estimated as

$$\varepsilon_3 = -(\varepsilon_1 + \varepsilon_2). \tag{31}$$

An effective strain measure $\varepsilon_{eff} = \varepsilon_{eff}(\mathbf{X},t)$ is then defined based on the von Mises norm as

$$\varepsilon_{eff} = \sqrt{\frac{2}{3}\left(\varepsilon_1^2 + \varepsilon_2^2 + \varepsilon_3^2\right)} = \sqrt{\frac{4}{3}\left(\varepsilon_1^2 + \varepsilon_1\varepsilon_2 + \varepsilon_2^2\right)} \tag{32}$$

It is noted that when (isoparametric) Q4 elements are used, the deformation gradient is constant within a single element. Thus, the effective strain values are firstly calculated for each element in the mesh and then the element strain values are distributed to generate an effective strain map $\varepsilon_{eff}(\mathbf{X})$ covering the measured region.

6. Development of a DIC code

The main part of this thesis work has focused on the development of a DIC code for analysis of images recorded from mechanical experiments. This section will provide an overview of the development process and the functionalities that have been incorporated into the developed DIC code.

Initial codes of both the subset-based DIC [5] and the "finite-element" based DIC [8] were built. The two formulations seemed to provide close to identical results in some initial tests. A choice was however made to apply the "finite-element" DIC formulation as basis for this study. Keeping similar formulations in experimental measurements (DIC) as in numerical modeling (FEM) was here seen as a potential advantage.

Figure 12 shows a pseudo-code representation of the "finite-element" based DIC core used as basis in this study. The input parameters to the DIC core is a structure, called "mesh", containing information on all elements and nodes in the mesh, the reference image and the

grayscale gradient in the reference configuration. The DIC core calculates the updated nodal displacements in the current image and returns the structure "mesh" with updated nodal displacements.

```
    global  mesh    (a struct which contains information on all elements and nodes)
            Ir      (reference image)
            gx,gy   (grayscale gradient in X- and Y-direction)

    Ic = load current image
    a = vector a[noDOF x 1] from node displacments in "mesh" (noDOF = number of active nodes * 2)
(a) M = Build (sparse) matrix M[noDOF x noDOF]
    for i = 1:maxIter
(b)     [u,v] = Displacement maps from node displacements in "a"
(c)     Ic_R = Current image "Ic" transformed to reference config using bi-cubic interpolation
(d)     b = Build vector b[noDOF x 1]
(e)     Solve: da = M\b
        Add increments in node displacements: a = a + da;
        if(mean(abs(da)) < dispLimit)
            break; (Correlation criteria reached))
        end
    end
    Update node displacements in "mesh" from "a"
```

Figure 12. Pseudo-code illustrating the core of the DIC implementation. The code shows the correlation of a single image (the current image, "Ic"). The input parameters to the DIC core are a structure containing information on all elements and nodes ("mesh"), the reference image ("Ir") and the grayscale gradient ("gx" and "gy") in the reference configuration. The nodal displacements in "mesh" are updated after the correlation has finished.

Two vital parameters for the correlation have to be set by the user, i.e. the maximum number of iterations ("maxIter") and the correlation criterion on the mean nodal displacement increments ("dispLimit"). Throughout this study, the maximum number of iterations ("maxIter") has been set to 10 and the mean nodal displacement limit ("dispLimit") has been set to $1 \cdot 10^{-6}$. It is appreciated that the correlation criterion in DIC is an important topic of research, especially for the subset-based DIC approach, where correlation criteria based on grayscale differences are widely used [28]. A detailed study on different correlation criteria has not been carried out here. However, the correlation criterion described above has provided satisfactory results in the image analyses carried out throughout this study.

Another important feature when analyzing image series using DIC, is the choice of reference image I_r. When analyzing a current image I_c where high displacement gradients are present, the Q4 elements may not be able to describe the relevant displacement field with their first-order shape functions. This appears if there are large displacement gradients

between the current I_c and the reference image I_r. Updating the reference image (to the current image) "resets" the high correlation residuals caused by high-displacement gradients in the specimen and thus helps the DIC analysis to proceed even when high-displacement gradients are present. The downside of reference-image updates is that the measurement errors in the new reference image are added to the remaining images in the series. In this study, the reference-image update has been kept to a minimum, but has been applied for image series where large displacement gradients have been present.

6.1 Increasing computational speed

This subsection will contain a description of the work carried out to increase the computational speed of the DIC code. The DIC code was firstly developed in MathWorks MATLAB [29]. MATLAB provides a straight-forward development environment with fast and easy debugging and without the need for compilation of the code. Also, the visualization features of MATLAB have been found valuable and are therefore widely used throughout this study. The downside of using MATLAB is the computational speed, and even though the initial versions of the DIC code were implemented using standard MATLAB scripting, it was proven to be impractically slow when analyzing large series of high-resolution images.

The most computationally expensive routines in the DIC code are (a) the building of $\mathbf{M}$, (b) the generation of displacement maps, (c) the bi-cubic interpolation of the current image, (d) the building of $\mathbf{b}$ and (e) the solving for $\mathbf{a}$ (see **Figure 12**). The latter four, (b) – (e) are routines that are carried out for each iteration in the DIC core and will therefore significantly influence the computational time of the analysis. For the routines (a) – (d), precompiled MEX functions were made and incorporated into the code. The MEX application programming interface (API) in MATLAB allows functions to be coded in the programming language C and called directly from MATLAB scripts or functions. The precompiled MEX functions of (a) – (d) have significantly decreased the computation time in the DIC code.

When it comes to the routine (e), solving for the incremental node displacements in $\mathbf{a}$, it was as expected found that the operations ran significantly faster if $\mathbf{M}$ was firstly defined as a sparse matrix. Also applying the "left-division operator" in MATLAB (see **Figure 12**) was significantly faster than the operation $\mathbf{M}^{-1} \cdot \mathbf{b}$. In the latter (and slower) case, the matrix $\mathbf{M}$ is first inverted (before the iteration loop) and then multiplied with $\mathbf{b}$ (inside the iteration loop).

The inversion of large matrices is a computationally expensive process which was here avoided by applying the "left-division operator" in MATLAB.

To further increase the computational speed of the code, effort was made to implement some of the computational expensive routines in parallel, using the OpenMP API [30]. This was directly incorporated into the precompiled MEX functions. The routines in (a) - (d) were all found to be significantly faster when implemented in parallel. However, as the routines in (b) and (c) was easily converted to parallel implementation with single threads acting on single elements and single pixels, the parallelization of (a) and (d), i.e. the building of $\mathbf{M}$ and $\mathbf{b}$, required reformulations of Equations (23) and (24) in Section 5.4.

In Equation (23) and (24) the element contributions $M^e_{\alpha m \beta n}$ and $b^e_{\alpha m}$ are first calculated, and these are further used to assemble the global variables $\mathbf{M}$ and $\mathbf{b}$ in Equation (25). Each column and row in $\mathbf{M}$ and each component in $\mathbf{b}$ corresponds to a single node. Because each node may be connected to several elements and the nodal contribution is calculated as an accumulation of contributions of its connected elements, the assembly of $\mathbf{M}$ and $\mathbf{b}$, in Equations (25), has to be carried out in a serial fashion. However, by assembling the global $\mathbf{M}$ and $\mathbf{b}$ from nodal contributions directly, the process can be carried out in parallel. The building of the global $\mathbf{M}$ and $\mathbf{b}$ now becomes

$$M_{\alpha m \beta n} = \sum_{e \in E_{mn}} \sum_{\Omega^e} N^e_m N^e_n \frac{\partial I_r}{\partial X_\alpha} \frac{\partial I_r}{\partial X_\beta} \tag{33}$$

$$b_{\alpha m} = \sum_{e \in E_m} \sum_{\Omega^e} \left[I_r(\mathbf{X}) - I_c(\mathbf{x}') \right] N^e_m \frac{\partial I_r}{\partial X_\alpha} \tag{34}$$

where the index e indicates the element over which the summation is carried out, E_m contains all elements connected to node m, while E_{mn} contains all elements connected to both node m and n. It is noted that (m,n) here indicate the global node indices. When the degrees of freedom for each node are equal to two (horizontal and vertical displacement), each node-pair of rows in $\mathbf{M}$ and each node-pair of components in $\mathbf{b}$ are calculated independently. Thus, the calculations are suitable for a parallel implementation, and the number of independent computational threads may in principle be as high as the number of nodes in the mesh. The parallelized DIC code was compared to the serial DIC code, and a

speed-up factor of about five was accomplished for the parallel code when running on a dual quad-core (Intel Xeon E5430) platform (eight independent threads) using the OpenMP API.

Table 4 gives an evaluation of computational times of the final and optimized DIC core and its sub-functions for varying mesh sizes (number of elements). The DIC analyses are carried out on images with 2448×2050 spatial resolution and meshes with 30×30 Q4 elements. It is seen that the most computational expensive routines are now (b) the displacement map generation and (c) the bi-cubic interpolation. It is also seen that the DIC routine contains a significant amount of overhead, i.e. the computational time is still more than one second even for small meshes.

Table 4. The computational time for the algorithms (a) – (d) within the DIC core as well as the full DIC core with 5 iterations. Results are collected for different mesh sizes (number of Q4 elements). The element size is 30x30 and the spatial image resolution is 2448x2050.

Mesh size (No. of elements)		*50*	*100*	*500*	*1000*	*1500*
(a) Building M	[ms]	2.6	6.0	16	32	46
(b) Disp. map. generation	[ms]	14	18	43	70	103
(c) Bi-cubic interpolation	[ms]	95	99	116	130	132
(d) Build B	[ms]	1.8	3.2	13	17	32
(e) Solve da = M\b	[ms]	0.15	0.4	6	8	15
Full DIC core (5 iterations)	[ms]	1352	1344	1661	1951	2333

Even though the optimization of the code has been an important part of this work, it is appreciated that there are still room for improvement of the implemented DIC algorithm when it comes to computational speed. Because MATLAB was used as the development environment, the computational speed of the DIC code can be further increased by developing a stand-alone DIC code in e.g. C++. However, because all the computational expensive routines already are coded in precompiled MEX functions, it is believed that a stand-alone C++ application will only provide a minor speed-up factor compared to the MATLAB code. This has also been supported by some initial implementations in C++.

Further effort was made to apply the computational architecture CUDA [31], and thus running the computationally expensive processes of the DIC core on a Graphical Processing Unit (GPU). Especially, the bi-cubic interpolation (c) seemed like a likely candidate for a GPU implementation, but also the other computational expensive routines in the DIC core which now were already parallelized. CUDA was firstly released in 2007, and at the time of this particular work, the CUDA implementation was only available through a stand-alone

C++ application. Lately, it has however been possible to incorporate the CUDA functionality through MATLAB`s "MEX API providing the possibilities of calling custom-made GPU functions directly from MATLAB scripts or functions. The bi-cubic interpolation function [27] was implemented in CUDA and ran on an Nvidia Quadro FX 370 GPU. It was compared to the same bi-cubic interpolation function implemented in a serial fashion on an Intel Xeon E5430 CPU. The GPU implementation did not provide any significant speed-up compared to the serial CPU implementation. The bi-cubic interpolation of a single point in an image includes 16 texture (image) look-ups which seemed particular expensive for this specific GPU hardware. In addition, the CUDA implementation was not optimized with shared memory within thread blocks (see [31] for a discussion on memory optimization in CUDA). Because of the results described above, the particular available GPU hardware was only being capable of single-precision (floating point) operations, and the coding in CUDA was time-consuming and far from straight forward, the work on a CUDA-DIC implementation was not continued in this study. It is however believed that with increasingly faster GPUs on the market, the DIC formulation will become a very suitable candidate for a GPU implementation.

These efforts on speeding up the DIC code have been absolutely vital for the work presented in this thesis. A future goal is to carry out real-time analysis of images in quasi-static tests with recording rates in the range 1-5 Hz. This involves analyzing images at the same rate as they are recorded, providing e.g. strain-field measurements during experimental tests. This goal has not been reached during this study. However, due to the continuously ongoing development of faster computational hardware (especially for general-purpose GPUs), real-time DIC analyses may become practical by applying suitable optimized heterogeneous programming, i.e. combining serial and parallel codes on different computing platforms.

6.2 Handling cracked specimens

In the DIC algorithm, a current image I_c is compared (correlated) to a reference image I_r. The fundamental assumption of DIC is the "conservation of optical flow", i.e. that the current image is assumed equal to the reference image given a specific continuous displacement field. A crack that propagates through the specimen will, in this respect, represent a diversion from this initial assumption. The propagating crack adds a new artifact into the deformed image which is not present in the reference image, i.e. the crack opening

region. If the crack propagates through a region covered by the DIC mesh, this will give increased grayscale residuals Φ in this particular region. The grayscale residual Φ is here defined as

$$\Phi(\mathbf{X}_i) = \sqrt{[I_c(\mathbf{x}_i) - I_r(\mathbf{X}_i)]^2} \tag{35}$$

where the index i denotes a specific pixel. The increased residuals will give increased values in $\mathbf{b}$, and thus increased and erroneous values in the incremental node displacements $\mathbf{a}$. The propagating crack will first affect the nodes connected to elements directly cut by the crack. However, because of the preserved continuity in the "finite-element" based DIC, the propagating crack will indirectly affect nodes in a relatively large region around the cracked region of the specimen. Also, in many cases of material testing, the cracked region is the most interesting part of a particular specimen. Thus, effort has to be made to carry out measurements as closely as possible to the crack and at the same time avoiding the crack-induced degradation of the DIC process. A typical example of the raised grayscale residuals Φ, caused by a propagating crack is shown in **Figure 13**(a).

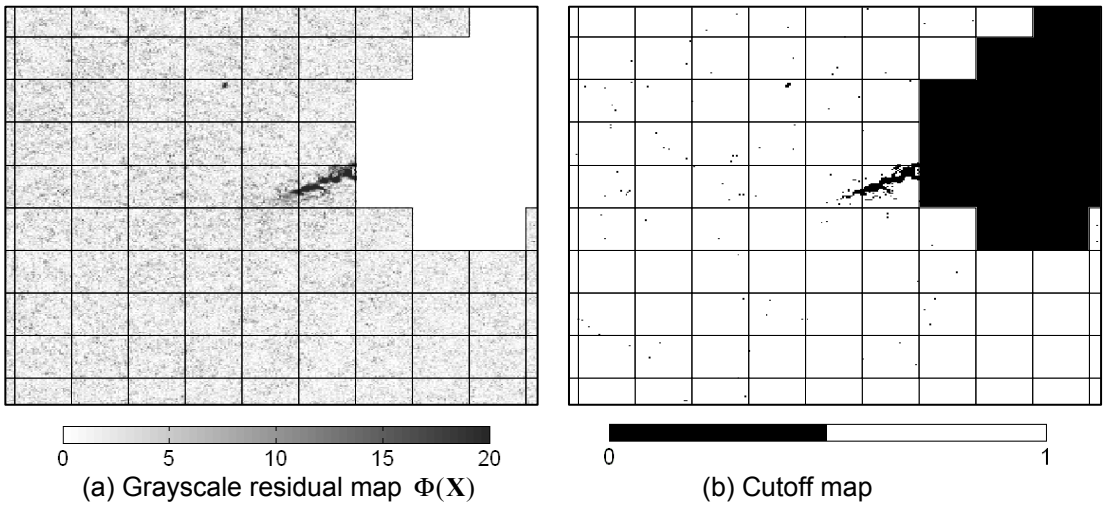

Figure 13. (a) Gray scale residual map $\Phi(\mathbf{X})$ in a region of a propagating crack. The emerging crack is still not visible in the corresponding current image I_c, but can easily be identified in the grayscale residual map. (b) The cutoff map calculated from the residual map in (a) with a cutoff multiplier of $C_{cut} = 3.5$.

6.2.1 PIXEL CUTOFF

In this study, the initial effort to avoid the crack-induced grayscale residuals was to apply a certain filtering of pixels based on grayscale values. The pixels with grayscale residuals above a certain limit $\Phi_i > \Phi_{\lim}$, called cutoff-pixels, were neglected in the building of $\mathbf{M}^e$ and $\mathbf{b}^e$ in Equations (23) and (24). The cutoff limit was defined as a user-specific parameter C_{cut} multiplied with the mean grayscale residual level $\bar{\Phi}$ within the measured region of the current image, such that $\Phi_{\lim} = C_{cut}\bar{\Phi}$. **Figure 13**(b) shows the corresponding cutoff map for the grayscale residual map in **Figure 13**(a) where the cutoff multiplier is $C_{cut} = 3.5$. The cutoff-pixel approach is described in Part IV of this thesis, and is shown to increase the robustness of the correlation in regions which are compromised by a propagating crack.

6.2.2 ELEMENT REFINEMENT AND EROSION

Next, an automatic mesh adaptation approach was developed and tested. The governing idea was to avoid the cracked region of the specimen and at the same time obtaining valid measurements close to the crack. The developed mesh adaptation technique involved refinement and erosion of elements, carried out based on a set of criteria, during the analysis of an image series.

The erosion of a single element was done by merely setting an element as inactive. This technique is known as element erosion standard finite element codes (see e.g. [34]).The element refinement, on the other hand, was carried out by adding an extra node in the centre of the element and replacing the parent element with four sibling elements. This procedure is similar to element refinement techniques (h-adaptivity) used in the finite element method [35]. The four sibling elements are also isoparametric Q4 elements with the same shape functions as their parent. **Figure 14** illustrates the process of refinement of the DIC mesh. In Mesh 1, a parent element has been split into 4 sibling elements (E7, E8, E9 and E10). In order to preserve continuity of the shape functions, the nodes generated for the sibling elements that borders to a parent element (n14, n15 and n17) must be slave nodes (indicated as diamond shape in **Figure 14**). Thus, these nodes are not optimized in the DIC analysis as opposed to the master nodes (indicated as circles in **Figure 14**) The displacements of the slave nodes are calculated as a weighted sum of the displacements of its neighboring master nodes. Mesh 2 in **Figure 14** shows a further refinement of Mesh 1. Element (E3) has been split into 4 new sibling

elements. In this case, node (n14) no longer needs to be a slave node in order to preserve continuity. Thus, node (n14) is upgraded to a master node and its displacement is then optimized in the DIC analysis.

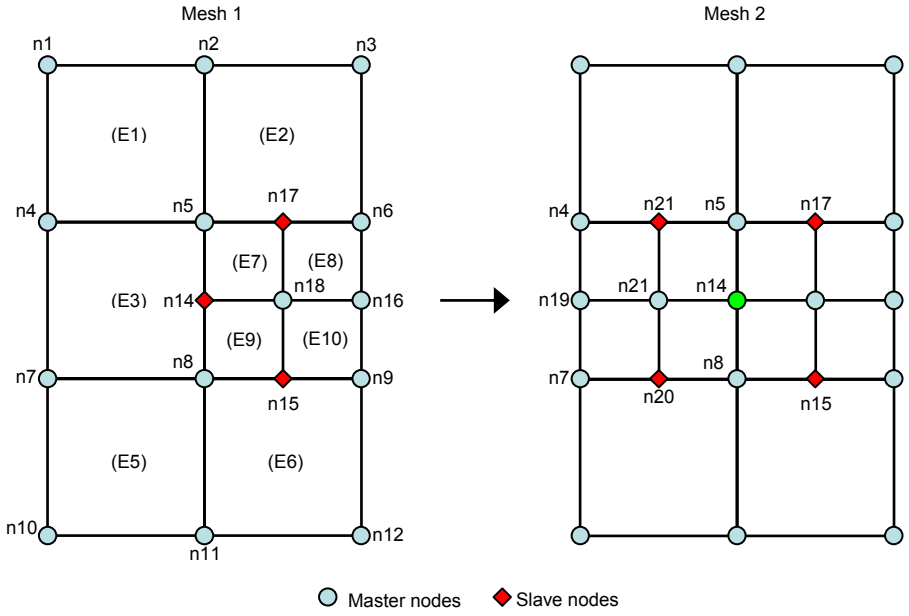

Figure 14. The principle of element refinement of Q4 elements. Slave nodes (nodes that are not optimized in the DIC process) are indicated as diamond shapes. Master nodes (nodes that are part of the DIC optimization) are indicated as circles. E# indicates the element indexing and n# indicates the node indexing, where # denotes a specific index.

The criteria for refinement and erosion during the DIC analysis were based on the calculated cutoff map described above, and illustrated in **Figure 13**(b). An element which had more than 5% cutoff pixels was refined. A lower limit (10 pixels) on element side lengths was also incorporated, preventing the elements to reach a size that is too small for optimal correlation. An element which had reached the lower size limit and had more than 20% cutoff pixels was eroded. The process of refinement and erosion is illustrated in **Figure 15**. Here the DIC mesh is plotted on top of the cutoff map. An element which is cut by the crack is first refined and then the sibling elements that eventually reach the erosion criteria are eroded.

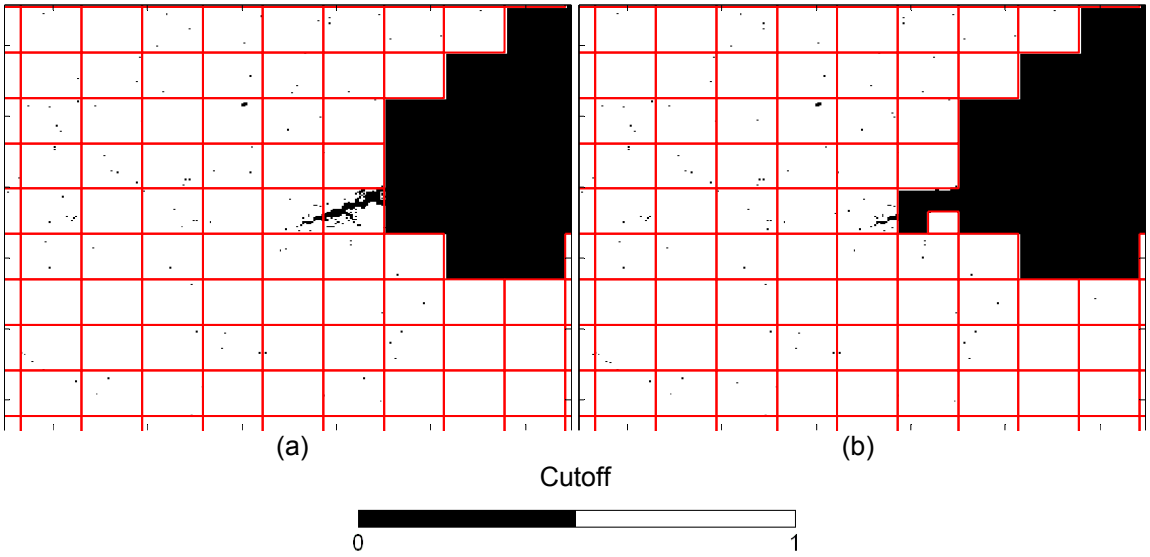

Figure 15. (a) A cutoff map generated from the grayscale residual map. An emerging crack causes an accumulation of cutoff pixels in the region of the crack. (b) Adaption of the DIC mesh due to a high degree of cutoff pixels in an element. The parent element is first split into four equally sized elements, and then three of the sibling elements are found to have a relative amount of cutoff pixels above the erosion limit and are thus eroded.

The automatic mesh adaptation procedure concerning refinement and erosion of elements was applied in the experimental study presented in Part II of this thesis. It is however noted that for this approach to succeed, a certain degree of tuning of parameters was needed. The cutoff multiplier C_{cut}, the refinement limit and the erosion limit had to be tuned in initial analyses to obtain satisfactory evolution of the automatically adapted mesh. The approach also had a drawback in that it did not provide a proper discontinuous displacement field of the cracked region. Further, the small and refined elements close to the crack had significant reduced measurement accuracy compared to elements in the remaining part of the mesh. The reasons for this may be reduced accuracy in the small elements and in the elements at the boundary of the mesh, as is discussed in Part IV of this thesis.

6.2.3 NODE SPLITTING AND OVERLAPPING MESH

Because of the drawbacks described for the refinement-erosion approach, the work on this technique was not continued. Instead, mesh adaptation techniques based on node splitting were investigated. These techniques require that the crack path (in reference configuration) is determined in an initial DIC analysis. This is done by applying a DIC analysis with standard Q4 elements. The cutoff-pixel approach is used to increase the robustness of the analysis.

Then the crack path is extracted by manually studying the grayscale residual maps (as illustrated in **Figure 13**(a)) or the current image I_c transformed back to reference configuration. An adapted mesh of isoparametric Q4 elements is then generated with duplicate nodes along the crack path. **Figure 16** illustrates the principle of node splitting in DIC. It is seen that the duplicate nodes separate and the mesh "opens up" as the crack propagates through the specimen.

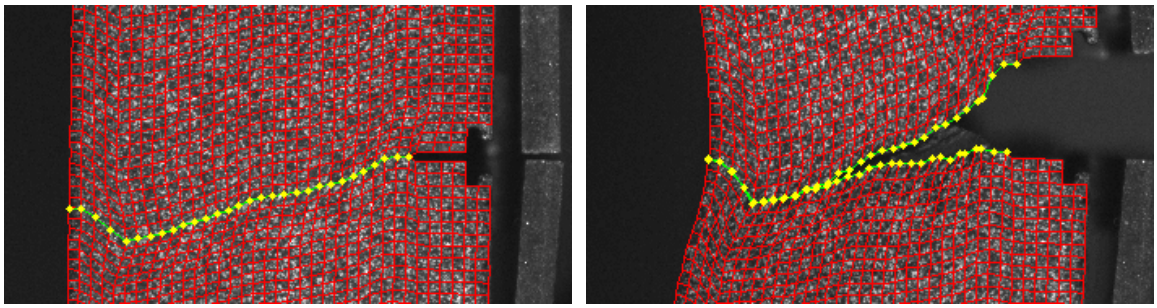

(a) (b)

Figure 16. Illustration of the principle of node-splitting in DIC. The mesh is plotted on top of (a) the reference image and (b) the current image.

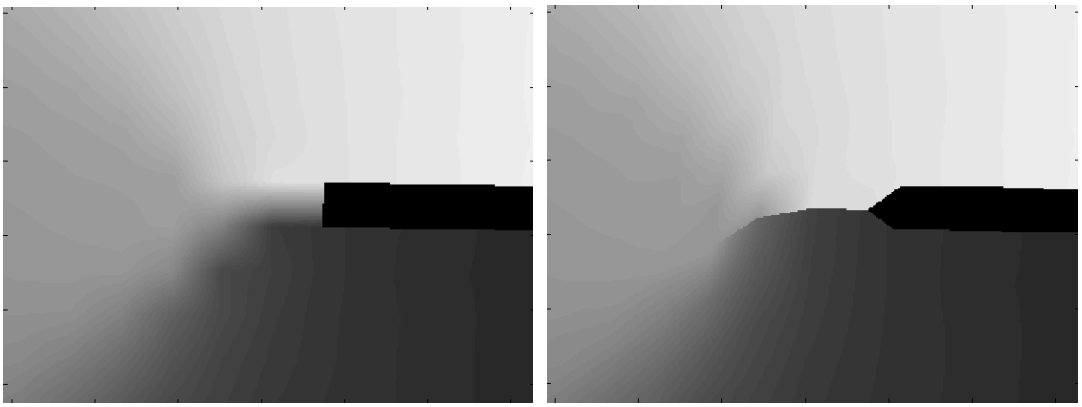

(a) (b)

Figure 17. Measured displacement field in a cracked region for DIC analysis using (a) standard Q4 elements and (b) node splitting with isoparametric Q4 elements.

In **Figure 17**, measured displacement fields in a cracked region from two different DIC analyses are presented, one displacement field from a standard analysis using Q4 elements and one displacement field from an analysis using node splitting. It is seen that the node-splitting approach successfully captures the discontinuous displacement field of the crack, whereas the displacements in the cracked region are averaged out in the standard DIC analysis. An experimental study where the node-splitting approach is incorporated is

presented in Part III of this thesis. Also, an investigation of measurement uncertainties in displacement and strains in the cracked region, using DIC with node splitting, is presented in Part IV of this thesis.

The node-splitting approach has been further improved using a novel technique called "overlapping mesh". In this technique the elements containing duplicate nodes are extended across the crack path. Thus, the elements along the crack path are overlapping in a region covering the crack path. A crack-path mask is then applied to determine which side of the crack path a specific pixel belongs. The overlapping-mesh technique is illustrated in **Figure 18**. The mesh is divided in two parts, one on each side of the crack path. The pixels located within mesh part 1, but outside the defined region of part 1 in the mask, are neglected in the building of $\mathbf{M}^e$ and $\mathbf{b}^e$ in Equations (23) and (24). The same yields for part 2.

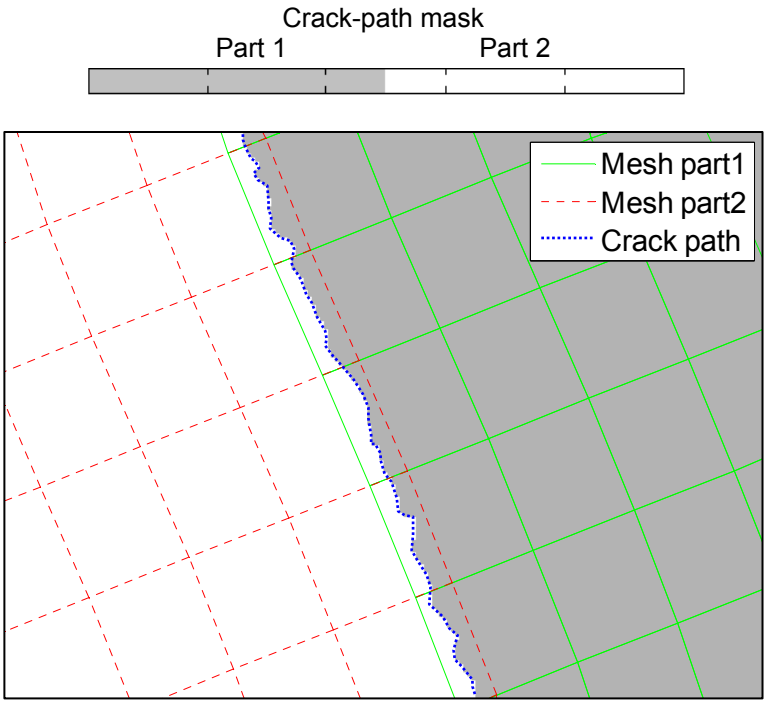

Figure 18. Principle of overlapped mesh with crack-path mask. The image shows the part mask (in reference configuration) defined by the location of the crack path (indicated in blue) and the overlapping mesh. The pixels located within mesh part 1, but outside the defined region of part 1 in the mask, are neglected in the correlation. The same yields for part 2. The crack path (and thus the part mask) is not restricted to the same part-wise linearization as the element boundaries and may be defined at pixel level.

Applying the overlapping-mesh technique, the crack path may be defined down to pixel level in the reference image. This is an improvement compared to the node-splitting technique, where the crack path is partwise linearized by the element side lengths. Part IV in

this thesis gives a detailed description of the overlapping-mesh technique and also introduces a technique for optimization of the crack path, similar to the crack-path optimization in [13]. By applying this crack-path optimization, the crack path may be located with sub-pixel accuracy in the reference configuration. The crack-path optimization will not be described here, as it is covered in detail in Part IV.

When applying the node-splitting and overlapping-mesh approaches, the correlation is carried out close to the crack boundaries. The boundaries of the elements in the mesh are sharply defined such that the pixels located within the crack opening region of the current image should be avoided in the DIC optimization. However, it should here be noted that the bi-cubic interpolation, which uses a 4×4 pixel-region look-up, may violate this sharply defined boundary. Thus, pixels that are located close to the crack boundary may be affected by the crack-opening region through the bi-cubic interpolation. An example of bi-cubic interpolation close to a sharply defined boundary is presented in **Figure 19**. It is seen that the bi-cubic interpolation averages out the grayscale values across such a sharp boundary.

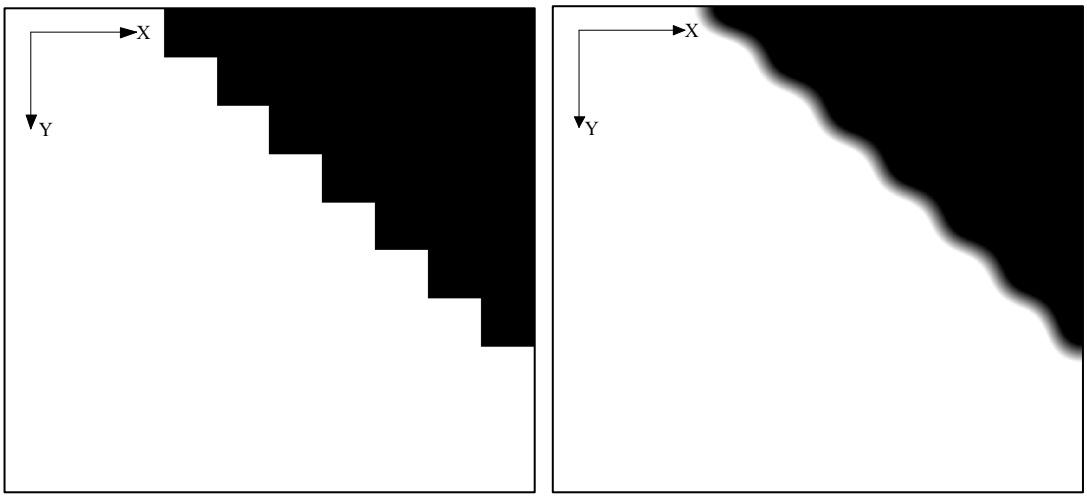

Figure 19. Bi-cubic interpolation at a sharply defined boundary. (a) A raw 10×10 pixel region with a sharply defined boundary. (b) Bi-cubic sub-sampling of the 10×10 pixel region in (a).

The negative effect on the bi-cubic interpolation close to a crack has been appreciated throughout this study. Considerations have been made to reduce the order of interpolation for the pixel affected by this degradation. The problem has been partly solved by adding a fixed mask, neglecting the pixels closest to the crack in the DIC analysis. This has (to some extent)

helped increasing the robustness of the DIC analyses using node splitting and overlapping mesh.

6.3 Uncompleted studies

Throughout the thesis work carried out on the DIC code, a number of different techniques and approaches have been tested. The main achievements in the DIC code are covered in Sections 6.1 and 6.2, as well as in Parts II, III and IV. This subsection aims to give a brief overview of all techniques (in DIC) that have been tested throughout this study, whether or not they have led to successful or publishable results. **Figure 20** shows a graphical representation of all DIC techniques that have been subject to investigation in this study. The two-dimensional "finite-element" based DIC approach, using isoparametric Q4 elements, represents the basis for all the work done on DIC. The boxes with solid borders represent techniques that have successfully led to results presented in Parts II, III and IV. These techniques are also covered in Sections 6.1 and 6.2. However, the boxes with dashed borders represent techniques which have been subject to investigation, but have not led to any significant results within the time frame available in this Ph.D.-study. These techniques will here be given a brief discussion.

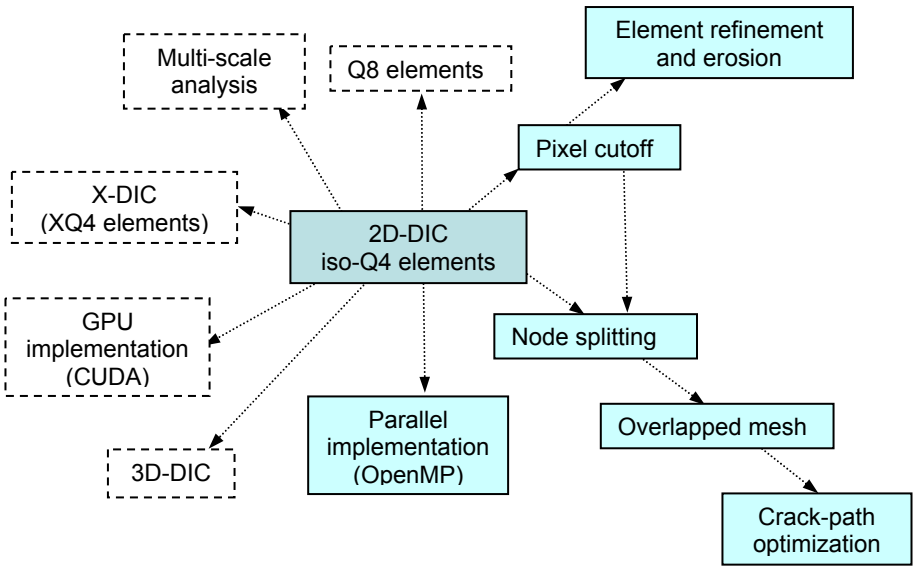

Figure 20. A graphical overview of the functionality that has been investigated and tested in the DIC code. In the centre is the two-dimensional DIC approach using isoparametric Q4 elements, which represents the basis for the work done on DIC in this study.

Q8 elements using second order shape functions N_i have been incorporated into the DIC code and briefly tested. However, due to the 16 degrees of freedom per element (compared to 8 degrees of freedom for a Q4 element), Q8 elements are more susceptible to grayscale noise in the images when compared to an equally sized Q4 element. Thus, Q8 elements need in general to be larger than Q4 elements to overcome the grayscale noise. However, it is appreciated that the higher order shape functions of the Q8 elements may represent a benefit when measurements are carried out in regions with high displacement gradients, such as close to a crack. Bornert et al. [25] stated that quadratic shape functions gave poorer results than first order shape functions and should only be used when particularly needed.

A multi-scale "finite-element" DIC approach was presented by Hild et al [9]. The multi-scale approach aims to increase robustness and reliability to the DIC algorithm when the analysis is compromised by e.g. large displacement jumps between subsequent images. Similar approaches exist for the subset based DIC formulation, where e.g. coarse-to-fine searches [36] are used to provide suitable initial values of the displacement in a current image I_c, before the final correlation is carried out at the finest resolution. These techniques increase the robustness of the DIC algorithm usually at the cost of computational speed. In most mechanical problems involving ductile specimens, the problem of large displacement jumps between subsequent images can be avoided by increasing the recording frame rate of the camera. In this study the multi-scale technique by Hild et al. [9] was only partly implemented. However, the mechanical image series analyzed during this work did not specifically require initial guesses of the deformation to be found. Thus, the multi-scale technique was not taken any further in this study.

The extended DIC approach (X-DIC) as presented by Réthoré et al. [13] was also partly implemented in the DIC code during this Ph.D.-work. The X-DIC approach is based on the element types and the formulation presented in the extended finite element method (X-FEM) [15]. Only elements with discontinuous enrichments were implemented, and not elements with singular enrichments (crack-tip elements). Q4 elements were used as basis for the enrichments. **Figure 21** illustrates the principle of discontinuous enrichments in X-DIC. All nodes that are connected to an element cut by the crack are enriched. The enrichment involves giving a node two extra degrees of freedom [13]. Thus, each enriched node has four degrees of freedom. The X-DIC formulation further implies that each element that is cut by the crack has two sub-parts, where each sub-part has a distinct "independent" displacement field.

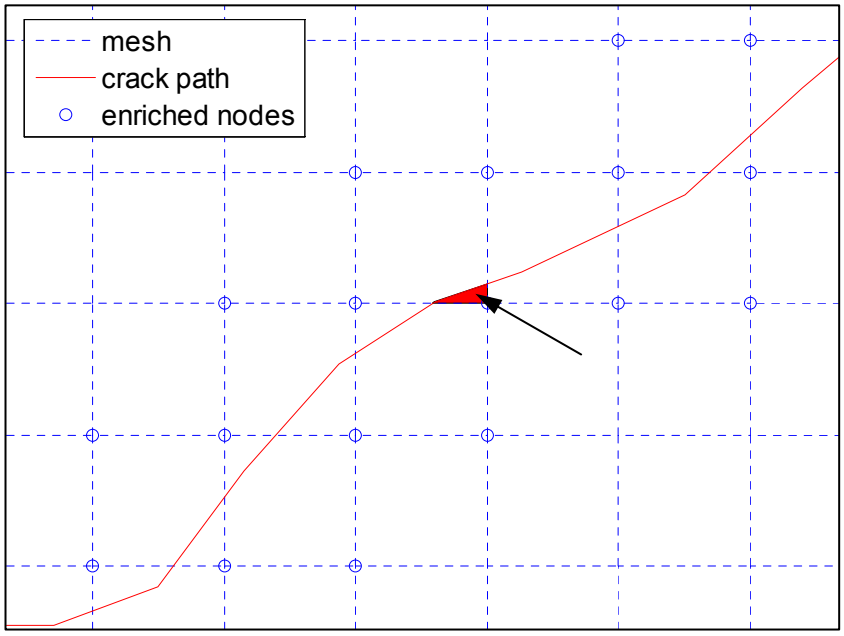

Figure 21. Principle of discontinuous enrichment in X-DIC. A mesh of Q4 elements is shown together with a random crack path going through the mesh. The enriched nodes are indicated. Also a particularly small sub-part of an enriched element is indicated.

If a random crack path is applied to a given mesh, some elements may be cut into a large and a small sub-part. Problems arise for the particularly small sub-parts, and an example of this is presented in **Figure 21** (indicated with an arrow). The deformation field of this sub-part has to be optimized based on the pixels that are located within this particular sub-part. The number of pixels may in principle become so low that a valid correlation becomes impossible. Thus, the mesh may have to be optimized prior to the analysis for the particular crack path, by applying larger elements in the crack region and/or optimizing the location and shape of the elements such that the crack cuts the elements in approximately equally sized sub-parts.

Because of these challenges with the X-DIC implementation, this approach was not continued in this study. Instead, effort was made to develop the node-splitting approach described in Section 6.2.3. The node-splitting also required the mesh to be optimized prior to the analysis, but without the need to apply enrichment of nodes. It is noted that the node-splitting and overlapping-mesh approaches (as presented in Section 6.2.3 and Part IV) do not provide an equivalent feature to the singularly-enriched crack-tip element in X-DIC [13]. However, it should be possible to combine the node-splitting and/or overlapping-mesh approaches with a singularly enriched element at the crack tip.

Implementations on a Graphical Processing Unit (GPU) using CUDA was attempted as described. However, due to difficulties obtaining faster algorithms running on the GPU compared to the CPU this work was not continued, as described in Section 6.1. However, this approach is very interesting and is an important subject for further work.

Throughout this Ph.D.-study, the mathematical formulations for three-dimensional DIC (3D-DIC) have become available. By applying the three-dimensional camera model described in Section 5.1 on a stereo-vision camera setup, and the developed DIC code, three-dimensional displacement and strain field measurements are available. This 3D-DIC approach was applied to measure the necking in Single Edge Notch Tension (SENT) specimens. The results from these tests are presented in Part III. However, a full study on 3D-DIC has not been carried out during this Ph.D.-work.

6.4 Graphical User Interface (GUI)

The developed DIC code has also been supported by a Graphical User Interface (GUI). This GUI was developed in MATLAB and includes functionality for mesh generation and modification, generation of DIC input files, running of single or multiple DIC input files and post-processing of the DIC results.

Figure 22 illustrates a snap-shot of the developed GUI in the post-analysis mode. Here the displacement fields, strain fields and grayscale residual maps can be studied in detail, as well as extracting time series of e.g. nodal displacements or element strains. The remaining functionalities include (among others) manual crack-path extraction and the comparison of results from two different analyses.

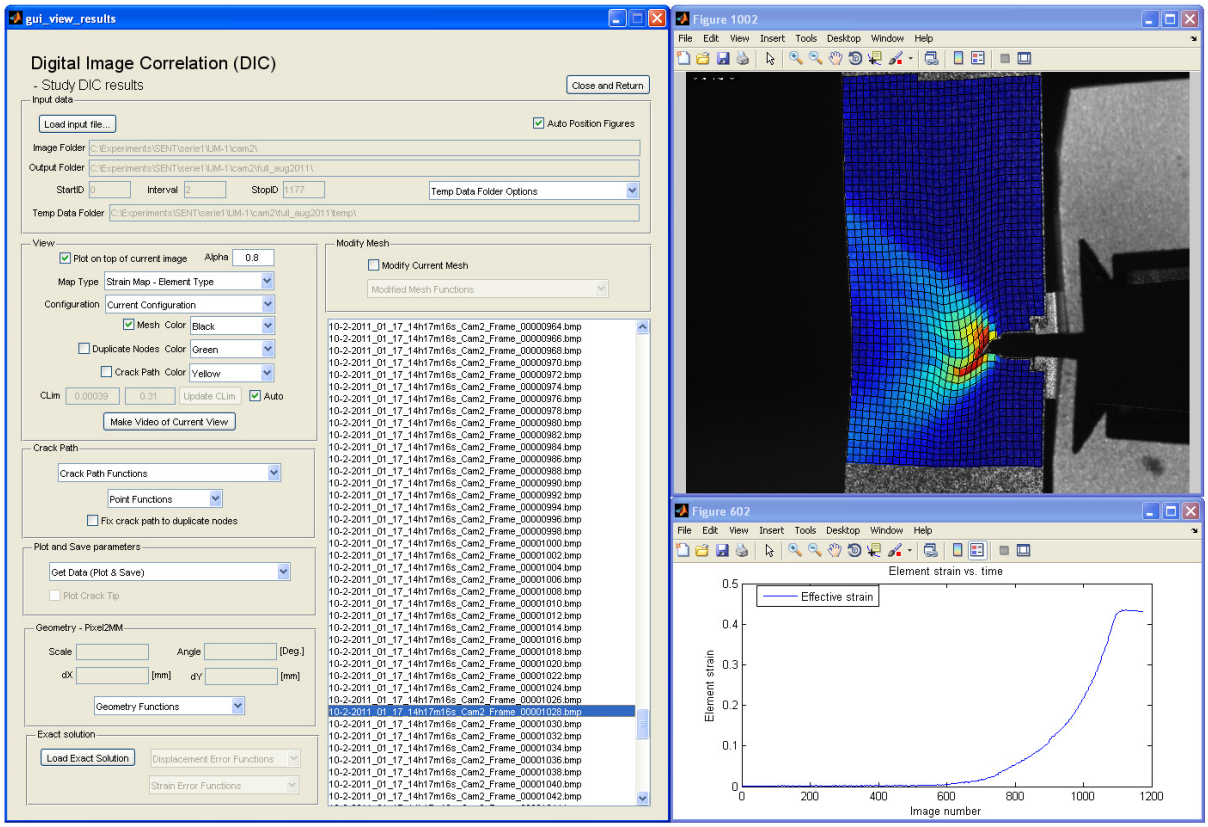

Figure 22. Snap-shot of the developed GUI in post-processing mode.

7. Concluding remarks

Conclusions for each individual part of this thesis may be found at the end of each part. However, some main conclusions from the thesis work are given in the following:

- A full-field three-dimensional shape-measurement technique using structured light has been established and applied to measure the out-of-plane deformation of plates subjected to quasi-static penetration and impact. The technique requires a projector and a (high-speed) camera which both need to be calibrated prior to the experimental tests. For each recorded image during the experiment, the geometry of the plate is captured. However, the displacements of material points on the specimen surface, and thus material strains, are not available using this technique. The absolute accuracy of measurements of the full-field out-of-plane deformation measurements (up to 30 mm) of a 500×500 mm plate was estimated to be smaller than 0.3 mm.
- A "finite-element" based DIC code has been developed and optimized for computational speed. The DIC code has also been supported by a GUI that has been developed throughout this study. Functionalities for handling of cracked specimens have been a major concern and are implemented into the DIC code. Such functionalities include:
    - Pixel cutoff: Pixels with high-correlation residuals are neglected from the correlation and by that increasing the robustness of the DIC analysis in problem areas, such as regions close to a crack.
    - Element refinement and erosion: An algorithm applied to avoid the cracked regions in a DIC analysis has been developed. This is done by automatic mesh adaption based on a set of user-defined parameters, i.e. refinement and erosion of Q4 elements in the mesh.
    - Node splitting and overlapped mesh: Mesh adaptation techniques used to capture the discontinuous displacement fields of a cracked specimen are developed. In the node-splitting approach, the crack path is partwise linearized by the element side length, while in the overlapping-mesh approach the crack path may be defined at pixel level. Both techniques require the crack path to be determined in an initial analysis.

- Crack-path optimization: Using the overlapping-mesh approach, a method for crack-path optimization has been implemented and tested. Using this optimization technique, the crack path may be located with sub-pixel accuracy in the reference configuration.

- The developed DIC code has been applied to measure a range of different mechanical tests in a two-dimensional configuration, including modified Arcan tests (Part II) and Single Edge Notch Tension (SENT) tests (Part III). Three-dimensional DIC measurements have also been carried out to measure the necking of SENT specimens (Part III).
- The optical measurements provided in this study have further been used for validation of both numerical (Parts I and II) and analytical models (Part I). Also, the measurements have been used to extract time series of fracture mechanics parameters such as Crack Mouth Opening Displacement (CMOD), Crack Tip Opening Displacement (CTOD) and crack length (Part III).

8. Suggestions for further work

Based on the thesis work, some suggestions for further work may be:

- Applying the structured light technique on high-velocity impact or blast-loading problems. The challenges here are mainly to develop a robust and safe setup of the optical equipment. Increasing the illumination intensity of the projected pattern may also become necessary.
- Increasing computational speed of the DIC code with optimized heterogeneous programming running on both the CPU and GPU.
- Improving the routines for three-dimensional camera calibration, which in this study have required a cumbersome setup of the calibration target. The accuracy of the camera calibration can in principle not be better than the accuracy of the applied calibration target. In this study a planar glass plate is used as calibration target. However, because the calibration of the full three-dimensional camera model in Equation (9) requires the calibration points to be non-coplanar, a non-planar calibration target should be made and tested. Other camera calibration routines and approaches should also be tested to see if this can ease the calibration process.
- Applying 3D-DIC on problems with propagating cracks (e.g. structural impact problems). The DIC functionalities for the handling of cracked specimens presented in this study are extendable to three-dimensional problems. It would have been interesting to apply theses techniques on more complex three-dimensional mechanical problems.
- Applying integrated material-model optimization in DIC. The vast amount of measurement data from a DIC analysis may be used in combination with analytical or numerical models to optimize certain material-model parameters. This is a particular interesting field of research that has been investigated the later years (see e.g. [16] and [17]).
- Development of a user-friendly graphical user interface for analysis of mechanically recorded image series.

9. References

[1] Gåsvik KJ (2002) Optical metrology, Third Edition, John Wiley & Sons, Ltd.
[2] Rastogi PK (ed.) (1999) Photomechanics, Topics in Applied Physics, Springer.
[3] Sutton MA, McNeill SR, Helm JD, Chao YJ (2000) Advances in two-dimensional and three-dimensional computer vision. Topics Appl. Phys. 77:323-372.
[4] Pan B, Qian K, Xie H, Asundi A (2009) Two-dimensional digital image correlation for in-plane displacement and strain measurements: a review. Meas Sci Technol 20:0620001.
[5] Sutton MA, Cheng M, Peters WH, Chao YJ, McNeill SR (1986) Application of an optimized digital correlation method to planar deformation analysis. Image Vis Comput 4:143-150.
[6] Helm JD, McNeill SR, Sutton MA (1996) Improved 3-D Image Correlation for Surface Displacement Measurement, Opt.Eng. 35:1911.
[7] Bay BK, Smith TS, Fyhrie DP, Saad M (1999) Digital Volume Correlation: Three-dimensional Strain Mapping using X-ray Tomography. Exp. Mech. 39(3) 217-226.
[8] Besnard G, Hild F, Roux S (2006) "Finie-element" displacement fields analysis from digital images: application to Portevin-Le Chatelier bands. Exp. Mech. 46:789-804.
[9] Hild F, Raka B, Baudequin M, Roux S, Cantelaube F (2002) Multiscale displacement field measurements of compressed mineral wool samples by digital image correlation. Appl Opt 41:6815-6828.
[10] Benallal A, Berstad T, Børvik T, Hopperstad OS, Koutin I, Nogeira de Codes R (2008) An experimental and numerical investigation of the behaviour of AA5083 aluminium alloy in presence of the Portevin-Le Chatelier effect. Int. J. Plasticity 24:1916-1945.
[11] Zhang J, Cai Y, Ye W, Yu TX (2010) On the use of the digital image correlation for heterogeneous deformation measurements of porous solids, Opt Laser Eng 49:200-209.
[12] Rèthore J, Roux S, Hild F (2007) From pictures to extended finite elements: extended digital image correlation (X-DIC). C R Mechanique 335:131-137.
[13] Réthoré J, Hild F, Roux F (2007) Extended digital image correlation with crack shape optimization. Comput Methods Appl Mech Engrg 196:5016-5030.
[14] Réthoré J, Tinnes JP, Roux S, Buffière JY, Hild F (2008) Extended three-dimensional digital image correlation (X3D-DIC) C. R. Mecanique (336) 643-649.
[15] Belytschko T, Möes N, Usui S, Parimi C (2001) Arbitrary discontinuities in finite elements. Int. J. Num. Meth. Engng. 50(4)993-1013.
[16] Hild F, Roux S (2006) Digital image correlation: from displacement measurement to identification of elastic properties – a review. Strain (42) 75-83.
[17] Avril S, Bonnet M, Bretelle AS, Grédiac, Hild F, Ienny P, Latourte F, Lemosse D, Pagano S, Pagnacco E, Pierron F (2008) Overview of identification methods of mechanical parameters based on full-field measurements. Exp. Mech. 48:381-402.
[18] Atkinson KB (1996) Close-range photogrammetry and machine vision, Whittles Publishing.
[19] Heikkilä J (1997) Accurate camera calibration and feature based 3-D reconstruction from monocular image sequences, Ph.D.-thesis, University of Oulo, Finland.
[20] Heikkilä J, Silven O (1997) A four-step camera calibration procedure with implicit image correction. Proc. IEEE Conference on Computer Vision and Pattern Recognition, San Juan, Puerto Rico, pp. 1106-1112.
[21] Yoneyama S, Kikuta H, Kitagawa A. Lens distortion correction for digital image correlation by measuring rigid body displacement. Opt. Eng. 45, 023602 (2006).

[22] Abdel-Aziz YI, Karara HM. Direct linear transform from comparator coordinates into object space coordinates in close-range photogrammetry. In: Proceedings of the ASP/UI symposium on close-range photogrammetry, p. 1-18, Urbana, IL, January 1971.
[23] http://en.wikipedia.org/wiki/Scheimpflug_principle [Cited: 30.11.2011]
[24] Fazzini M, Mistou S, Dalverny O, Robert L (2010) Study on image characteristics on digital image correlation error assessment. Opt. Laser. Eng.48:335 – 339.
[25] Bornert M, Brémand, Doumalin P, Dupré JC, Fazzini M, Grédiac, Hild F, Mistou S, Molimard J, Oretu JJ, Robert L, Surrel Y, Vacher P, Wattrisse B (2007) Assessment of digital image correlation measurement errors: methodology and results Exp. Mech. 49:353-370.
[26] Schreier HW, Braasch JR, Sutton MA (2000) Systematic errors in digital image correlation caused by intensity interpolation. Opt. Eng. 39: 2915.
[27] Press WH, Teukolsky SA, Vetterling WT, Flannery BP, (2007) Numerical recipies - Third edition. Cambridge University Press.
[28] Pan B, Xie H, Wang Z (2010) Equivalence of digital image correlation criteria for pattern matching. Appl. Opt. 49:28 5501-5509.
[29] http://www.mathworks.se/index.html [Cited 30.11.2011]
[30] http://openmp.org/wp/ [Cited 30.11.2011]
[31] http://www.nvidia.com/object/cuda_home_new.html [Cited 30.11.2011]
[32] Harris C, Stephens M (1988) A combined corner and edge detector. In Proc. 4th Alvey Vision Conf. pp 189-192.
[33] Cook RD, Malkus DS, Plesha ME, Witt RJ, Concepts and applications of finite element analysis, fourth edition. Jon Wiley & Sons (2002).
[34] LSTC, LS-DYNA keyword user's manual, version 971. (2007) Livermore Software Technology Corporation.
[35] Belytschko T, Wong BL, Plaskacz EJ (1989) Fission-Fusion adaptivity in finite elements for nonlinear dynamics of shells. Computers & Structures 33:1307-1323.
[36] Zhang ZF, Kang YL, Wang HW, Qin QH, Qiu Yu, Li XQ (2006) A novel coarse-fine search scheme for digital image correlation method. Measurement (39) 710-718.

Part I

E. Fagerholt, F. Grytten, B.E. Gihleengen, M. Langseth and T. Børvik.

Continuous out-of-plane deformation measurements of AA5083-H116 plates subjected to low-velocity impact loading

International Journal of Mechanical Sciences, Volume 52, Issue 5, Pages 689-705, 2010.

International Journal of Mechanical Sciences 52 (2010) 689–705

Contents lists available at ScienceDirect

International Journal of Mechanical Sciences

journal homepage: www.elsevier.com/locate/ijmecsci

Continuous out-of-plane deformation measurements of AA5083-H116 plates subjected to low-velocity impact loading

E. Fagerholt [a,*], F. Grytten [b], B.E. Gihleengen [c], M. Langseth [a], T. Børvik [a,d]

[a] Structural Impact Laboratory (SIMLab), Centre for Research-based Innovation (CRI), and Department of Structural Engineering, Norwegian University of Science and Technology, NO-7491 Trondheim, Norway
[b] SINTEF Materials and Chemistry, NO-0314 Oslo, Norway
[c] Department of Physics, Norwegian University of Science and Technology, NO-7491 Trondheim, Norway
[d] Norwegian Defence Estates Agency, Research and Development Department, PB 405, Sentrum, NO-0103 Oslo, Norway

ARTICLE INFO

Article history:
Received 19 February 2009
Received in revised form
12 November 2009
Accepted 17 November 2009
Available online 2 December 2009

Keywords:
Optical measurements
Structured light
Aluminium plates
Low-velocity penetration
Profilometry
Numerical simulations

ABSTRACT

An optical system based on structured light and close-range photogrammetry has been developed and is in this study used to continuously measure the full-field out-of-plane deformation of aluminium plates subjected to low-velocity impact loading. During testing, square AA5083-H116 aluminium plates with thickness 5 mm were mounted in a circular frame and impacted by a 30 mm diameter blunt-nose projectile with velocities ranging from 7 to 11 m/s, while the out-of-plane deformations were measured at the opposite side. A fringe pattern was projected onto the rear target surface by a slide projector and the variation in the pattern during penetration was observed by a high-speed camera recording 10,000 images per second. The recorded images were subsequently computer processed to provide full-field topography information of the target surface during deformation. Degradation of measurement data due to impact induced vibration has been evaluated and reduced to a minimum by isolating the optical system from the mechanical experiment. The out-of-plane deformation measurements were compared to non-linear finite element simulations, and the agreement between experimental and predicted results was in general found to be good.

1. Introduction

Structural impact problems have become increasingly important for the modern society. Both the civilian industry and the military may be addressing problems as dropped objects, collisions, explosions and penetration by fragments. Adequate designs of protective structures in transportation, process industry and fortification installations are today crucial and depend on a good knowledge of the energy absorbing potential of different materials and structures.

The literature on the subject of ballistic impact loading encompasses a variety of different materials, thicknesses and projectile geometries, as well as velocity ranges from 5 m/s to the hypervelocity domain of up to 15 km/s (see Goldsmith [1]). Comprehensive reviews on the research into the penetration and perforation of structures by free-flying projectiles can be found in Backman and Goldsmith [2], Corbett et al. [3] and Zukas et al. [4,5], while work covering low-velocity impacts on metal plates can be found in e.g. Wen and Jones [6,7], Langseth and Larsen [8–10], Langseth et al. [11] and Grytten et al. [12,13]. Even though Langseth et al. [11] used a high-speed film camera to measure deformation profiles based on a limited number of discrete points in the cross-section of a plate, none of the mentioned studies include continuous full-field measurements of the deformation of the target plate during impact.

Ballistic impacts on metal plates are still considered as complex problems both from an experimental, analytical and numerical point of view. Numerical techniques, such as the Finite Element Method (FEM), have on the other hand become increasingly powerful during the last two decades and FEM is today accepted as a general computation tool within most branches of industry. A major benefit of the numerical tools is that they provide the possibility to investigate complicated problems in full detail. However, care should be taken when conclusions are made on numerical simulations solely. In general, knowledge on structural impact problems should come from a combination of experiments and numerical simulations based on appropriate material models.

The gap between mechanical experiments and numerical simulations can be bridged by measurements. Parameters such as geometry and strains are measured to give information on the structural response to a specific loading. Conventional measurement techniques, i.e. strain gauges, linear transducers, etc, are now challenged by a collection of optical techniques, such as Digital Image Correlation (DIC) [14,15] and Digital Infrared Thermography (DIT) [16]. The considerable development of

* Corresponding author. Tel.: +47 73 59 46 93; fax: +47 73 59 47 01.
E-mail address: egil.fagerholt@ntnu.no (E. Fagerholt).

0020-7403/$ - see front matter © 2009 Elsevier Ltd. All rights reserved.
doi:10.1016/j.ijmecsci.2009.11.013

digital cameras in later years when it comes to resolution, recording rate and data storage has made it possible to obtain non-contact, full-field and high-quality measurements of both strain fields and three-dimensional geometry of complex mechanical problems. Such full-field measurement techniques can easily provide enormous amount of data from a single mechanical experiment and represent a natural foundation for correlating and validating numerical simulations to mechanical experiments.

This paper presents an optical system using structured light, i.e. projected fringes, to measure the continuous full-field topography of the surface of a plate subjected to low-velocity impact. As opposed to a 3D Digital Image Correlation (DIC) technique [14,17], which uses two cameras to obtain a 3D model of a target surface, the technique presented in this paper uses only one camera in addition to a projector that projects a continuous pattern onto the target surface. Typically 50 images, at a frame rate of 10000 Hz, are recorded and computer analyzed, providing the same number of topography maps of the plate surface during the impact process. The post-processing of images concerns the tracking of points in the projected pattern as opposed to a traditional DIC application where the tracking of material points in the target surface is the objective. The calculated topography maps are further used in the evaluation of a numerical model implemented in the non-linear finite element code LS-DYNA [18]. Three impact tests have been carried out on 5 mm thick plates of the aluminium alloy AA5083-H116 at impact velocities ranging from 7 to 11 m/s. Results from both experiments and numerical simulations are presented and compared.

2. Optical measurements

2.1. Projected fringes

The measurement principle and setup used in this project are based on structured light, i.e. projected fringes and close-range photogrammetry. A similar approach was also used in Grytten et al. [19] for out-of-plane deformation measurements during quasi-static punching. The object of interest, i.e. the surface of which we want to measure the topography, is illuminated by a fringe pattern using a slide projector. The projected pattern is a binary pattern consisting of black and white stripes or fringes. This surface is observed and recorded through a high-speed greyscale camera, providing intensity maps of the projected fringe pattern. Due to the difference in inclination angles of the projector and the camera, the appearance of the recorded intensity maps will depend on the geometrical shape of the plate surface. Fig. 1 illustrates the technique by showing two recorded images; the first at the initial unloaded stage and the second at a stage during impact where the plate has been deformed.

A software algorithm has been developed to analyze all images in the recorded series by locating the contours, or edges, in the fringe pattern. By interpolation of greyscale values in the image, sub-pixel accuracies below 1/10 of a pixel may be achieved. By analyzing subsequent images in the recorded series, it is possible to track each edge in the pattern during impact. Fig. 2 illustrates the extracted edges of the images in Fig. 1. The vertical translation of a specific point on an edge in an image may be related to the out-of-plane deformation at that specific point on the plate. For an ideal case with collinear illumination and observation, and if focus variations are disregarded, the relation between the vertical edge translation and the out-of-plane deformation of the plate can be assumed linear. However, for a real setup with both the camera and the projector positioned relatively close to the target object, this becomes more complicated. To determine the relation between the vertical edge translation and the out-of-plane deformations, a pattern calibration routine that provides a 3D matrix which holds information on how each edge in the pattern behaves as a function of deformation along the normal axis of the target plate is applied. This matrix works as a lookup table when calculating deformation values in the analysis of an experiment.

2.2. Camera model

Three Cartesian coordinate systems are defined as illustrated in Fig. 3. These are the target coordinate system (X, Y, Z), the

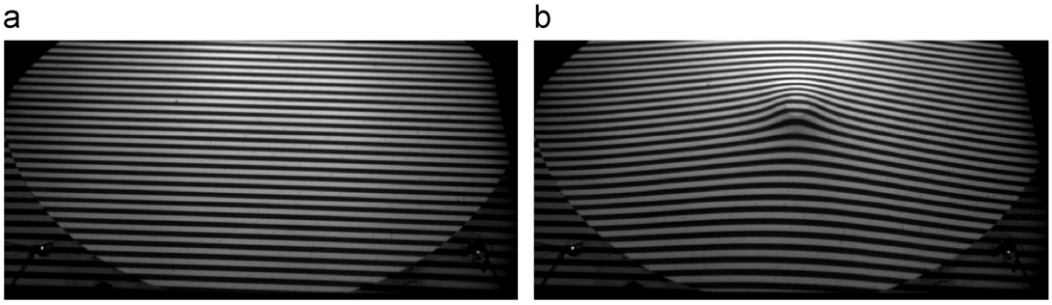

Fig. 1. Two recorded intensity maps from the high-speed camera during impact. (a) The initial un-deformed plate and (b) the plate deformed by the projectile.

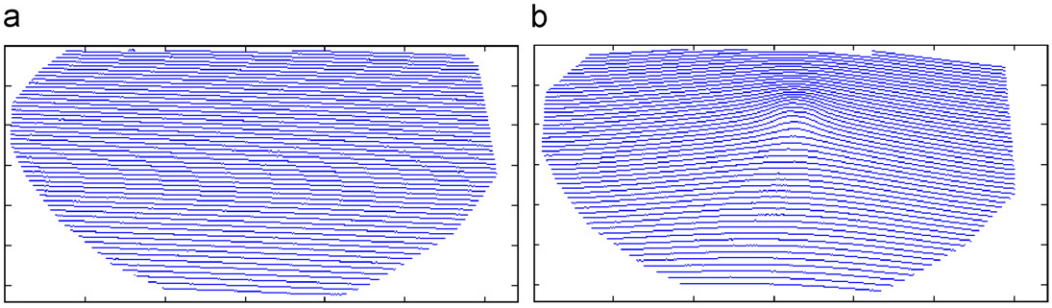

Fig. 2. Extracted fringe pattern edges from the images in Fig. 1. (a) The initial un-deformed plate and (b) the plate deformed by the projectile.

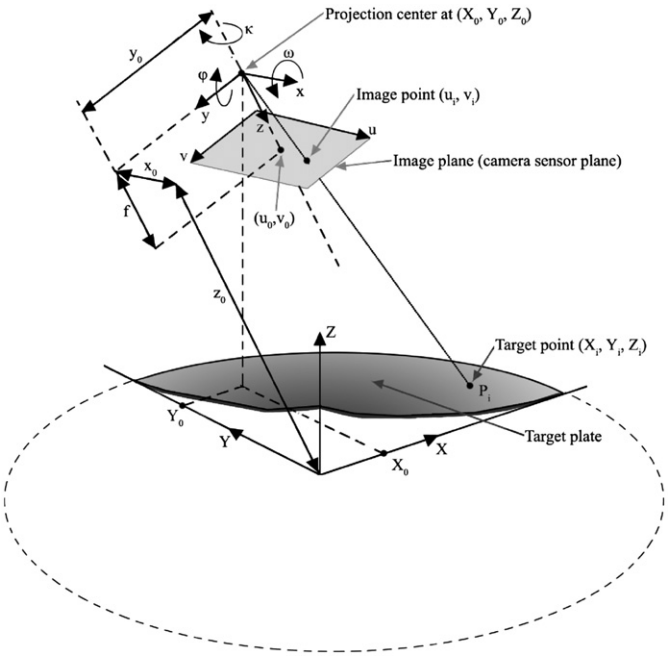

Fig. 3. Pinhole projection model, illustrating the target coordinate system (X, Y, Z), the camera coordinate system (x, y, z) and the image pixel coordinate system (u, v).

camera coordinate system (x, y, z) and the image (pixel) coordinate system (u, v). As described above, analysis of the edges in the fringe pattern is able to predict the out-of-plane deformation (Z_i) at a specific point (u_i, v_i) in an image. However, in order to obtain 3D topography maps of the plate surface, the measured deformation value (Z_i) must be provided with its corresponding X_i- and Y_i-coordinates. Thus, a transformation of coordinates from the image pixel coordinates (u_i, v_i) to the target coordinates (X_i, Y_i) when the out-of-plane deformation (Z_i) is known must be developed. This transformation is called the camera model. It consists of a pinhole projection model with correction for radial and decentring lens distortions, and is determined by 14 physical parameters which must be optimized in a calibration routine (see also Heikkilä [20]). The basic pinhole projection model, which is a mathematical projection of the target coordinates (X_i, Y_i, Z_i) to the undistorted image pixel coordinates($\tilde{u}_i, \tilde{v}_i$), is illustrated in Fig. 3.

The target coordinate system (X, Y, Z) holds the target plate, while the camera coordinate system (x, y, z) contains the image sensor plane of the camera and its origin is defined as the projection centre. Assuming a point P_i at the target plate with the coordinates (X_i, Y_i, Z_i), the transformation of coordinates from target coordinates to camera coordinates is a standard rotation and a translation, given by

$$\begin{bmatrix} x_i \\ y_i \\ z_i \end{bmatrix} = \mathbf{M} \cdot \begin{bmatrix} X_i \\ Y_i \\ Z_i \end{bmatrix} + \begin{bmatrix} x_0 \\ y_0 \\ z_0 \end{bmatrix} \tag{1}$$

where $\mathbf{M}$ is a 3×3 rotational matrix defined by the three rotations ω, ϕ and κ around the three camera coordinate axes x, y and z. [x_i, y_i, zi]T *are* the coordinates of the point P_i in the camera coordinate system, $[X_i, Y_i, Z_i]^T$ are the coordinates of the point in the target coordinate system and $[x_0, y_0, z_0]^T$ are the origin of the target coordinate system denoted in camera coordinates. After the target coordinates are translated to camera coordinates, the camera coordinates are projected on to the image sensor plane of the camera. The projection is described as

$$\begin{bmatrix} \tilde{u}_i \\ \tilde{v}_i \end{bmatrix} = \frac{f}{z_i} \begin{bmatrix} x_i \\ y_i \end{bmatrix} \tag{2}$$

where $[\tilde{u}_i, \tilde{v}_i]^T$ are the undistorted image coordinates and f is the effective focal length of the camera lens. It is noted that when trying to invert Eq. 2, one of the camera coordinates must be provided in order to obtain a unique solution. In the measurement technique presented in this paper, the target coordinate Z_i (out-of-plane deformation) is provided from the analysis of the fringe pattern, making it possible to solve for X_i and Y_i using Eqs. 1 and 2.

The image coordinates are then transformed from millimetres to pixels by

$$\begin{bmatrix} u' \\ v' \end{bmatrix} = \begin{bmatrix} D_U \tilde{u}_i \\ D_V s_V \tilde{v}_i \end{bmatrix} + \begin{bmatrix} u_0 \\ v_0 \end{bmatrix} \tag{3}$$

where S_V is a scaling factor between the horizontal and vertical direction. D_U and D_V are the proportional constants between millimetres and pixels. So far the camera model describes a linear camera model, i.e. the pinhole projection model, without any distortion factors. To obtain a satisfying accuracy, the camera model must correct for radial and decentring distortion. These distortion factors are common for most lens systems in various extents [21]. In this study, radial distortions are modelled as

$$\begin{bmatrix} \delta u_i^{(r)} \\ \delta v_i^{(r)} \end{bmatrix} = \begin{bmatrix} \tilde{u}_i (k_1 r_i^2 + k_2 r_i^4 + \ldots) \\ \tilde{v}_i (k_1 r_i^2 + k_2 r_i^4 + \ldots) \end{bmatrix} \tag{4}$$

where $k_1, k_2, \ldots, k_n$ are coefficients of the radial distortion and $r_i = \sqrt{\tilde{u}_i^2 + \tilde{v}_i^2}$, while decentring distortions are modelled by

$$\begin{bmatrix} \delta u_i^{(t)} \\ \delta v_i^{(t)} \end{bmatrix} = \begin{bmatrix} 2p_1 \tilde{u}_i \tilde{v}_i + p_2 (r_i^2 + 2\tilde{u}_i^2) \\ p_1 (r_i^2 + 2\tilde{v}_i^2) + 2p_2 \tilde{u}_i \tilde{v}_i \end{bmatrix} \tag{5}$$

where p_1 and p_2 are decentring distortion coefficients. The transformation from undistorted image coordinates in mm to distorted image coordinates in pixel values is then given by

$$\begin{bmatrix} u_i \\ v_i \end{bmatrix} = \begin{bmatrix} D_U (\tilde{u}_i + \delta u_i^{(r)} \delta u_i^{(t)}) \\ D_V s_V (\tilde{v}_i + \delta v_i^{(r)} + \delta v_i^{(t)}) \end{bmatrix} + \begin{bmatrix} u_0 \\ v_0 \end{bmatrix} \tag{6}$$

The complete transformation from target coordinates to distorted image pixel coordinates are thus given by Eqs. 1, 2 and 6. The transformation from target coordinates (X_i, Y_i, Z_i) to distorted image coordinates (u_i, v_i) is determined by a number of physical parameters. These parameters are listed in Table 1 together with obtained values for the Photron Ultima APX-RS high-speed video camera used in the impact tests reported in this paper.

2.3. Camera calibration

To obtain values for the parameters that define the transformation of coordinates from target coordinates to image coordinates, the camera model must be calibrated in an optimization algorithm. The input to this optimization algorithm is calibration points obtained by recording images of a calibration target. These calibration points are a set of corresponding image coordinates (u_i, v_i) and target coordinates (X_i, Y_i, Z_i). To make the optimization routine to converge towards a proper solution of the 14 camera parameters, a requirement is that the calibration points must have a non-planar distribution in the target coordinate system. Thus, the calibration points must have a distribution over all 3 axes of the target coordinate system.

The camera calibration target used in these tests is a glass plate with a chess pattern surface. The glass plate is prearranged to lie

Table 1
Camera parameters that determine the transformation from target coordinate system to image coordinate system and their values from the camera calibration carried out in this study.

Parameter	Description	Value (Photron)	Units
D_U	Proportional constant between mm and pixels	128	pixels/mm
D_V	Proportional constant between mm and pixels	128	pixels/mm
S_V	Scale factor between horizontal and vertical direction	1.0145	–
f	Effective focal length	22.6674	mm
u_0	Principal point in image pixel coordinates	787.1050	pixels
v_0	Principal point in image pixel coordinates	70.8566	pixels
k_1	Radial distortion coefficient	−0.0025	–
k_2	Radial distortion coefficient	2.2991e−5	–
p_1	Decentring distortion coefficient	−3.1266e−5	–
p_2	Decentring distortion coefficient	−0.0034	–
x_0	Origin of target coordinate system in camera coordinates	366.0	mm
y_0	Origin of target coordinate system in camera coordinates	60.7	mm
z_0	Origin of target coordinate system in camera coordinates	2252.6	mm
ω	Rotation of the target coordinate system about x-axis	148.0	deg.
ϕ	Rotation of the target coordinate system about y-axis	8.6	deg.
κ	Rotation of the target coordinate system about z-axis	0.9	deg.

in the XY-plane. It is then moved along the Z-axis while the process is being recorded by the camera. For each image a corner finding algorithm [22] is applied to find all corners of the black and white squares in the chess pattern with sub-pixel accuracy in the XY-plane, while the Z-value is recorded by a linear displacement transducer. By analyzing the series of images, a set of calibration points are obtained, each containing the target object coordinates (X, Y, Z) and the corresponding image coordinates (u, v).

The camera model optimization is done by a least squares fitting algorithm on the set of calibration points, minimizing the sum of the squared residuals. The object function to be minimized is expressed as

$$F = \sum_{i=1}^{N} (U_i - u_i)^2 + \sum_{i=1}^{N} (V_i - v_i)^2 \tag{7}$$

where N is the number of calibration points. U_i and V_i are observations of the image coordinates and u_i and v_i are image coordinates calculated from the corresponding target coordinates (X_i, Y_i, Z_i) using the previously described camera model.

The proportional constants D_U and D_V included in Eq. 6 and listed in Table 1 are linearly dependent on the focal length f and the scale factor S_V. Thus, D_U and D_V are not included as optimization variables, but initially provided as fixed camera parameters provided from the camera specification. The remaining 14 parameters in the camera model are optimized by the least squares algorithm. For the least squares algorithm to converge towards the correct solution, proper initial values for the 14 parameters must be provided. Initial values for 9 of the 14 camera parameters (focal length, principal point coordinates, object coordinate origin and rotation parameters) are provided by a Direct Linear Transform (DLT) algorithm [20,23]. Initial values for the four distortion parameters are set to zero, while the scaling factor S_V is set to one.

The least squares algorithm determines the 14 camera parameters and the coordinate transformation from target coordinates (X, Y, Z) to image coordinates (u, v). However, in the calculations of the topography of a deformed plate, we are interested in the inverse transformation, going from image coordinates to target coordinates. Problems arise when trying to inverse Eq. 6 to obtain undistorted image coordinates from distorted image coordinates. This results in fifth order polynomials which are not trivial to solve. The solution applied is an approximation presented by Heikkilä [20]. He showed that the proposed model gives insignificant residuals even with severe radial and decentring distortions. The eight parameter model which computes undistorted image coordinates from distorted image coordinates is given by the following relations:

$$\tilde{u}_i = \frac{\tilde{u}'_i + \tilde{u}'_i(a_1 r_i^2 + a_2 r_i^4) + 2a_3 \tilde{u}'_i \tilde{v}'_i + a_4(r_i^2 + 2\tilde{u}'_i 2)}{(a_5 r_i^2 + a_6 \tilde{u}'_i + a_7 \tilde{v}'_i + a_8) r_i^2 + 1} \tag{8}$$

$$\tilde{v}_i = \frac{\tilde{v}'_i + \tilde{v}'_i(a_1 r_i^2 + a_2 r_i^4) + a_3(r_i^2 + 2\tilde{v}'_i 2) + 2a_4 \tilde{u}'_i \tilde{v}'_i}{(a_5 r_i^2 + a_6 \tilde{u}'_i + a_7 \tilde{v}'_i + a_8) r_i^2 + 1} \tag{9}$$

where $\tilde{u'}_i = \frac{u_i - u_0}{D_U}$, $\tilde{v'}_i = \frac{v_i - v_0}{D_V S_V}$ and $r = \sqrt{\tilde{u'}_i^2 + \tilde{v'}_i^2}$.

In order to solve the eight unknown parameters (a_1, a_2, …, a_8), calibration points covering the whole image area must be generated. A set of 2000 such calibration points are generated using the previously described camera model. The eight parameters are then solved using a least squares fitting algorithm [20]. Obtained parameters for the Photron Ultima APX-RS high-speed camera used in this study are presented in Table 1. Its corresponding inverse parameters are presented in Table 2. Obtained RMS values of the X- and Y-coordinate residuals from the camera calibration are given in Table 3. As seen, the RMS values are about 0.2 mm.

Table 2
Inverse camera parameters from the camera model calibration that determine the image coordinate to target coordinate transformation.

Parameter	Value
a_1	−0.0036
a_2	5.2598e−5
a_3	2.1914e−5
a_4	0.0031
a_5	7.3655e−5
a_6	−3.7049e−6
a_7	2.2832e−6
a_8	−0.0059

Table 3
RMS-values of the residuals of target coordinates X and Y from the calibrated camera model.

Target coordinate direction	RMS-value [mm]
X	0.2394
Y	0.1770

3. Experimental setup

3.1. Target material

The target material used in this study is 5 mm thick plates of the aluminium–magnesium alloy AA5083-H116. This alloy is extensively used in naval structures such as ship hulls and offshore topsides, but is also applied in ballistic protection due to its high strength [24]. The alloy has been developed to resist stress corrosion which may occur in corrosive media and the main alloying elements are magnesium (4.75 wt%), manganese (0.84 wt%) and iron (0.18 wt%) [12]. Important characteristics of the alloy are anisotropy, both in strength and plastic flow [25], variation of material properties with plate thickness due to cold rolling, and jerky flow due to dynamic strain aging (also referred to as the PLC effect) [16,26]. Comprehensive material test programs on AA5083-H116, determining the flow and fracture characteristics of the alloy as function of plate thickness, strain rate, temperature and stress triaxiality, can be found in e.g. Grytten et al. [12] and Clausen et al. [27].

3.2. Test rig

The drop rig used in the impact tests is shown in Fig. 4(a) [8]. It consists of a pneumatic accelerator and a supporting frame for the test specimen. The projectile is accelerated by the pneumatic accelerator and gravity from the top of the rig through a pipe onto the target plate. By varying the air pressure inside the accelerator, impact velocities from 5 to 50 m/s may be obtained. The projectile consists of a central rod with a replaceable nose. A blunt, hardened (HRC 62) steel nose with diameter 30 mm were used in the tests presented in this study, making the total weight of the projectile 19.0 kg. Fig. 4(b) shows a sketch of the projectile and the replaceable nose used in these tests.

AA5083-H116 target plates with dimensions $600 \times 600 \times 5$ mm^3 were carefully cut from a larger plate, and holes for mounting were drilled. The surface of the plate to be optically measured was painted matt white to enhance the projected pattern. Prior to the impact test, the plate was mounted between two massive circular steel rings with an inner diameter of 500 mm, using 24 pre-stressed M16 bolts. The frame and the clamped plate were then inserted in the drop rig, and adjusted to make sure that the projectile would hit the plate in the centre. Fig. 5(a) shows the target plate before and after mounting in the circular frame, while Fig. 5(b) gives the location of the target plate and the clamping rings in the impact rig.

3.3. Instrumentation

During impact, the full-field out-of-plane deformation of the plate surface was measured using the method described in Section 2. Fig. 6 illustrates the setup of the optical measurements. A Kodak Carousel S-AV 1030 250 W slide projector projected a fringe pattern onto the target plate surface. The projector was equipped with a Kodak Retinar lens with focal length of 85 mm and a 2″ high precision Ronchi rulings by Edmund Optics with 50 lines per inch. A Photron Ultima APX-RS high-speed video camera equipped with a 50 mm f/1.4D AF Nikkor lens recorded the plate surface and the projected pattern with a constant framing rate of 10,000 images per second. Due to the safety of the camera, it was arranged to view the target plate through a mirror as shown in Fig. 6.

Preliminary impact tests were carried out to investigate vibrations in the optical equipment. Based on the preliminary impact tests, the optical equipment, i.e. the projector, the camera and the mirror, were mounted onto the rigid concrete floor with no direct contact with the deformation rig. Also, different types of isolation material between the concrete floor and the optical equipment were tested, resulting in a vibration isolation layer

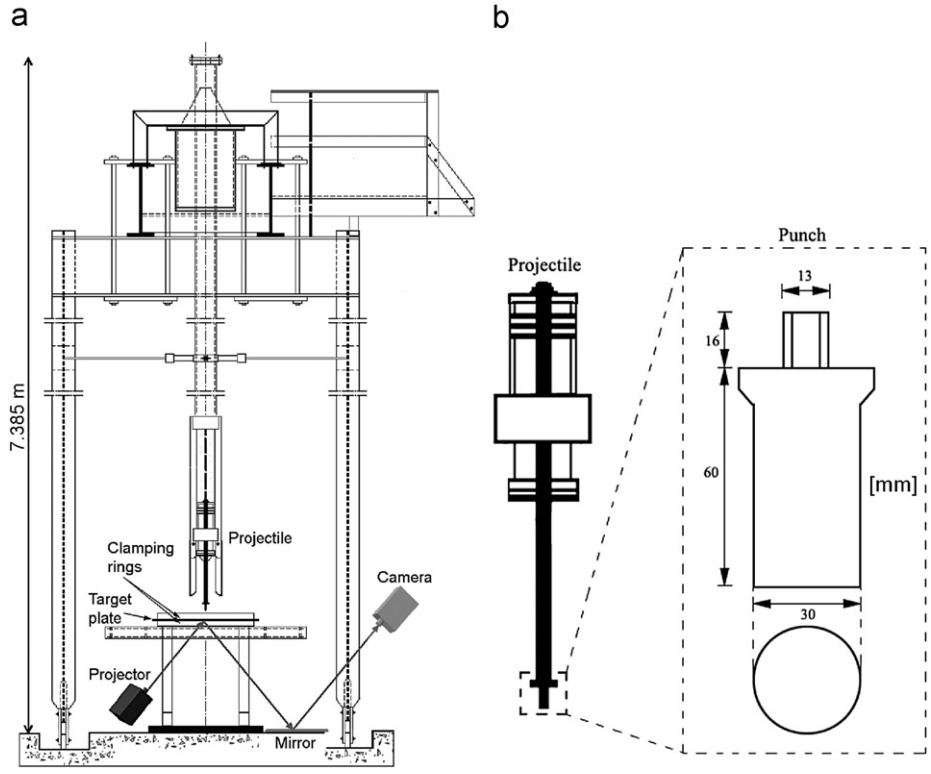

Fig. 4. (a) Test rig used in impact tests and (b) the projectile with its replaceable nose.

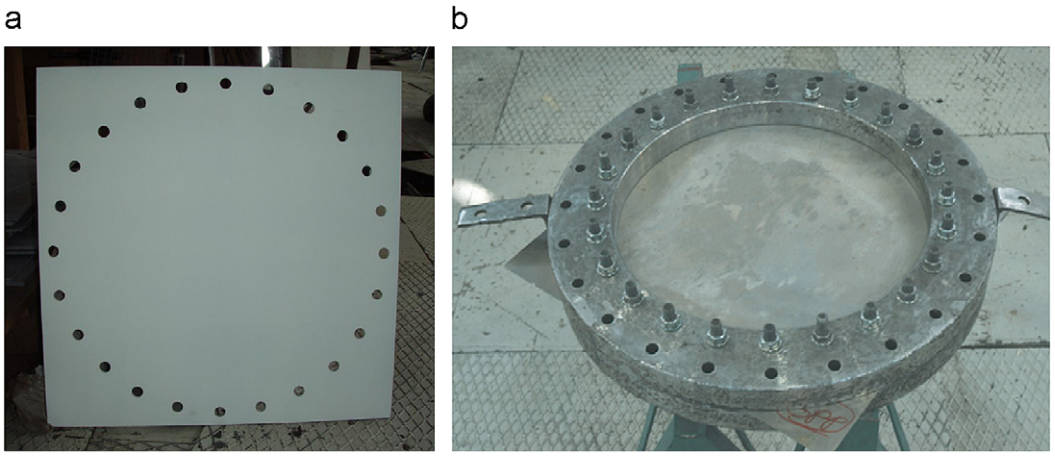

Fig. 5. (a) Target plate before and (b) after the mounting in the clamping rings.

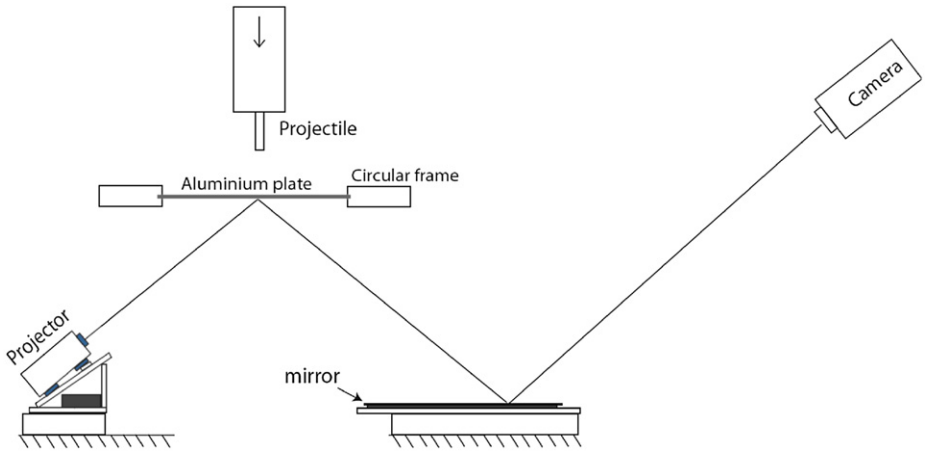

Fig. 6. Setup of out-of-plane measurements.

consisting of a combination of wood and rubber mats. To keep control of the degree of vibration during testing, accelerometers were placed on all optical measurement components and the supporting frame. Vibration levels sufficient to degrade the optical measurements may also be observed through the recorded images.

To measure the interface force between the projectile and the target plate during impact, a full bridge strain gauge circuit was mounted in the nose of the central rod of the projectile [8,10]. A connecting cable for the recorded strain signals was attached to the rear end of the projectile (see Fig. 4) and a computer. Prior to the tests, the force versus strain gauge characteristics were found from quasi-static calibration tests in a 500 kN Dartec universal testing machine. The velocity of the projectile was measured just before impact by a photocell system. The photocell system also served as trigger for the high-speed camera, various accelerometers and impact-force readings.

4. Results from impact tests

Three impact tests on 5 mm thick plates of AA5083-H116 were carried out with varying impact velocities. Recordings were made of the out-of-plane deformation, interface force and projectile velocity. Some data from the three tests are presented in Table 4. In the two first tests (Mar08-5-30-14 and Mar08-5-30-15), the blunt-nose projectile did not have enough energy to perforate the plate, and it rebounded after impact. In the third test (Mar08-5-30-16), the plate was completely perforated by the projectile, mainly by a plugging type of failure mode.

4.1. Out-of-plane deformations

Typical plots of the out-of-plane deformation measurements and its corresponding recorded interface forces for various stages during impact of the three tests are presented in Figs. 7–9. Note that these data only represent a small set of the optically measured out-of-plane deformations available from the tests.

Table 4 gives the number of recorded images from impact to max deformation in the various tests. For each recorded image, a topography map of the plate surface was calculated. Fig. 7 illustrates a collection of 6 topography maps of the aluminium plate from the first test, Mar08-5-30-14. The measurements cover approximately two thirds of the plate and include the centre with maximum deformation. In these tests, about 25,000 independent out-of-plane measurement points are obtained for each recorded image. The plate surfaces, as shown in Fig. 7, are generated by a bilinear interpolation of the measured values.

Fig. 8 gives deformation profiles through the centre of the plate surface for the three tests. The plots show the out-of-plane deformations of the plates from time-of-impact to max deformation. Note that in the two first tests perforation did not occur, while in the third test the plate was completely perforated by the projectile.

Table 4
Typical data from impact tests.

Test #	Impact velocity [m/s]	Maximum force [kN]	Impact energy [J]	Maximum deformation [mm]	# of images to max def.	Plugging Yes/No
Mar08-5-30-14	7.31	48.1	507.6	23.67	51	No
Mar08-5-30-15	7.92	51.4	595.9	25.30	49	No
Mar08-5-30-16	10.69	59.0	1085.6	29.20	31	Yes

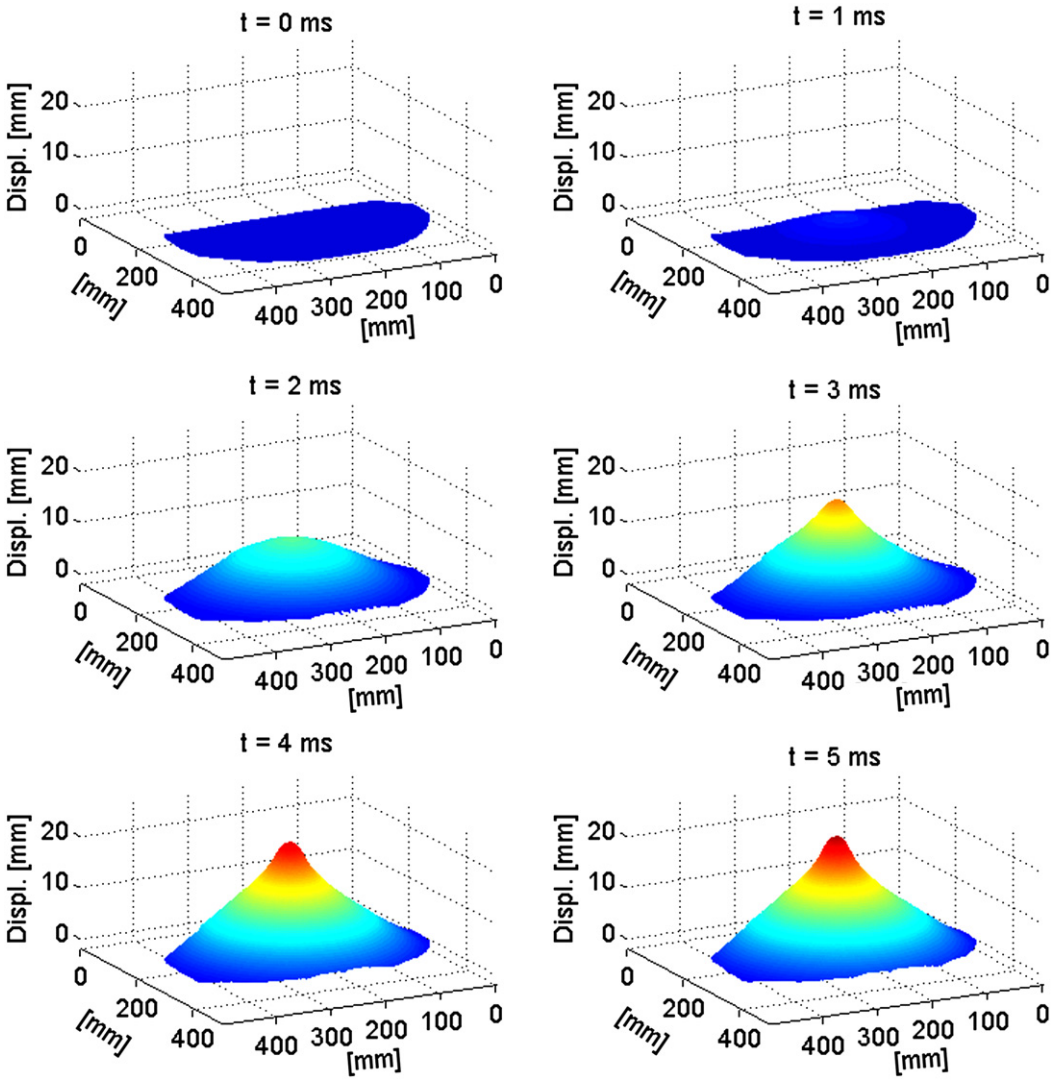

Fig. 7. A selection of 3D topography maps of the plate surface, calculated from the recorded images of the test "Mar08-5-30-14".

Fig. 9 shows a selection of images from test "Mar08-5-30-16" with its corresponding impact forces and deformation profiles through the centre of the plate. In the last picture shown, the plate was perforated by the projectile. Because the projectile causes discontinuities in the pattern after perforation, the out-of-plane deformations in the region just around the projectile nose is hard to measure, and the measurements in this region are unsure.

Displacement–time curves of the projectile during impact were found by integration of the recorded force–time curves and the measured impact velocities. In Fig. 10, calculated displacement–time curves of the projectile are plotted together with the centre deformation of the plate obtained from the optical measurements. A very good correlation between these two independent measurements is seen. However, the deviations become larger when approaching the maximal deformation or perforation. This is caused by indentation of the projectile into the plate or by noise components in the force measurement. In any case, the good correlation between these measurements verifies in large the optical measurements.

4.2. Vibration evaluation

In the initial phase of this work, accelerometers were used to analyze the vibration levels of the camera, the projector, the mirror and the circular mounting frame of the target plate. It became clear that vibrations in the components of the measurement system were difficult to completely remove (they could only be reduce to a minimum). Accelerometers were useful to investigate the degree of vibration in each component and the effect of different kinds of vibration isolation of the components. However, when evaluating the qualitative degradation of the

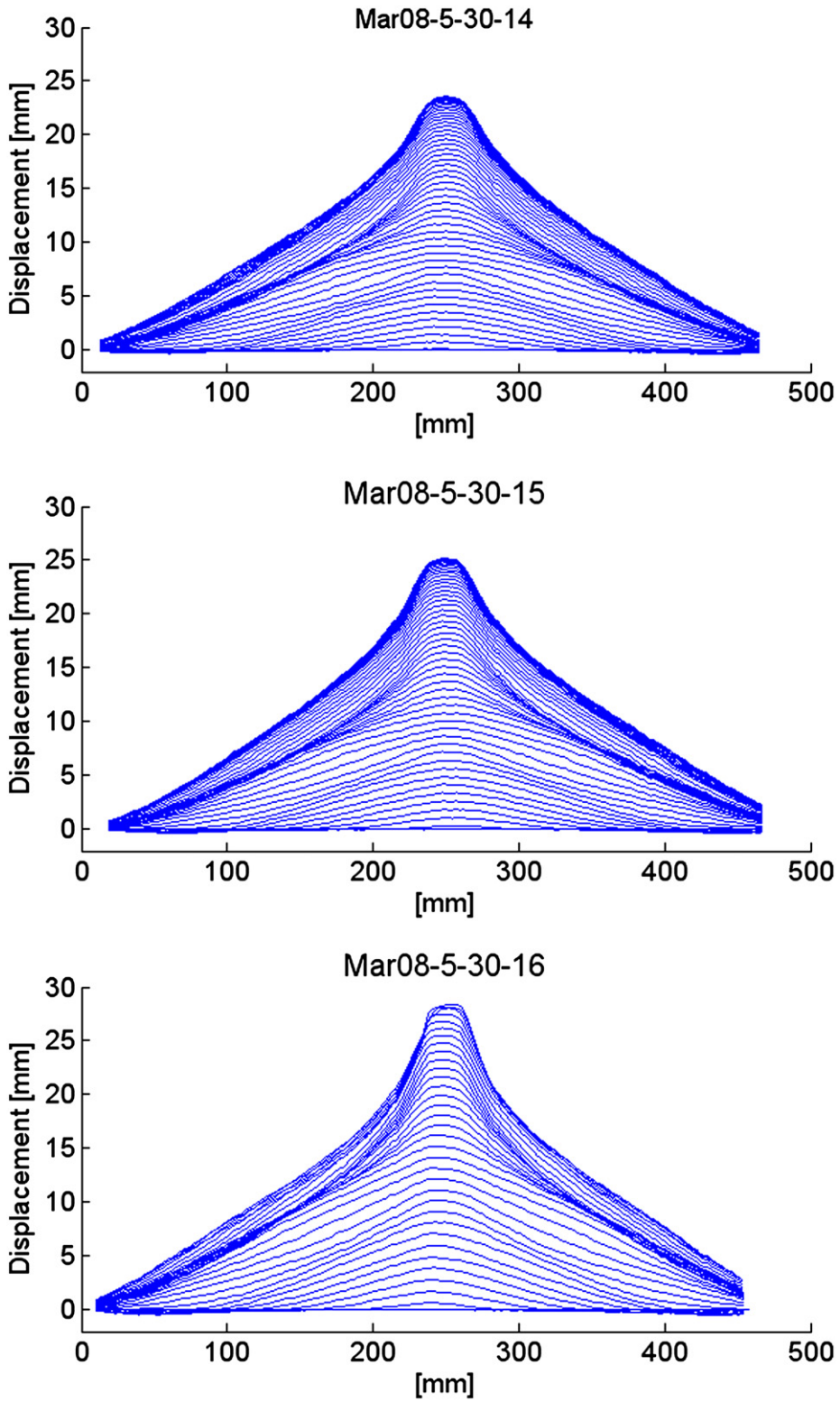

Fig. 8. Out-of-plane deformation profiles from the three presented impact tests. Only profiles from time of impact to the time of max deformation are plotted. The two first tests had no plugging, while the third had plugging.

optical measurements due to vibration, accelerometers were not suitable. Instead an alternative method was developed, where the projected pattern on the circular mounting frame was analyzed (see Fig. 11).

The massive circular frame, shown in Fig. 5(b), is assumed to be rigid during the experiment and any variations in the pattern on the circular frame will be due to vibration in the projector, the camera, the mirror and/or the circular frame itself. Also, the vertical variations of the pattern on the circular frame can be directly translated to the degradation of the optical out-of-plane deformations of the plate using information from the pattern calibration. Fig. 12 shows the vertical variations of the projected pattern on the circular frame, converted to out-of-plane deformations (Z) in mm for the three tests. It is noted that this

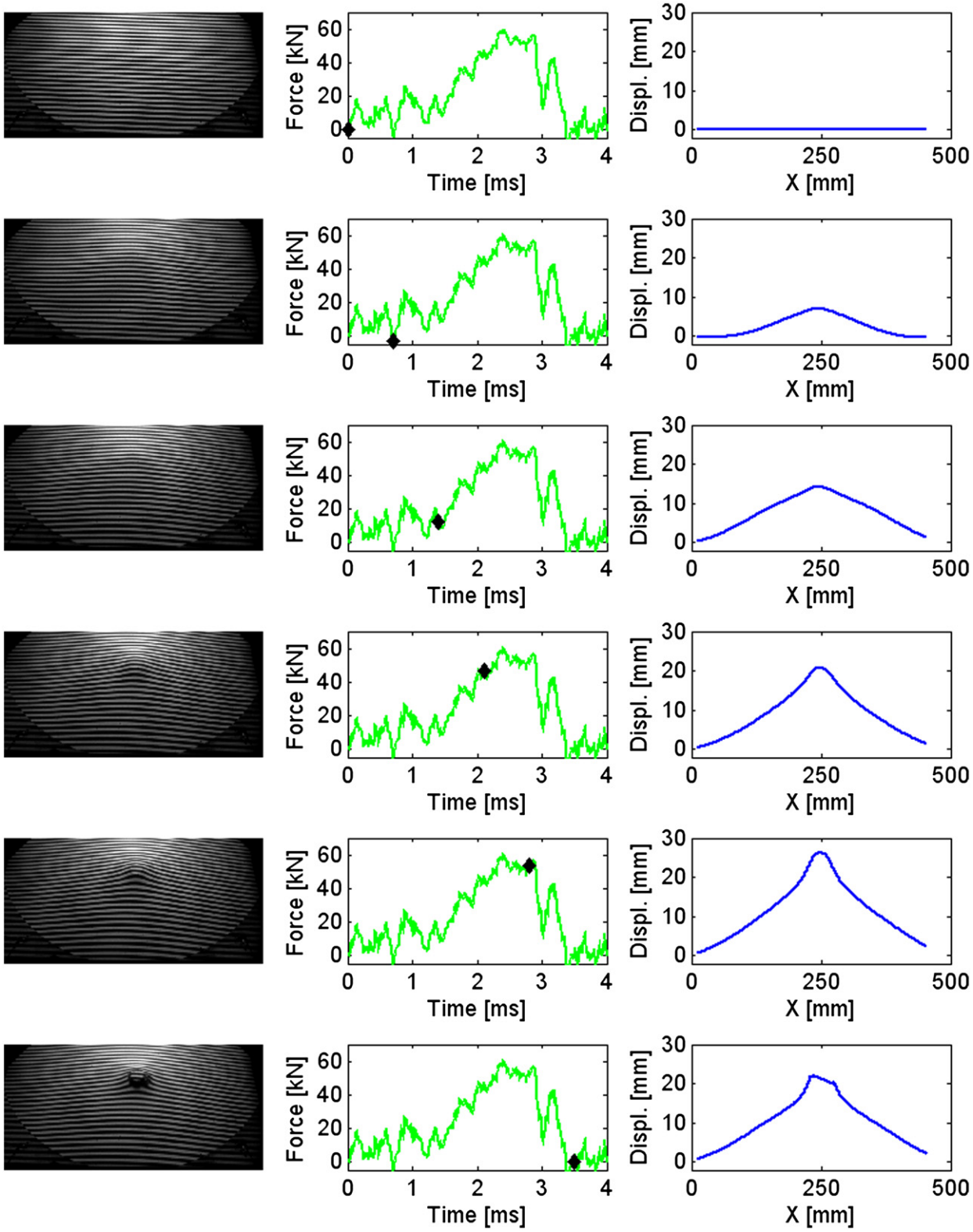

Fig. 9. A selection of recorded images (left) from the test "Mar08-5-30-16" with its corresponding deformation profiles (right). In the middle, the force recordings are plotted. Black rectangles show the corresponding time of the recordings.

is not real out-of-plane deformations of the circular frame, because it is a combined effect of vibration in the frame and the optical components. Fig. 12 shows that the degradation of the optical measurements due to vibrations is less than 0.25 mm in all tests when looking at the time span from impact to maximum deformation (a dot illustrates the time of maximum deformation for the three tests). The degradation caused by vibration increases after this point. However, since this work is concerned on measuring the deformations of the plate until maximum deformation, this has little effect on the deformation measurements. The measured degradation induced by vibration presented in Fig. 12 may in principle have been used to correct the

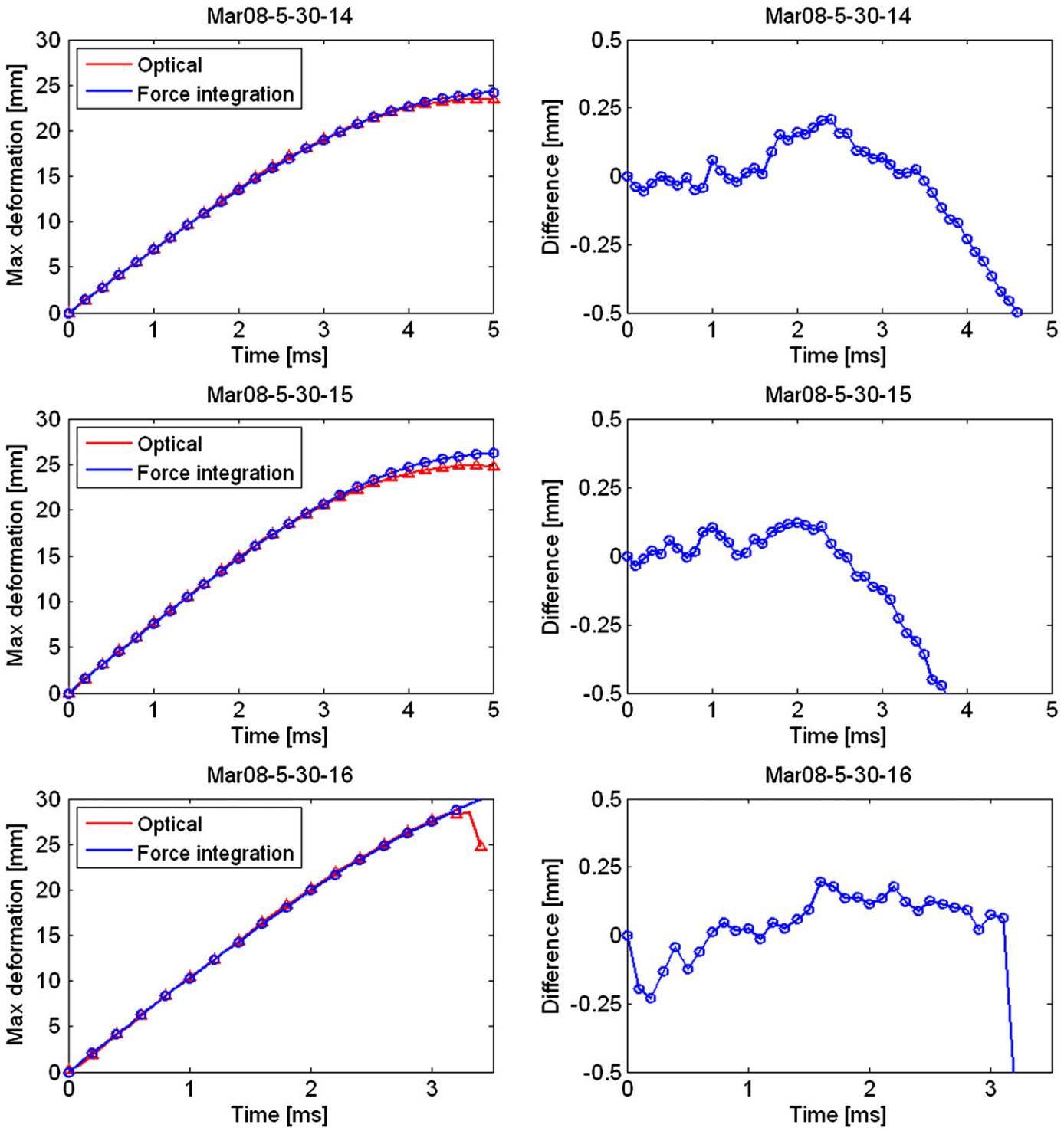

Fig. 10. To the left, the maximum deformations from the optical measurements are plotted together with the position of the projectile nose tip, integrated from the strain gauge force measurements. The deviations between the two curves are plotted to the right.

measured out-of-plane deformations of the plate. However, this has not been done in the present study.

4.3. Measurement accuracy

The error in the measurement of the plate topography will be a combination of uncertainties in the out-of-plane deformations (Z) measured by the fringe pattern analysis, the residuals defining uncertainties in the X- and Y- coordinates from the camera model and in degradation induced by vibrations.

Earlier works by the authors [19,28] have proven the fringe interpolation algorithm to have sub-pixel accuracies below 1/10 of a pixel. Using the setup in this study, this will give an uncertainty of the measured out-of-plane deformation below 0.05 mm. Clearly the residuals of the camera model presented in Table 3 (res_X=0.24 mm and res_Y=0.18 mm) dominates the measurement uncertainty. However, since the gradient of the plate

topography (dZ/dX and dZ/dY) is small in all tests, uncertainties in the XY-plane have a significantly smaller effect on the measured topography than what these residuals indicate.

Based on these arguments it is assumed that the impact induced vibrations are the most significant uncertainty of the out-of-plane measurements, and the resultant uncertainty should therefore be less than 0.3 mm (see Fig. 12). That the accuracy in the optical measurements is high was also confirmed in Fig. 10. It should finally be noted that Grytten et al. [19] found an uncertainty less than 0.1 mm using a similar setup for quasi-static loading and multiple cameras for several independent deformation measurements.

5. Numerical simulations and validations

5.1. Material model

The multiaxial stress state of metallic materials under impact generated loading conditions is usually expressed by the equivalent stress σ_{eq} in terms of the equivalent plastic strain ε_{eq}, plastic strain rate $\dot{\varepsilon}_{eq}$ and temperature T. Johnson and Cook [29] proposed a phenomenological constitutive relation based on these variables, which has been frequently used in impact analysis due to its simplicity and accuracy (see e.g. [24]). Here, a slightly modified version of the JC constitutive relation as proposed by Børvik et al. [30] is used. The equivalent stress is given as

$$\sigma_{eq} = (A + B\varepsilon_{eq}^{n})(1 + \dot{\varepsilon}_{eq}^{*})^{C}(1 - T^{*m}) \tag{10}$$

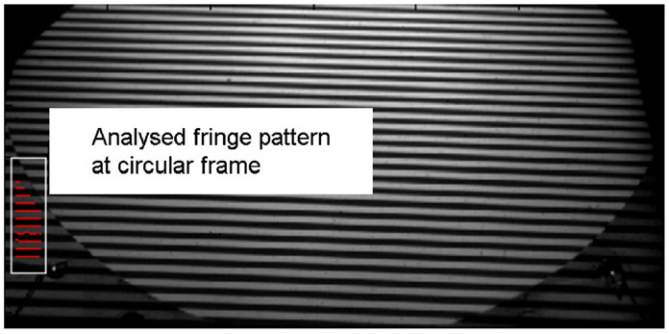

Fig. 11. Vibration evaluation by analyzing the projected pattern at the circular frame.

The model has five material constants A, B, n, C and m. The dimensionless strain rate is given by $\dot{\varepsilon}_{eq}^{*} = \dot{\varepsilon}_{eq}/\dot{\varepsilon}_{0}$, where $\dot{\varepsilon}_{eq}$ is the equivalent plastic strain rate and $\dot{\varepsilon}_{0}$ is a user-defined reference strain rate. The homologous temperature is given as $T^{*}=(T-T_r)/(T_m-T_r)$, where suffixes r and m are the room and melting temperatures, respectively. The temperature increase caused by dissipation of plastic work due to adiabatic heating is calculated as

$$\Delta T = \int_{0}^{\varepsilon_{eq}} \chi \frac{\sigma_{eq} d\varepsilon_{eq}}{\rho C_p} \tag{11}$$

where ρ is the material density, $C_p$is the specific heat and χ is the Taylor-Quinney coefficient that represents the proportion of plastic work converted into heat.

Johnson and Cook [31] also proposed a fracture criterion that accounts for strain path, strain rate, temperature and stress triaxiality. The fracture criterion is based on damage evolution, where the damage D of a material element is expressed as

$$D = \Sigma(\Delta\varepsilon_{eq}/\varepsilon_{f}) \tag{12}$$

Here, $\Delta\varepsilon_{eq}$ is the increment of accumulated plastic strain that occurs during an integration cycle and ε_f is the fracture strain. Failure occurs by element erosion when D equals unity. The fracture strain is constructed in a similar way as the Johnson–Cook constitutive relation. A slightly modified version of the original model [30] reads

$$\varepsilon_{f} = (D_1 + D_2 \exp(D_3\sigma*))(1 + \dot{\varepsilon}_{eq}^{*})^{D_4}(1 + D_5 T^{*}) \tag{13}$$

where $D_1, \ldots, D_5$ are material constants. σ^{*} is the stress triaxiality ratio defined as σ_H/σ_{eq}, where σ_H is the hydrostatic stress. The model has been implemented as material model # 107 in the commercial non-linear finite element code LS-DYNA [18].

5.2. Identification of material constants

To reveal the mechanical properties of AA5083-H116 under impact generated loading conditions, the flow and fracture characteristics of the alloy as function of strain rate, temperature and stress triaxiality have been investigated in detail by Grytten et al. [12,13], Benallal et al. [16,26] and Clausen et al. [27]. Typical true stress–strain curves from quasi-static tensile tests at room temperature on smooth, axisymmetric specimens are shown in Fig. 13. The specimens were taken from a 10 mm thick plate and in three different directions with respect to the rolling direction, and the alloy is as seen anisotropic both in strength and plastic flow. The mechanical properties of this plate thickness have been found to be very similar to the 5 mm thick plate used in this study

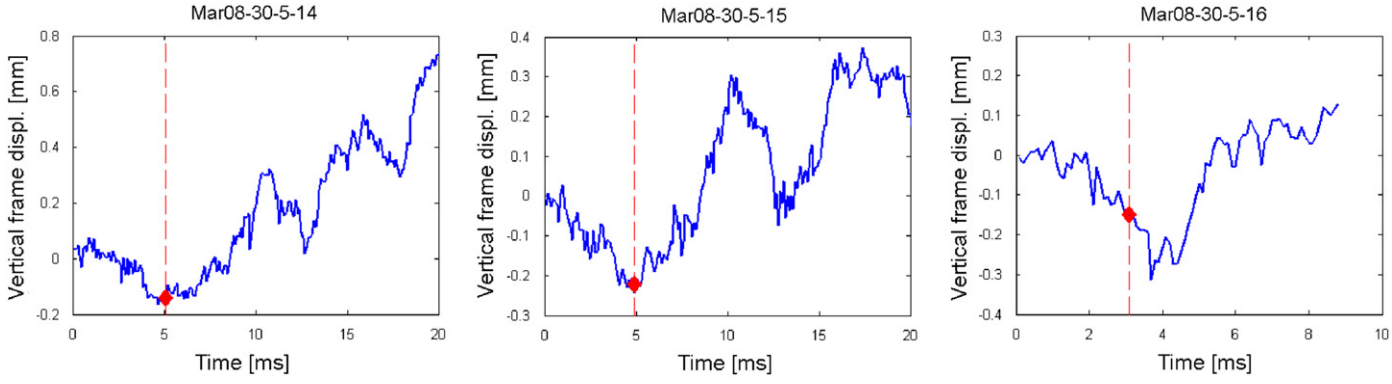

Fig. 12. Measured out-of-plane deformations of the circular frame due to vibrations in the circular frame and the optical components. Rectangles illustrate the time of max deformation or perforation for each experiment.

[12]. The data from Clausen et al. [27] were obtained from a 25 mm thick plate, but are used here to determine the fracture parameters. This may be done since cold rolling take place at low stress triaxialities, so that the damage accumulation during rolling is assumed negligible [12]. Thus, the test results from Grytten et al. [12] were used to calibrate the flow stress, while the data from Clausen et al. [27] were used to determine the remaining material constants for AA5083-H116 and the modified Johnson–Cook model. From these results, material constants to be used in the subsequent numerical simulations are listed in Tables 5 and 6.

Note that the Johnson–Cook model neither accounts for the anisotropic behaviour nor dynamic strain aging. Further, adiabatic heating is assumed in the Johnson–Cook model. However, in the current cases, some heat conduction occurs during the impact. The effect of anisotropy, dynamic strain aging and heating were investigated in a recent study by Grytten et al. [13]. It was concluded that the effects of anisotropy and heating were negligible for the present problem, but that dynamic strain aging influenced the force level. However, adequate agreement between experimental data from low-velocity impact tests and numerical simulations was in general observed for the present target material when using the von Mises (isotropic) yield criterion, axisymmetric elements and neglecting both strain rate and temperature effects. Motivated by these conclusions, the effect of strain rate and temperature will be neglected in this study by setting the material constants C, χ, D_4 and D_5 to zero in all simulations. It is referred to [13] for a more thorough discussion regarding these choices.

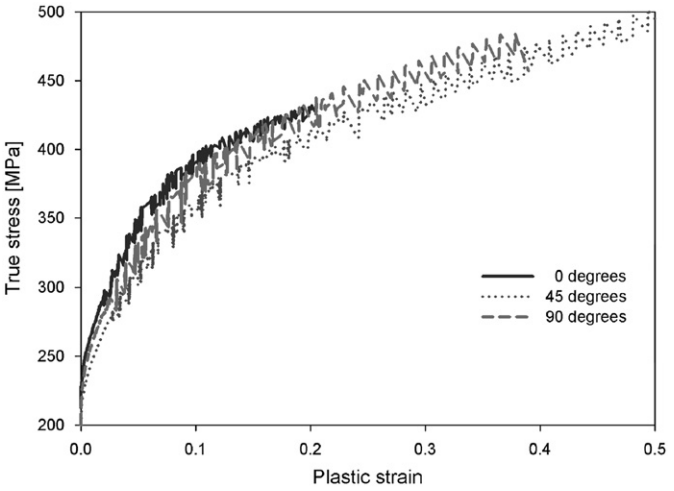

Fig. 13. Anisotropic hardening with PLC and difference in ductility from quasi-static tensile tests on smooth, axisymmetric specimens taken from a 10 mm thick plate [12].

5.3. Numerical model

Simulations of the impact tests were performed in LS-DYNA [18] using under-integrated axisymmetric volume weighted elements (type 15 in LS-DYNA) and Flanagan–Belytschko stiffness based hourglass control. A plot of the finite element model reflected about the *yz*-plane is depicted in Fig. 14(a). The section of the plate within 1.2 times the radius of the projectile is defined as the local part, while the rest of the plate is defined as the global part. Fig. 14(b) shows a close-up of the mesh in the transition zone between the global and the local part of the FE model. In the global part, 10 elements were used over the target thickness, making the element size 0.5×0.5 mm^2. In the shear zone, the mesh density was gradually increased to 90 elements over the thickness, giving an element size of 0.055×0.055 mm^2 in this area. These element sizes resulted in about 16000 elements in the numerical model.

Material constants for the Johnson–Cook constitutive relation and fracture criterion are given in Tables 5 and 6, respectively. The steel projectile was modelled as a rigid body with Young's modulus E equal to 210000 MPa and Poisson's ratio of 0.33. Contact between the projectile and the plate was modelled with the *contact_2d_automatic_surface_to_surface algorithm and self-contact in the plate was modelled using the *contact_2d_automatic_single_surface algorithm available in LS-DYNA.

5.4. Numerical results and comparison

Good agreement between the numerical simulations and the test results was in general observed. Fig. 15(a) shows a fringe plot of the vertical plate displacement from simulation of test "Mar08-5-30-14" at maximum load showing no perforation as in the test, while Fig. 15(b) shows a similar plot from simulation of test "Mar08-5-30-16" where the target plate failed by plugging as in the test. Fig. 16(a) shows a close-up of the plastic strain in the local part of the aluminium plate just before plugging.

A comparison between measured and predicted out-of-plane deformation profiles is given in Fig. 17. The final profiles are taken at maximum displacement before rebound or fracture in the simulations, which may not correspond exactly with the corresponding test. In general, the simulated profiles follow the measured profiles very well. Note also that the measured profiles showed some asymmetric deformation (just barely seen in Fig. 17) of the plates, but this behaviour cannot be predicted

Table 6
Fracture constants for AA5083-H116 [12,27].

D_1	D_2	D_3	D_4	D_5
0.178	0.389	−2.25	0.147	16.8

Table 5
Material constants for AA51083-H116 [12,27].

Elastic constants			Yield stress and strain hardening			Strain rate hardening	
E [GPa]	v	ρ [kg/m^3]	A [MPa]	B [MPa]	n	$\dot{\varepsilon}_0$ [s^{-1}]	C
70	0.3	2660	206.2	424	0.362	1	0.01
Temperature softening and adiabatic heating							
T_r [K]	T_m [K]	m	Cp [J/kg/K]	χ	α [K^{-1}]		
293	862	1	904	0.9	2.6×10^{-5}		

using 2D axisymmetric elements. These plots strengthen the confidence both for the optical measurements and the numerical simulations.

Fig. 18 compares the measured interface force between the projectile and the plate versus time with the interface force–time curves from the simulations. As seen, the force–time curves from the simulations display the same type of behaviour as the measured curves. Also the fracture in test "Mar08-5-30-16" is well predicted. However, in all the simulations the force level is somewhat overestimated. The reason for this discrepancy may be that in the numerical simulations the effects of dynamic strain aging is neglected. This causes the plate to appear too stiff in the simulations, which can also explain why the maximum deformations of the plates in some of the simulations were

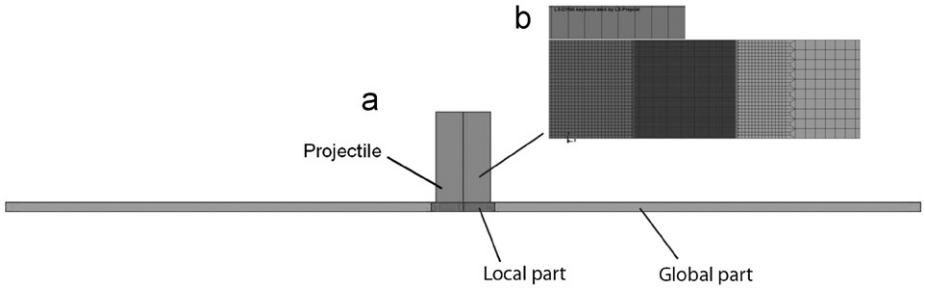

Fig. 14. Finite element model showing (a) the local and global parts of the plate in addition to the blunt nose projectile and (b) close-up of the mesh in the transition zone between the global and the local parts of the target plate.

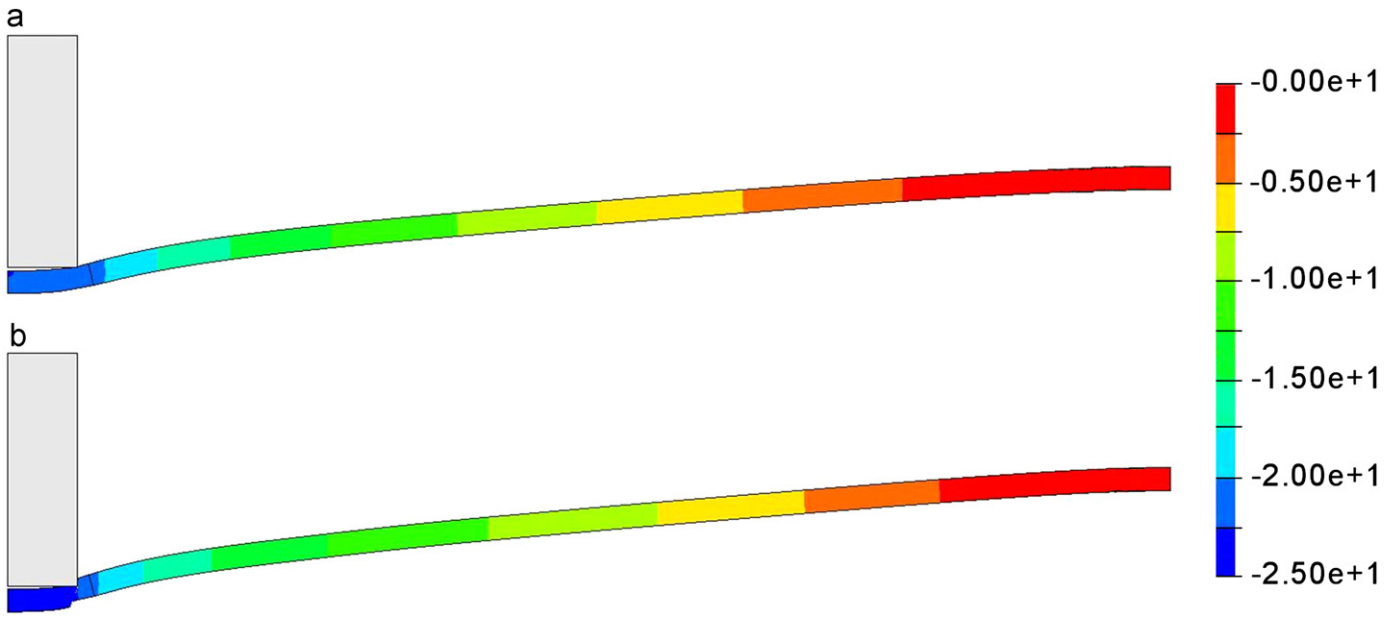

Fig. 15. Fringe plot of vertical displacement from simulation of (a) test "Mar08-5-30-14" at maximum load (t=4.4 ms) and (b) of test "Mar08-5-30-16" just after plugging (t=2.8 ms).

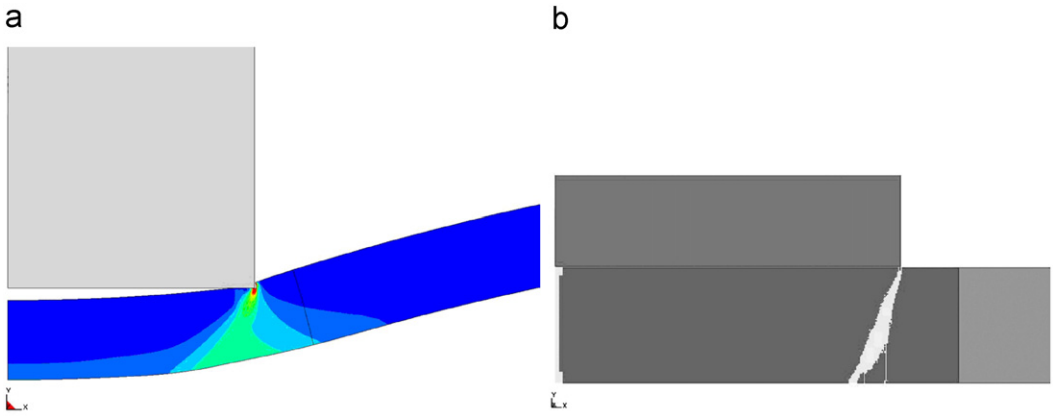

Fig. 16. (a) Plastic strain just before plugging (t=2.4 ms) and (b) plug and fracture pattern from the "Mar08-5-30-16" simulation.

smaller than the maximum deformation measured in the tests. It was shown in Grytten et al. [13] that when strain rate effects were included through a constitutive relation accounting for dynamic strain ageing, material softening is introduced and a better prediction of the force level may be made.

Finally, Fig. 16(b) shows the predicted plug and fracture pattern from the numerical simulations of test "Mar08-5-30-16". Both the inclined edges and the central cracking of the plug (as also seen experimentally by Grytten et al. [13]) seem to be captured in the simulations. Approximately 1000 elements failed due to damage during plugging. This rather large number is caused by a combined shear and tensile type of ductile failure mode in the axisymmetric target, and a rather low ductility of the alloy at positive stress triaxialities (see e.g. [12] for the failure locus of AA5083-H116 as a function of σ^*). However, the energy ratio (ratio between current total energy and initial total energy) in these simulations is always checked and found to be close to unity, so that the energy losses due to eroded elements are almost zero.

6. Discussion

As the presented optical method in general is able to measure the three-dimensional topography of any continuous surface based on a single recorded image the limitations of its use lie basically in the camera technology, i.e. recording rate, image resolution and light sensitivity. Further, sensible applications of the method may be a problem concerning blast loading or high-speed impacts. It is also noted that the size of the target surface is

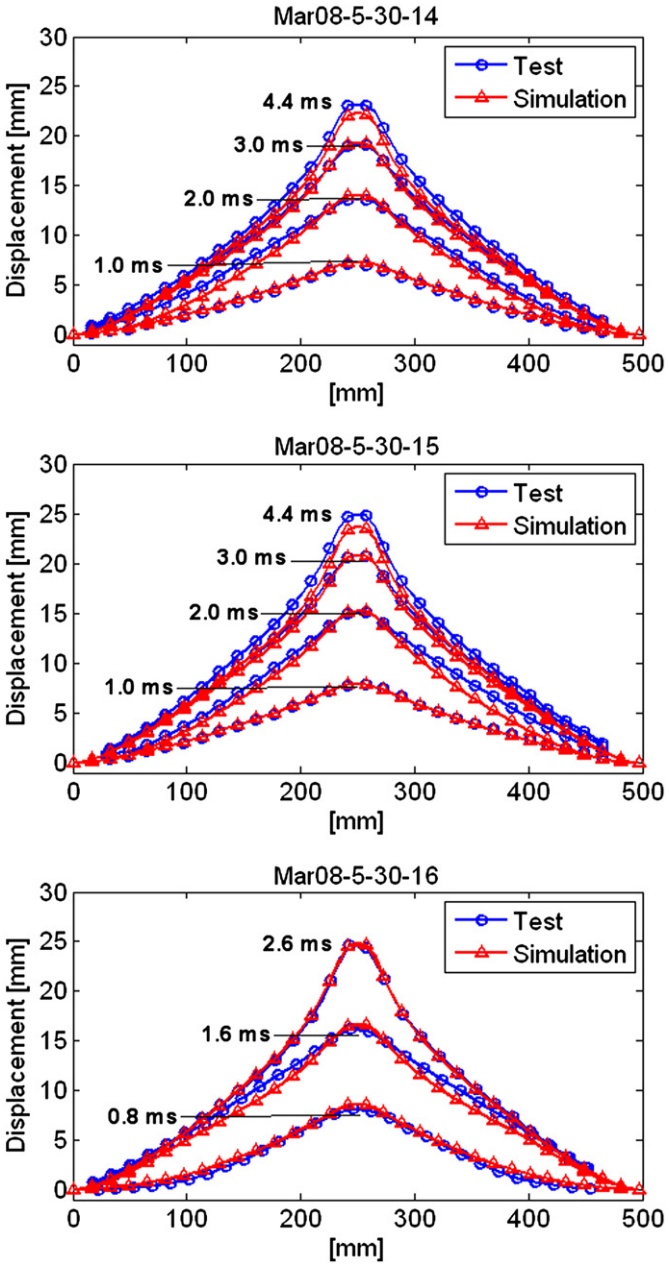

Fig. 17. Comparison between experimentally measured and numerically simulated out-of-plane deformation profiles for the three impact tests.

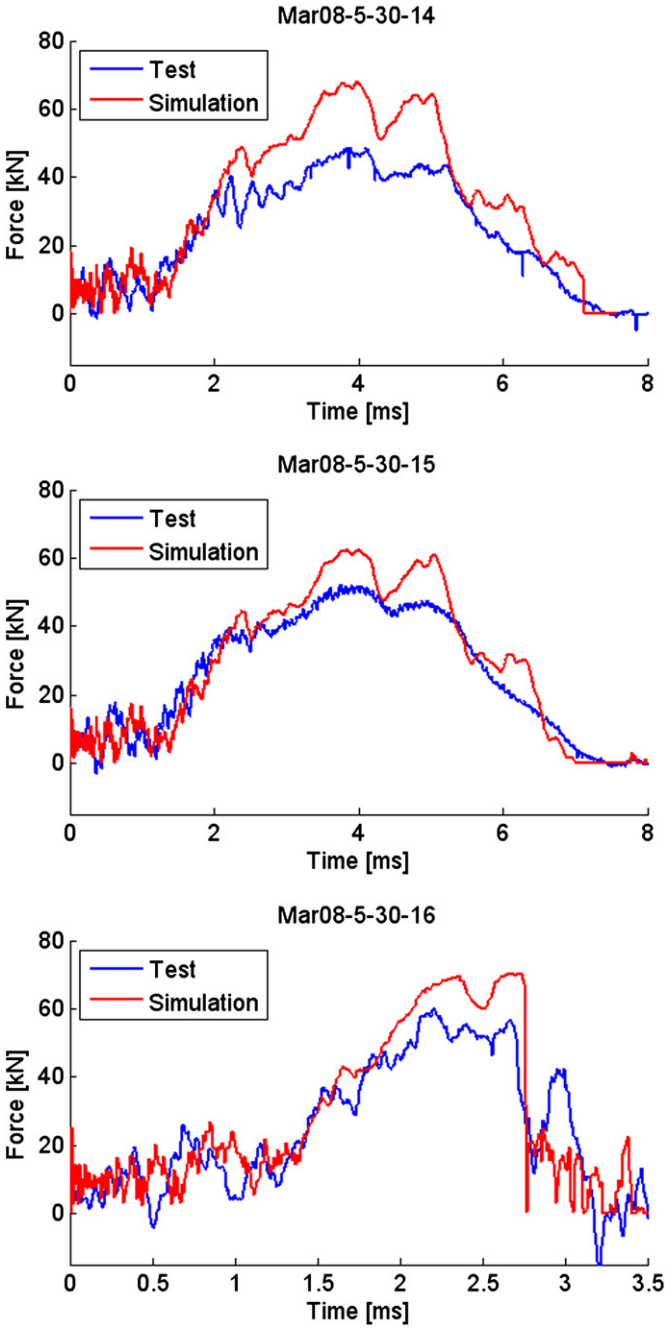

Fig. 18. Measured force in impact tests compared to simulated force for the three scenarios.

irrelevant to the principle of the method. However, practical limitations when it comes to projector and camera lenses may limit the size of the target surface from a few centimetres to several meters. A natural extension to the presented method is to use a three-dimensional Digital Image Correlation (3D-DIC) application which is able to measure the strain field as well as the out-of-plane deformations in a target surface [17]. This particular method requires a setup with two calibrated cameras.

Post-processing of large series of high-resolution images may be computational expensive. The first implementation of the algorithms was developed in MathWorks MATLAB, a reasonable and easy-to-use development environment for new algorithms. However, a new implementation developed in the programming language C++ has increased the processing speed considerably, providing the ability to process thousands of megapixel images in a matter of a few hours on a standard workstation.

As presented in this paper, one application of the measurement technique is the validation of numerical simulation for impact problems. However, the acquired data may also provide useful information in order to validate previous findings related to the low-velocity impact of metallic plates. Langseth and Larsen [10] studied the behaviour of aluminium plates subjected to an impact from a projectile with a mass of 50 kg in the velocity range 8–20 m/s. They concluded that the impact can be divided into a transient phase and a global mode phase where the supports are fully activated. In the transient phase, flexural waves are travelling away from the impact point. The velocity of the projectile in this phase was estimated by Langseth and Larsen [10] to be

$$v(t) = \frac{1}{1+0.48\,\frac{\pi r_0(t)^2 h\rho}{M_p}} \tag{14}$$

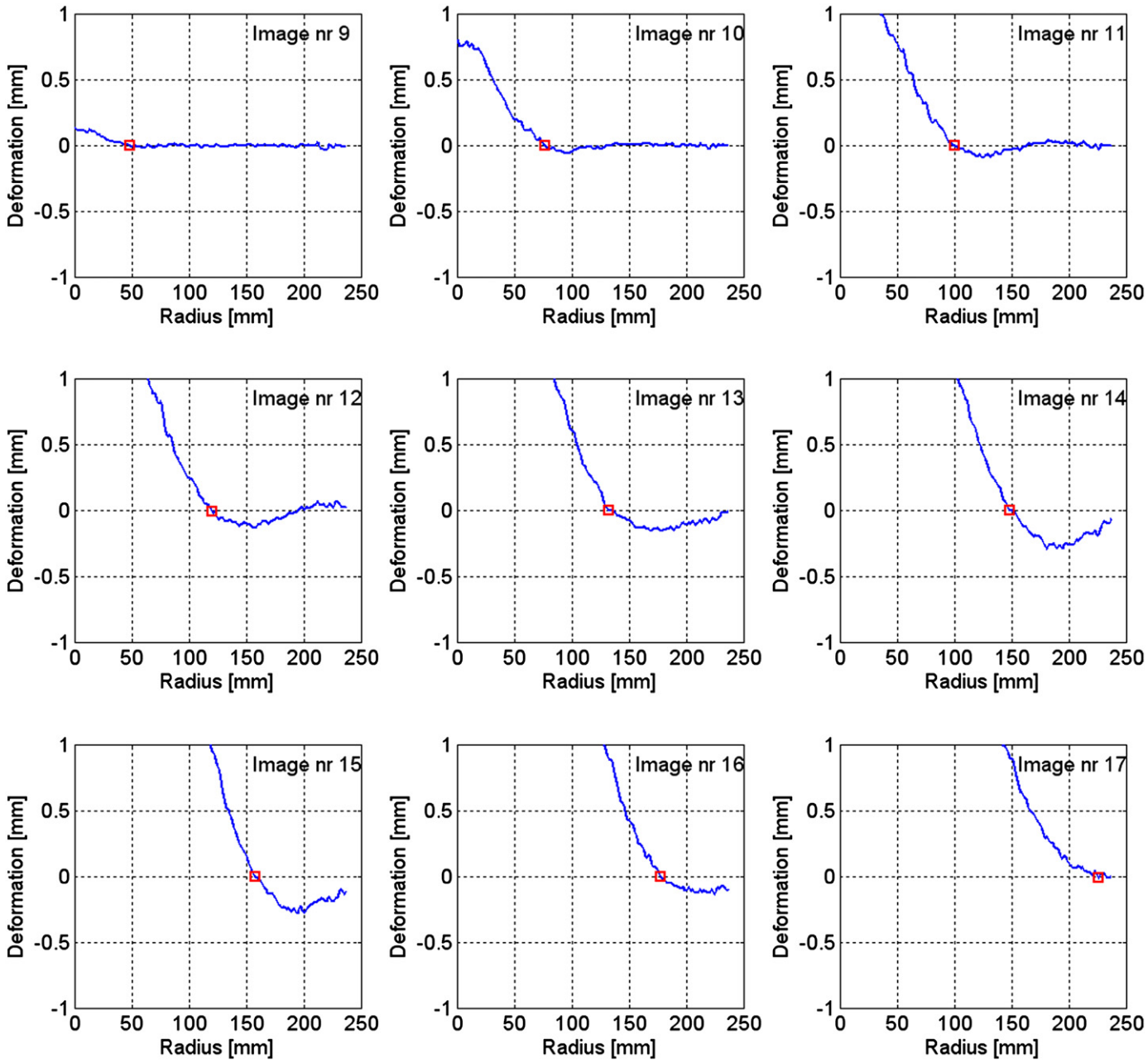

Fig. 19. Propagation of wave front in transient phase until supporting frame is activated in experiment "Mar08-5-30-14". Each plot shows the out-of-plane deformation as a function of radius, i.e. the distance from the centre of the plate. A square illustrates the hinge position $r_0(t)$. The time between each plot is 0.1 ms.

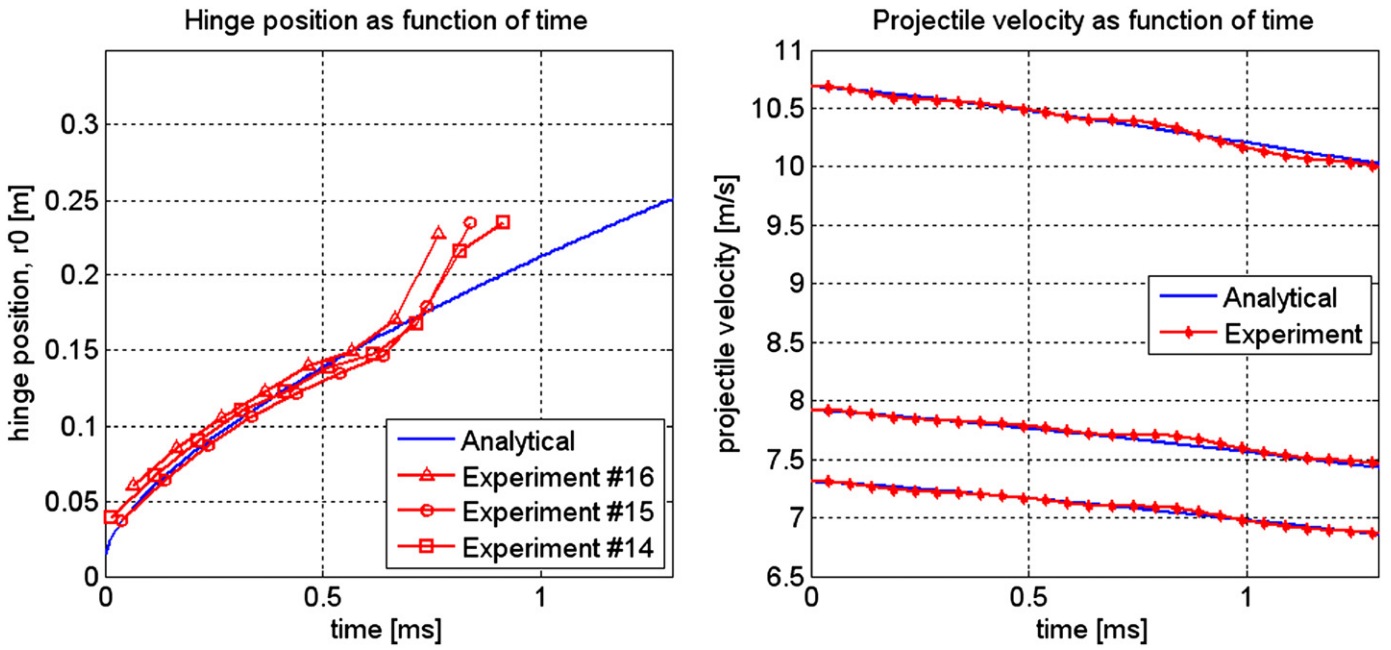

Fig. 20. (a) The analytical solution of the hinge position from Eq. 14 compared with the experimental data from the three experiments Mar08-5-30-14, -15 and -16. (b) The analytical solution of the projectile velocity in the transient phase compared to experimental data from the three tests.

where

$$r_0(t) = \frac{d}{2}\left[0.81\left(\frac{h}{d}\right)^{0.375}\left(\frac{ct}{d}\right)^{0.673} + 1\right] \tag{15}$$

is defined as the hinge position of the travelling wave. In Eqs. 14 and 15, h is the plate thickness, d is the diameter of the blunt nose projectile, $c = \sqrt{E/\rho}$ is the uniaxial elastic wave speed and M_p is the mass of the projectile. The propagating wave and the position of the hinge as a function of time are shown in Fig. 19 for one of the present tests, "Mar08-5-30-14". It is to be noted that since the measured data are three-dimensional it is possible to study the propagation of the wave front in any directions from the centre of the plate. From Fig. 19 it is also evident that even if the absolute accuracy of the measurements is estimated to be 0.3 mm, the resolution of the measurements is substantially higher and it is possible to study dynamic effects of much smaller extent.

In Fig. 20(a), the optically measured hinge position as a function of time $r_0(t)$ for all three experiments are compared with the semi-analytical model in Eq. 15, proposed by Langseth and Larsen [10]. The plot shows a good correlation between the model and the measured data up to approximately 0.7 ms, while some deviation started to occur at this point. At the end of the transient phase which was estimated to take place at around 1.3 ms, the wave seems to be affected by reflections from the supporting frame, giving deviations from the calculated wave front. It is noted that because of the 10,000 Hz recording rate of the high-speed camera, only $\sim$10 images are recorded during the transient phase of the impact. If this phase should be studied in more detail, a higher recording frame rate should be used, and the setup of the optical equipment should be optimized to get the best possible resolution along half the cross-section of the plate. In Fig. 20(b) the velocity of the projectile in the transient phase is calculated based on Eq. 14. Good agreement is found compared to the integrated signal from the strain gauges on the nose of the projectile. Based on the impact velocity and the velocity of the projectile at the end of the transient phase, it can be concluded that the energy absorption in the transient phase is small and less than 15%. Thus, based on the present study and the study by Langseth and Larsen [10] it is reasonable to conclude that the energy absorption in the target, from a design perspective, when subjected to large mass projectiles in the low-velocity regime, can be calculated based on the global mode phase only.

7. Concluding remarks

An optical system using structural light, i.e. projected fringes, has been successfully applied to provide accurate measurements of the full-field continuous deformation of aluminium plates subjected to low-velocity impact. The system uses a projector that projects a fringe pattern onto the rear surface of the target plate and a high-speed camera that captures the changes in the pattern during the deformation of the plate at a rate of 10,000 images per second. Images are post-processed to provide topography maps of the observed surface of the target plate for each recorded image. Vibration levels have been evaluated and reduced to a minimum, resulting in an absolute accuracy of about 0.3 mm in the out-of-plane deformation measurements. Three impact tests have been carried out on 5 mm thick AA5083-H116 aluminium plates with initial projectile velocities between 7 and 11 m/s.

The measured out-of-plane deformations from the tests have been evaluated using the non-linear finite element code LS-DYNA. In the numerical simulations of the impact process, axisymmetric elements and slightly modified versions of the Johnson–Cook constitutive relation and fracture criterion were used. Good correlation between measured and simulated out-of-plane deformations of the plate was obtained. The optical measurements were also compared to a semi-analytical model available in the literature. Also here, the agreement between measured and predicted results was in general good. Thus, it may be concluded that the proposed optical technique gives appropriate results both for direct measurements of the out-of-plane behaviour of impacted structures and for validation of numerical and analytical calculations.

Acknowledgements

The financial support of this work from the Structural Impact Laboratory (SIMLab), Centre for Research-based Innovation (CRI) at the Norwegian University of Science and Technology (NTNU), is gratefully acknowledged. The authors would also like to acknowledge Mr. Trond Auestad at SIMLab and Mr. Bernt Førre and Dr. Erik Wahlstrøm at the Department of Physics, NTNU, for valuable support throughout this work.

References

[1] Goldsmith W. Review: non-ideal projectile impact on targets. Int J Impact Eng 1999;22:95–395.
[2] Backman ME, Goldsmith W. The mechanics of penetration of projectiles into targets. Int J Eng Sci 1978;16:1–99.
[3] Corbett GG, Reid SR, Johnson W. Impact loading of plates and shells by free-flying projectiles. Int J Impact Eng 1996;18(2):141–230.
[4] Zukas JA, et al. In: Impact dynamics. New York: John Wiley & Sons; 1982.
[5] Zukas JA, et al. In: High velocity impact dynamics. New York: John Wiley & Sons; 1990.
[6] Wen H-M, Jones N. Experimental investigations into the dynamic plastic response and perforation of a clamped circular plate struck by a mass. J Mech Eng Sci 1994;208(C2):113–37.
[7] Wen H-M, Jones N. Low-velocity perforation of punch-impact-loaded metal plates. J Pressure Vessel Technol 1996;118:181–7.
[8] Langseth M, Larsen PK. Dropped objects' plugging capacity of steel plates: an experimental investigation. Int J Impact Eng 1990;9(3):289–316.
[9] Langseth M, Larsen PK. The behaviour of square steel plates subjected to a circular blunt ended load. Int J Impact Eng 1992;12(4):617–38.
[10] Langseth M, Larsen PK. Dropped objects' plugging capacity of aluminium alloy plates. Int J Impact Eng 1994;15(3):221–41.
[11] Langseth M, Hopperstad OS, Berstad T. Impact loading of plates: validation of numerical simulations by testing. Int J Offshore Polar Eng 1999;9(1):10–5.
[12] Grytten F, Børvik T, Hopperstad OS, Langseth M. Quasi-static perforation of AA5083-H116 aluminium plates. Int J Impact Eng 2009;36(3):486–97.
[13] Grytten F, Børvik T, Hopperstad OS, Langseth M. Low velocity perforation of AA5083-H116 aluminium plates. Int J Impact Eng 2009;36(4):597–610.
[14] Sutton M, McNeil S, Helm J, Chao Y. Advances in two-dimensional and three-dimensional computer vision, in photomechanics. Top Appl Phys 2000;77:323–72.
[15] Roux S, Réthoré J, Hild F. Recent progress in digital image correlation: from measurement to mechanical identification. J Phys: Conf Ser 2008;135.
[16] Benallal A, Berstad T, Børvik T, Hopperstad OS, Nogueira de Codes R. Effects of strain rate on the characteristics of PLC deformation bands for AA5083-H116 aluminium alloys. Philos Mag 2008;88(28–29):3311–38.
[17] Tiwari V, Sutton MA, McNeill SR, Xu S, Deng X, Fourney WL, Bretall D. Application of 3D image correlation for full-field transient plate deformation measurements during blast loading. Int J Impact Eng 2008, doi:10:1016/j.ijimpeng.2008.09.010.
[18] LSTC. LS-DYNA Keyword User's Manual, Version 970. Livermore Software Technology Corporation, March, 2003.
[19] Grytten F, Fagerholt E, Auestad T, Førre B, Børvik T. Out-of-plane deformation measurements of an aluminium plate during quasi-static perforation using structured light and close-range photogrammetry. Int J Solids Struct 2007;44(17):5752–73.
[20] Heikkilä J. . Accurate camera calibration and feature based 3D reconstruction from monocular image sequences, PhD. thesis, University of Oulu, Finland, 1997.
[21] Atkinson KB. In: Close Range Photgrammetry and Machine Vision. Whittles Publishing; 1996.
[22] Harris C., Stephens M.. A combined corner and edge detector. In: Proceedings of the fourth alvey vision conference, p. 189–192, 1988.
[23] Abdel-Aziz Y.I., Karara H.M.. Direct linear transformation from comparator coordinates into object space coordinates in close-range photogrammetry. In: Proceedings of the ASP/UI symposium on close-range photogrammetry, p. 1–18, Urbana, IL, January 1971.
[24] Børvik T, Forrestal MJ, Hopperstad OS, Warren T, Langseth M. Perforation of AA5083-H116 aluminium plates with conical-nose steel projectiles–calculations. Int J Impact Eng 2009;36(3):426–37.
[25] Grytten F, Holmedal B, Hopperstad OS, Børvik T. Evaluation of identification methods for YLD2004-18p. Int J Plasticity 2008;24(12):2248–77.
[26] Benallal A, Berstad T, Børvik T, Hopperstad OS, Koutiri I, Nogueira de Codes R. An experimental and numerical investigation of the behaviour of AA5083 aluminium alloy in presence of the Portevin-Le Chatelier effect. Int J Plasticity 2008;24(10):1916–45.
[27] Clausen AH, Børvik T, Hopperstad OS, Benallal A. Flow and fracture characteristics of aluminium alloy AA5083-H116 as function of strain rate, temperature and triaxiality. Mat Sci Eng A 2004;365:260–72.
[28] Fagerholt E.. Accurate measurements of out-of-plane deformations using structured light and close-range photogrammetry, M.Sc. Thesis, Department of Physics, Norwegian University of Science and Technology, Trondheim, Norway, 2004.
[29] Johnson G.R., Cook W.H.A. Constitutive model and data for metals subjected to large strains, high strain rates and high temperatures. In: Proceedings of seventh international symposium on ballistics, The Hague, The Netherlands, April 1983.
[30] Børvik T, Hopperstad OS, Berstad T, Langseth M. A computational model of viscoplasticity and ductile damage for impact and penetration. Eur J Mech—A/Solids 2001;20(5):685–712.
[31] Johnson GR, Cook WH. Fracture characteristics of three metals subjected to various strains, strain rates, temperatures and pressures. Eng Frac Mech 1985;21:31–48.

Part II

E. Fagerholt, C. Dørum, T. Børvik, H.I. Laukli and O.S. Hopperstad.

Experimental and numerical investigation of fracture in a cast aluminium alloy

International Journal of Solids and Structures, Volume 47, Issue 24, Pages 3352-3365, 2010.

International Journal of Solids and Structures 47 (2010) 3352–3365

Contents lists available at ScienceDirect

International Journal of Solids and Structures

journal homepage: www.elsevier.com/locate/ijsolstr

Experimental and numerical investigation of fracture in a cast aluminium alloy

E. Fagerholt [a,*], C. Dørum [a,b], T. Børvik [a,c], H.I. Laukli [a,d], O.S. Hopperstad [a]

[a] Structural Impact Laboratory (SIMLab), Centre for Research-based Innovation (CRI) and Department of Structural Engineering, Norwegian University of Science and Technology, Rich. Birkelands vei 1A, NO-7491 Trondheim, Norway
[b] SINTEF Materials and Chemistry, Rich. Birkelands vei 2B, NO-7465 Trondheim, Norway
[c] Norwegian Defence Estates Agency, Research and Development Department, PB 405, Sentrum, NO-0103 Oslo, Norway
[d] Norsk Hydro ASA, Research and Technology Development, NO-6600 Sunndalsøra, Norway

ARTICLE INFO

Article history:
Received 23 February 2010
Received in revised form 12 August 2010
Available online 17 August 2010

Keywords:
Arcan tests
Digital image correlation
Crack propagation
Stochastic variation
Element erosion

ABSTRACT

This paper describes an experimental and numerical investigation on the fracture behaviour of a cast AlSi9MgMn aluminium alloy. In the experiments, a modified Arcan test set-up was used to study mixed-mode fracture. During testing, the tension load and the displacement of the actuator of the test machine were recorded, simultaneously as a high-resolution digital camera was used to record a speckle-patterned surface of the specimen. The recorded images were post-processed using an in-house digital image correlation (DIC) software to obtain information of the displacement and strain fields in the specimen during the test. In addition, some newly implemented features in the DIC software allowed us to detect and follow the crack propagation in the material. The numerical calculations were carried out with a user-defined material model implemented in an explicit finite element code. In the model, the material behaviour is described by the classical J_2 flow theory, while fracture was modelled by the Cockcroft–Latham criterion, assuming the fracture parameter to follow a modified weakest-link Weibull distribution. With the proposed probabilistic fracture modelling approach, the fracture parameter can be introduced as a random variable in the finite element simulations. Crack propagation was modelled by element erosion, and a non-local damage formulation was used to reduce mesh-size sensitivity. To reveal the effect of mesh density and meshing technique on the force–displacement curves and the crack propagation, several different meshes were used in the numerical simulations of the modified Arcan tests. The numerical results were finally compared to the experimental data and the agreement between the measured and predicted response was evaluated.

1. Introduction

In design of thin-walled structural components for ultimate or accidental loads, it is important to evaluate the risk of failure by buckling for compressive loads and necking and fracture for tensile loads. Several approaches may be used to describe fracture in thin-walled components. In a recent paper, Mediavilla et al. (2006) distinguished between three approaches for modelling fracture in finite element analysis, namely the discontinuous, continuous and combined approaches. In the discontinuous approach, the geometry of the crack is modelled explicitly, i.e. the finite element model includes a strong discontinuity. The cohesive zone method (e.g. Needleman, 1990; Scheider and Brocks, 2006) and the extended finite element method (e.g. Moës et al., 1999; Song et al., 2008) are examples of the discontinuous approach. In the continuous approach, the degradation of the material in the fracture process zone is described by a constitutive model, while cracks are described by continuous regions that have altogether lost their load-carrying capacity due to damage softening (Mediavilla et al., 2006). Examples of the continuous approach are porous plasticity (e.g. Gurson, 1977; Rousselier, 1987) and continuum damage mechanics (e.g. Lemaitre, 1992). The combined continuous–discontinuous approach consists of modelling the degradation in the process zone by porous plasticity or continuum damage mechanics and then introducing a strong discontinuity for instance at a given porosity or a critical damage. Mediavilla et al. (2006) proposed an uncoupled continuous–discontinuous approach, where the damage in the fracture process zone is computed but its influence on the material behaviour is neglected. The ductile damage variable was then used as an indicator for crack initiation and propagation, while an advanced remeshing and node-splitting approach was developed for predicting crack propagation.

Digital image correlation (DIC) has been an increasingly popular and applicable tool, the last decades for gaining information about displacement and strain fields in mechanical experiments (Rastogi, 2000). Traditionally, the measurements of these field properties have been limited to specimens or regions of interest experiencing

* Corresponding author. Tel.: +47 73 59 46 93; fax: +47 73 59 47 01.
E-mail address: egil.fagerholt@ntnu.no (E. Fagerholt).

0020-7683/$ - see front matter © 2010 Published by Elsevier Ltd.
doi:10.1016/j.ijsolstr.2010.08.013

continuous displacement fields. Trying to implement DIC field measurements in experiments where specimens undergo crack propagation, opens up to a series of new challenges depending on the application. Usually a significant amount of manual interaction is needed to deal with a propagating crack which may have different properties from experiment to experiment. With the ongoing technical revolution in digital cameras, particularly when it comes to image resolution and frame rate, huge amount of data may be generated from a single mechanical experiment. This facilitates better resolution and accuracy in DIC measurements. However, manual interaction becomes less desirable. Typical challenges using DIC in experiments involving crack propagation are automatic handling and modelling of a growing crack through the measured area of the specimen. A number of studies regarding these topics have been presented. Helm (2008) published a procedure for automatic handling of multiple growing cracks in a concrete specimen using the Newton–Raphson based DIC process, while Rèthorè et al. (2007) showed how the discontinuity in the displacement field caused by a crack can be modelled by using enrichment of nodal degrees of freedom in an "extended finite element" DIC process (X-DIC). However, the analysis of propagating cracks in a specimen is still considered a challenging task when it comes to automatic detection and handling of the discontinuous displacement field. In this study, an automatic crack detection and handling technique, developed and presented by Fagerholt et al. (in preparation), was used in combination with a "finite element" DIC algorithm to analyze images of specimens experiencing crack propagation in mechanical experiments.

The fracture behaviour of cast aluminium alloys has been studied by e.g. Mohr and Henn (2007) and Teng et al. (2008). In these studies, experiments in combined tension and shear loading were conducted. Combining the experimental results with finite element simulations, the fracture strain as a function of stress triaxiality (fracture locus) was established for the material. In this paper, we have studied the fracture behaviour of thin-walled cast aluminium components experimentally and numerically. The cast components had U-shaped geometry with wall thickness 2.5 mm. Samples were cut from the component walls for testing under quasi-static loading conditions in a modified Arcan test set-up (Amstutz et al., 1996; Amstutz et al., 1997; Arcan et al., 1978), which facilitated mixed-mode fracture experiments by varying the orientation of the sample in the fixture. The cast components were made of the aluminium alloy AlSi9MgMn which has applications in automotive components. The material behaviour of the cast components has previously been thoroughly characterized by Dørum et al. (2009). Large variations in tensile ductility between parallel tests were found, and a probability distribution of the tensile ductility was established.

During testing, a high-resolution digital camera was used to record a speckle-pattern on the surface of the sample, and the recorded images were post-processed using an in-house DIC software to obtain the displacement and strain fields in the sample. Some newly implemented features in the DIC software allowed us to detect and follow the crack propagation in the sample, which is essential for assessment of numerical methods for predicting fracture and crack propagation. The numerical calculations were carried out with the commercial explicit finite element code LS-DYNA (LSTC, 2003) using shell elements and an uncoupled continuous–discontinuous approach to describe crack propagation. The classical J_2 flow theory was adopted to describe the material behaviour, the damage evolution in the fracture process zone was computed according to the Cockcroft–Latham criterion (Cockcroft and Latham, 1968), while element erosion was used to model the crack propagation. The fracture parameter was assumed to follow a modified weakest-link Weibull distribution and introduced as a random variable in the finite element simulations. This was done to account for the scatter found in the tensile ductility of the AlSi9MgMn alloy. A non-local damage formulation was adopted to reduce mesh-size sensitivity. To reveal the effect of mesh density and meshing technique on the force–displacement curves and crack propagation, several different meshes were used in the numerical simulations of the modified Arcan tests. The numerical results were finally compared to the measured data. It will be shown that good agreement is in general obtained between the measured and predicted response.

2. Material

All castings were produced with an AlSi9MgMn alloy using Hydro Aluminium's high pressure die casting (HPDC) machine dedicated for aluminium alloy research. The machine is a Bühler shot-controlled development machine with a locking force of 4.1 MN. An illustration of a casting with gating system and vacuum channels is shown in Fig. 1. The castings were produced without vacuum in the present investigations. The casting has a generic U-shaped geometry with 2.5 mm wall thickness. Details of the alloy composition and the HPDC production parameters are provided in Dørum et al. (2009). Fig. 2 shows the typical microstructure of the AlSi9MgMn alloy in T1-condition.

Flat dogbone specimens were machined from the wide web, the inlet wall and the outlet wall of the cast U-profiles in Fig. 1. A total of 30 specimens were tested under quasi-static tensile loading conditions using 10 parallel tests from each part of the U-profile. The strain rate during the tests was approximately $2 \times 10^{-3}\,s^{-1}$. The specimens were aligned with the longitudinal direction of the cast component. It is referred to Dørum et al. (2009) for a complete description of the material characterization (including uniaxial tension, notched tension, shear and plate bending tests) of the AlSi9MgMn alloy.

As expected in T1 condition, most of the test specimens were found to fail before the point of diffuse necking. Typical work-hardening curves in terms of Cauchy stress and logarithmic plastic strain are provided in Fig. 3 for different parts of the component. It is observed that the material in the outlet wall is far less ductile than the material in the inlet wall and the web. The work-hardening curves are represented in parametric form

$$\sigma = \sigma_0 + \sum_{i=1}^{2} Q_i(1 - \exp(-C_i\varepsilon^p)), \tag{1}$$

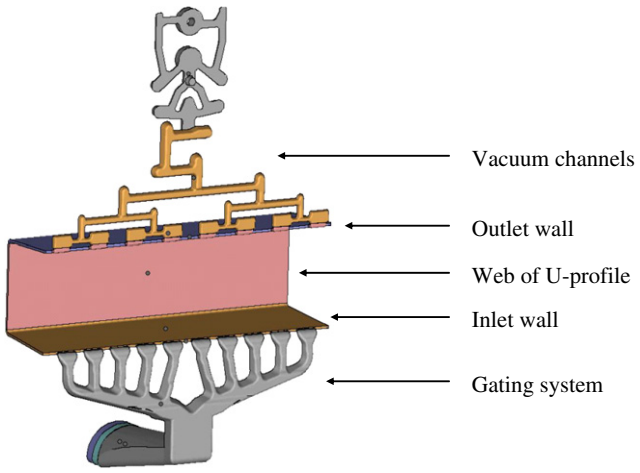

Fig. 1. Illustration of the U-profile casting with gating and vacuum channels. The length of the profile is 300 mm, the web 90 mm and the walls 75 mm. The thickness is 2.5 mm.

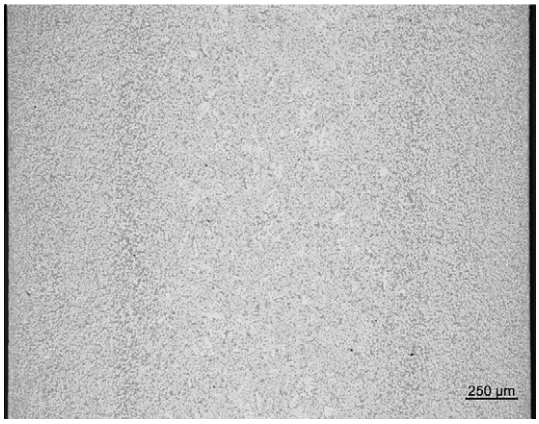

Fig. 2. Typical through-thickness microstructure of HPDC AlSi9MgMn in T1-condition taken from the outlet wall of the casting. Note that the darkest grey phase exhibits Al–Si eutectic.

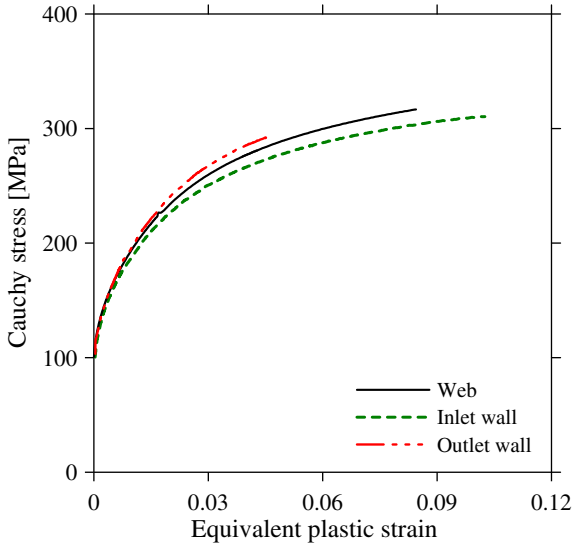

Fig. 3. Typical Cauchy stress versus equivalent (or logarithmic) plastic strain curves obtained from uniaxial tensile tests of AlSi9MgMn. Note that fracture occurs prior to necking in all tests.

where σ is the Cauchy stress, ε^p is the logarithmic plastic strain, σ_0 is the proportionality limit, and Q_i and C_i are hardening parameters. A least squares method was used to determine the parameters of this equation for each of the experimental work-hardening curves. It is noted that in uniaxial tension, the equivalent plastic strain equals the logarithmic plastic strain. Material parameters representing the mean work-hardening curve of the web are given in Table 1.

As seen from Fig. 3, the difference in measured values of fracture strain is significant for specimens cut from different parts of the profile. The largest scatter is found for the specimens cut from the outlet wall. The material in the inlet wall of the casting is in average significantly more ductile than the material in the web and the outlet wall of the component. It should be noted that the scatter in yield stress and work-hardening is relatively low (Dørum et al., 2009).

Table 1
Work hardening parameters representing the mean curve of the web.

Alloy	Position	σ_0 (MPa)	Q_1 (MPa)	C_1	Q_2 (MPa)	C_2
AlSi9MgMn	Web	104.8	39.6	373.2	181.2	33.2

Several defects, some of which are inherent to the HPDC process, play a role in the mechanical performance of die-castings. Macrosegregation of eutectic, intermetallic particles (Laukli et al., 2005) and primary α-Al crystals (Laukli et al., 2005), porosity (Gourlay et al., 2007), oxide bifilms (Campbell, 2005) and confluence welds (Campbell, 1988) are addressed as typical HPDC defects. It is thus not possible to point out a single defect controlling the mechanical performance. The works by Gokhale and Patel (2005) and Gokhale and Patel (2005) on the mechanical properties of cast aluminium alloys showed that there is a strong quantitative correlation between the area fraction of defects and the tensile ductility. For a tilt-pour-permanent mould cast aluminium alloy the controlling defects were identified as oxide films and shrinkage pores, while for a semi-solid metal cast aluminium alloy the controlling defects were essentially residues of modifiers, fluxes, grain refiners and mould release agents. When looking at the attractive features of a HPDC microstructure, it is well known that a very fine-grained (grain size of less than 10 μm) and commonly defect-free surface layer is important for the mechanical properties. The surface layer, up to several hundred microns thick, forms due to the very high cooling rate in HPDC.

3. Experimental set-up

3.1. Modified Arcan tests

Fig. 4 illustrates the experimental set-up used in this study, which is based on Arcan et al. (1978) and Voloshin and Arcan (1980). The set-up consists of two rigid steel platens and a notched butterfly specimen. The geometry and dimensions of the specimen are shown in Fig. 5. The specimen is connected to the steel platens using 12 M6-bolts and the assembly is mounted in a standard servo-hydraulic tensile machine using bolted connections. As indicated in Fig. 4, the orientation of the specimen may be changed to obtain different loading angles β. Changing the loading angle, mode I is obtained for $\beta = 90°$, mode II for $\beta = 0°$, while other loading angles give mixed modes. This feature of the test set-up facilitates studies of mixed-mode fracture. Since the fixtures are loaded through single pins on each side, see Fig. 4, they are allowed to rotate during displacement. This rotation may lead to lateral displacements of the fixtures which affect the loading of the specimen. Prior to the test, one side of the specimen was spray-painted with a combination of black and white paint, giving a fine-grained and high-contrast speckle-pattern (see e.g. Fig. 8) required to enhance the optical measurements. The test series conducted in this study consisted of 5, 5 and 4 tests with β equal to 0°, 45° and 90°, respectively.

During a test, the tension load and the displacement of the hydraulic actuator were recorded at a rate of 15 Hz. In addition, 8-bit grey-scale images of the speckle-patterned specimen surface were recorded at a frame rate of 10 Hz using a Prosilica GC2450 digital camera equipped with a 28–105 mm Nikon lens. The spatial resolution of the recorded images was 2448 × 2050 pixels. The recorded images were post-processed using an in-house digital image correlation (2D-DIC) software (Fagerholt et al., in preparation), obtaining information on displacement and strain fields as well as information on the crack propagation in the specimen. The camera was pre-arranged with its optical axis normal to the specimen surface. A linear relationship between coordinates on the specimen surface and the image coordinates was assumed in the 2D-DIC analysis. The spatial resolution of the image recordings are calculated to 0.03 mm/pixels and the "finite element" size used in the 2D-DIC analysis is 32 pixels or 0.96 mm.

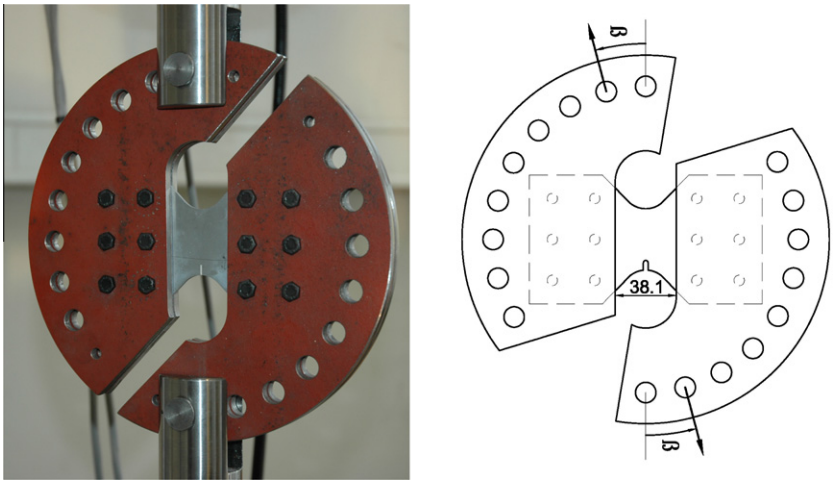

Fig. 4. Picture with $\beta = 0^\circ$ (left) and sketch (right) of the Arcan test set-up.

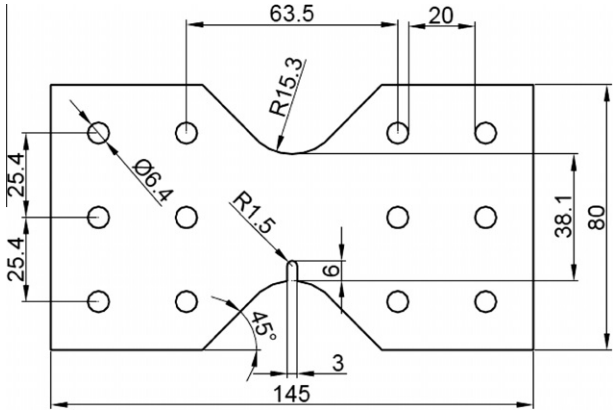

Fig. 5. Geometry and dimensions of notched butterfly test specimen (in mm).

3.2. Digital image correlation (2D-DIC) measurements

The post-processing procedures of the images were based on the "finite element" digital image correlation procedure proposed by Besnard et al. (2006), where the displacement fields are calculated by carrying out a global optimization of the nodal displacements in a mesh of Q4 elements. The DIC algorithm is essentially based on the conservation of optical flow, which limits the algorithm to continuous displacement fields. Discontinuities in the displacement field, such as cracks propagating through the specimen, may cause the solution to diverge and give erroneous results. To overcome the problem of propagating cracks, modifications to the DIC algorithm are implemented. These modifications consist of automatic detection and handling of crack propagation. The details of this technique have been presented in Fagerholt et al. (in preparation).

The automatic detection of cracks is based on statistical evaluation of grey-scale correlation residuals with a set of predefined levels. Based on this evaluation a weight map is generated, giving each pixel inside the correlation region a weight factor between 0 and 1. The weight factor indicates the quality of the correlation in the corresponding pixel. A pixel with weight factor 0 is totally disregarded in the DIC optimization procedure, while a pixel with weight factor 1 is fully contributing to the correlation. Typically a pixel located in an area where a crack is present, should not be part of the correlation and is given a weight factor 0. The introduction of this weight factor map helps the DIC optimization algorithm to converge to the correct solution of the displacement field, even for large propagating cracks, because the pixels located in a cracked region are "weighted out" of the solution.

The final step of handling crack propagating in the DIC algorithm is to carry out modifications to the mesh so that the elements (and the displacement field) are not defined in the cracked region. In this study, this is carried out by mesh adaptivity, motivated by the techniques developed for the finite element method. Based on predefined levels, elements which contain a high degree of low-weighted pixels are refined (split in four new smaller elements) or eroded (completely removed from the solution).

The crack handling procedure described above, with properly adjusted predefined levels for weight factor map generation and mesh adaptivity, helps the DIC optimization algorithm to calculate the continuous displacement field in the parts of the specimen not affected by the crack. In Section 4, example images from tests with the calculated strain fields plotted on top of the image will be given. It can then be seen that the strain field is not defined in the cracked area, due to the erosion of elements in this region. The reader is again referred to Fagerholt et al. (in preparation) for further details on the DIC procedures used in these experiments.

4. Experimental results

A total of 14 successful notched butterfly tests were carried out varying the loading angle β between 0°, 45° and 90°. Displacement, force and digital images were recorded for all tests. The images were post-processed using the previously described DIC algorithm to obtain the two-dimensional displacement and strain fields of the specimen surface.

Fig. 6 illustrates the force–displacements curves for these 14 tests. The figure shows that significant scatter between replicate tests appears, which is consistent with the scatter found in the tensile tests presented in Dørum et al. (2009). Note that the displacement and force measurements in the plots of Fig. 6 were taken directly from the linear transducer and the load cell of the testing machine. In contrast, later plots will use displacement measurements from the DIC analysis. Fig. 7 shows the reference points on the specimen used in the DIC analysis to obtain an overall measure of the specimen's deformation. Let w_x and w_y denote the x- and y-components of the relative displacement between points 1 and 2. For $\beta = 0^\circ$, w_x is taken as a measure of overall deformation, while for $\beta = 45^\circ$ and $\beta = 90^\circ$ the overall deformation is defined by $w = \sqrt{w_x^2 + w_y^2}$. The same procedure is used to extract the overall deformation in the finite element analysis presented in Section 5.

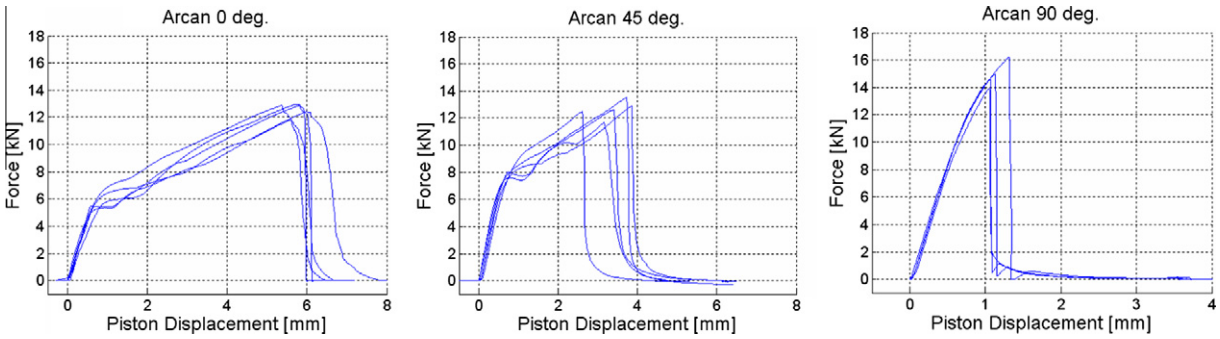

Fig. 6. Force–displacement curves for the 14 experiments for (from left to right) $\beta = 0°$, 45° and 90°.

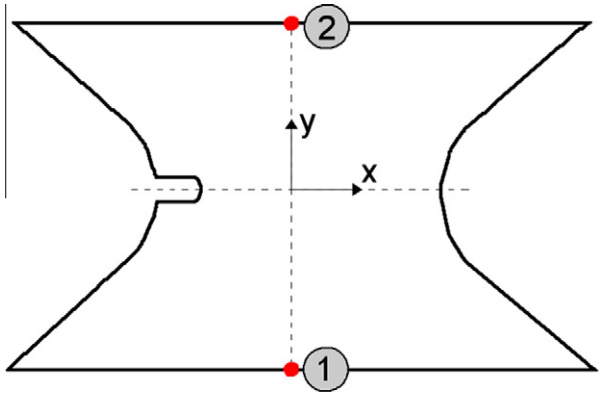

Fig. 7. Definition of measured relative displacements from the DIC analysis.

Fig. 8 shows a set of selected images from a test with $\beta = 45°$. The propagating crack can clearly be seen in the images. Typical examples of crack paths from replicate tests with β equal to 0°, 45° and 90° are shown in Fig. 9. Except maybe for $\beta = 90°$ (i.e. mode I fracture), there are apparent differences in the crack path between the replicates. It can also be seen that slant fracture occurs through the thickness in all tests. It is noted that two of the specimens loaded in mode II exhibits a kinked crack. The reason for this may be the small rotations of the fixtures during displacement, as discussed in Section 3.1, which implies that the configuration is not exactly mode II.

Based on the two-dimensional displacement field $\mathbf{u} = \mathbf{u}(\mathbf{X}, t)$ generated by the DIC analysis, where $\mathbf{X}$ are the material coordinates and t is time, the deformation gradient $\mathbf{F} = \mathbf{F}(\mathbf{X}, t)$ is calculated as

$$\mathbf{F} = \frac{\partial \mathbf{x}}{\partial \mathbf{X}} = \mathbf{1} + \frac{\partial \mathbf{u}}{\partial \mathbf{X}}, \tag{2}$$

where $\mathbf{x}(\mathbf{X}, t) = \mathbf{X} + \mathbf{u}(\mathbf{X}, t)$ are the spatial coordinates of the material point $\mathbf{X}$ and $\mathbf{1}$ is the second-order identity tensor. The Green deformation tensor $\mathbf{C} = \mathbf{C}(\mathbf{X}, t)$ is then calculated as

$$\mathbf{C} = \mathbf{F}^T\mathbf{F}. \tag{3}$$

The in-plane principal stretches $\mu_i = \mu_i(\mathbf{X}, t)$, $i = 1, 2$, are found by solving the eigenvalue problem for the Green deformation tensor

$$(\mu_i^2\mathbf{1} - \mathbf{C}) \cdot \mathbf{n}_i = \mathbf{0}, \tag{4}$$

where $\mathbf{n}_i$ are the principal directions of $\mathbf{C}$. The logarithmic principal strains $\varepsilon_i = \varepsilon_i(\mathbf{X}, t)$, $i = 1, 2$, are then calculated as

$$\varepsilon_i = \ln(\mu_i). \tag{5}$$

Assuming negligible elastic strains and plastic incompressibility, the logarithmic principal strain in the thickness (out-of-plane) direction is estimated as

$$\varepsilon_3 = -(\varepsilon_1 + \varepsilon_2). \tag{6}$$

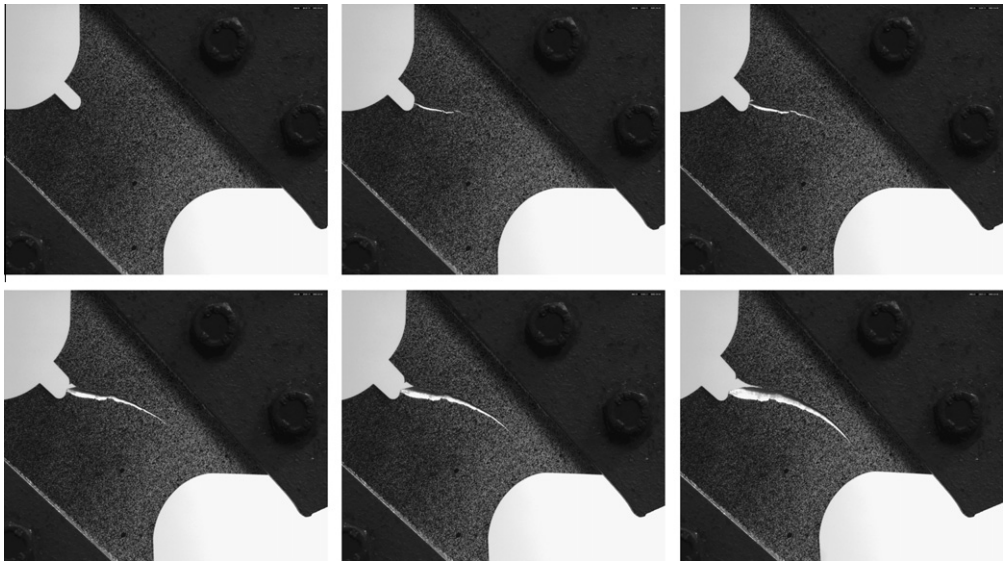

Fig. 8. Recorded images from a modified Arcan test for $\beta = 45°$, showing the development of the crack path during the test.

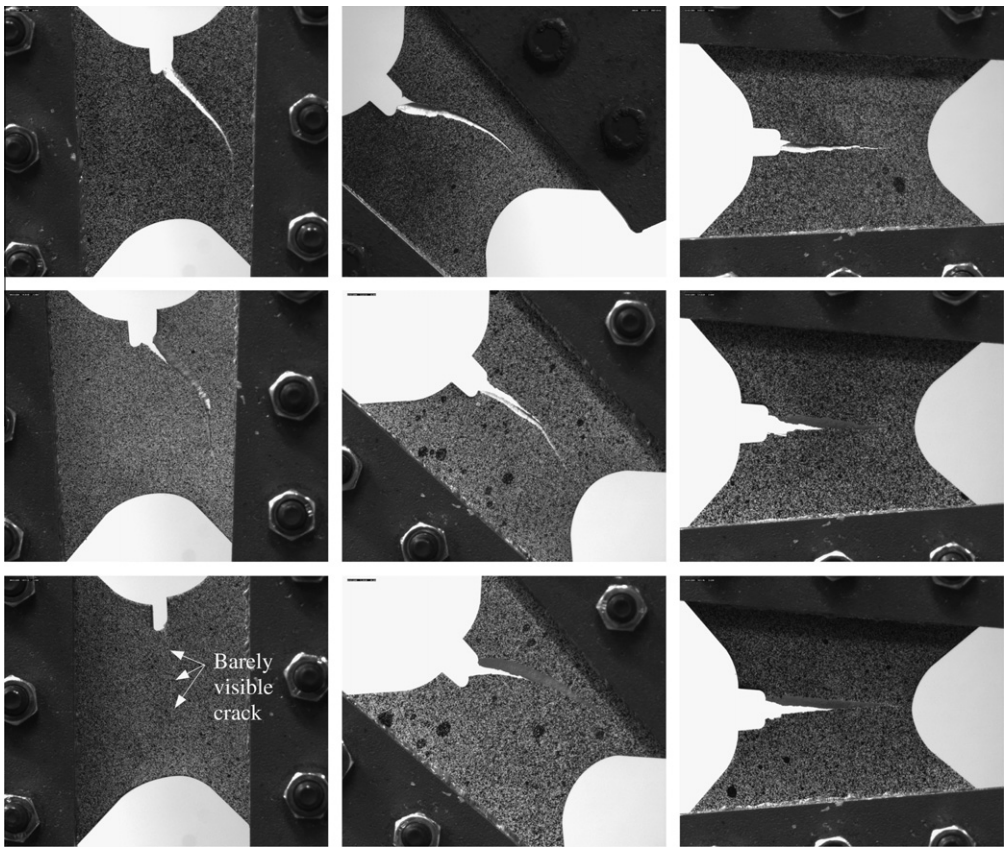

Fig. 9. Crack paths from three replicate tests (top–down). From left to right $\beta = 0°$, $45°$ and $90°$.

An effective strain measure $\varepsilon_{eff} = \varepsilon_{eff}(\mathbf{X}, t)$ is defined according to

$$\varepsilon_{eff} = \sqrt{\frac{2}{3}\left(\varepsilon_1^2 + \varepsilon_2^2 + \varepsilon_3^2\right)} = \sqrt{\frac{4}{3}\left(\varepsilon_1^2 + \varepsilon_1\varepsilon_2 + \varepsilon_2^2\right)}, \tag{7}$$

where Eq. (6) was used to obtain the latter equality. It is noted that ε_{eff} represents the norm of the total strain tensor, and should not be confused with the equivalent plastic strain (here denoted ε_{eq}) used to describe work-hardening in the constitutive model in Section 5.

Figs. 10–12 show the evolution of the calculated effective strain field $\varepsilon_{eff} = \varepsilon_{eff}(\mathbf{X}, t)$ in three of the performed tests plotted on top of the corresponding images for $\beta = 0°$, $45°$ and $90°$. Note that the colour scaling in these figures is logarithmic due to the exponential spatial variation of the effective strain in the specimens. It should also be noted that the strain calculations are based on the DIC "finite element" size of 32 pixels (0.96 mm) which sets limitations to the strain calculations, especially around the notch where high strain gradients are present. Fig. 13 gives the corresponding force–displacement curves for the experiments shown with effective strain maps in Figs. 10–12. The instants of the strain maps in Figs. 10–12 have been noted with a numbers 1–6 in the force–displacement curves in Fig. 13. The results show that different force–displacement response and fracture mode are obtained by varying the loading angle. It is particularly noted that the fracture is much more abrupt for $\beta = 90°$ (mode I) than for the other load cases. This is evident in Fig. 13 for $\beta = 90°$ where the time interval between points 4 and 5 equals the frame rate of 10 Hz. Fig. 14 illustrates the correlation grey-scale residual maps at a late stage in tests with β equal to $0°$, $45°$ and $90°$, respectively. Due to the poor correlation in the crack region, the residuals become high and the residual map can be used to view the crack path in material coordinates.

5. Finite-element models

The numerical simulations of the modified Arcan tests were carried out with an user-defined material model implemented in the commercial explicit FE-code LS-DYNA. The load is applied to the test specimen as a prescribed rigid body motion in the loading direction of the steel plate support. The rigid steel plate supports can rotate in-plane around the pinned connections, allowing for lateral displacements. In the model, the material behaviour is described by the classical J_2 flow theory, i.e. an elastic–plastic constitutive model including the von Mises yield criterion, the associated flow rule and isotropic hardening. Fracture is modelled by the Cockcroft–Latham criterion (Cockcroft and Latham, 1968), assuming the fracture parameter to follow a modified weakest-link Weibull distribution (Dørum et al., 2009; Dørum et al., 2009; Weibull, 1951). With the present probabilistic fracture modelling approach, the fracture parameter can be introduced as a random variable in the finite element simulations. More details about the implemented user-defined material model are given by Dørum et al. (2009).

The yield function is defined by

$$f(\boldsymbol{\sigma}, \varepsilon_{eq}) = \sigma_{eq}(\boldsymbol{\sigma}) - \sigma_Y(\varepsilon_{eq}) = 0, \tag{8}$$

where $\boldsymbol{\sigma}$ is the Cauchy stress tensor, σ_{eq} is the von Mises equivalent stress and ε_{eq} is the corresponding equivalent plastic strain. The flow stress σ_Y is defined by the isotropic hardening rule given by Eq. (1), and the corresponding work-hardening parameters provided in Table 1. This implies that any variation in flow stress with position in the casting was not accounted for in the simulations. The Cockcroft–Latham fracture criterion is adopted

$$W = \int_0^{\varepsilon_{eq}} \max(\sigma_1, 0) d\varepsilon_{eq} \leqslant W_c, \tag{9}$$

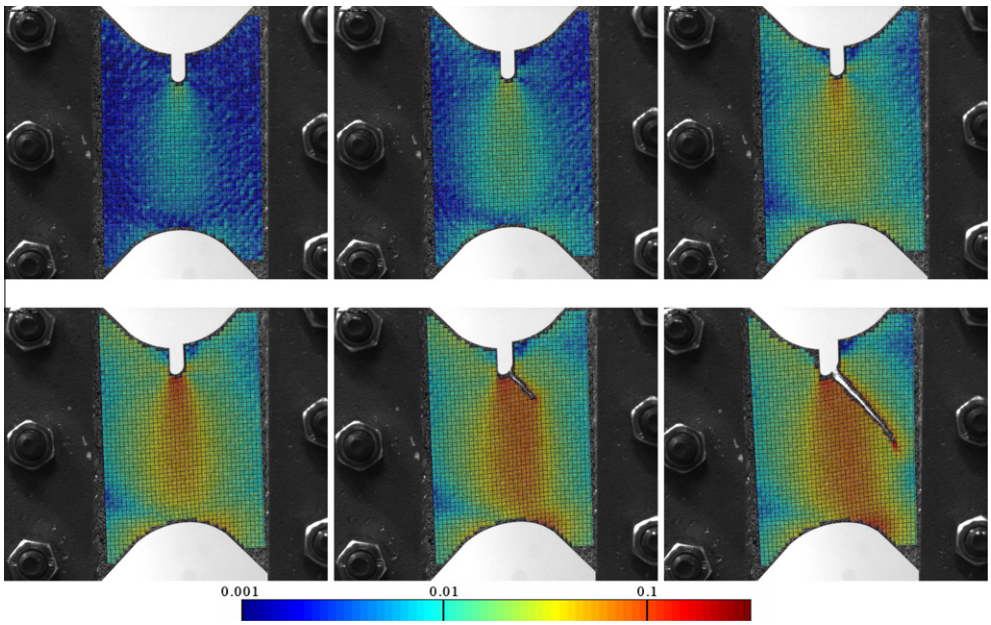

Fig. 10. Measured effective strain fields for a selection of images in a test for $\beta = 0°$ (mode II). The strain fields are plotted on top of the recorded images in current configuration as logarithmic scaled colour maps.

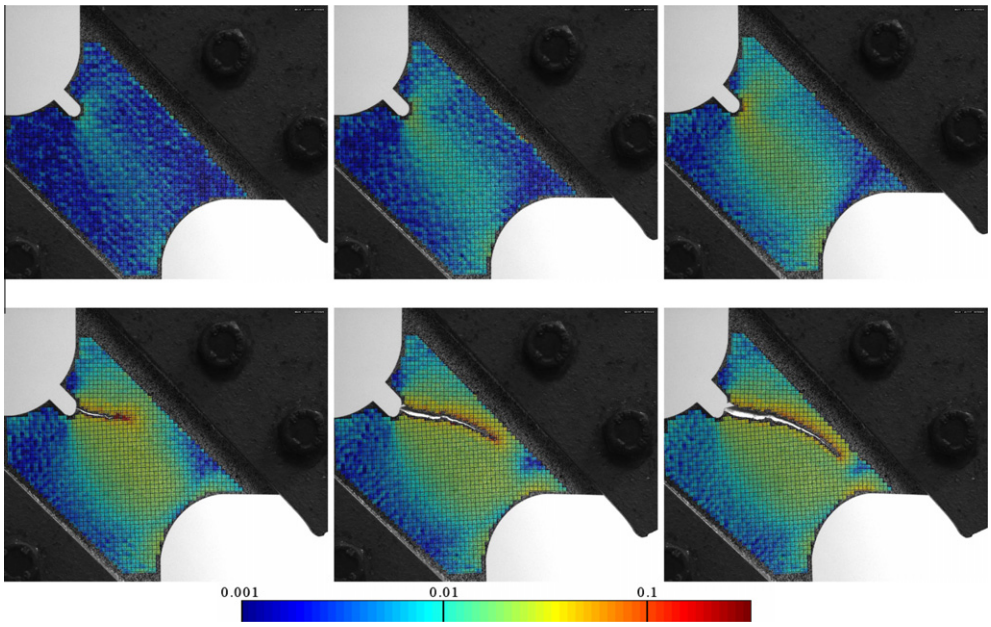

Fig. 11. Measured effective strain fields for a selection of images in a test for $\beta = 45°$ (mixed-mode). The strain fields are plotted on top of the recorded images in current configuration as logarithmic scaled colour maps.

where W is denoted the Cockcroft–Latham integral, σ_1 is the maximum principal stress, and W_c is the critical value of the integral W at which fracture occurs. It is convenient to re-write this fracture criterion as a damage evolution law in the form

$$\dot{D} = \begin{cases} \frac{\sigma_1}{W_c}\dot{\varepsilon}_{eq} & \text{for } \sigma_1 > 0, \\ 0 & \text{for } \sigma_1 \leqslant 0, \end{cases} \tag{10}$$

where D is the damage variable. Fracture occurs when D equals unity. As the Cockcroft–Latham fracture criterion is based upon only one parameter, a single material test is sufficient for the calibration. In the present study, the fracture parameter was identified from uniaxial tension tests ($\sigma_1 > 0$) as

$$W_c = \int_0^{\varepsilon_f} \sigma_1 d\varepsilon_{eq}, \tag{11}$$

where ε_f is the fracture strain. Note that fracture occurs without any sign of necking for the actual material, thus facilitating the determination of W_c. It should be noted that the Cockcroft–Latham fracture criterion is but one of many fracture criteria applicable to the current problem, see e.g. Wierzbicki et al. (2005). The Cockcroft–Latham criterion was chosen here because of its simplicity with respect to both formulation and calibration procedures (Reyes et al., 2009). Furthermore, it has been successfully used in previous studies of cast materials (Dørum et al., 2009; Dørum et al., 2009; Dørum et al., 2009).

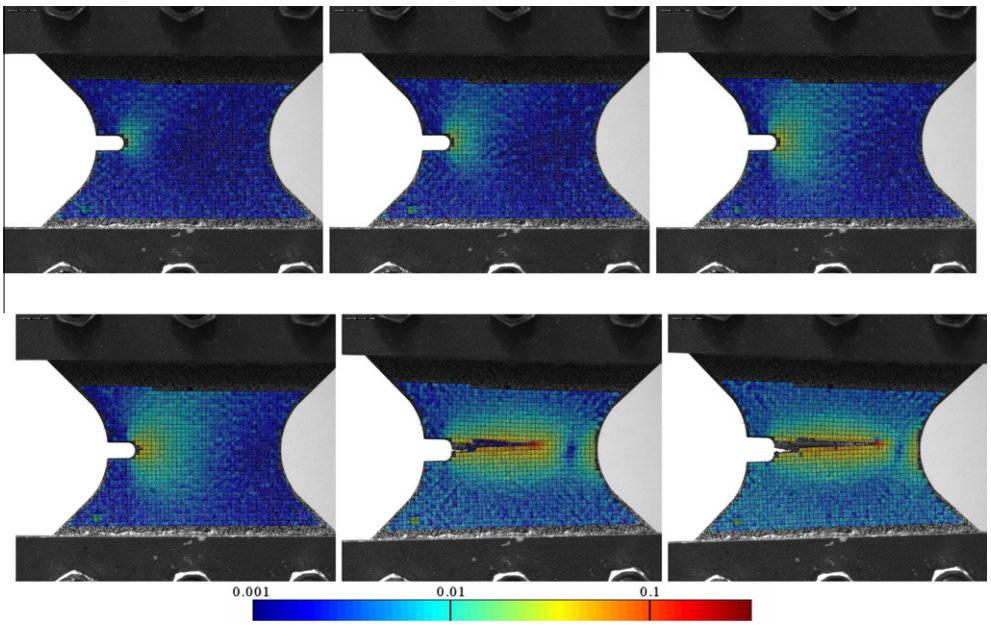

Fig. 12. Measured effective strain fields for a selection of images in a test for $\beta = 90°$ (mode I). The strain fields are plotted on top of the recorded images in current configuration as logarithmic scaled colour maps.

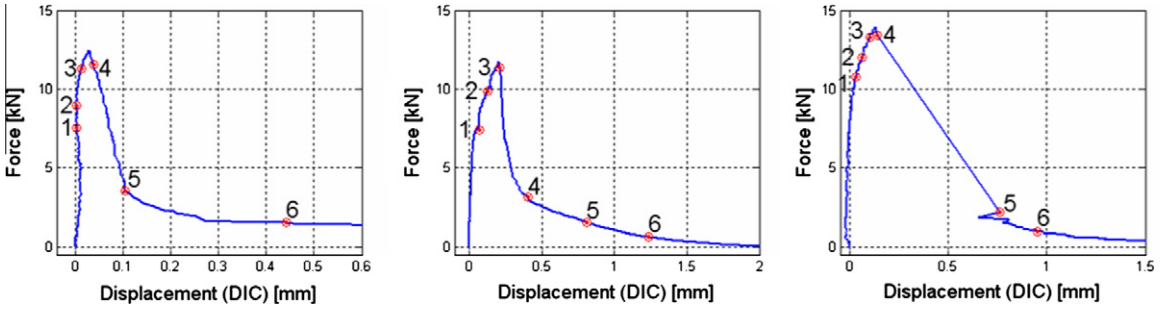

Fig. 13. Force–displacement curves from the experiments for (from left to right) $\beta = 0°$, 45° and 90°. The corresponding strain maps in Figs. 10–12 are indicated on the force displacement curves with numbers 1–6.

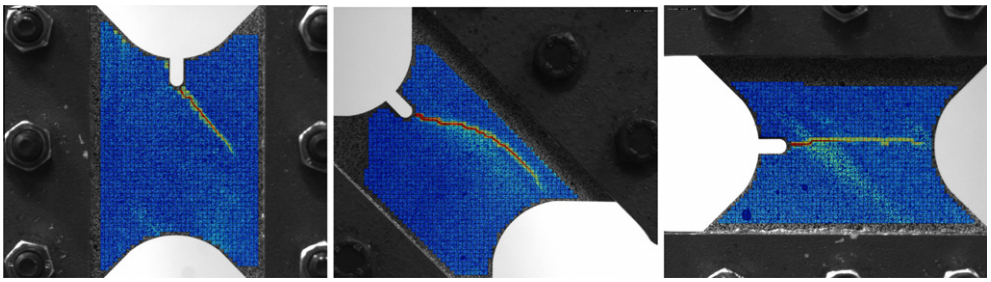

Fig. 14. Correlation residuals indicating crack paths in reference coordinates for (from left to right) $\beta = 0°$, 45° and 90°. The correlation residual fields are plotted on top of the reference image (or un-deformed state) as colour maps.

To reduce the mesh-size sensitivity of the simulations with fracture, the non-local regularization available in LSTC (2003) was used (see e.g. Pijaudier-Cabot and Bažant, 1987). To this end, the local values of the damage rate $\dot{D}$ and the plastic strain rate $\dot{\varepsilon}_z^p$ in the thickness direction of the profile were replaced by non-local values $\bar{\dot{D}}$ and $\bar{\dot{\varepsilon}}_z^p$ defined within the neighbourhood Ω_r, i.e.:

$$\bar{\dot{D}}(\mathbf{x}_r) = \frac{1}{W_r}\int_{\Omega_r} w(\mathbf{x}_r - \mathbf{y})\dot{D}(\mathbf{y})d\Omega, \tag{12}$$

$$\bar{\dot{\varepsilon}}_z^p(\mathbf{x}_r) = \frac{1}{W_r}\int_{\Omega_r} w(\mathbf{x}_r - \mathbf{y})\dot{\varepsilon}_z^p(\mathbf{y})d\Omega, \tag{13}$$

where

$$W_r = \int_{\Omega_r} w(\mathbf{x}_r - \mathbf{y})d\Omega, \tag{14}$$

$$w(\mathbf{x}_r - \mathbf{y}) = \frac{1}{\left[1 + \left(\frac{\|\mathbf{x}_r - \mathbf{y}\|}{L}\right)^p\right]^q}. \tag{15}$$

Here, w is the non-local weight function, $\mathbf{x}_r$ and $\mathbf{y}$ are position vectors and the parameters L, p and q determine the shape of the weight function. The radius of the non-local domain Ω_r is taken as $L_{\max} = 1.5L$.

The reason for taking both damage D and through-thickness plastic strain ε_z^p as non-local variables is as follows. For thin-walled components under tension loading there are generally two different failure modes, namely local necking and fracture. When modelling such components with shell elements, local necking becomes, in addition to damage, severely mesh dependent because the shell elements fail to account for the stabilizing effect of stress triaxiality. It is therefore necessary to regularize both these variables to improve mesh convergence.

The fracture parameter W_c of an element is assumed to follow a modified weakest-link Weibull distribution in this study. The fracture probability of a material volume is given as

$$P(W) = 1 - \exp\left[-\left(\frac{V}{V_0}\right)\left(\frac{W}{W_{c0}}\right)^m\right], \tag{16}$$

where V is the volume of the element, V_0 is the scaling volume, W_{c0} is the scaling fracture parameter and m is the Weibull modulus. Consequently, the corresponding probability density function for the local material ductility reads

$$f(W_c) = \left.\frac{dP}{dW}\right|_{W=W_c} = \frac{m}{W_{c0}}\left(\frac{V}{V_0}\right)\left(\frac{W_c}{W_{c0}}\right)^{m-1}\exp\left[-\left(\frac{V}{V_0}\right)\left(\frac{W_c}{W_{c0}}\right)^m\right]. \tag{17}$$

To limit the local ductility of the material, an upper limit $W_c^{\max}$ was introduced as an additional parameter (Dørum et al., 2009).

It is seen that the probability of fracture increases with increasing volume V, and in this sense the adopted fracture criterion accounts for size effects. It should be noted that size effects are important with respect to identification of fracture parameters for aluminium die-castings as demonstrated by Dørum et al. (2009), since the probability of testing a part of the material having a defect that initiates fracture increases with increasing volume. However, Dørum et al. (2009) show that the fracture modelling approach combining the Cockcroft–Latham fracture criterion with Weibull theory effectively handles size effects.

In the user-defined material model implemented in LS-DYNA, the scaling volume V_0 was taken as the volume of the gauge area of the tensile specimen, while V is the volume of the actual element. As the calibrated Weibull parameters rely on observed macroscopic failure, a minimum length scale is introduced to avoid simulating microcracks when the element lengths in the finite element models are very small. This is done by defining a non-local fracture parameter $\bar{W}_c$ for each integration point in the finite element model as the minimum value of W_c within the neighbourhood Ω_r of radius $L_{\max}$, viz

$$\bar{W}_c(\mathbf{x}_r) = \min_{\|\mathbf{x}_r - \mathbf{y}\| \leqslant L_{\max}} W_c(\mathbf{y}). \tag{18}$$

Table 2 shows the Weibull parameters that were calibrated for Al-Si9MgMn-T1 in a previous work (Dørum et al., 2009). With respect to the non-local regularization, L was set equal to 2 mm with $p = 4$ and $q = 20$. Fig. 15 shows the bell shape of the weight function obtained using these parameter values. It is seen that the effective part of the non-local neighbourhood has a diameter similar to the thickness of the component. This is reasonable because local necking occurs at a length scale of the same order as the thickness.

In a previous work (Dørum et al., 2009) numerical simulations of the uniaxial tensile tests were carried out. It was found that the predicted engineering stress–strain curves from simulations

Table 2
Weibull parameters.

V_0 (mm^2)	m	W_{c0} (MPa)	$W_c^{\max}$ (MPa)
320	3.06	16.0	58

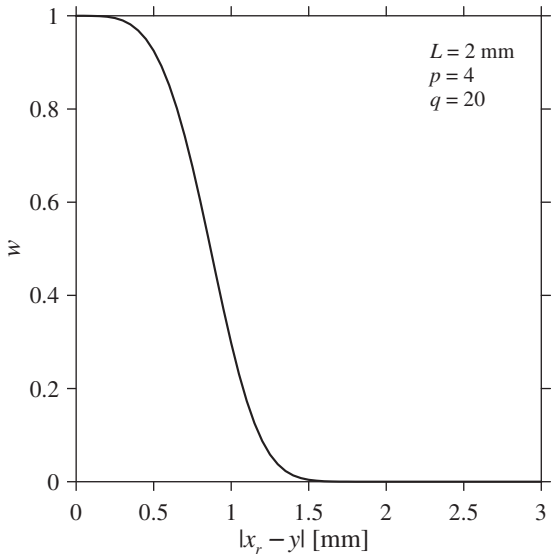

Fig. 15. Bell function used for non-local regularization with $L = 2$ mm, $p = 4$ and $q = 20$.

are very similar to the experimental curves. Numerical simulation of the uniaxial tensile test assuming homogeneous material properties and the ductility of the cast aluminium plates defined by the upper limit $W_c^{\max}$ will overestimate the ductility in the uniaxial tensile test. Experimentally, the probability of reaching $W_c^{\max}$ increases as the material volume decreases.

6. Numerical results

The modified Arcan tests were simulated in LS-DYNA using shell elements. First, a structured mesh with characteristic element lengths of 1.0 mm was created. This gave 1214 quadrilateral elements for the cast aluminium specimen. To examine the mesh-size sensitivity of the simulations, two refined meshes were made with element lengths equal to 0.5 and 0.25 mm, giving 5704 and 22,816 elements for the cast aluminium specimen, respectively. Second, meshes with the same characteristic lengths where generated using free quadrilateral meshing in LS-PREPOST 3.0. The corresponding number of elements for these arbitrary meshes are 1644, 6930 and 27559. In the following, the structured meshes are called M1–M3, while the arbitrary meshes are called A1–A3. Fig. 16 shows close-ups at the notch of the different meshes used in the simulations. Thus, the tests could now be simulated to evaluate the sensitivity of the predictions of fracture and crack propagation with respect to both mesh orientation and mesh density. An overview of the meshes used in the present work is provided in Table 3. It should be noted that shell elements cannot describe the slanted fracture seen in the experiments, cf. Fig. 9. However, we adopted shell elements here because we wanted to establish methods applicable for large-scale industrial applications and to evaluate the accuracy and robustness of this approach.

Fig. 17 shows predicted force–displacement curves obtained using meshes M1–M3 and A1–A3 when homogeneous material properties are assumed. From the Weibull distribution of fracture parameters, an average value of W_c can be calculated as a function of the volume of the material. As the stress and strain gradients are relatively steep in the cases studied here, the volume of the material where fracture is likely to initiate will be much smaller than the volume of the specimen gauge section used in calibration, but different for each load case. Further, as it is not straight-forward to establish the size of the fracture-relevant volume, it has

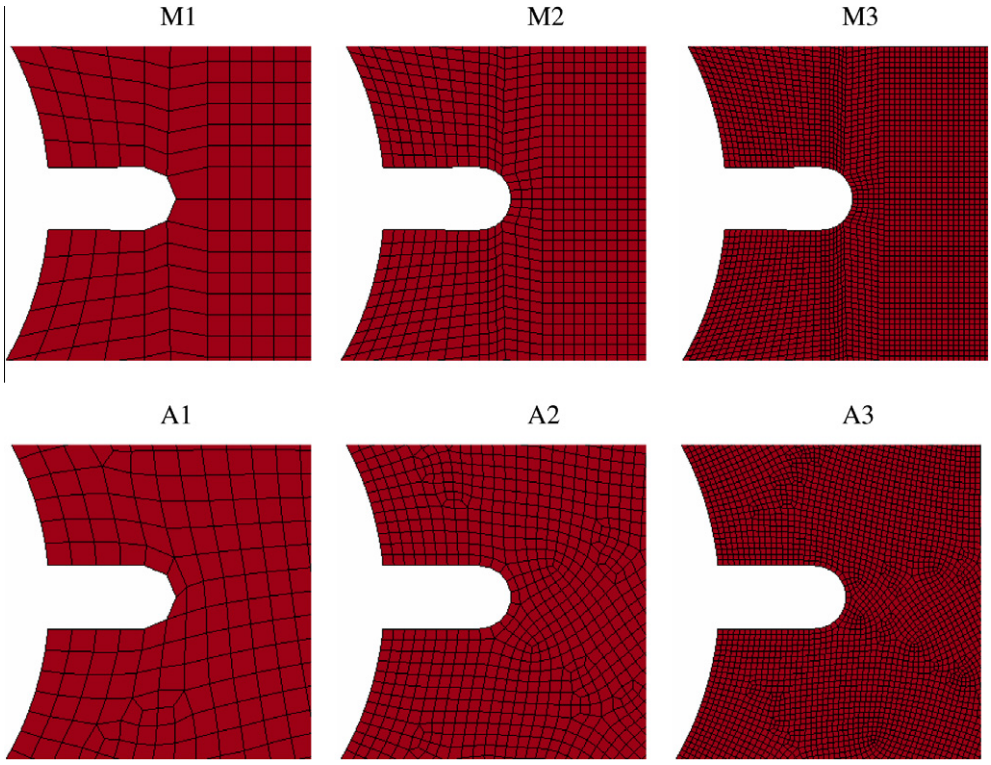

Fig. 16. The different meshes used to examine mesh-size sensitivity. Above, the structured meshing (M1–M3) and below, the automatic meshing (A1–A3).

Table 3
Finite-element meshes.

Meshing technique	Mesh identification	Number of elements	Characteristic element length (mm)
Structured meshing	M1	1214	1.0
	M2	5704	0.5
	M3	22,816	0.25
Automatic meshing	A1	1644	1.0
	A2	6930	0.5
	A3	27,559	0.25

been chosen to define the ductility of the cast aluminium plates by the upper limit $W_c = W_c^{\max} = 58$ MPa. This should lead to non-conservative estimates. The figure shows that with the adopted non-local regularization scheme, there is generally limited effect of mesh-size and mesh orientation on the predicted force–deformation curves. In the present study, local necking is of minor importance while the in-plane stress and strain gradients are steep. Therefore, mesh convergence mainly depends on the introduction of damage as a non-local variable. Simulations were also conducted without non-local regularization and then strong mesh sensitivity was observed. These results are not shown in the present study. The predicted force–deformation curves are in reasonable agreements with the experimental data until fracture occurs in the test, but with homogeneous material properties and the chosen value of W_c the ductility is over-predicted for all loading angles. The corresponding crack propagation paths for the two finest meshes A3 and M3 are given in reference configuration in Fig. 18. Some deviation between predicted and experimental crack paths is evident by comparing these plots to e.g. Fig. 9, but the overall agreement is reasonable. It is further noted that the crack width depends on the mesh-size in these simulations, since element erosion was adopted to propagate the crack.

To investigate the influence of using a probability distribution for fracture parameter, the three load cases were simulated with the arbitrary mesh A3. The resulting force–deformation curves from three parallel simulations are plotted in Fig. 19 together with the representative experimental data. Significantly better estimates of the ductility are now obtained. We also get similar scatter in the simulated and experimental results. The significant drop in force level observed in one of the simulations for $\beta = 0^\circ$ is due to a considerable change in crack direction during fracture. Variations in crack paths also occur between parallel simulations in a similar way as seen experimentally. Note that the regularization leads to some areas where the crack width exceeds the characteristic element size due to the non-local averaging procedure.

Finally, Figs. 20–22 show the effective strain field $\varepsilon_{eff} = \varepsilon_{eff}(\mathbf{X}, t)$ from simulations for the three loading angles, adopting the fracture parameter as a random variable. It should be emphasized that the effective strain fields were obtained in exactly the same manner as in the experiments. This was done by importing nodal data from LS-DYNA into the in-house DIC software and using the formulas presented in Section 4. If compared to those obtained from the DIC measurements (Figs. 10–12), close correlation between the strain fields are seen even though some differences exist in the crack patterns and crack extension at similar force levels. It should, however, be kept in mind that these plots represent only one realization of the stochastic response for each loading case, and significant scatter has been shown to occur between replicate tests both experimentally and numerically. These plots show that both the displacement and strain fields in the modified Arcan tests can be accurately predicted using the described numerical approach.

7. Concluding remarks

In this paper, the quasi-static fracture behaviour of thin-walled cast aluminium components has been studied both experimentally and numerically.

Experimental tests were carried out using a modified Arcan set-up, making it possible to study fracture in modes I, II and

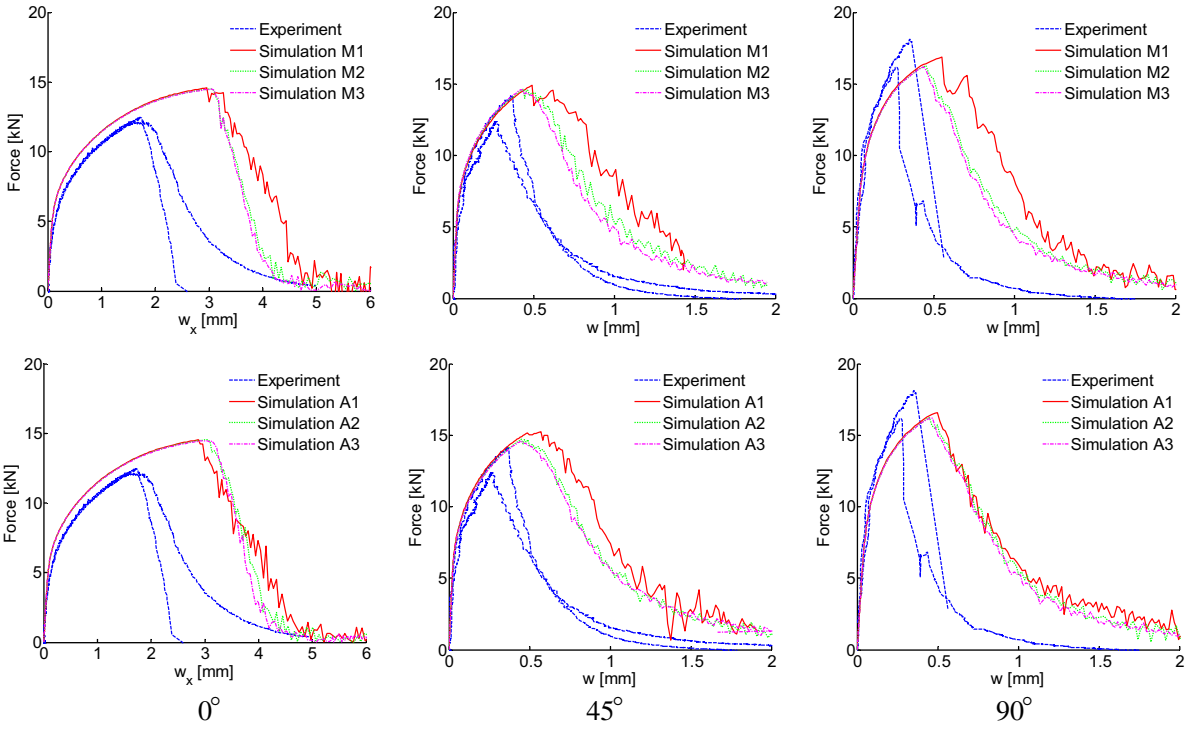

Fig. 17. Comparison of experimental and predicted force–deformation curves assuming homogeneous material properties. From left to right, $\beta = 0°$, 45° and 90°.

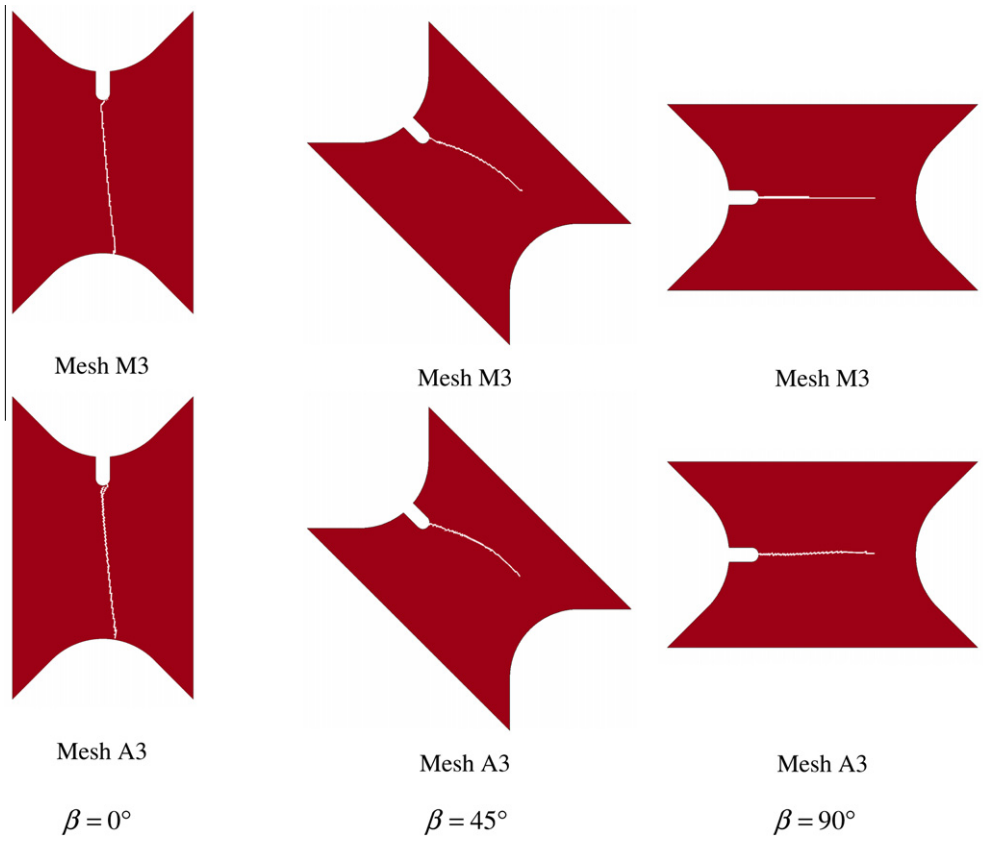

Fig. 18. Predicted crack propagation paths for the finest meshes M3 and A3. From left to right, $\beta = 0°$, 45° and 90°. Homogeneous material properties are assumed.

mixed-modes. During testing, a digital camera was used to record a speckle-pattern on the surface of the sample. The recorded images were post-processed using an in-house DIC software to obtain the displacement and strain fields in the sample. This software allows

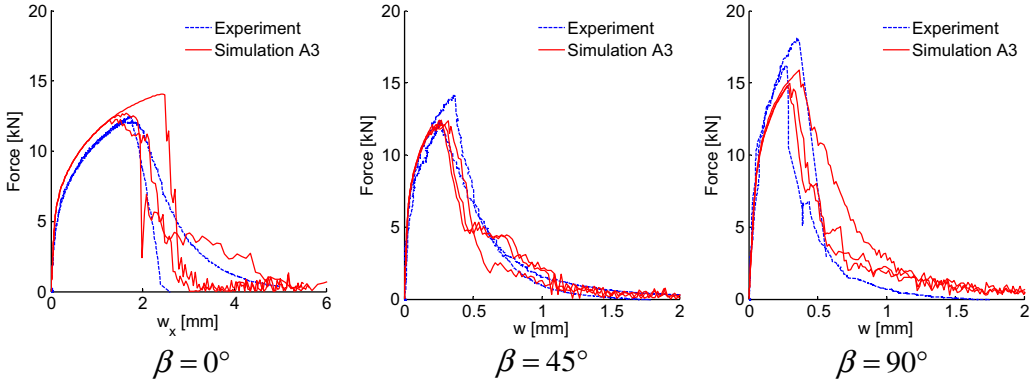

Fig. 19. Comparison of experimental and predicted force–deformation curves, adopting the fracture parameter as a random variable. From left to right, $\beta = 0°$, 45° and 90°.

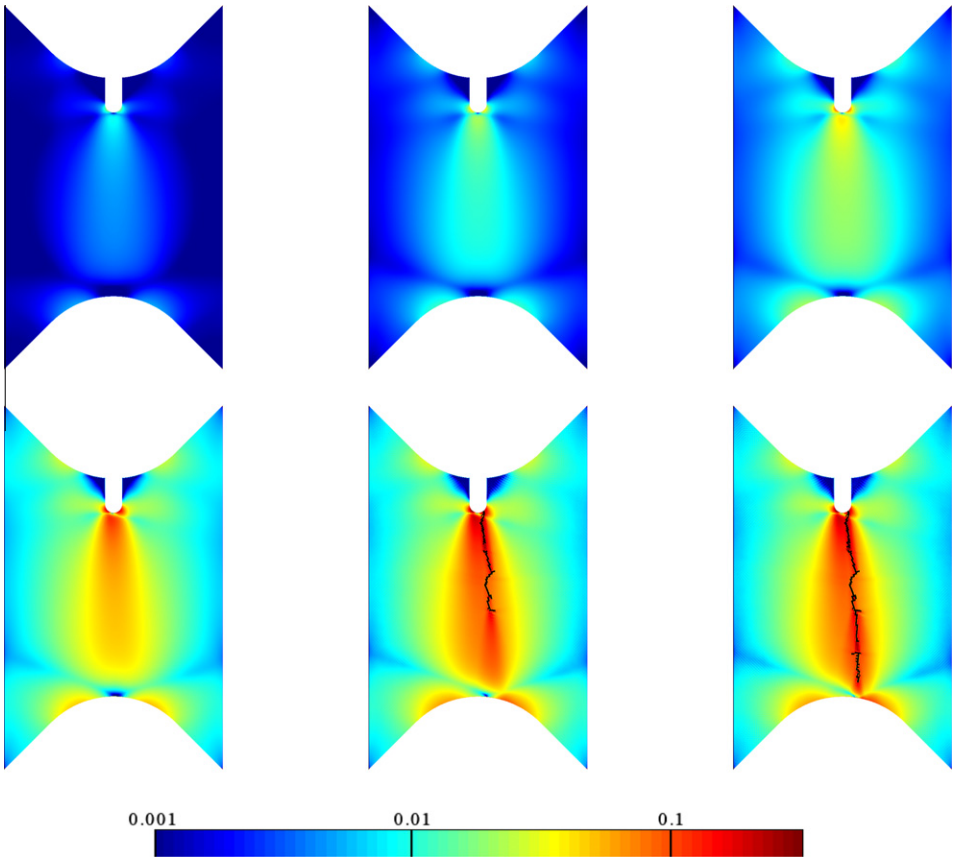

Fig. 20. Effective strain fields for $\beta = 0°$ (mode II) from finite element analysis with the fracture parameter introduced as a random variable, plotted as logarithmic scaled colour maps. The model is plotted in the reference (or un-deformed) configuration.

for discontinuous displacement fields and thus makes it possible to establish the strain fields in the neighbourhood of a propagating crack.

Nonlinear finite element simulations were carried out using shell elements and an uncoupled continuous–discontinuous approach to describe damage, fracture and crack propagation. The classical J_2 flow theory was adopted to describe the material behaviour, while the damage evolution in the fracture process zone was computed according to the Cockcroft–Latham criterion. Element erosion was used to model crack propagation in the specimen. Since large variations in tensile ductility between parallel tests were found in a previous study, the fracture parameter was introduced as a random variable in the finite element simulations, adopting a modified weakest-link Weibull distribution. Non-local regularization was adopted to reduce mesh-size sensitivity. To reveal the effect of mesh density and meshing technique on the force–displacement curves and crack propagation, several different meshes were used in the simulations. The numerical results were finally compared to the measured data.

It was found that the force–deformation curves, the fracture modes and the effective strain fields of the modified Arcan tests were predicted with reasonable accuracy using the described numerical approach. Without non-local regularization strong mesh sensitivity was found, while failing to account for the probability distribution of the fracture parameter led to non-conservative estimates on the ductility of the notched butterfly test specimen with

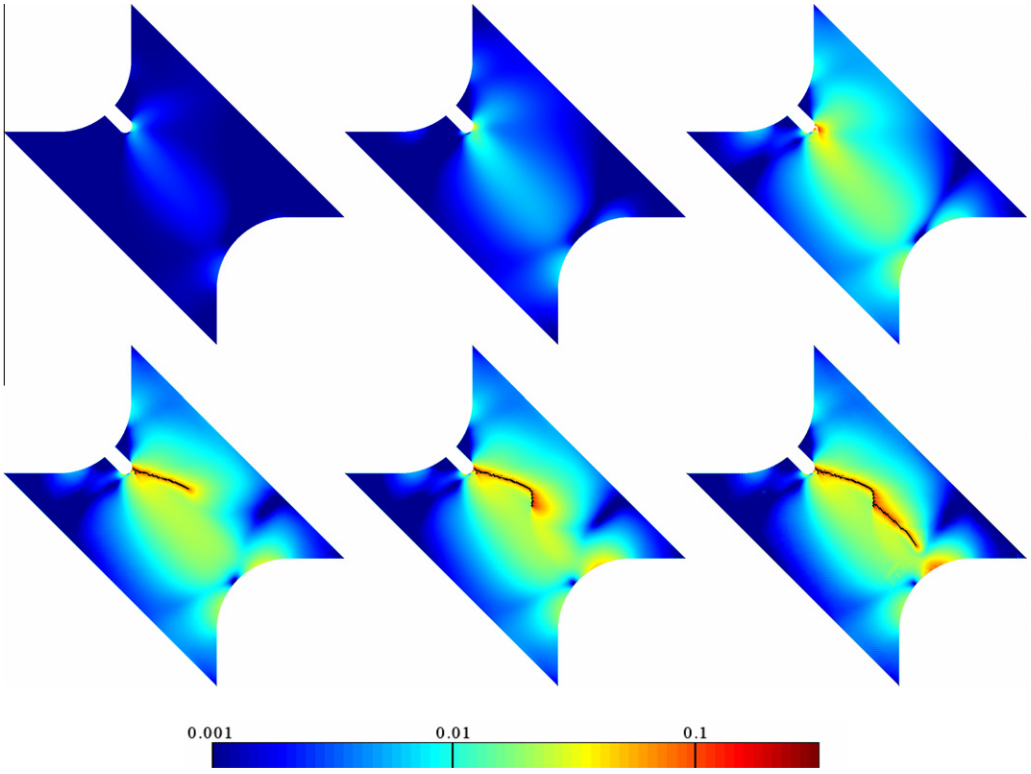

Fig. 21. Effective strain fields for $\beta = 45^\circ$ (mixed-mode) from finite element analysis with the fracture parameter introduced as a random variable, plotted as logarithmic scaled colour maps. The model is plotted in reference (or un-deformed) configuration.

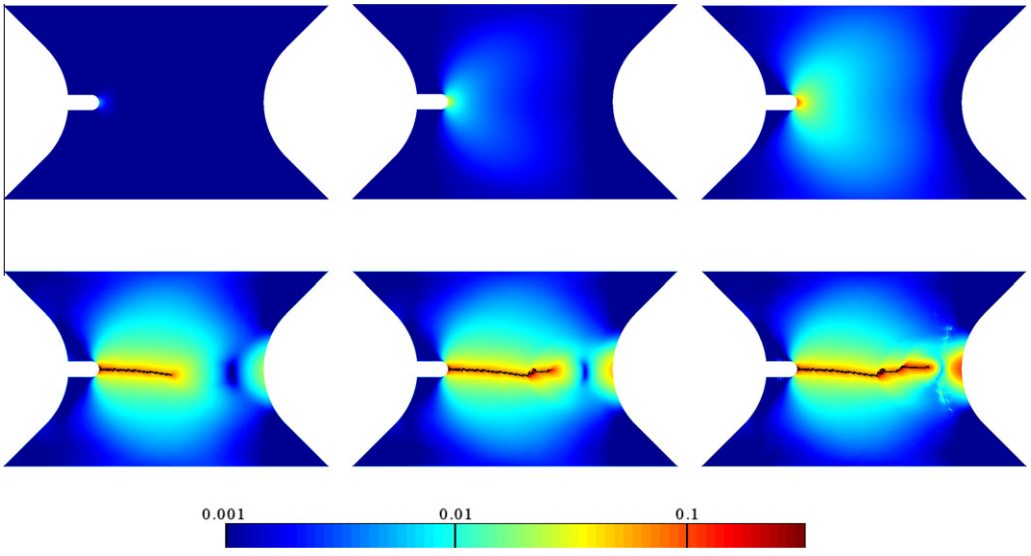

Fig. 22. Effective strain fields for $\beta = 90^\circ$ (mode I) from finite element analysis with the fracture parameter introduced as a random variable, plotted as logarithmic scaled colour maps. The model is plotted in reference (or un-deformed) configuration.

the current choice of the homogeneous fracture parameter. Some differences were also seen between the experimental and predicted crack paths. The use of element erosion to propagate the crack forces it to follow the element mesh, and thus imposes a constraint on the solution. For this reason use of arbitrary meshing may provide improved results over structured meshing. However, there were also marked differences in the crack paths between replicate tests in both the experiments and the simulations. Even if there are limitations in the proposed modelling approach, the results are believed to be satisfactory for applications to large-scale simulations of industrially relevant problems.

Acknowledgement

The financial support of this work from the Structural Impact Laboratory (SIMLab), Centre for Research-based Innovation (CRI) at the Norwegian University of Science and Technology (NTNU), is gratefully acknowledged.

References

Amstutz, B.E., Sutton, M.A., Dawicke, D.S., Newman, J.C., 1996. An experimental study of CTOD for mode I/mode II stable crack growth in thin 2024-T3 aluminium specimens. Fract. Mech. ASTM 26, 256–271.

Amstutz, B.E., Sutton, M.A., Dawicke, D.S., Boone, M.L., 1997. Effects of mixed mode I/II loading and grain orientation on crack initiation and stable tearing in 2024-T3 aluminium. Fatigue Fract. 27, 217–224.

Arcan, M., Hashin, Z., Voloshin, A., 1978. Method to produce uniform plane stress states with applications to fibre-reinforced materials. Exp. Mech. 18, 141–146.

Besnard, G., Hild, F., Roux, S., 2006. Finite-element displacement fields analysis from digital images: application to Portevin-le Châtelier bands. Exp. Mech. 46, 789–803.

Campbell, J., 1988. Thin wall castings. Mater. Sci. Technol. 4, 194–204.

Campbell, J., 2005. Shape Casting – The John Campbell Symposium. In: TMS Conference, pp. 3–12.

Cockcroft, M.G., Latham, D.J., 1968. Ductility and workability of metals. J. Inst. Met. 96, 33–39.

Dørum, C., Hopperstad, O.S., Berstad, T., Dispinar, D., 2009. Numerical modelling of magnesium die-castings using stochastic fracture parameters. Eng. Fract. Mech. 76, 2232–2248.

Dørum, C., Laukli, H.I., Hopperstad, O.S., 2009. Through-process numerical simulations of the structural behaviour of Al–Si die-castings. Comput. Mater. Sci. 46, 100–111.

Dørum, C., Laukli, H.I., Hopperstad, O.S., Langseth, M., 2009. Structural behaviour of Al–Si die-castings: experiments and numerical simulations. Eur. J. Mech. A. Solids 28, 1–13.

Fagerholt, E., Børvik, T., Hopperstad, O.S., in preparation. Handling of crack propagation in specimens using two-dimensional digital image correlation (2D-DIC).

Gokhale, A.M., Patel, G.R., 2005. Analysis of variability in tensile ductility of a semi-solid metal cast A356 Al-alloy. Mater. Sci. Eng. A 392, 184–190.

Gokhale, A.M., Patel, G.R., 2005. Origins of variability in the fracture-related mechanical properties of a tilt-pour-permanent mould cast Al-alloy. Scr. Mater. 52, 237–241.

Gourlay, C.M., Laukli, H.I., Dahle, A.K., 2007. Defect band characteristics in Mg–Al and Al–Si high-pressure die castings. Metall. Mater. Trans. A 38A, 1833–1844.

Gurson, A.L., 1977. Continuum theory of ductile rupture by void nucleation and growth. Part I: Yield criteria and flow rule for porous ductile media. J. Eng. Mater. Technol. 99, 1–15.

Helm, J.D., 2008. Digital image correlation for specimens with multiple growing cracks. Exp. Mech. 48, 753–762.

Laukli, H.I., Gourlay, C.M., Dahle, A.K., 2005. Effects of Si content on defect band formation in hypoeutectic Al–Si die castings. Mater. Sci. Eng. A, 92–97.

Laukli, H.I., Gourlay, C.M., Dahle, A.K., 2005. Migration of crystals during the filling of semi-solid castings. Metall. Mater. Trans. A 36A, 805–818.

Lemaitre, J., 1992. A Course on Damage Mechanics. Springer-Verlag, Berlin.

LSTC, 2003. LS-DYNA Keyword User's Manual, Version 970. Livermore Software Technology Corporation.

LS-PREPOST 3.0. Available from: <http://www.lstc.com/lspp/> (accessed 07.01.10).

Mediavilla, J., Peerlings, R.H.J., Geers, M.D.G., 2006. A robust and consistent remeshing-transfer operator for ductile fracture simulations. Comput. Struct. 84, 604–623.

Moës, N., Dolbow, J., Belytschko, T., 1999. A finite element method for crack growth without remeshing. Int. J. Numer. Methods Eng. 46, 131–150.

Mohr, D., Henn, S., 2007. Calibration of stress-triaxiality dependent crack formation criteria: a new hybrid experimental method. Exp. Mech. 47, 805–820.

Needleman, A., 1990. An analysis of decohesion along an imperfect interface. Int. J. Fract. 42, 21–40.

Pijaudier-Cabot, G., Bǎzant, Z.P., 1987. Nonlocal damage theory. J. Eng. Mech. 113, 1512–1533.

Rastogi, P.K. (Ed.), 2000. Photomechanics. Springer, Berlin, Germany.

Rèthorè, J., Hild, F., Roux, S., 2007. Shear-band capturing using a multiscale extended digital image correlation technique. Comput. Methods Appl. Mech. Eng. 196, 5016–5030.

Reyes, A., Eriksson, M., Lademo, O.-G., Hopperstad, O.S., Langseth, M., 2009. Assessment of yield and fracture criteria using shear and bending tests. Mater. Des. 30 (3), 596–608.

Rousselier, G., 1987. Ductile fracture models and their potential in local approach of fracture. Nucl. Eng. Des. 105, 97–111.

Scheider, I., Brocks, W., 2006. Cohesive elements for thin-walled structures. Comput. Mater. Sci. 37, 101–109.

Song, J.-H., Wang, H., Belytschko, T., 2008. A comparative study on finite element methods for dynamic fracture. Comput. Mech. 42, 239–250.

Teng, X., Mae, H., Bai, T., Wierzbicki, T., 2008. Statistical analysis of ductile fracture properties of an aluminium casting. Eng. Fract. Mech. 75, 4610–4625.

Voloshin, A., Arcan, M., 1980. Failure of unidirectional fiber-reinforced materials – new methodology and results. Exp. Mech. 20 (8), 280–284.

Weibull, W., 1951. A statistical distribution function of wide applicability. J. Appl. Mech. 18, 293–297.

Wierzbicki, T., Bao, Y., Lee, Y.-W., Bai, Y., 2005. Calibration and evaluation of seven fracture models. Int. J. Mech. Sci. 47, 719–743.

Part III

E. Fagerholt, E. Østby, T. Børvik and O.S. Hopperstad.

Investigation of fracture in small-scale SENT tests of a welded X80 pipeline steel using Digital Image Correlation with node splitting

Submitted for possible journal publication.

Investigation of fracture in small-scale SENT tests of a welded X80 pipeline steel using Digital Image Correlation with node splitting

E. Fagerholt[a,*], E. Østby[b], T. Børvik[a,c] and O.S. Hopperstad[a]

[a] *Structural Impact Laboratory (SIMLab), Centre for Research-based Innovation (CRI) and Department of Structural Engineering, Norwegian University of Science and Technology, Rich. Birkelands vei 1A, NO-7491 Trondheim, Norway*

[b] *SINTEF Materials and Chemistry, Department of Applied Mechanics and Corrosion, NO-7465 Trondheim, Norway*

[c] *Norwegian Defence Estates Agency, Research & Development Department, PB 405, Sentrum, NO-0103 Oslo, Norway*

Abstract

Single Edge Notch Tension (SENT) tests have been carried out on a girth welded X80 pipeline steel using two different weld materials. The focus has been to obtain information on the effect of weld metal mismatch on fracture strength of the pipe. In addition to the traditional clip gauge CMOD/CTOD measurements, information has been obtained by applying Digital Image Correlation (DIC). The DIC mesh has been modified to allow for node splitting in order to capture the discontinuous displacement field of the propagating crack. Parameters such as crack path, crack length and crack opening have been successfully measured using this modification to the standard DIC analysis. The paper contains a description of the material and the experimental setup, as well as results from the experimental tests. Emphasis is laid on the DIC analysis and the additional information gained from this approach. Parallelization of the DIC algorithm and a discussion on the accuracies of 2D vs. 3D DIC analyses are also included in this paper.

Keywords: DIC; SENT specimens; fracture mechanics; ductile fracture; pipeline steel.

[*] Corresponding author. Tel.: + 47-73-59-46-93; fax: + 47-73-59-82-04

E-mail address: egil.fagerholt@ntnu.no (E. Fagerholt).

1. Introduction

Modern pipeline design faces several challenges as one move into new areas like deep waters and arctic regions. At the same time there is a drive to develop more cost effective installation procedures by e.g. reducing intervention work. To meet these requirements it becomes necessary to allow for pipeline designs with larger deformation, often well into the plastic range. This has lead to a strong interest in applying so-called strain-based approaches [1-3]. Ensuring the structural integrity of the pipeline is of vital importance. The use of SENT (Single Edge Notched Tension) specimens to obtain information of fracture toughness of pipeline steels and girth welds has received great interest in this respect [4][5]. This has been driven by the similar geometry constraint levels found in SENT specimens and real pipeline defects.

It is also recognized that applying weld metal filler materials with higher strength than the pipe material, often termed overmatch, results in shielding of the girth weld defects and lower the applied crack driving force as a function of the globally applied deformation. In some of the more challenging upcoming pipeline projects, accounting for this effect might be necessary to demonstrate sufficient deformation capacity. However, current standards for pipeline design usually do not allow taking advantage of this possible beneficial effect. Thus, there is a need to develop robust fracture assessment schemes directly incorporating quantitative use of weld metal overmatch. This does not only influence the crack driving force, but could also influence the crack growth direction, leading to crack growth deviation from the original crack plane [6]. This feature must also be accounted for in accurate pipeline fracture assessments.

While there have been some studies on the ductile crack growth deviation under non-symmetrical loading of defects [7][8], there is in general a lack of a solid framework to predict when this will occur and to determine the extent of crack growth deviation. SENT specimens are also candidates for small-scale experimental investigations of possible crack growth deviations in pipeline girth welds. However, there is a need to establish robust criteria to predict possible crack growth deviations. Experimental techniques that can provide quantitative information of parameters like local strain fields will provide very valuable input in the quest for such criteria and data for validation of models to simulate this feature.

The use of Digital Image Correlation (DIC) provides an interesting approach in this respect and is the main motivation for the work carried out in this paper. As DIC is able to

provide full-field displacement and strain fields covering the surface of the test specimen, additional information is provided compared to traditional measurement techniques such as extensometers and clip gauges. However, the discontinuous displacement fields of propagating cracks represent challenges that need special attention in DIC analyses. Besnard et al. [9] proposed a formulation of DIC where the image correlation was carried out on a mesh of elements, similar to the finite element method (FEM). Thus, analyzing specimens with discontinuous displacement fields puts demand on the mesh geometry and/or the element shape functions. Réthoré et al. [10] presented a procedure where enrichment of the nodal degrees of freedom and discontinuous shape functions (X-DIC) was applied to measure the displacement field of cracks.

The advantages of using the "finite element" DIC approach compared to the traditional subset-based DIC algorithm are among others that functionality developed for FEM, such as mesh techniques and element shape functions, can be directly applied in the DIC analysis. Also, using a global mesh of elements, the analysis can easily be adapted to complex geometries and discontinuous areas [11]. Further, Besnard et al. [9] reported an increase in spatial resolution and reduced uncertainty compared to traditional DIC algorithms. However, due to the global nature of the "finite element" based DIC, discontinuities which are not handled properly represent possible degradation of the resulting displacement field. This yields not only for elements in the discontinuous region, but for a larger part of the measured surface. This feature stands in contrast to the subset based DIC were subsets (elements) are optimized individually.

In this study, a novel "finite element" 2D-DIC approach with splitting of duplicate nodes is used to capture discontinuous displacement fields of specimens experiencing large plastic deformations and ductile fracture during mechanical testing. A parallelized DIC code has been implemented and run on a multiple-core CPU in order to reduce processing time. A series of SENT tests is carried out on a girth welded X80 pipe material. The weld materials are chosen to obtain one set of specimens with overmatch (OM) and one set of specimens with undermatch (UM). Two different specimen geometries are tested. The paper describes the materials as well as the experimental setup with a subsequent presentation of the experimental results. Then, a description of the node-splitting DIC analysis is given, before the results from the DIC analysis is presented. An assessment on measurement uncertainties due to out-of-plane deformations in 2D vs. 3D DIC are given at the end of the paper together with some concluding remarks.

2. Experimental study

The base material used in this study is from an X80 seamless offshore pipe with an outer diameter of 12” and a 13.5 mm wall thickness. The pipe was girth welded with two different filler materials, obtaining an OM and a UM case. The girth weld had a root opening of about 3 mm and a weld bevel angle of approximately 60˚. Stress-strain curves for the base material were obtained using standard smooth tensile specimens. Notched tensile specimens were used to obtain the weld metal stress-strain curves, based on a procedure presented in [13]. The resulting engineering stress-strain curves for base material, OM and UM are presented in **Figure 1**. Here, the upper and lower case from 8 material tests for each material are illustrated [6].

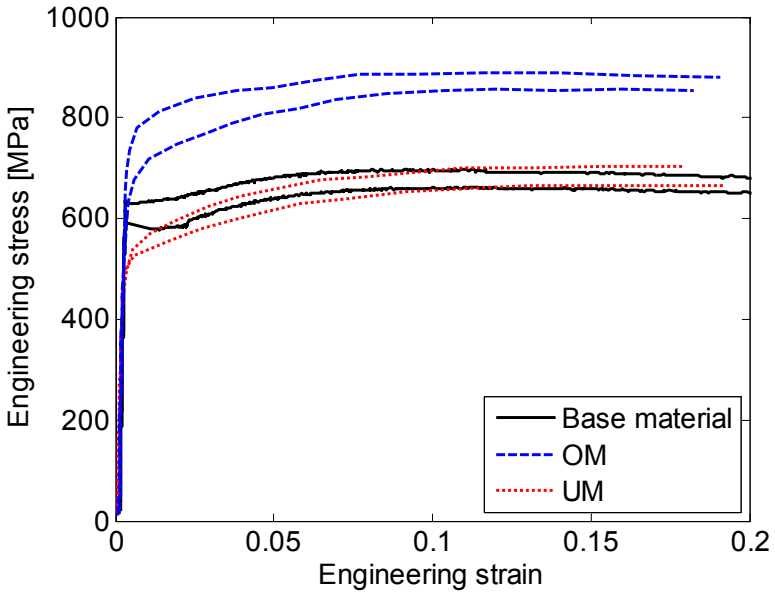

Figure 1. Comparison of engineering stress-strain curves for the BM and the different welded specimens (OM and UM).

The characteristic material parameters are given in **Table 1**. SENT specimens were machined from an X80 pipe containing two different welds with over- and undermatched weld metals, respectively. Two different geometries of the SENT specimens were prepared, referred to as specimen type I (width = 3 mm) and specimen type II (width = 24 mm). The geometries of the two specimen types are illustrated in **Figure 2**, and parameters are given in **Table 2**.

Table 1. Characteristic material parameters for base material (BM), overmatch (OM) and undermatch (UM).

Material	Average yield stress [MPa]	Average tensile strength [MPa]	Relative yield stress to BM
BM	612	685	1.0
OM	728	899	1.19
UM	544	682	0.88

Table 2. Specimen geometry parameters for the two different SENT specimens type I and II, with 3 mm and 24 mm widths.

Specimen type	Width W [mm]	Length L [mm]	Thickness T [mm]	Notch depth a_0 [mm]	Initial crack $\Delta a(t=0)$ [mm]	Notch width b [mm]
I	3	150	12	2.7	1.0	0.3
II	24	300	12	2.3	1.0	0.3

The Electrical Discharge Machined (EDM) notches were entered at the root side of the welds aiming at the fusion line. For specimens type I and II, the notch depths a_0 were slightly different, i.e. 2.7 mm and 2.3 mm respectively. However, the notches were located such that the notch tips were situated approximately 1 mm from the fusion line. Sharp initial cracks were introduced by fatigue loading. The tips of the initial cracks were located close to the fusion line. The initial fatigue crack is included in the schematic view of the SENT specimens in **Figure 2**.

The micro hardness for two specimens of type II (OM and UM) was measured prior to testing in a region covering the weld material, the Heat Affected Zone (HAZ) and the base material. The results of the hardness measurements (in Vickers scale HV1) are presented as color maps in **Figure 3**. The higher hardness of the OM weld material can clearly be seen, corresponding to the higher tensile properties seen in **Figure 1**, as well as an approximately 2 mm wide softer region due to the HAZ. For the UM weld metal the measured micro hardness was close to the micro hardness of the base material, in line with the rather small mismatch in strength between these two materials, also seen in **Figure 1**.

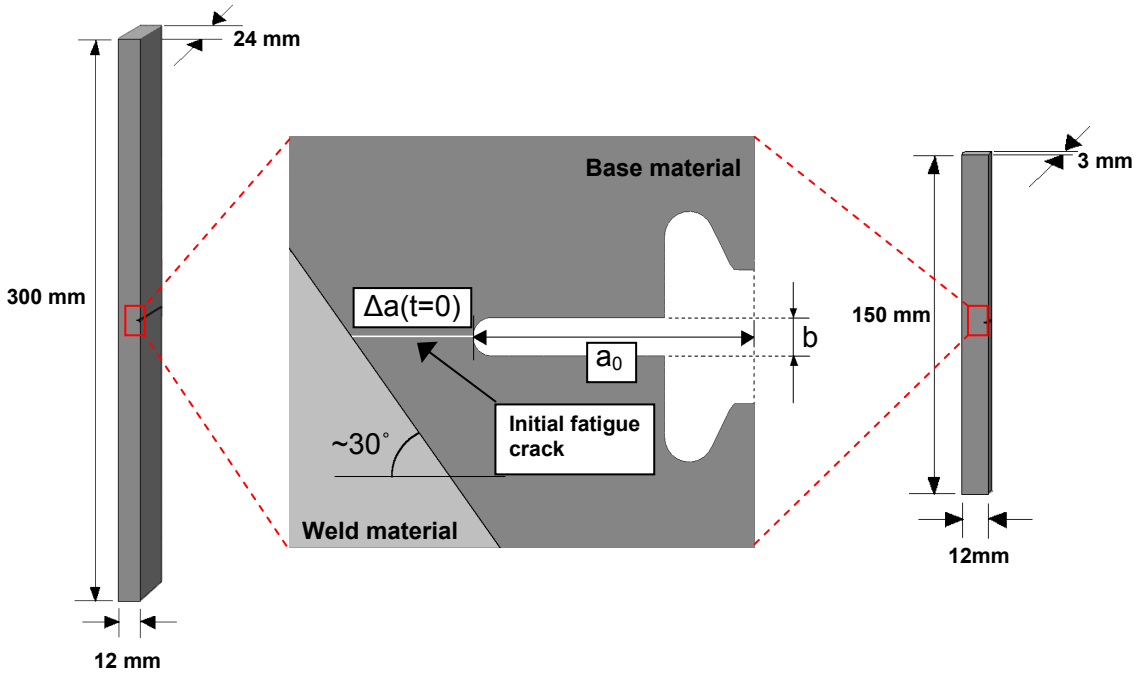

Figure 2. Illustration of the geometry of the two different SENT specimens, with 24 mm (left) and 3 mm thickness (right). In the center, the notch geometry is presented. The crack length is defined as $a = a(t) = \Delta a(t) + a_0$.

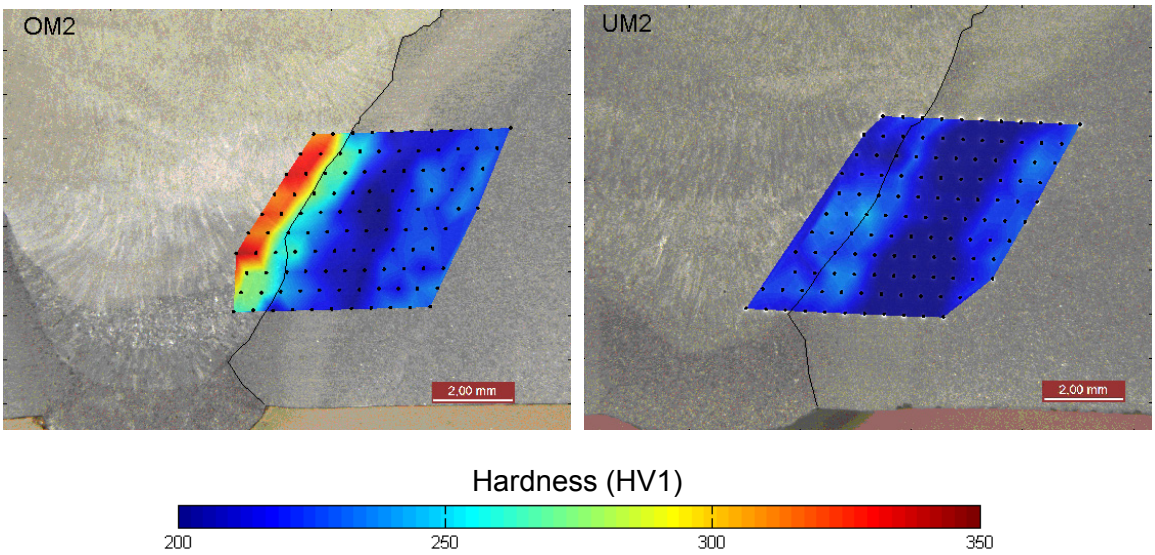

Figure 3. Results from hardness measurements for OM (left) and UM (right). The measurements are carried out on a region covering the fusion line of the weld (indicated as a black line). Distance between measurement points is 0.5 mm.

There is currently no established standard for SENT testing. However, the testing was carried out according to the recommendations given in DNV RP-F108 [14]. The SENT specimens were loaded in displacement control with clamped end conditions at room

temperature under quasi-static conditions. Type I specimens were tested using a Zwick/Roell Z030 testing machine, while type II specimens were tested in a Dartec 500 testing machine. In addition to load and stroke measurements, the Crack Mouth Opening Displacement (CMOD) and Crack Tip Opening Displacement (CTOD) were calculated from recordings of double clip gauges, one inner (Z = 3.7 mm) and one outer (Z = 12.7 mm) (see **Figure 4** for definition of the Z-axis). The thickness side of the specimens (front side in **Figure 4**) was painted with a fine grained speckle pattern. Images were recorded during loading at a recording rate of 3Hz using a Prosilica GC2450 digital camera equipped with a 28-105 mm Nikon lens. The image resolution was 2448×2050 at 8 bit pixel depth. Typically 800 images were recorded for each test. The image series were analyzed in a post procedure using an in-house DIC code, providing displacement and strain fields of the observed specimen surface. No additional extensometers were used during these tests, as the global strain of the specimens can easily be calculated from the DIC analysis.

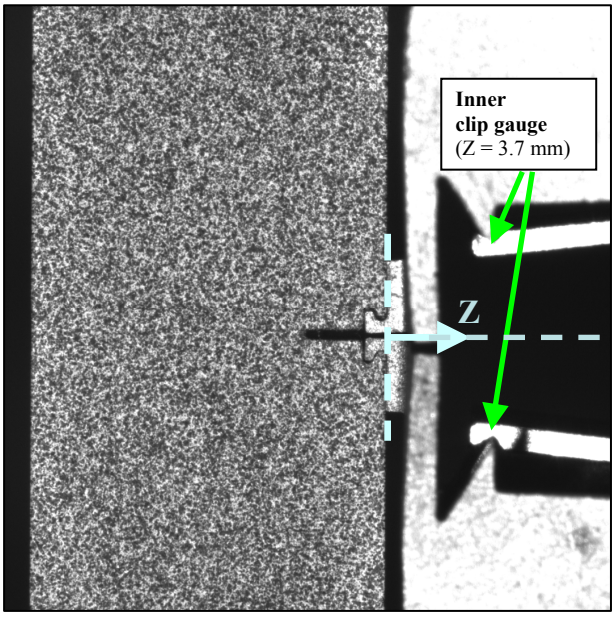

Figure 4. Example of recorded image of SENT specimen with speckle pattern prior to loading. The inner clip gauge (at a distance of Z = 3.7 mm from the specimen) is visible in the image.

Prior to the spray painting of the specimens, pictures were taken of the specimens in order to determine the fusion line of the weld at the specimen surface. **Figure 5** shows an example of the recorded image and the extracted fusion line prior to spray painting and testing.

The SENT specimens were loaded until failure. However, for specimen type II (24 mm width) two of the tests for each material (OM and UM) were aborted and unloaded at different displacement stages in order to investigate the crack profile through the width of the specimens. These specimens were subsequently cooled in liquid nitrogen before they were broken. The crack surfaces were studied in a microscope and the initial and final profiles of the cracks through the width of the specimen were determined.

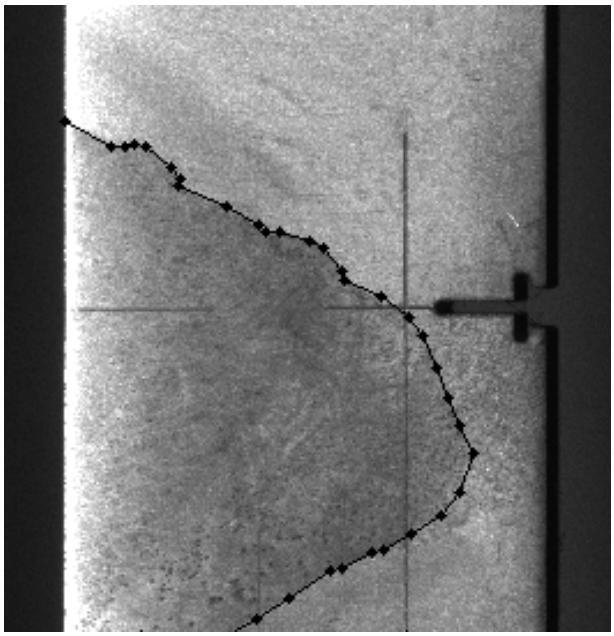

Figure 5. Estimated fusion line from studying images prior to testing. Fusion line is plotted as a dotted line on top of image.

3. Experimental results

In total 5 SENT tests for specimen type I (3 OM + 2 UM) and 6 SENT tests for specimen type II (3 OM + 3 UM) were carried out. **Figure 6** illustrates examples of the specimens after testing. The force-CMOD curves from the tests are presented in **Figure 7**. For the tests which were prematurely aborted (see Section 2), the point-of-abortion is indicated with dots in the force-CMOD curves in **Figure 7**. The CMOD at specimen surface $(Z = 0)$ was extrapolated from the double clip gauges.

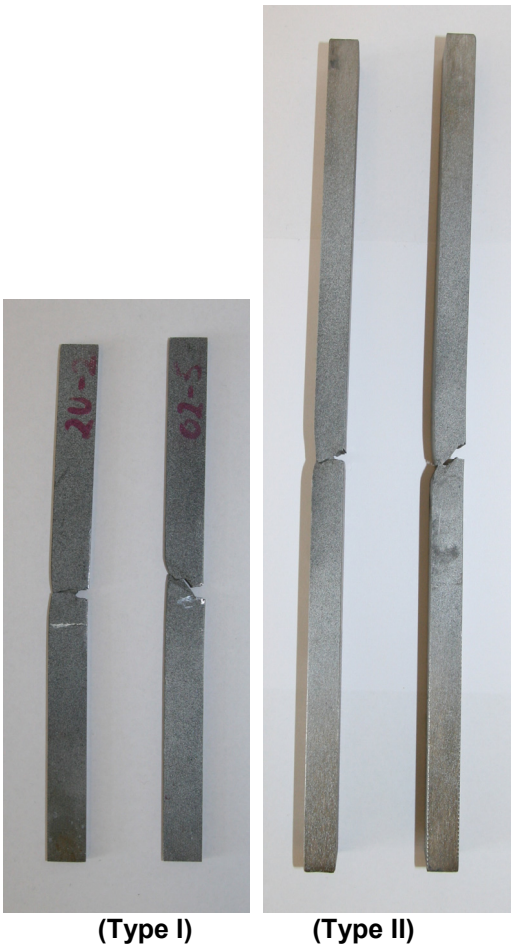

Figure 6. Examples of specimens after tension testing, specimen type I (3 mm width) and specimen type II (24 mm width).

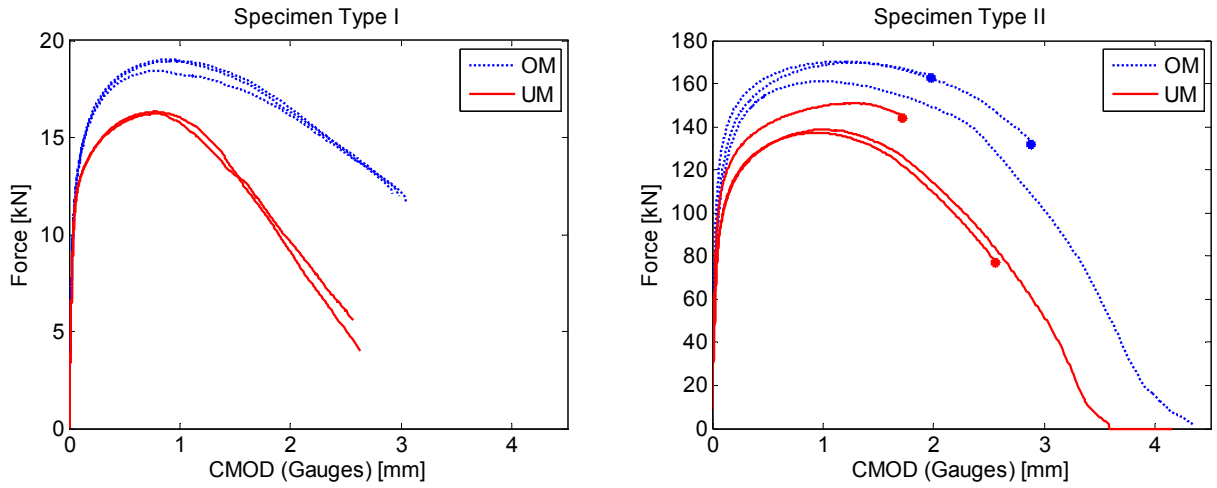

Figure 7. Force-CMOD (Z=0) curves from the test series of type I and II SENT specimens. CMOD was measured by a set of double clip gauges. Dots indicate the four tests for specimen type II which were prematurely stopped.

The higher load levels in the OM curves corresponding to the higher tensile strength are clearly evident. For type I specimens it can be observed that the ascending part of the curve is steeper for the UM curves compared to the OM curves. This steeper slope is an indication of a lower crack growth resistance, and could be due to the crack growth taking place in the weld metal for the former, whereas it grows out into the HAZ/base material for the latter, as will be shown in Section 4. Further, the crack growth deviation is stronger in the OM compared to the UM, which could also contribute to the apparently higher crack growth resistance in the former. It is noted that this effect is not so clearly seen in the wider type II specimen.

For type II specimens, four tests were aborted prematurely prior to failure, as described in Section 2. These specimens were subsequently cooled in liquid nitrogen and then broken. Due to the different textures of the crack surface, the different crack profiles in the width-thickness plane were obtained by studying the cross sections in a microscope. **Figure 8** illustrates the measured crack profiles of these four specimens. The profiles of the EDM notch (a_0), the initial fatigue crack ($a_{initial}$) and the final crack (a_{final}) are plotted. The specimen surfaces observed by the camera during the tests are indicated with arrows in the plots and the corresponding values for $a_{initial}$ and a_{final} are indicated. It is noted that the crack length $a = a(t) = \Delta a(t) + a_0$ is defined as the length of the crack path projection along the thickness direction of the specimen. In general the crack extends further in the middle region of the specimens, as expected from the higher stress triaxiality found here.

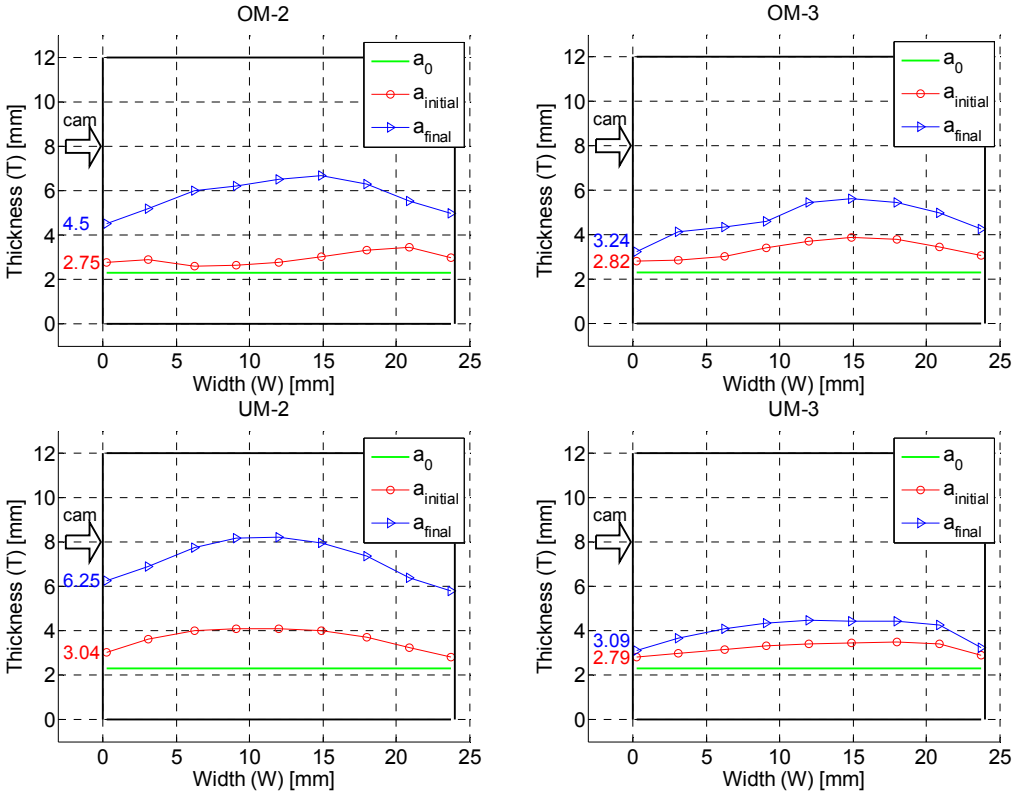

Figure 8. Crack profiles (in the width-thickness plane) of the four prematurely stopped SENT tests of specimen type II. The side of the specimens observed by the camera is indicated with arrows, and the value of the crack length (in mm) for this particular surface is indicated in each plot.

4. Image analysis

4.1 Digital Image Correlation

The basic principle of DIC is based on finding the correlation between a reference image and the current image, i.e. an image at a deformed stage. The correlation is found by optimizing a set of degrees of freedom (DOFs) for a pixel subset, by minimizing the sum of gray value differences between the two images within the particular subset. The global "finite element" approach presented by Besnard et al. [9] deviates from the traditional DIC algorithm in that the correlation is found globally for a mesh of elements. The nodal degrees of freedom are optimized as opposed to the traditional DIC approach where parameters describing the translation and displacement gradient are correlated individually for a set of pixel subsets. The "finite element" DIC approach is chosen as basis for the work presented in this paper. The nodal displacements are solved in an iterative fashion by building a linear system of equations

$$\mathbf{Ma} = \mathbf{b} \tag{1}$$

where $\mathbf{a}$ is a vector containing the incremental nodal displacements. $\mathbf{M}$ is a matrix and $\mathbf{b}$ is a vector obtained from the assembly of element contributions ($\mathbf{M}^e$ and $\mathbf{b}^e$)

$$M^e_{\alpha m \beta n} = \sum_{i \in \Omega^e} N_m(\mathbf{X}_i) N_n(\mathbf{X}_i) \frac{\partial f_i}{\partial X_\alpha} \frac{\partial f_i}{\partial X_\beta} \tag{2}$$

$$b^e_{\alpha m} = \sum_{i \in \Omega^e} \left[f(\mathbf{X}_i) - g(\mathbf{x}_i) \right] N_m(\mathbf{X}_i) \frac{\partial f_i}{\partial X_\alpha} \tag{3}$$

where (N_m, N_n) are the shape functions of the element e. Ω^e is the pixel region corresponding to the element, and i indicates a particular pixel (in reference configuration). (α, β) identify the coordinate axes and (m, n) identify the local node number of the element. f and g are the grayscale maps of the reference and current image, while $\mathbf{X}$ and $\mathbf{x}$ are the position vectors in the reference and the current (deformed) configuration. Bi-cubic interpolation is used in this study to obtain grayscale values from the grayscale maps at sub-pixel locations.

The matrix $\mathbf{M}$ and vector $\mathbf{b}$ in the global equation (Eq. 1) are assembled by element contributions. By utilizing that the matrix $\mathbf{M}$ is sparse and symmetric, the number of calculations in the assembly code can be significantly reduced. However, when the mesh consists of a large number of elements and nodes, the assembly process becomes a computational expensive process. Each column and row of the matrix $\mathbf{M}$ and each row of the vector $\mathbf{b}$ correspond to a particular degree of freedom for a particular node. Because each node may be connected to several elements, and the nodal contribution is calculated as an accumulation of the contribution of its connected elements, the assembly process has to be carried out in a serial fashion. However, by assembling $\mathbf{M}$ and $\mathbf{b}$ from nodal contributions, the process can be carried out in parallel. A global assembly of $\mathbf{M}$ and $\mathbf{b}$ based on nodal contributions has been carried out as

$$M_{\alpha m \beta n} = \sum_{e \in E_{mn}} \sum_{i \in \Omega^e} N_m^e(\mathbf{X}_i) N_n^e(\mathbf{X}_i) \frac{\partial f_i}{\partial X_\alpha} \frac{\partial f_i}{\partial X_\beta} \tag{4}$$

$$b_{\alpha m} = \sum_{e \in E_m} \sum_{i \in \Omega^e} \left[f(\mathbf{X}_i) - g(\mathbf{x}_i) \right] N_m^e(\mathbf{X}_i) \frac{\partial f_i}{\partial X_\alpha} \tag{5}$$

where E_m contains all elements connected to node m while E_{mn} contains all elements connected to both node m and n. It is noted that (m, n) here indicate the global node indices. The assembly of nodal contributions was implemented in a parallel code on a two-processor quad-core platform (eight independent threads) using the OpenMP API [12]. The parallel code provided an increased computation speed of approximately 5 times compared to the serially implemented assembly of element contributions.

4.2 Mesh generation for DIC with node splitting

The 2D-DIC analysis presented in this paper is based on a two-step technique where node splitting is used to model the discontinuous displacement fields of SENT specimens with crack propagation. The technique is described in detail in [15]. First, because the crack may take a more or less random path through the specimen, an initial DIC analysis is carried out in order to estimate the crack path. Based on this initial analysis a new mesh is generated, where a set of duplicate nodes are situated at the crack path. The mesh is generated such that the mesh "opens up" as the crack propagates through the specimen. The procedure is illustrated in **Figure 9**.

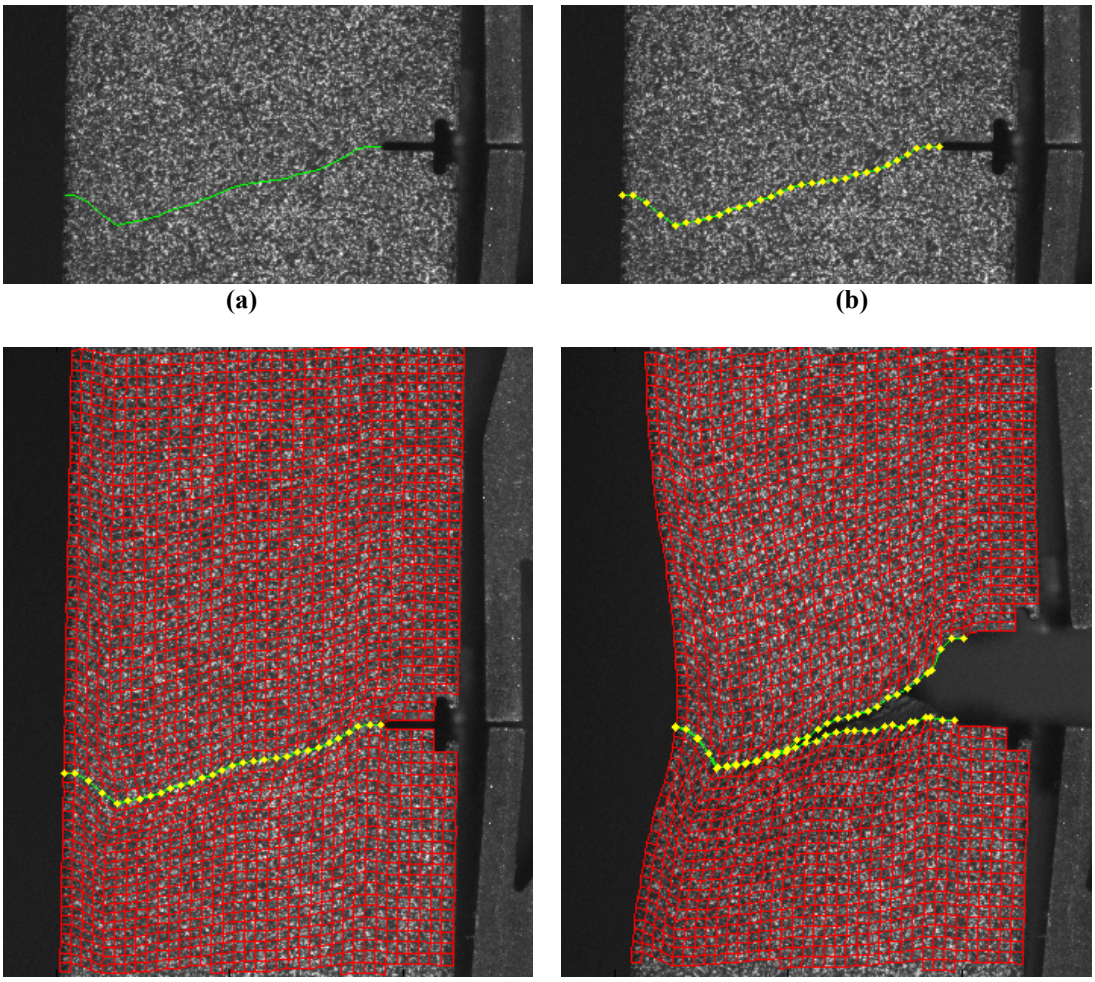

Figure 9. Illustration of the crack handling procedure based on node splitting. First an initial analysis is carried out to determine the crack path (a). Duplicate nodes are distributed along the crack path (b), and a modified mesh is generated to allow node splitting (c). As the crack propagate through the specimen, the duplicate nodes separate, and the mesh "opens up" (d).

A comparison of the measured displacement field between a standard DIC analysis with a Q4 mesh and the modified analysis using a mesh with duplicate nodes along the crack path is presented in **Figure 10**. In the standard analysis, the discontinuous displacement field is averaged over the elements cut by the crack, giving substantial errors in the measured displacement field. However, when using a mesh optimized for node splitting, the discontinuous displacement field is successfully captured. Another benefit of applying this method is that the crack path through the specimen is accurately captured. Also parameters of vital importance in fracture mechanics tests, such as crack length Δa, CTOD and CMOD as a function of time can easily be extracted from the analysis.

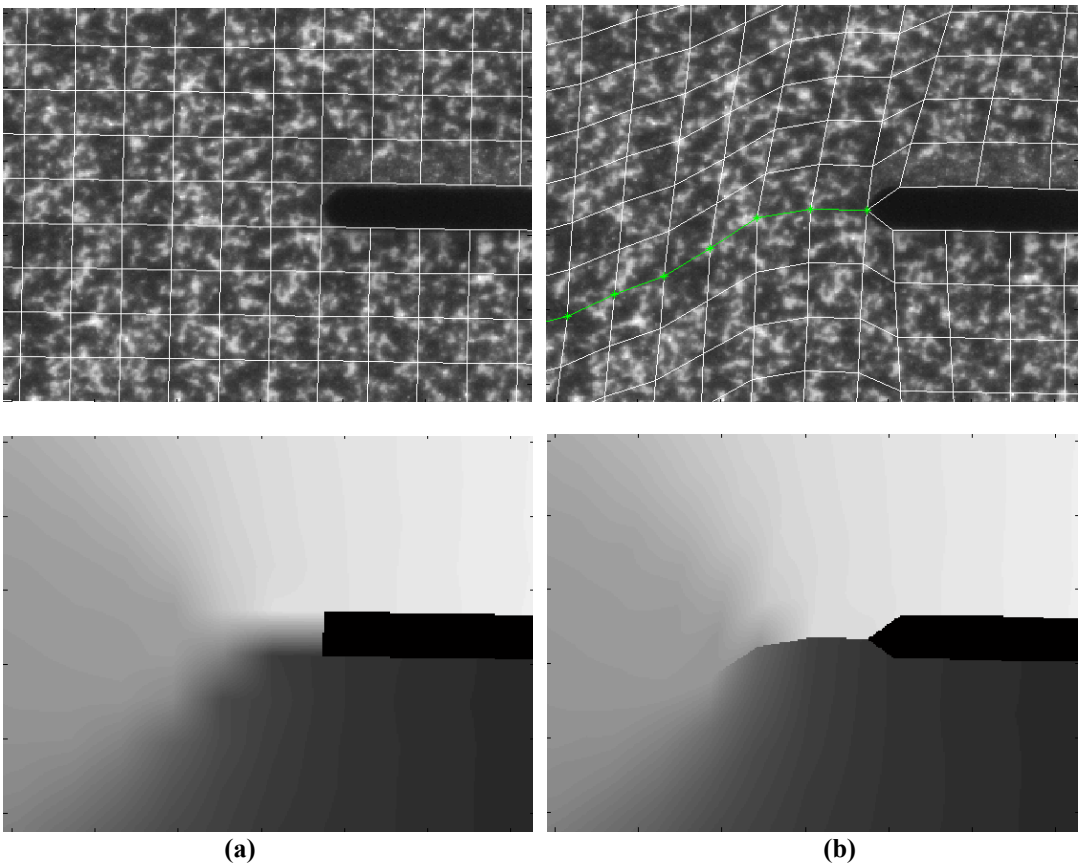

Figure 10. Measured displacement field with (a) standard Q4 mesh and (b) optimized mesh with isoparametric Q4 elements and duplicate nodes along crack path. In the first case (a), the discontinuous displacement field is averaged over the area of the elements cut by the crack. For the node-splitting case (b), the discontinuous field of the cracked region is successfully captured.

4.3 Results from DIC analysis

In total 11 tests were carried out (5 for specimen type I and 6 for specimen type II) with varying weld material (OM and UM) as shown in Section 3. For all tests, series of approximately 800 images with resolution of 2448×2050 at 8 bit pixel depth were recorded. All image series were analyzed using the node-splitting DIC analysis described above with an average element size of 25 pixels (0.28 mm). Examples of the resulting effective strain fields for specimen type II are presented in **Figure 11** and **Figure 12**, for OM and UM respectively. These effective strain fields, $\varepsilon_{eff} = \varepsilon_{eff}\left(\mathbf{X},t\right)$, were calculated from the DIC analysis based on the von Mises norm, viz.

$$\varepsilon_{eff} = \sqrt{\frac{2}{3}\left(\varepsilon_1^2+\varepsilon_2^2+\varepsilon_3^2\right)} = \sqrt{\frac{4}{3}\left(\varepsilon_1^2+\varepsilon_1\varepsilon_2+\varepsilon_2^2\right)} \tag{6}$$

where plastic incompressibility and negligible elastic strains have been assumed. Thus, the logarithmic principal strain component in the out-of-plane direction (ε_3) is calculated from the logarithmic principal strain components $(\varepsilon_1, \varepsilon_2)$ measured in the 2D-DIC analysis as

$$\varepsilon_3 = -(\varepsilon_1 + \varepsilon_2). \tag{7}$$

It is noted that the out-of-plane direction is here assumed to be a principal-strain direction (see [16] for details). It is referred to [17] for further details on the calculation of the in-plane strain components $(\varepsilon_1, \varepsilon_2)$.

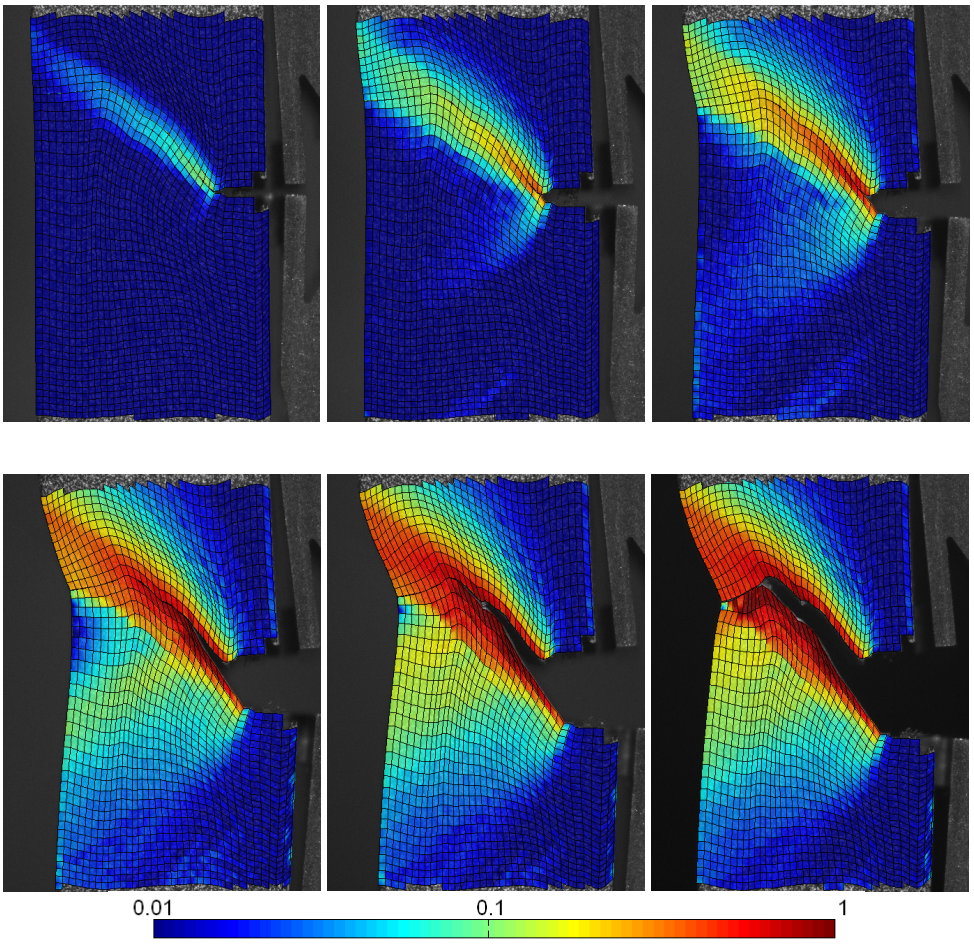

Figure 11. Effective strain fields of SENT specimen type II (24 mm width) during loading for OM specimen. The strain fields are plotted in a logarithmically scaled color map.

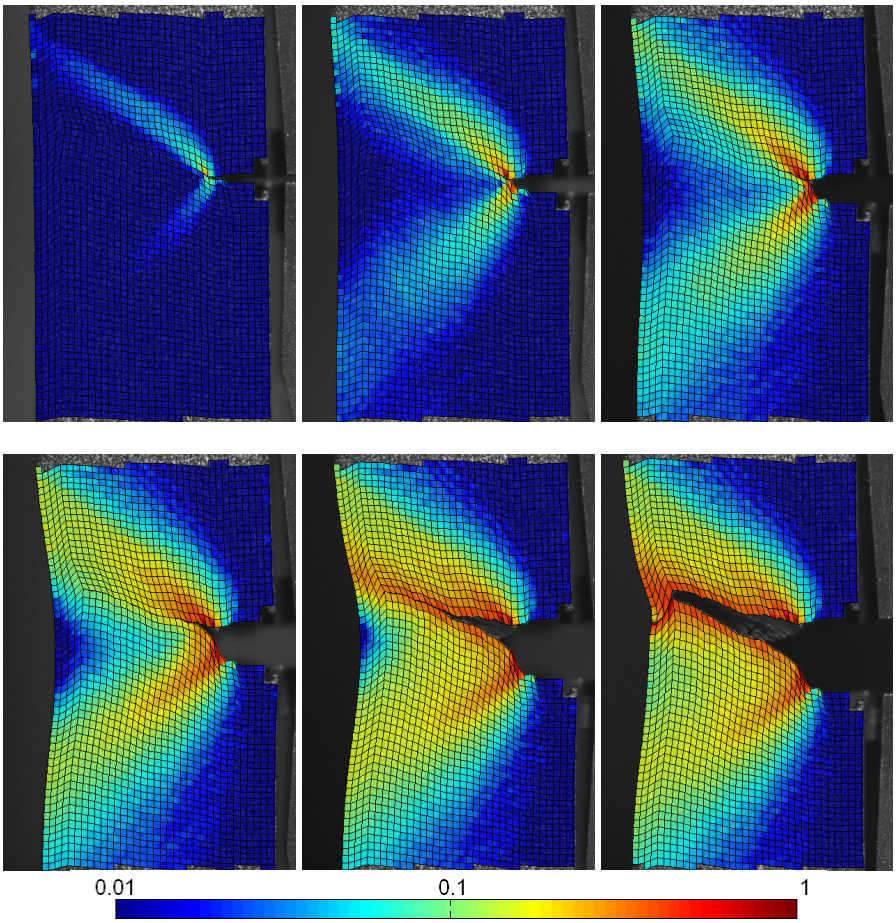

Figure 12. Effective strain fields of SENT specimen type II (24 mm width) during loading for UM specimen. The strain fields are plotted in a logarithmically scaled color map.

Such field measurements from DIC represent a huge amount of data and a natural use of these data is for validation of numerical models. In this paper, they are included for illustration of the strain fields of the specimens with different weld materials. The OM specimen is characterized by an asymmetric strain field and slightly higher strain values compared to the UM specimen.

Figure 13 shows the effective strains in couples of elements located on both sides of the crack paths as function of crack length (Δa). One OM and one UM test is presented for both specimen types I and II. The chosen elements are located at corresponding crack length values, $\Delta a \approx 2$ mm. It is noted that significant asymmetry in the effective strains is measured, especially for the OM specimens. Investigation of the crack surfaces of the specimens after testing shows that small shear lips are present. The asymmetric strains may have been caused by these shear lips as the crack propagates to surface of the specimen on the thickness side, which is the side of the specimen observed by the digital camera. The higher effective strain

values in the OM specimen compared to the UM specimen is also emphasized. This corresponds with the expected higher fracture resistance in the OM specimen.

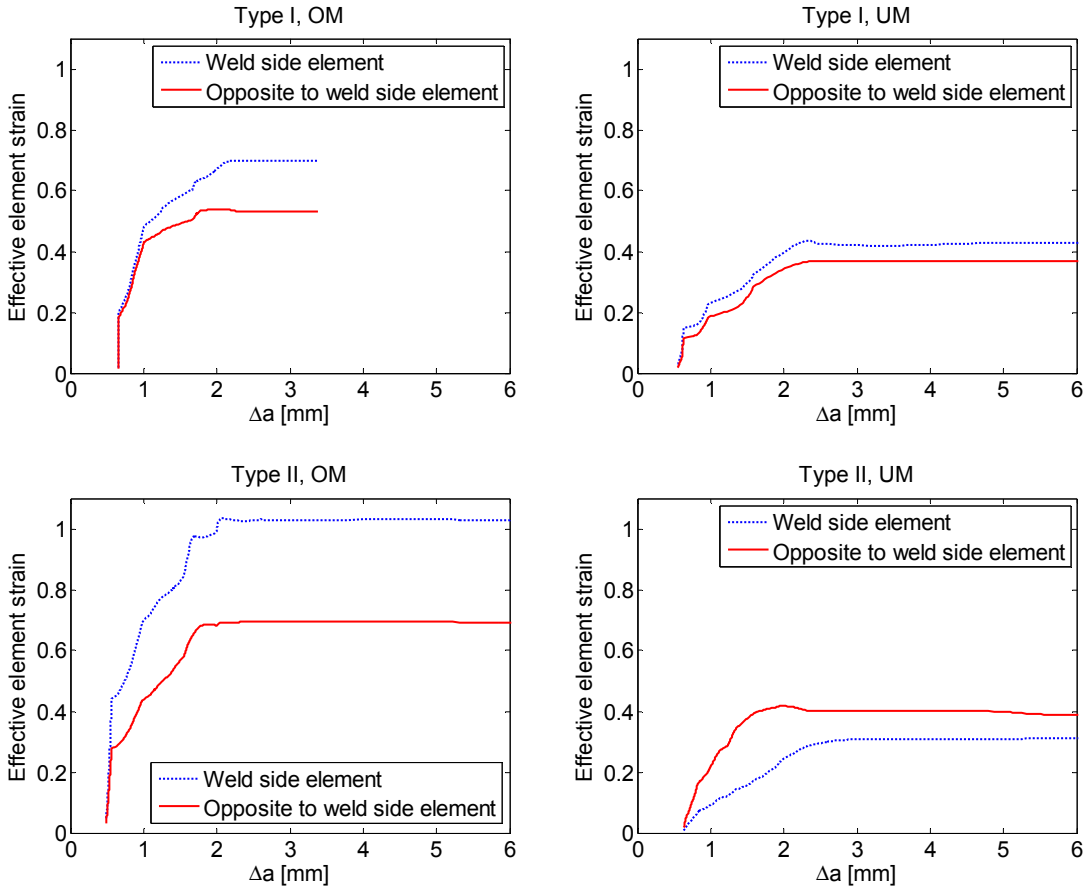

Figure 13. Effective strain in elements close to the crack path as function of crack length (Δa), for four tests of specimen type I (top) and specimen type II (below). The chosen elements are located at corresponding crack length values, $\Delta a \approx 2$ mm.

The calculated crack paths for all tests are presented in **Figure 14**. The consistency of the OM crack path is emphasized. The average inclination angle of the OM crack path is measured to 53° for specimen type I and 51° for specimen type II. The crack growth deviation observed in the OM specimens seems to be driven by the highly asymmetrical deformation field arising due to the strong overmatch in the weld metal. Thus, the consistency in crack growth direction is related to the strong strain localization towards the HAZ/base material side being the primary source to the crack growth path followed.

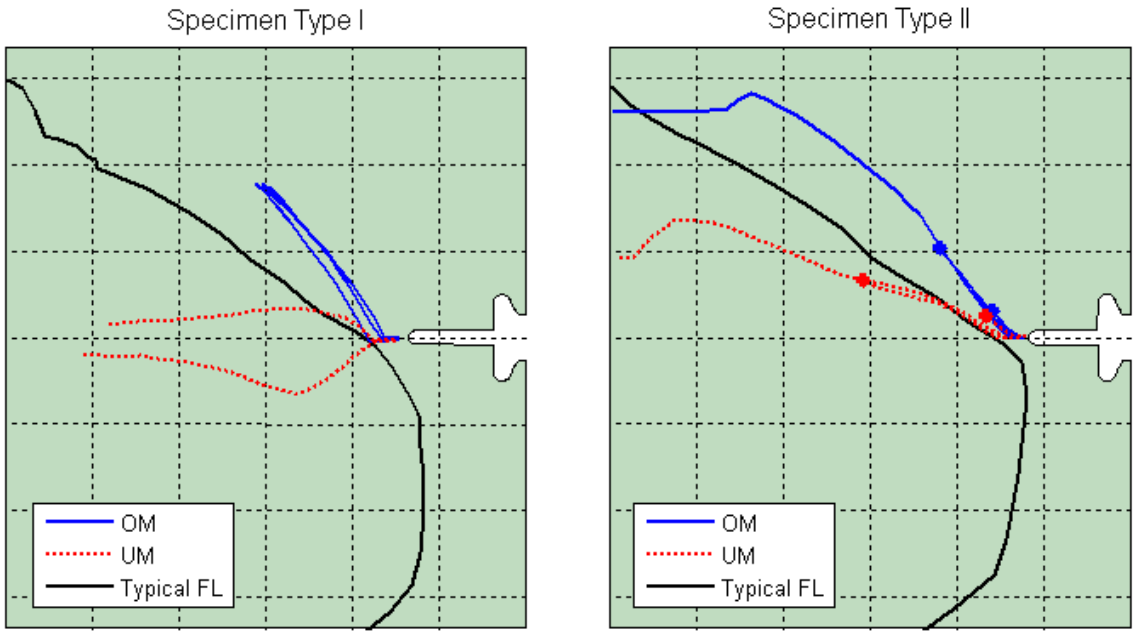

Figure 14. Crack paths in SENT specimens type I and II. Prematurely aborted tests are indicated with a dot at the end of the crack paths in specimen type II. Typical fusion lines (FL) are also indicated on the specimen plots.

More scatter is observed for the UM cracks. This may be due to varying material properties in the weld metal and fusion line region. Although the UM weld metal in general is undermatch in yield stress compared to the base material, it is more or less evenmatched with respect to tensile strength, as seen from **Figure 1**. Thus, the degree of mismatch is much less in the UM case, and local areas in the UM weld may actually have slight overmatch compared to the base material due to the scatter in tensile properties.

Figure 15 shows a comparison of the CTOD and CMOD measurements calculated from DIC analysis and the double clip gauges. The close correlation between the different measurements may act as a validation of both techniques, as the clip gauges is based on extrapolation of measured gauge values, and the DIC analysis may have uncertainties in lens distortions and pixel-to-mm transformations. It is also noted that the gauge measurements are carried out at the centre of the width-side of the specimen, while the DIC measurements are carried out on the surface of the thickness-side.

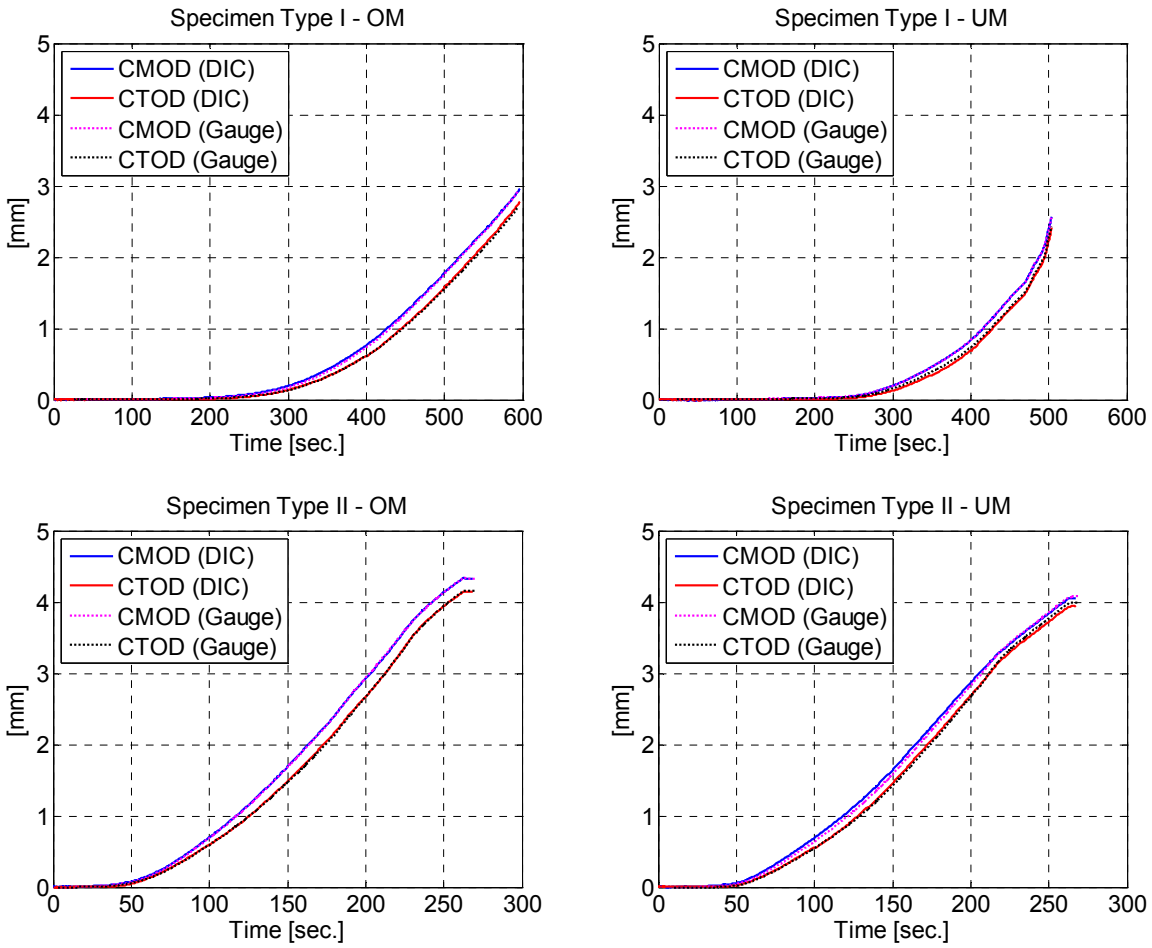

Figure 15. Examples of CTOD and CMOD comparison between measurements from DIC and gauges for specimen type I & II, for OM and UM series.

Figure 16 illustrates a comparison between the crack lengths a extracted from the DIC analysis on the one hand, and the initial ($a_{initial}$) and final (a_{final}) crack lengths measured by the post-experimental microscope analysis on the other hand. The plots show the results from two of the tests which were prematurely aborted, one OM test and one UM test. The estimated crack length a from DIC is presented as function of elongation, which is measured over a 10 mm gauge length. The initial and final crack lengths measured in the microscope are indicated with dotted and dashed lines, respectively. A relatively close correlation between the microscope analysis and results from DIC can be seen. It is noted that the microscope analysis has the benefit of measuring the crack profile through the width of the specimen (see **Figure 8**), while DIC only measures the crack length on the thickness surface. However, DIC gives information on how the crack evolves as a function of time during the experiment. Thus, the

two measurement techniques are complementary, and both techniques give valuable information on how the crack behaves during the experimental tests.

Finally, **Figure 17** illustrates the CTOD as function of crack length Δa in all tested specimens, both type I and II. The results are calculated from the DIC analysis. These plots show the difference between OM and UM weld metal which is plotted with dotted and solid lines, respectively. The higher crack resistance for the OM specimens compared to the UM specimens (seen in **Figure 17**) corresponds to the higher effective strain values for the OM specimen presented in **Figure 13**.

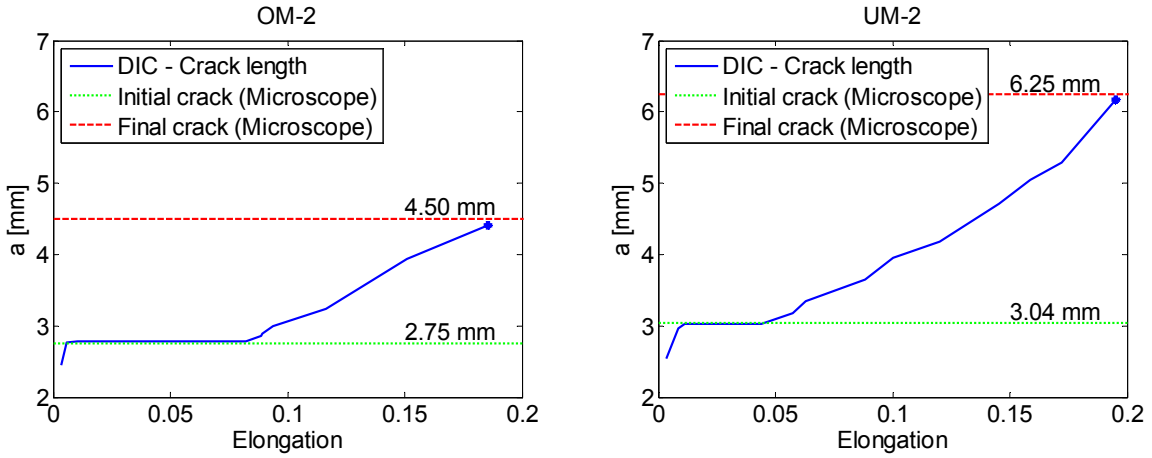

Figure 16. Comparison of crack lengths (in specimen type II) between DIC analysis and microscope analysis for one OM and one UM test which were aborted before failure. The crack lengths are plotted as function of the elongation, measured at a 10 mm gauge reference distance. The microscope reading of the initial and final crack length values are indicated with dotted lines for comparison (see **Figure 8**).

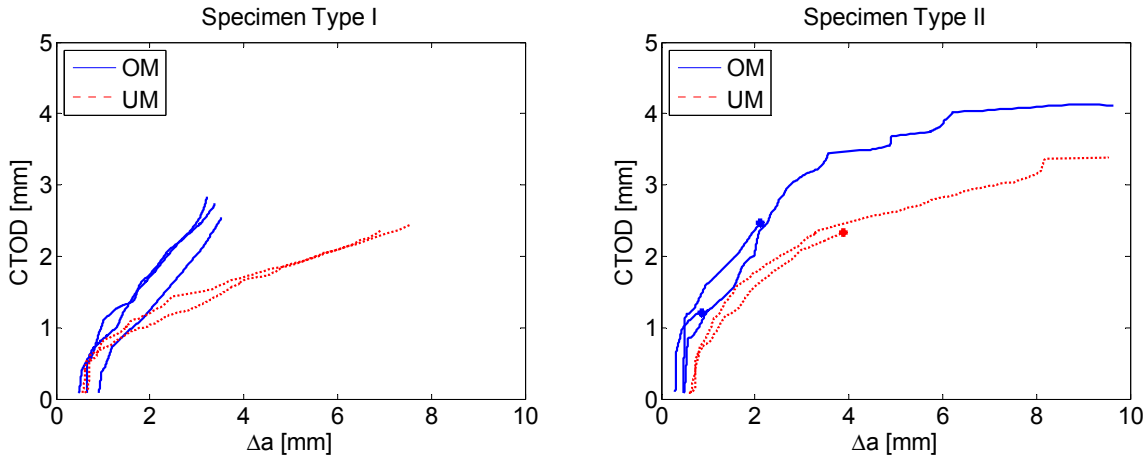

Figure 17. CTOD as function of crack length Δa in SENT specimens type I and II. Values are calculated from DIC analysis. For specimen type II, dots indicate the end of the tests which were prematurely aborted.

5. Assessment of 2D vs. 3D DIC

One of the main drawbacks using 2D-DIC to extract information from fracture mechanics tests, such as SENT tests, is that the out-of-plane deformation of the specimen is neglected from the measurements. Such out-of-plane deformations, caused by necking of the specimen, may lead to systematic errors to the measured in-plane components (in addition to the out-of-plane components which are neglected). These systematic errors are particular evident in strain calculations. Lenses with high focal lengths and increased camera-specimen distance may reduce the errors in the in-plane components caused by out-of-plane deformation to a minimum. In order to investigate these systematic errors, two of the SENT tests in this study (one OM and one UM), were carried out using an additional camera. The camera models of this stereo vision setup were calibrated prior to testing using a camera calibration routine presented in [18]. Image series from the two cameras were then analyzed applying the proposed DIC approach. Using the calibrated camera models and combining the DIC results from the two image series, three-dimensional node displacements were obtained. **Figure 18** illustrates the out-of-plane displacement profiles for an overmatch and an undermatch SENT test during loading. The profiles are collected from the center of the thickness side and along the length direction of the specimens. **Figure 19** shows the measured out-of-plane deformation field from the 3D-DIC analysis for the final image in two SENT tests for specimen type II (one OM and one UM). The three-dimensional results in **Figure 18** and **Figure 19** show significant necking of the specimens and out-of-plane deviations up to 1.2 mm for both OM and UM tests.

The effective strains from the 3D-DIC analyses have been calculated based on the in-plane components using Eq. (6) and compared to the corresponding 2D analyses. The highest deviations in effective strain levels for the final images in the series were about 0.08 for both OM and UM tests. These maximum deviations in strain levels were encountered for elements close to the crack path were the highest strains and out-of-plane displacements were observed. However, the RMS of the strain residuals (for all elements) compared between the 2D and 3D analyses were below 0.006 for all images, in both OM and UM tests. This indicates that, as the overall strain field is successfully captured using the 2D analysis, some elements located in the necking region (close to the crack path), may have reduced accuracy due to systematic errors.

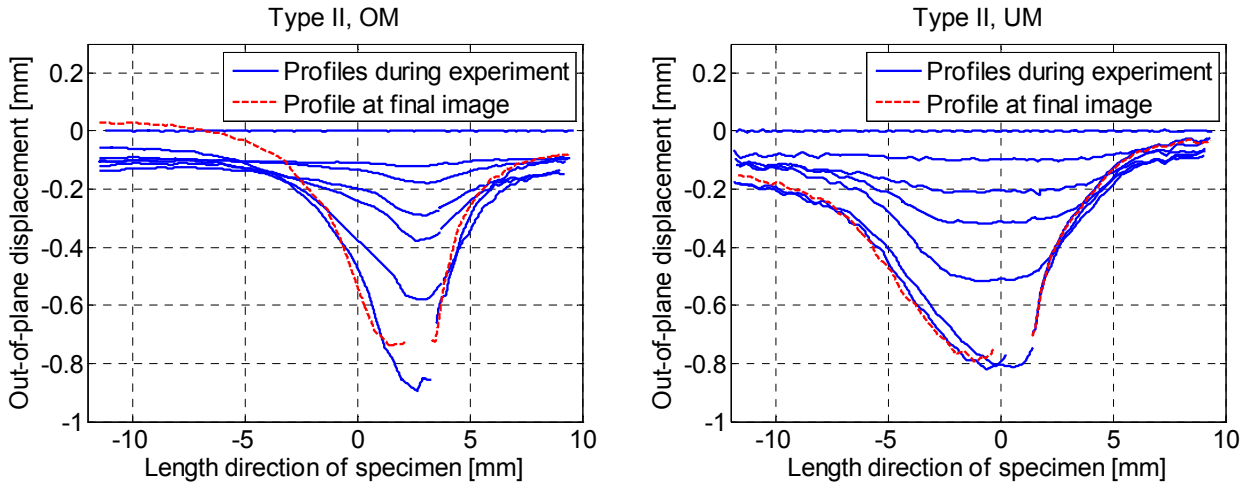

Figure 18. Out-of-plane displacement profiles during experiment for one OM (left) and one UM (right) specimen. The profiles are collected at the center of the thickness side and along the length direction of the specimen. The out-of-plane displacement for the final image in the series is plotted with a dashed line.

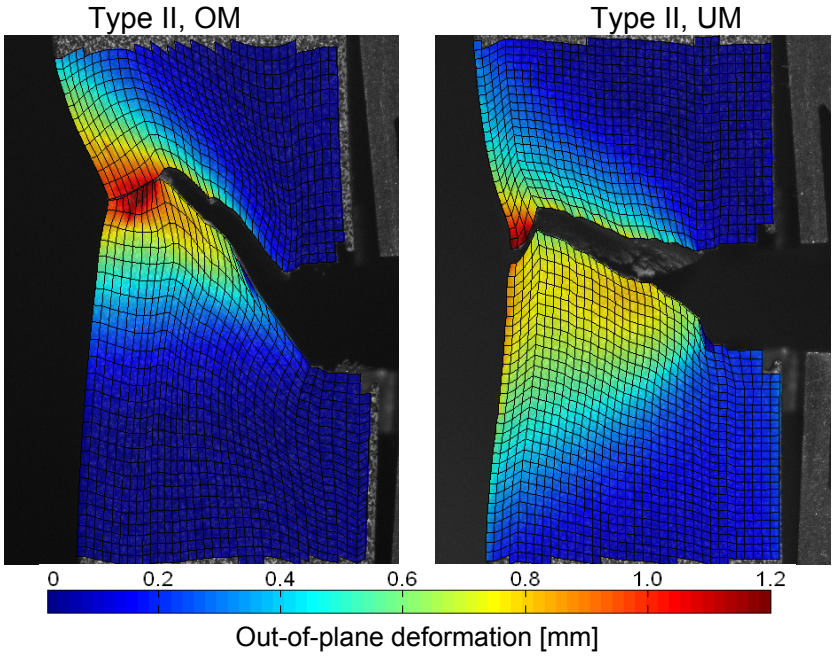

Figure 19. Calculated out-of-plane deformation (necking) from 3D-DIC analysis at the final recorded image, for one OM (left) and one UM (right) specimen. The color scale is given in mm.

The disadvantage of applying 3D-DIC is mainly that it requires significant preparation in setup and calibration of the cameras. Also, the image post-processing becomes considerably more extensive. However, when significant necking is present and strain measurements close to the crack path and crack tip are of vital importance, three-dimensional analyses may be

preferred. It is finally remarked that the node-splitting method developed in this work is equally valid for 2D and 3D DIC analyses.

6. Concluding remarks

Understanding the crack behavior in pipelines close to welds is a challenging task. The SENT test represents an applicable approach to obtain information of crack behavior on different mismatch levels in pipeline weld materials. This is particular important in the quest for increased safety in the utilization of pipeline girth welds. The novel DIC method proposed in this study, utilizing an adapted mesh with node splitting, has demonstrated potential to provide valuable information regarding complex phenomena like crack growth deviation, which is not accounted for in today's engineering practice. As the DIC analysis of large image series is computational expensive, the parallelization of the DIC code has decreased processing time considerably when run on a multiple-core CPU. The discontinuous displacement and strain fields of the propagating cracks have been successfully captured. Also parameters such as CMOD, CTOD, crack paths and crack lengths can be extracted from the DIC analysis. Further, it is evident that the results from the DIC analysis provide valuable input for validation of numerical models. However, care should be taken when applying two-dimensional DIC analyses to such mechanical tests, as significant necking of the specimen may degrade the measured displacement and strain fields. This is particularly evident when strain measurements close to the crack path and crack tip is of vital importance. For such cases three-dimensional analyses (3D-DIC) should be implemented. However, the node-splitting method presented in this paper is equally valid for both 2D and 3D DIC analyses.

Acknowledgement

The financial support of this work from the Structural Impact Laboratory (SIMLab), Centre for Research-based Innovation (CRI) at the Norwegian University of Science and Technology (NTNU), is gratefully acknowledged.

References

[1] Østby E, Jayadevan KR, Thaulow C. Fracture response of pipelines subjected to large plastic defromations under bending. Int J Pres Ves Pip 2005;82:201-215.

[2] Budden PJ. Failure assessment diagram methods for strain-based fracture. Engng Fract Mech 2006;73:537-552.

[3] Nourpanah N, Taheri F. Development of a reference strain approach for assessment of fracture response of reeled pipelines. Engng Fract Mech 2010;77:2337-2353.

[4] Nyhus B, Polanco ML, Ørjasæter O. SENT specimens – an alternative to SENB specimens for fracture mechanics testing of pipelines. Proceedings of the 22nd OMAE Conference, Cancun, Mexico; 2003.

[5] Cravero S, Ruggieri C. Correlation of fracture behavior in high pressure pipelines with axial flaws using constraint designed test specimens—Part I: Plane-strain analyses. Engng Fract Mech 2005;72:1344-1360.

[6] Østby E, Nyhus B, Kane PA, Thaulow C. The effect of weld metal mismatch level on the failure mode in small-scale SENT testing of an X80 Material. Proceeding of the twentieth ISOPE Conference, Beijing, China; 2010.

[7] McClintock FM. Plasticity aspects in fracture. In: Liebowitz H, editor. Fracture, Vol 3, New York: Academic Press; 1971, p. 47-225.

[8] Kardomateas GA, McClintock FA, Carter WT. Directional effects in asymmetric fully plastic crack growth. Engng Fract Mech 1985;21:341-351.

[9] Besnard G, Hild F, Roux S. 'Finite-element' displacement fields analysis from digital images: application to Portevin-le Châtelier bands. Exp Mech 2006;46:789-804.

[10] Réthoré J, Hild F, Roux S. Extended digital image correlation with crack shape optimization. Int J Numer Meth Engng 2008;73:248-272.

[11] Zhang J, Cai Y, Ye W, Yu TX. On the use of the digital image correlation method for heterogeneous deformation measurement of porous solids. Opt Laser Eng 2010;49:200-209.

[12] http://openmp.org/wp/ [cited 08.09.2011]

[13] Zhang ZL, Hauge M, Thaulow C, Ødegård J. A notched cross weld tensile testing method for determining true stress-strain curves for weldments. Engng Fract Mech 2002;69:353-366.

[14] http://exchange.dnv.com/publishing/Codes/download.asp?url\x3d2006-01/rp-f108.pdf [cited 08.09.2011]

[15] Fagerholt E, Børvik T, Hopperstad OS. Measuring discontinuous displacement fields in cracked specimens using Digital Image Correlation with mesh adaptation and crack-path optimization. Submitted for possible journal publication.

[16] Kajberg J, Lindkvist G. Characterisation of materials subjected to large strains by inverse modeling based on in-plane displacement fields. Int J Solids Struct 2004;41:3439-3459.

[17] Fagerholt E, Dørum C, Børvik T, Laukli HI, Hopperstad OS. Experimental and numerical investigation of fracture in a cast aluminium alloy. Int J Solids Struct 2010;47(24):3352-3365.

[18] Fagerholt E, Grytten F, Gihleengen BE, Langseth M, Børvik T. Continuous out-of-plane deformation measurements of AA5083-H116 plates subjected to low-velocity impact loading. Int J Mech Sci 2010;52(5):689-705.

Part IV

E. Fagerholt, T. Børvik and O.S. Hopperstad.

Measuring discontinuous displacement fields in cracked specimens using Digital Image Correlation with mesh adaptation and crack-path optimization

Submitted for possible journal publication.

Measuring discontinuous displacement fields in cracked specimens using Digital Image Correlation with mesh adaptation and crack-path optimization

E. Fagerholt[a,*], T. Børvik[a,b] and O.S. Hopperstad[a]

[a] *Structural Impact Laboratory (SIMLab), Centre for Research-based Innovation (CRI) and Department of Structural Engineering, Norwegian University of Science and Technology, Rich. Birkelands vei 1A, NO-7491 Trondheim, Norway*

[b] *Norwegian Defence Estates Agency, Research & Development Department, PB 405, Sentrum, NO-0103 Oslo, Norway*

Abstract

This paper evaluates mesh adaptation techniques in two-dimensional Digital Image Correlation (2D-DIC) analyses of specimens with large deformations and a single propagating crack. The "finite element" formulation of DIC is chosen as basis for this study. The focus has been on the challenges caused by high-gradient and discontinuous displacement fields in the region of a propagating crack, and the aim has been to improve both the robustness and the accuracy of the correlation in such regions. Mesh adaptation based on node splitting and a novel overlapping-mesh technique have been implemented in a DIC code and used to capture the discontinuous displacement fields of cracked specimens. In addition, a procedure for optimization of the location of the crack path is presented. Synthetic image series with known displacement fields, generated from finite element simulations, have been analyzed to evaluate the performance of the presented techniques. Additionally, an experimental image series of a modified Arcan test has been analyzed using the proposed mesh adaptation and crack-path optimization. The paper contains a detailed description of the proposed techniques and results from the evaluation. It is found that both the node-splitting and overlapping-mesh techniques can be applied to successfully capture the discontinuous displacement field of a propagating crack. In the latter technique, the crack path is described down to pixel level. The crack-path optimization is capable of locating the crack path with sub-pixel accuracy, reducing correlation residuals and thus increasing the robustness of the DIC analysis. In addition, a certain filtering of pixels based on high correlation residual is found to increase the robustness of the correlation in areas affected by a propagating crack.

Keywords: DIC; crack propagation; crack- path optimization; discontinuous displacement field

[*] Corresponding author. Tel.: + 47-73-59-46-93; fax: + 47-73-59-47-01

E-mail address: egil.fagerholt@ntnu.no (E. Fagerholt).

1. Introduction

In the last decades Digital Image Correlation (DIC) has gained increasing popularity in mechanical testing and has become a well-established tool for measuring displacement fields in a wide range of specimens [1,2]. This is partly due to its low-cost and easy-to-use features, as well as the revolution in camera technology when it comes to resolution and recording rates. Also faster computational hardware has made it possible to analyze large series of high-resolution images with reasonable time consumption.

In 1986-89, Sutton et al. [3] and Bruck et al. [4] presented a numerical approach employing Newton-Raphson methods for optimization of two-dimensional displacements in a test specimen. This founded the basis for the subset-based two-dimensional Digital Image Correlation method (2D-DIC) as it is used today. Since then, a wide range of problems has been addressed using the subset-based DIC method in solid mechanics problems measuring two-dimensional displacement and strain fields in a wide range of materials.

In 2006, Besnard et al. [5] proposed a new numerical formulation of the 2D-DIC approach. Here the correlation problem was formulated as a (global) finite-element decomposition of a mesh of Q4 elements. The nodal displacements were optimized, providing a natural interface with finite element modeling of material behavior. Several papers have since then been published where the "finite-element" DIC approach has been further improved and used to study different mechanical problems [6,7]. Zhang et al. [8] emphasized the excellent shape adaptation ability of the "finite-element" DIC, i.e. the mesh can easily be adapted to fit complex specimen geometries. This is also valid when a mesh is fitted to a random crack path, as will be shown in this paper. However, it is reported that elements close to the boundary of the mesh experience larger measurement uncertainties than elements within the mesh [8].

The success of using a global optimization of a mesh of elements depends on the element degrees of freedom and their ability to describe the global displacement field properly. Because of the global formulation of the "finite element" DIC approach, failing to describe the displacement field close to a crack may also degrade the solution in larger parts of the specimen showing continuous displacement fields, and not only the elements directly cut by the crack. A particular benefit of the "finite-element" DIC is the possibility of taking advantage of the many numerical techniques specially designed for the finite element method in the development of the DIC algorithms. Réthoré et al. [9,10] showed how enrichment of

the nodal degrees of freedom, as formulated in the extended finite element method (X-FEM) [11], can be used in DIC to model discontinuous displacement fields in the test specimen. In addition, Réthoré et al. presented an optimization algorithm for the crack shape.

In this study, an in-house DIC code, based on the finite-element formulation of DIC, has been developed and applied to analyze synthetic and experimental image series of specimens with large plastic deformations and a propagating crack. The tests of interest are characterized by a slowly propagating crack (compared to the camera recording rate) and high displacement gradients in the regions close to the crack. A modified Arcan test [12] is used as basis for this study (see **Figure 1**). Synthetic image series, generated by bi-cubic interpolation of displacement maps from finite-element (FE) simulations, have been analyzed in order to study and evaluate the effect of discontinuous displacement fields on the robustness and measurement uncertainty of the DIC analyses.

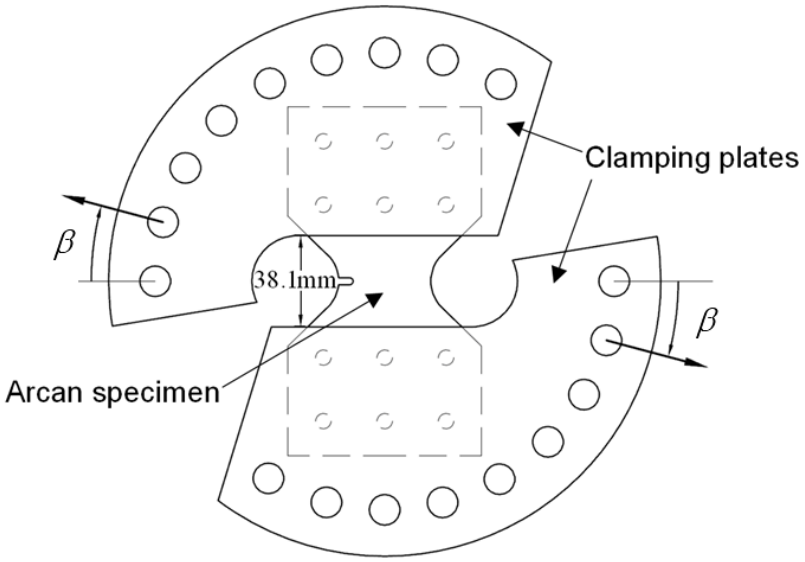

Figure 1. A sketch of the modified Arcan test. The modified Arcan specimen with a notch is shown together with clamping plates. The loading angle β which can be varied is indicated in the sketch.

Two different mesh adaption techniques have been implemented into the DIC code and tested, i.e. node splitting and a novel technique based on overlapping meshes. The techniques require that the crack path is first estimated in an initial analysis. Both techniques are capable of capturing the discontinuous displacement fields caused by propagating cracks. In the node-splitting technique a crack path is part-wise linearized by the element boundaries of the elements close to the crack. This may lead to high correlation residuals and robustness

problems in DIC analyses of specimens with random crack paths. To overcome this problem, a technique based on overlapping meshes was developed. Using this latter technique, a crack-path mask allows the crack path to be defined at pixel level along the crack, regardless of the chosen element size. Further, a crack-path optimization procedure is implemented and tested. Based on analyses of synthetic image series, it is shown that the crack path can be located in the direction normal to the crack with sub-pixel accuracy. The crack-path optimization is shown to reduce correlation residuals and thus giving a better description of the relevant discontinuous displacement field. In addition, a proposed filtering of pixels based on high correlation residuals is found to improve the robustness of the correlation in areas affected by the propagating crack.

2. Digital Image Correlation

In its basic form the 2D-DIC algorithm can be viewed as a "point tracker", i.e. an algorithm that tracks the translation of a specific point on the surface of a plane specimen in a series of images. The translation is found by comparing an image of the specimen at current (deformed) state to an image of the specimen at a reference state. Normally a continuous, homogeneous displacement field is assumed within the measured region. This comparison is traditionally done for a small subset of pixels containing the specific point of interest, and the correlation is found by minimizing a chosen correlation function [1]. The correlation function is based on the differences in grayscale values of the current and the reference image. The optimized parameters are the translation of the point and the parameters defining the deformation of the subset.

Instead of finding the correlation for each point (or subset) individually, the correlation can be carried out globally for a set of nodes contained in a "finite-element" mesh, as presented by Besnard et al. [5]. In this algorithm, the nodal displacements are optimized to minimize the grayscale residuals within the region covered by the mesh. Thus, the continuity of the displacement field within the region of the defined mesh is introduced as an additional constraint in the analysis. The nodal displacements are found by iteratively building and solving a linear system of equations, i.e.

$$\mathbf{Ma} = \mathbf{b} \tag{1}$$

where **a** is a vector containing the unknown incremental nodal displacements. **M** is a matrix and **b** is a vector obtained from the assembly of element contributions ($\mathbf{M}^e$ and $\mathbf{b}^e$) defined as

$$M^e_{\alpha m \beta n} = \sum_{i \in \Omega^e} N_m(\mathbf{X}_i) N_n(\mathbf{X}_i) \frac{\partial f_i}{\partial X_\alpha} \frac{\partial f_i}{\partial X_\beta} \tag{2}$$

$$b^e_{\alpha m} = \sum_{i \in \Omega^e} \left[f(\mathbf{X}_i) - g(\mathbf{x}_i) \right] N_m(\mathbf{X}_i) \frac{\partial f_i}{\partial X_\alpha} \tag{3}$$

where (N_m, N_n) are the shape functions of the particular element e. Ω^e is the pixel region corresponding to the element, and i indicate a particular pixel (in reference configuration). (α, β) identify the coordinate axes (nodal degrees of freedom) while (m, n) identify the internal node number of the element. f and g are the grayscale maps of the reference and current image, and **X** and **x** are the position vectors in the reference and current (deformed) configuration. Bi-cubic interpolation is used to obtain grayscale values from the images (f and g) at sub-pixel locations. The matrix **M** is symmetric and sparse, which is exploited to make the building and solving process efficient.

The matrix **M** and vector **b** in the global equation are assembled by element contributions. If the mesh contains a large number of elements and nodes, the assembly process becomes a computational expensive process. Each column and row of the matrix **M** and each row of the vector **b** correspond to a single node. Because each node may be connected to several elements, and the nodal contribution is calculated as an accumulation of the contribution of its connected elements, the assembly process has to be carried out in a serial fashion. However, by assembling **M** and **b** from nodal contributions the process can be carried out in parallel. The nodal contributions are calculated as a sum of the contributions from the connected elements. The building of the global **M** and **b** becomes

$$M_{\alpha m \beta n} = \sum_{e \in E_{mn}} \sum_{i \in \Omega^e} N^e_m(\mathbf{X}_i) N^e_n(\mathbf{X}_i) \frac{\partial f_i}{\partial X_\alpha} \frac{\partial f_i}{\partial X_\beta} \tag{4}$$

$$b_{m\alpha} = \sum_{e \in E_m} \sum_{i \in \Omega^e} \left[f(\mathbf{X}_i) - g(\mathbf{x}_i) \right] N^e_m(\mathbf{X}_i) \frac{\partial f_i}{\partial X_\alpha} \tag{5}$$

where E_m contains all elements connected to node m while E_{mn} contains all elements connected to both node m and n. It is noted that the indices (m,n) here indicate the global nodes. When the degrees of freedom for each node is equal to two (horizontal and vertical displacement), each node-pair of rows in $\mathbf{M}$ and each node-pair of components in $\mathbf{b}$ are calculated independently. Thus, the calculations are suitable for a parallel implementation. The assembly of nodal contributions was implemented in a parallel code on a two-processor quad-core (Intel Xeon E5430) platform using the OpenMP API [13], enabling eight independent threads. This parallel implementation increased the computation speed, and was approximately five times faster than the serial implementation of the assembly of element contributions, run on the same CPU platform.

A large variety of element types and shape functions N_m may be incorporated into Equations (1) – (5). In this study, isoparametric Q4 elements are applied, where each element is mapped onto a unit square $[0,1]^2$ in a normalized coordinate system (ξ,μ) giving the shape functions $N_1=(1-\xi)(1-\eta)$, $N_2=(1-\xi)\eta$, $N_3=\xi(1-\eta)$ and $N_4=\xi\eta$. This removes the rectangular restriction of the Q4 element such that meshes with any convex quadrilateral element shape can be applied. The displacement $\mathbf{u}(\mathbf{X})$ at a location inside an element is calculated as a weighted sum of the nodal displacement where the weight factor is given by the shape functions N_m.

From the displacement field the desired strain values may be calculated. In this study, an effective strain measure ε_{eff} is calculated for each element in the DIC analysis. The effective strain measure is defined as

$$\varepsilon_{eff}=\sqrt{\frac{2}{3}\left(\varepsilon_1^2+\varepsilon_2^2+\varepsilon_3^2\right)}=\sqrt{\frac{4}{3}\left(\varepsilon_1^2+\varepsilon_1\varepsilon_2+\varepsilon_2^2\right)} \tag{6}$$

where plastic incompressibility and negligible elastic strains have been assumed. It is here assumed that the out-of-plane direction is a principal-strain direction (see [14] for details). Thus, the logarithmic principal strain component in the out-of-plane direction ε_3 is calculated as

$$\varepsilon_3 = -(\varepsilon_1 + \varepsilon_2). \quad (7)$$

where ε_1 and ε_2 are the logarithmic principal strain components measured in the 2D-DIC analysis.

3. Generation of synthetic images

To investigate the performance of different modifications to the DIC algorithm, synthetic image series have been generated. The advantage of using such synthetic image series is that the displacement field is exactly known and can be used as a validation tool for the DIC analysis. In this study, a modified Arcan test [12] is used as basis for the synthetic image series, and a sketch of the test setup is provided in **Figure 1**. The modified Arcan specimen has been modeled and simulated in the commercial FE-code LS-DYNA [15] with a loading angle $\beta = 45°$. The Arcan specimen was modeled using 19424 quadrilateral 2D elements and a simple fracture criterion was applied to model crack initiation and propagation [16]. To provide proper discontinuous displacement fields in the cracked region, an algorithm allowing for node splitting in LS-DYNA was used to model fracture.

Displacement fields based on the nodal displacements were calculated for 450 steps. These displacement fields were further used to generate a corresponding series of 450 images of the modified Arcan specimen during deformation, using bi-cubic interpolation of a speckle pattern recorded from a real mechanical specimen. The spatial pixel resolution of the synthetic images was 2048×2048 at 8-bit digitization. The average element size in the finite element model, corresponding to the relevant spatial image resolution, was about 6×6 pixels. Thus, the FEM elements are significantly smaller than the DIC elements for all of the DIC analyses carried out in this study. An example of a synthetic image and its corresponding effective strain map (from FEM) is shown in **Figure 2**. The synthetic images used in this study were given a normally distributed grayscale pixel noise with standard deviation equal to 3.

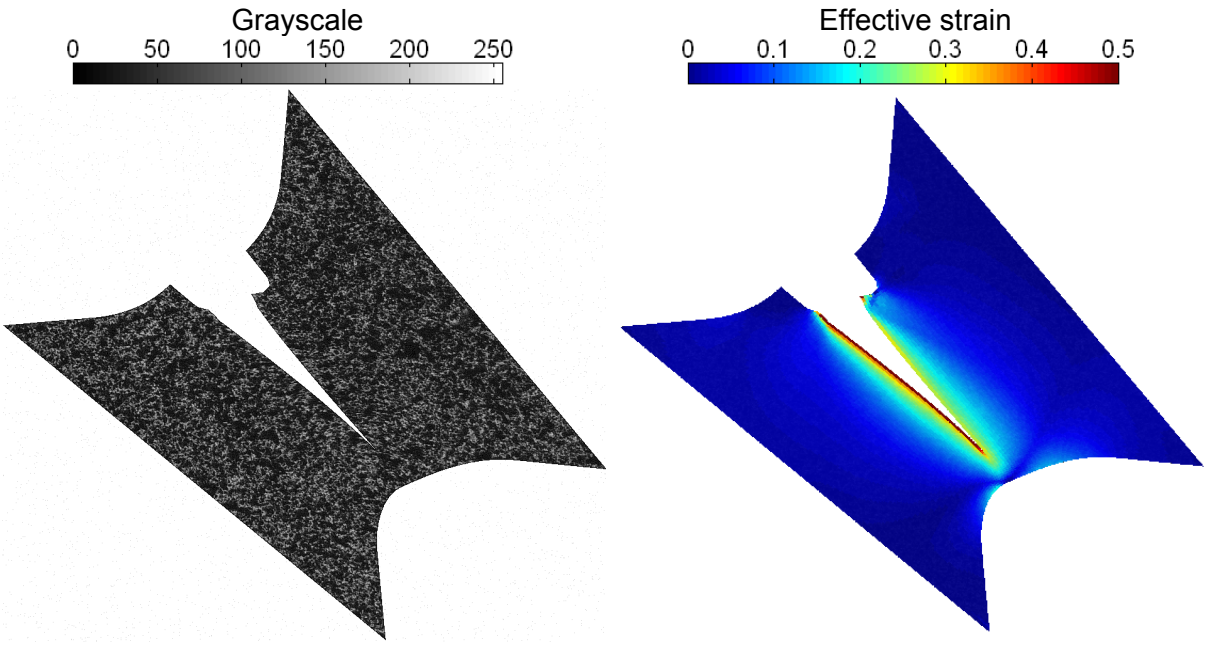

Figure 2. Example of (a) a synthetic image with its (b) corresponding effective strain map. A finite element simulation of a modified Arcan specimen with loading angle $\beta = 45°$ has founded the basis for the synthetic image generation. The synthetic images have spatial resolutions of 2048×2048 and 8-bit digitization.

4. Initial analyses

A study was carried out to investigate the effects of some initial modifications to standard DIC analyses with Q4 elements. The analyses were carried out on the Arcan image series described in Section 3, and deviations between the displacements in the FE simulations and the DIC analyses, i.e. displacement errors, were studied. The displacement errors were calculated in the center of each DIC element as the length of the displacement-error vector.

4.1 Element size

Measurement uncertainties in DIC are dependent on a range of parameters [16-18] and element size is one of the most important parameters in this sense. **Figure 3** shows the results from an element-size sensitivity analysis. Results are collected for images in the synthetic images series, before the crack has started to propagate through the specimen. **Figure 3**(a) shows the displacement errors for an early image where the strain level is low (max effective strain of 0.015). It is assumed that these displacement errors are mainly due to grayscale noise in the image, and displacement errors due to high gradients are negligible. The well-known

effect of increasing uncertainty with decreasing element size in DIC can clearly be seen. Due to the apparent exponential dependence between element size and measurement uncertainty, there seems to exist a lower limit in element size for robust correlation. Also, the higher uncertainties in elements at the boundary of the mesh compared to the rest of the elements are recognized. A possible reason for this is that the continuity preserved by the global mesh helps reducing the effect of grayscale noise on the uncertainty of the DIC measurements.

Figure 3(b) shows the displacement error vs. element size for three different images with different effective strain levels (max effective strain of 0.015, 0.13 and 0.45). As the strain in the specimen increases, the element degrees of freedom become less capable of describing the relevant displacement field, and large elements are more susceptible to this effect than small elements. The displacement continuity preserved by the global mesh may here have a negative effect, as will be shown in Section 5.

When choosing an ideal element size for a specific analysis, a compromise between small elements being more susceptible to pixel noise and large elements being less capable of describing the high gradient displacement fields needs to be addressed.

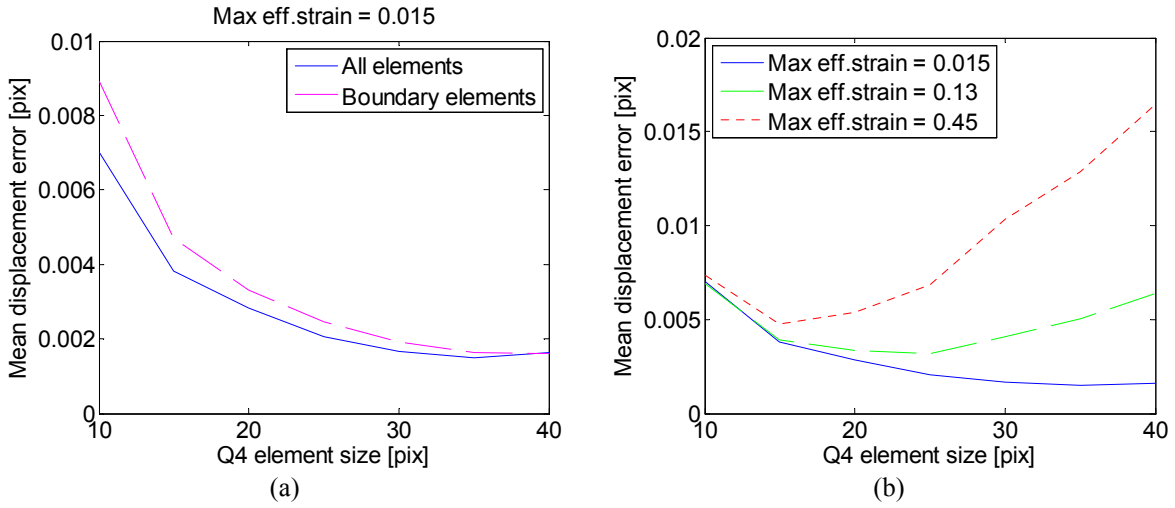

Figure 3. Results from a study on the effect of element size in a standard Q4 element analysis where strictly continuous displacement fields are present. The graph to the left (a) shows a comparison of the mean displacement error in all elements compared to the elements at the boundary of the mesh. The max effective strain in the current image is 0.015. The graph to the right (b) shows a comparison of displacement errors for images with different effective strain levels in the specimen.

4.2 Pixel cutoff

The robustness of a DIC analysis may be compromised by a number of different factors such as large displacement jumps between subsequent images or different artifacts that are introduced during recording of the particular image series like cracks, shadows, etc. Hild et al. [6] presented a technique based on a multi-scale DIC analysis to overcome such degrading factors. In this study, the robustness of the DIC analysis is improved by a certain filtering of poorly correlated pixels. This does not help on large displacement jumps, but may be advantageous when a slowly growing crack is degrading the correlation.

When a crack starts to propagate through the specimen, and if no effort has been made to avoid the cracked region, the measurement errors increase significantly. Because of the global nature of the "finite element"-based DIC approach, the degradation in measurement accuracy affects not only the elements cut by the crack, but a larger part of the mesh. This effect stands in contrast to the subset-based DIC approach where elements (or subsets) are correlated individually. When analyzing image series from mechanical experiments, the location of the crack path (in reference configuration) is in general not known. Thus, it may be of interest to carry out an initial analysis covering the entire specimen surface (including the crack region) to determine the location of the crack path. The crack path is then estimated by manual inspection of e.g. grayscale-residual maps or current grayscale maps g transformed back to reference configuration.

To overcome the problem of miscorrelation in the cracked region, a certain filtering of pixels based on correlation residuals was investigated. The pixels i with correlation residuals $\Phi_i = \sqrt{\left[g(\mathbf{x}_i) - f(\mathbf{X}_i)\right]^2}$ above a specified limit Φ_{cut}, referred to as cutoff pixels, were neglected from the summation in the building of the matrix $\mathbf{M}$ and vector $\mathbf{b}$ in Eq. (1). The cutoff limit Φ_{cut} was defined as

$$\Phi_{cut} = C_{cut}\overline{\Phi} = C_{cut}\frac{1}{P}\sum_{i=1}^{P}\sqrt{\left[g(\mathbf{x}_i) - f(\mathbf{X}_i)\right]^2} \tag{8}$$

where C_{cut} is a user specified value called cutoff multiplier and $\overline{\Phi}$ is the mean grayscale residual in the measured region. P is defined as the number of pixels covered by the mesh used in the analysis. The effect of the pixel-cutoff technique in the DIC analysis is presented

in **Figure 4** for three different pixel-cutoff multipliers: C_{cut} = 1, 3 and 5. The results are compared with one analysis where the cracked elements are removed prior to the correlation and one analysis where no effort has been made to avoid the crack region. Two different image series are analyzed; one where the grayscale value inside the crack region is the average of the speckle pattern, and one where the grayscale value inside the crack region is white and thus significantly different from the speckle pattern. For all analyses, the displacement errors are calculated in the region of the mesh not directly affected by the crack, i.e. the crack elements are removed prior to displacement error calculations. It is appreciated that this particular case, where a crack enters the correlated region, is an extreme case when it comes to miscorrelation.

The results show that the best possible accuracy in the continuous region of the specimen is gained by identifying and removing the crack elements prior to the analysis. It is, however, evident that the pixel-cutoff approach has the potential to reduce the measurement errors (in the continuous part of the specimen) to a minimum when still retaining the crack elements in the global analysis, i.e. the filtering on grayscale residuals helps improving the robustness of the analysis when problem areas are found in the measured region.

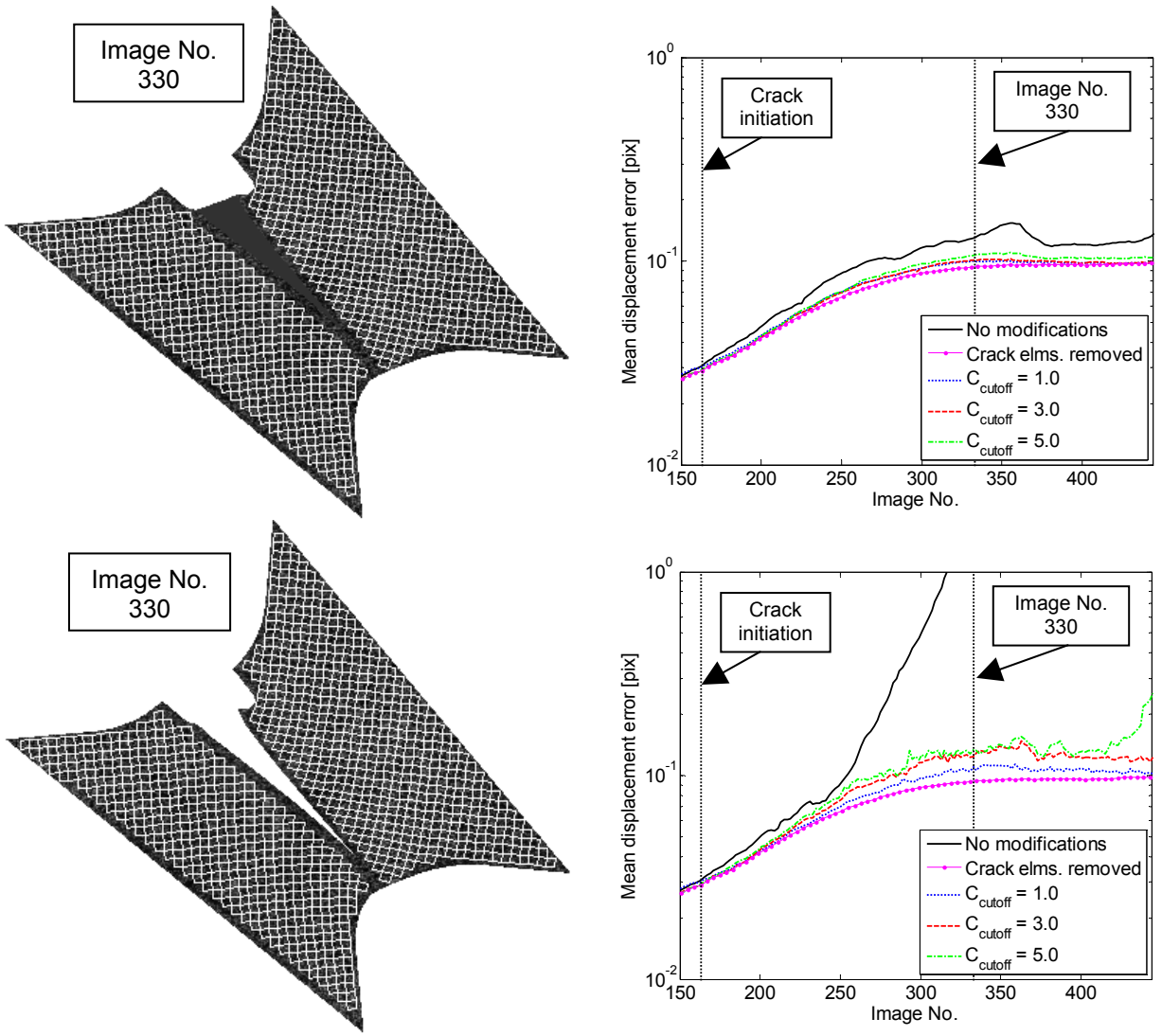

Figure 4. The pixel-cutoff multipliers effect on the robustness of a "finite element" DIC analysis on two different image series, one where the grayscale level inside the crack opening is the mean of the speckle pattern (top-left) and one where it is white (bottom-left). The graphs on the right show the corresponding mean displacement errors for different DIC analyses, one standard Q4 analysis (no modifications), one where the crack elements have been removed prior to the analysis and three analyses with varying cutoff multipliers. For all analyses, the displacement errors are calculated from the region covered by the mesh shown in the images to the left, i.e. the elements directly cut by the crack are removed prior to displacement error calculations.

Some important features about the pixel-cutoff weighting should be noted: 1) The cutoff multiplier C_{cut} should not be chosen too low as it may lead to singularities in the matrix $\mathbf{M}$. This may occur if most pixels in a single element are "weighted out" of the analysis. 2) For cases where a valid correlation is encountered for the entire mesh, the cutoff weighting will have a negative effect because it reduces the number of pixels available in the correlation and

the measurements will be more affected by pixel noise. The effect of the cutoff approach on a continuous displacement field is illustrated in **Figure 5**. It is observed that the reduction in measurement accuracy is highest for small elements, and when the displacement gradients are low and grayscale noise is dominating the measurement uncertainty. When the correlation is compromised by high displacement gradients between the current and reference images, the reduction in accuracy is lowered compared to a standard analysis.

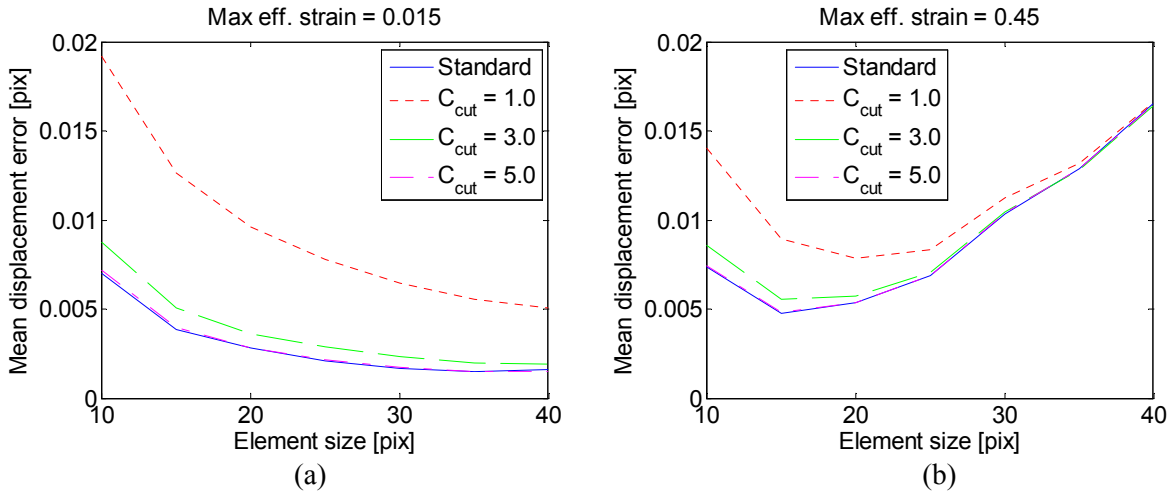

Figure 5. Effect of the cutoff multiplier C_{cut} on the measured displacement uncertainty when a strictly continuous displacement field is present in the measured region. Plots for two different stages (images) are presented; (a) low strains and (b) high strains.

5. Node splitting

The previous section has shown an initial analysis of parameters concerning the measurement uncertainty and robustness of DIC analyses. However, to capture the displacement field in the region of a propagating crack, the degrees of freedom in the DIC mesh have to be modified to allow for discontinuous displacement fields. Réthoré et al. [9] solved this problem by modifying the nodal degrees of freedom and element shape functions to allow for discontinuities, establishing the X-DIC technique. In this study, discontinuous displacement fields are described through mesh adaptation, keeping the shape functions of the isoparametric Q4 elements as presented in Section 2.

Figure 6 illustrates the principle of node splitting in a "finite element"-based DIC approach. The crack path has been identified in an initial analysis, and a mesh with duplicate nodes located along the crack path is generated. The duplicate nodes assure that the

discontinuity in the displacement field across the crack is captured. However, the elements close to the crack are particularly exposed to the most important degradation factors in DIC. For ductile specimens, large displacement errors may be encountered close to the crack path due to high gradients in the displacement field. Further, the elements close to the crack may experience a similar reduced accuracy as shown in **Figure 3** for elements at the boundary of the mesh. In addition, if pixels located in the crack opening region are captured within the elements located along the crack path, further degradation and miscorrelation may be expected. The multi-scale approach, presented by Hild et al. [6], may be used here to increase robustness and avoid miscorrelation in small elements. In this study, the pixel-cutoff technique presented in Section 4.2 is applied, and has proved valuable as long as large displacement jumps between subsequent images are avoided.

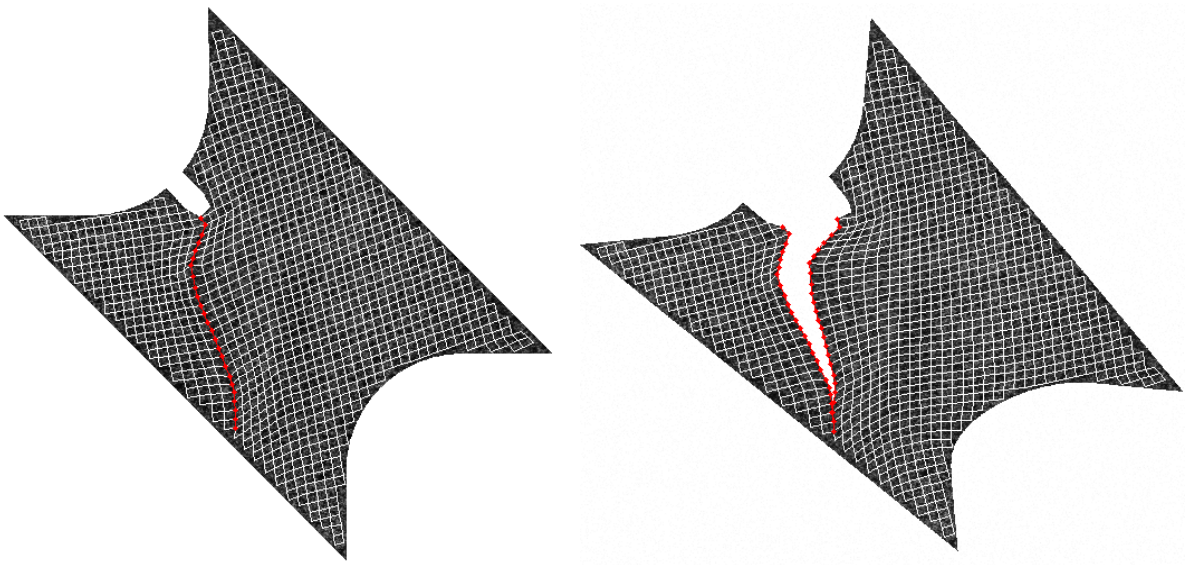

Figure 6. Illustration of the principle of the node splitting technique in DIC. To the left, the node-splitting mesh with duplicate nodes is plotted on top of the initial reference image. The duplicate nodes are located along the crack path and are indicated with red dots. To the right, the mesh is plotted on an image where the crack has propagated a certain distance into the specimen.

Figure 7(a) illustrates an element-size sensitivity analysis using the node-splitting DIC approach. The mean displacement error is plotted as function of normal distance to the crack path when the crack has propagated all the way through the specimen. Displacement errors increase dramatically when moving towards the crack, and this effect increases with increasing element size. **Figure 7**(b) shows that the high displacement errors close to the crack can be slightly reduced by relaxing the continuity criterion of the global mesh, i.e. by treating

the elements in the mesh as individual stand-alone elements. However, the main part of the displacement errors is caused by the element not being able to describe the displacement gradient close to the crack. The study illustrates the difficulties encountered when measuring displacements close to a crack with limited image resolution and high displacement gradients. Small elements are advantageous in such areas, but a decreasing element size makes the results increasingly affected by noise and may cause an unstable correlation (see **Figure 3**).

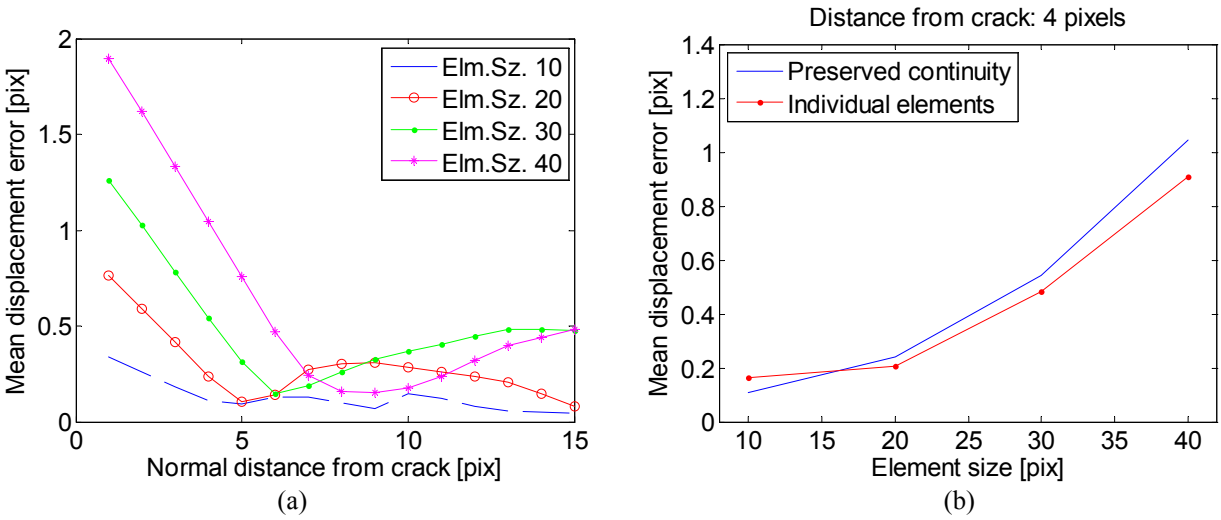

Figure 7. (a) The mean displacement errors for different element sizes in DIC are plotted as function of normal distance to the crack path. The displacement errors is calculated as an average over all elements along the crack. (b) The effect of relaxing the continuity criterion, i.e. treating the elements as individual subsets and not as part of a continuous mesh. The mean displacement error is calculated as an average for all elements along the crack at a 4 pixel normal distance from the crack path.

In **Figure 8** the measured effective strain from DIC analyses with different element sizes is compared to the effective strain in the finite element simulation of the modified Arcan specimen. It is assumed that the effective strain calculated for a single element is valid in the centre of the particular element. In **Figure 8**(a) the effective strain in the elements close to the crack in the DIC analyses is compared to the average effective strain in the FE simulation within the region of the particular DIC element. A similar trend as presented in **Figure 3**(b) for displacement errors vs. element size is obtained for the mean effective strain error, and an ideal element size for minimizing uncertainties in strain calculations seems to exist in this particular configuration. Even if satisfactory uncertainty values in the effective strain is measured in the centers of the elements close to the crack, the high gradients in the displacement and strains fields close to the crack prevents measuring the strains all the way

into the crack path, and the elements along the crack path may observe significant difference in strain levels when element size is varied. In **Figure 8**(b) the effective strains from multiple element sizes in DIC are plotted as function of normal distance to the crack, together with the effective strain from the FE simulation. It is seen that the strain levels in the region close to the crack are successfully measured for all element sizes. However, small element sizes give a better approximation of the strain-field gradient due to higher spatial resolution in the measurements.

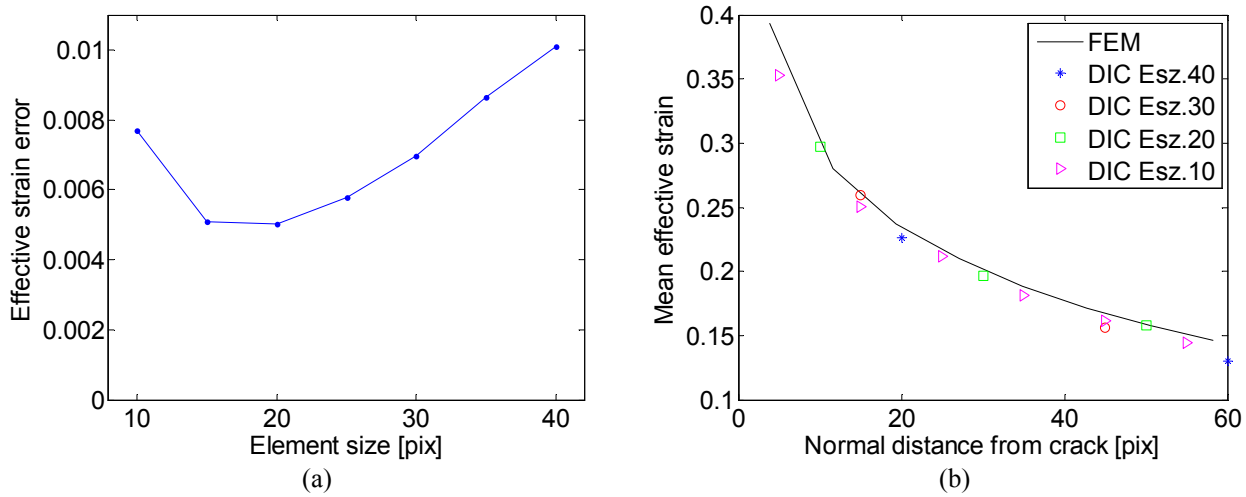

Figure 8. (a) The mean effective strain error for elements close to the crack as function of element size. It is assumed that the calculated effective strain is valid at the center of the particular element. (b) The mean effective strain is plotted as a function of normal distance to the crack path for the FEM analysis as well as node-splitting DIC analyses with varying element sizes.

When using a node-splitting approach in DIC, the crack path is part-wise linearized by the isoparametric Q4 elements connected to the duplicate nodes. A real crack in a mechanical experiment may however have random aberrations that will not be captured in a DIC analysis with node splitting. This may easily lead to degradation of the correlation if pixels inside the crack opening region are caught inside elements close to the crack. In this study, the pixel cutoff-factor introduced in Section 4.2 is applied to neglect pixels i with high correlation residuals $\Phi(\mathbf{X}_i) > \Phi_{cut}$ increasing the robustness of the node-splitting DIC analysis. In the following section, a novel mesh adaptation technique is presented, which lets the crack path be defined at pixel level regardless of the chosen element size.

6. Overlapped mesh with crack-path mask

A modification to the node-splitting technique, where the crack path may be defined at pixel level in the DIC analysis while the elements are kept at the desired size, is introduced. This technique is based on extending the elements containing the duplicate nodes across the crack as seen in **Figure 9**. Thus, the two parts (1 and 2) of the mesh are overlapping in a region covering the crack. A mask is then defined (in reference configuration) from a crack path which may be defined at pixel level, dividing the measured region in part 1 and 2. The pixels located within mesh part 1, but outside the masked region of part 1, are neglected in the DIC analysis. The same yields for part 2. In this paper, problems with a single growing crack are studied. However, the overlapped-mesh technique may be extended to problems concerning multiple cracks.

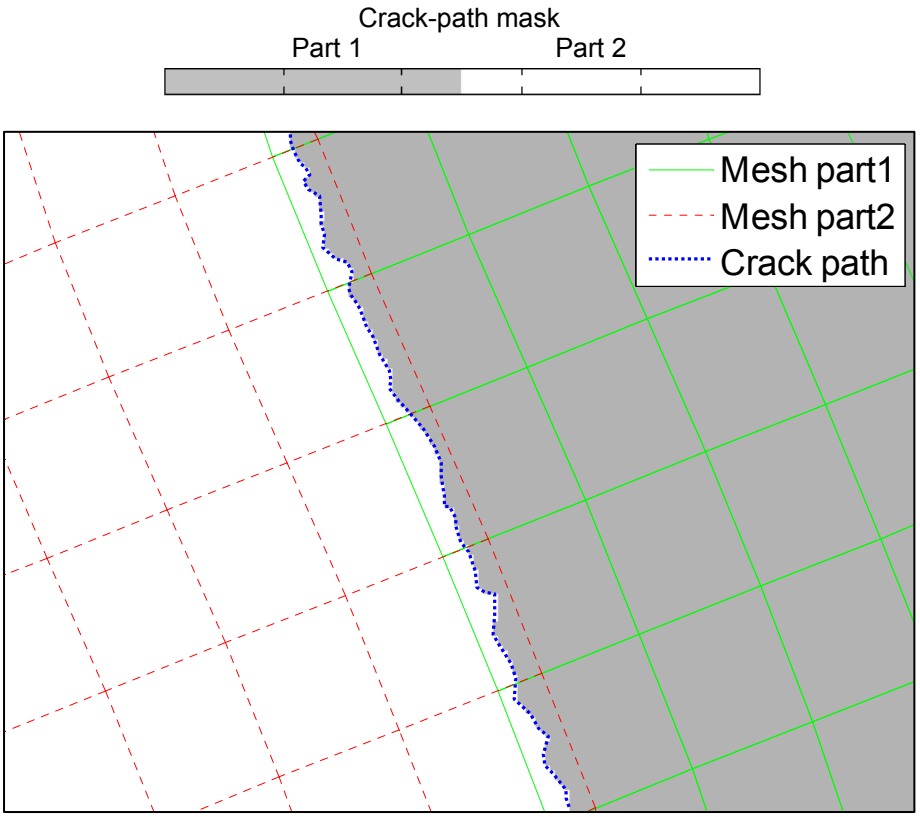

Figure 9. Principle of overlapped mesh with crack-path mask. The image shows the part mask (in reference configuration) defined by the location of the crack path (indicated in blue) and the overlapped mesh. The pixels located within mesh part 1, but outside the defined region of part 1 in the mask, are neglected in the correlation. The same yields for part 2. The crack path (and thus the part mask), is not restricted to the same part-wise linearization as the element boundaries and may be defined at pixel level.

To study the efficiency of the overlapping mesh technique a synthetic image series, with discontinuous rigid body translation and a random crack path, is analyzed. The images have 512×512 spatial resolution, 8-bit digitization and normally distributed grayscale noise with a standard deviation of 3. Examples of the images are presented in **Figure 10**.

The image series is generated from a speckle pattern of a real mechanical specimen and the displacement jump increment between subsequent images is 0.1 pixels. Bi-cubic interpolation is used to interpolate grayscale values. **Figure 11** illustrates a comparison between analyses of the "discontinuous rigid body translation" image series using standard Q4 elements, node splitting and overlapped mesh. For the node-splitting and overlapped-mesh analyses, it is assumed that the crack path is exactly known. The displacement jump for the current image is 1.7 pixels. Clearly, the analysis using Q4 elements is not able to capture the discontinuous displacement field and the displacements are averaged within the elements containing the crack. The node-splitting analysis captures the discontinuous displacement field. However, the crack is part-wise linearized and so is also the shape of the displacement field along the crack path. The overlapped-mesh analysis is however able to describe a random crack path down to pixel level and the mean correlation residual $\overline{\Phi}$ is reduced compared to the node-splitting analysis. Also, the mean displacement error $\overline{E}$ in the measured region is reduced compared to the node-splitting analysis.

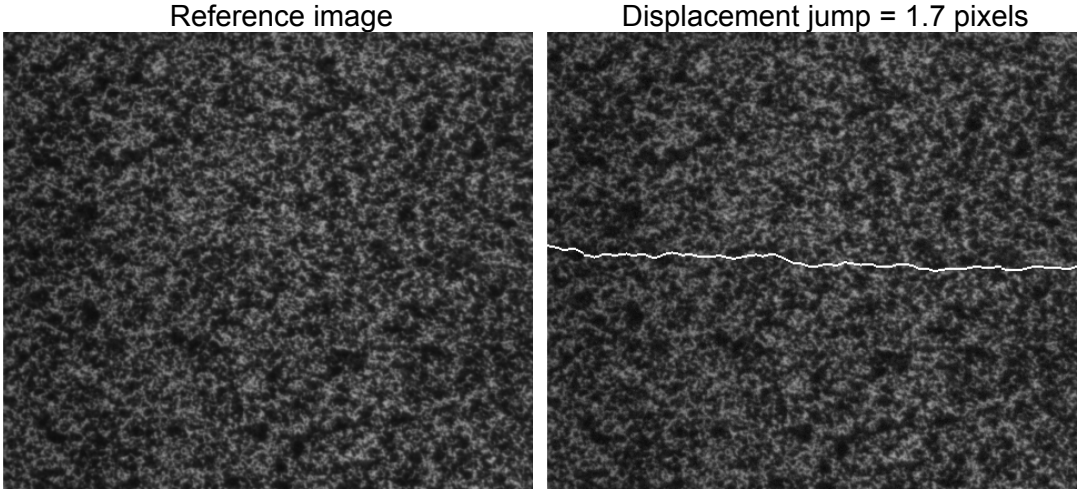

Figure 10. Discontinuous rigid body translation with a random crack path. The images have a spatial resolution of 512×512 at 8-bit digitization. The incremental vertical displacement jump between subsequent images is 0.1 pixels.

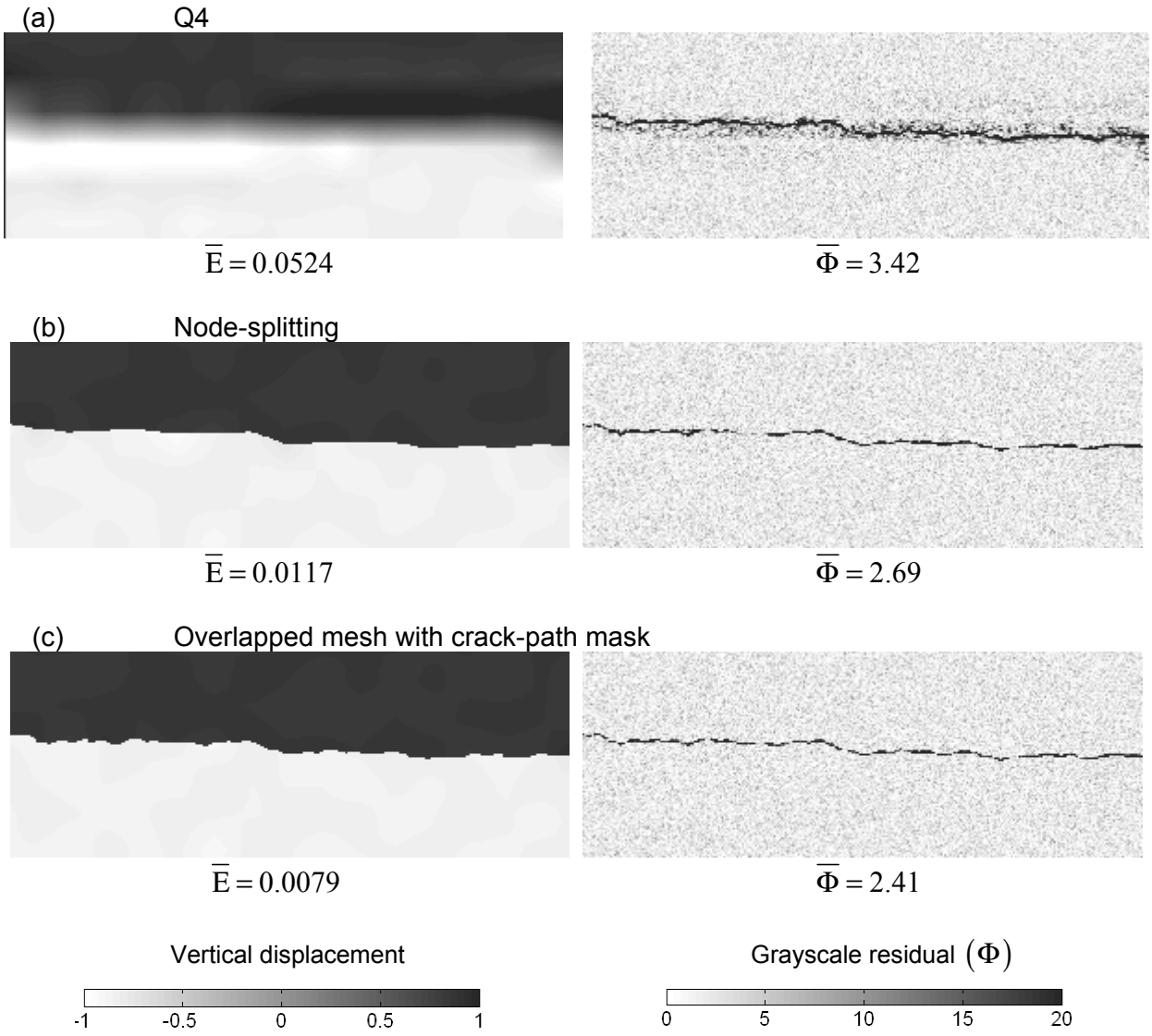

Figure 11. Vertical displacement (left) and grayscale residuals Φ (right) from three different analyses of the same synthetic image series with discontinuous rigid body translation and a random crack path: (a) standard Q4 elements, (b) node-splitting and (c) overlapped mesh with crack-path mask. The displacement jump at this particular image is 1.7 pixels. The mean displacement error $\bar{E}$ and the mean grayscale residual for the measured region $\bar{\Phi}$ is indicated for each analysis.

6.1 Crack-path optimization

The success of the overlapping-mesh technique is dependent on a good approximation of the crack path location in the reference configuration. From initial DIC analyses the crack path may be found by studying e.g. grayscale residual maps or the deformed image

transformed back to reference configuration. However, this initial approximation of the crack path may still have deviations from the real crack path that cause miscorrelation and increased grayscale residuals close to the crack. To overcome this problem, a crack-path optimization procedure, similar to the procedure presented by Réthoré et al. [9] for the X-DIC technique, is applied. **Figure 12** illustrates the principle of the crack-path optimization applied in this study.

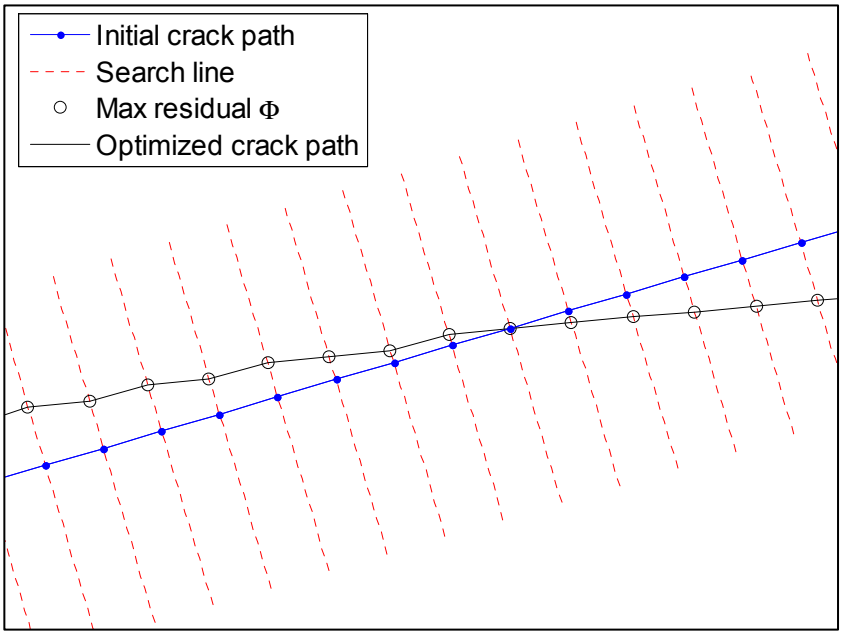

Figure 12. The principle of crack-path optimization. The initial crack path is defined with 1.0-pixel increments in the reference configuration. The grayscale residuals are calculated along a search line perpendicular to the initial crack path, and the crack path is then moved to the position of maximum grayscale residuals Φ_{max}.

The crack path is initially defined by nodes with 1-pixel increments. For each image that is correlated, the grayscale residuals are calculated along the normal vectors of the crack path, for each crack-path node. A suitable length of this search line is chosen, preferable a length similar to the assumed maximum deviation between the exact crack path and the initial guess of the crack path. In this study, the search length is set to 3 pixels, and the residuals were calculated with 0.1 pixel increments along the search line. The crack-path nodes are then moved to the location of the highest residual along their corresponding search lines. **Figure 13** shows the resulting grayscale maps from two analyses, i.e. with and without crack-path optimization, of the discontinuous rigid body translation image series shown in **Figure 10**.

A fairly rough initial estimate of the crack path is used. Applying the crack-path optimization the mean grayscale residual $\overline{\Phi}$ is reduced from 3.29 to 2.66, and the mean

deviation between the measured and the exact crack path is reduced from 1.6 to 0.2 pixels, compared to an analysis without optimization.

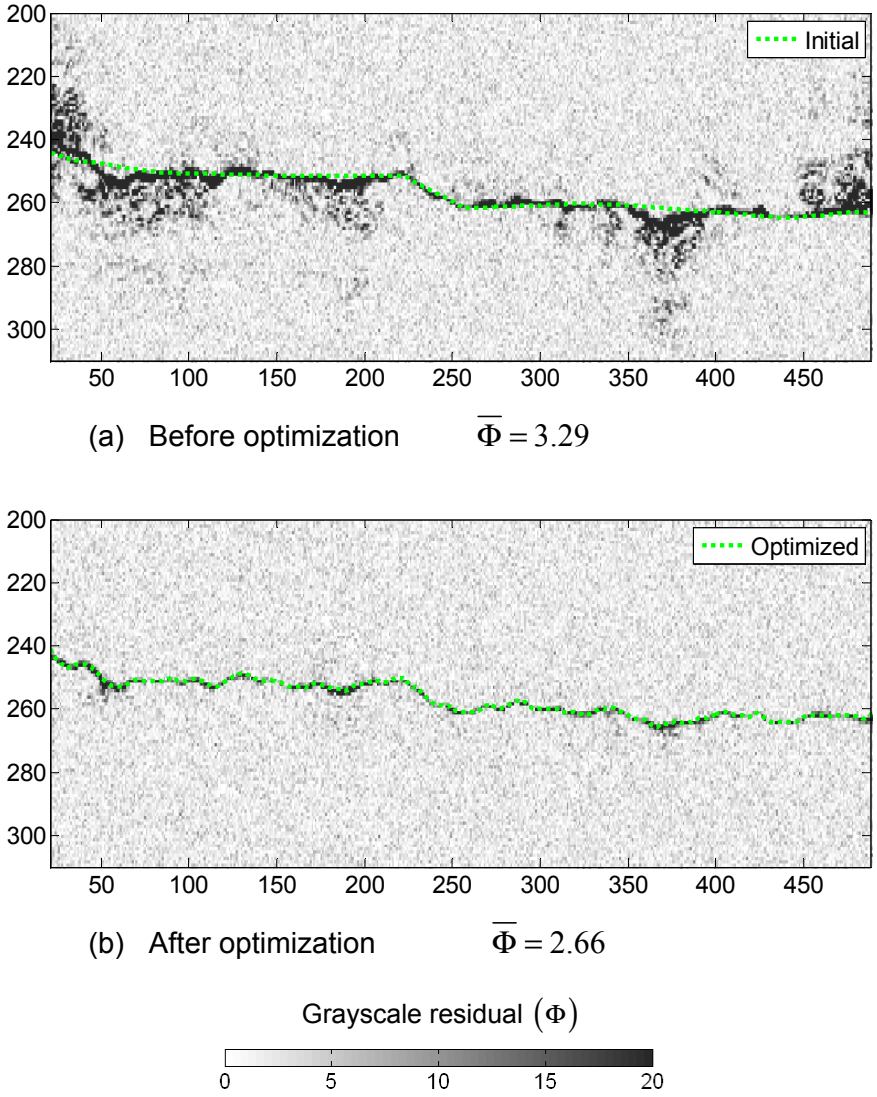

Figure 13. Crack-path optimization: Grayscale residual maps Φ (a) before and (b) after crack-path optimization. The initial guess and the optimized crack path are plotted on top of their respective residual maps. The displacement jump at this particular image is 1.7 pixels.

When ductile crack growth is present, the crack-path optimization becomes more difficult because the grayscale residuals Φ are not only caused by random grayscale noise and a discontinuous displacement field. Increased residuals are also caused by high displacement gradients close to the crack, which the elements are not able to describe properly (see **Figure 7**). Keeping control of the grayscale residuals by updating the reference image, i.e. the grayscale map f in Eq. (3), is of vital importance for a proper crack-path optimization.

Also, the crack-path optimization must be restricted to only be applied where a discontinuous field is actually present. A suitable lower limit of the crack opening has to be applied to assure that the crack-path optimization is not carried out when and where the displacement field is continuous. Thus, only the part of the crack path with a crack opening larger than this limit is optimized. A crack opening limit of 1.0 pixel was found to be suitable in the image series analyzed in this study. The synthetic Arcan image series presented in Section 3 is used to study the crack-path optimization for such cases of ductile crack growth. The exactly known crack path (from the finite element model) was given a sinus variation along its length and used as an initial guess of the crack path in the DIC analysis. The sinus variation had four cycles along the crack length and amplitude of 3.5 pixels, giving a mean location error of 2.22 pixels. If any part of the crack length was moved outside the overlapped region of the mesh during the optimization, the particular part of the crack length was moved back to its initial guess. **Figure 14** shows the resulting grayscale residual maps with and without crack-path optimization. The results are collected from an image where the crack has propagated all the way through the specimen. The mean deviation between the exact and the optimized crack path is reduced from 2.22 to 0.79 pixels and the mean grayscale residual $\overline{\Phi}$ is reduced from 4.44 to 3.64. The results show that the presented crack-path optimization also works well when ductile crack growth is present. The deviations in the optimized crack path compared to the exact crack path are mainly high frequency deviations. By applying a low-pass filter on the crack path location in the spatial domain, the deviation compared to the exact crack path is further reduced to 0.36 pixels.

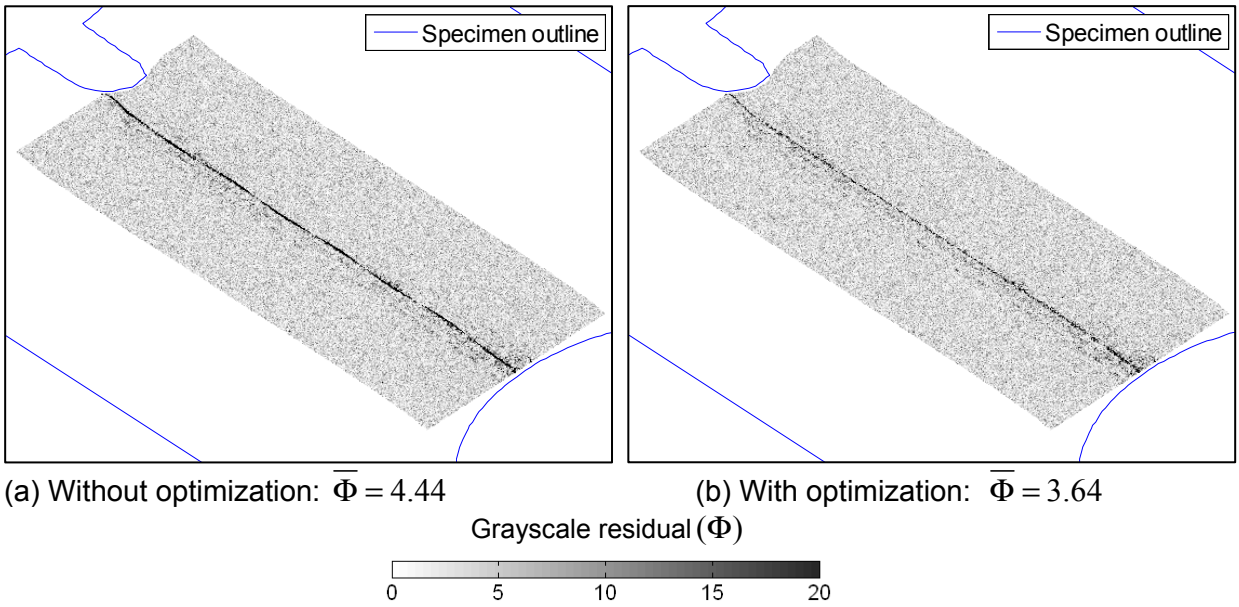

Figure 14. Results from DIC analyses of the synthetic Arcan image series (a) without and (b) with crack-path optimization. Grayscale residual maps are shown for an image where the crack has propagated through the specimen. The outline of the specimen is plotted on top of the maps. The mean residual $\bar{\Phi}$ is reduced from 4.44 to 3.64 by using the crack-path optimization.

6.2 Results from an experimental modified Arcan series

The overlapping mesh technique with crack-path optimization was tested on an image series of a mechanical experiment, i.e. a modified Arcan test with loading angle $\beta = 45°$ [16]. **Figure 15** shows a selected region of a recorded image containing a propagating crack. The crack surfaces, measured in DIC with and without crack-path optimization, are plotted on top of the image. Further, the corresponding grayscale residual maps Φ are illustrated in **Figure 16**. By using the crack-path optimization, the mean residuals $\overline{\Phi}$ have decreased from 3.57 to 3.15, indicating a more valid correlation. Also here, high-frequency fluctuations of the optimized crack path are observed. To reduce these fluctuations, a proper filtering in the time domain may be applied. However, this was not tested in this study.

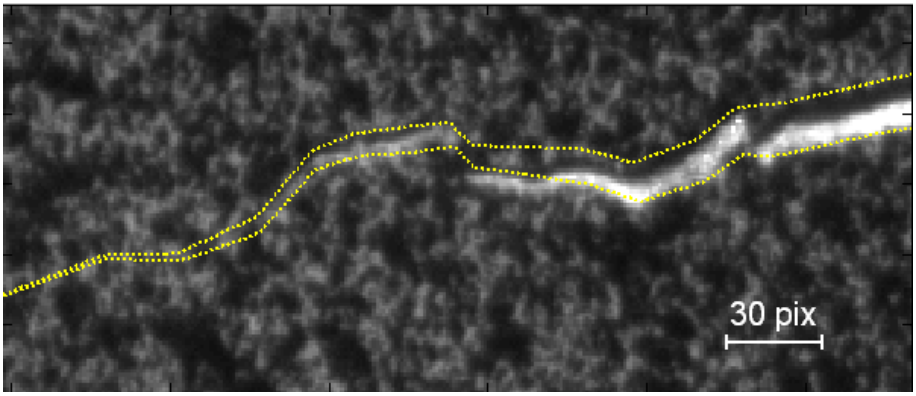

(a) Without optimization

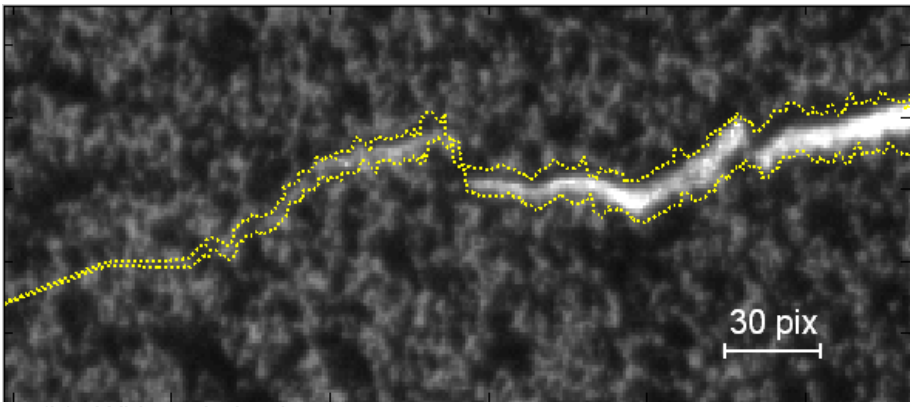

(b) With optimization

Figure 15. A selected region of an image from an experimental Arcan test image series where the crack has started to propagate through the specimen. The crack boundaries are plotted for analyses without (a) and with (b) crack-path optimization on top of the current image. The element size used in the DIC analyses (30 pixels) is indicated in the figure.

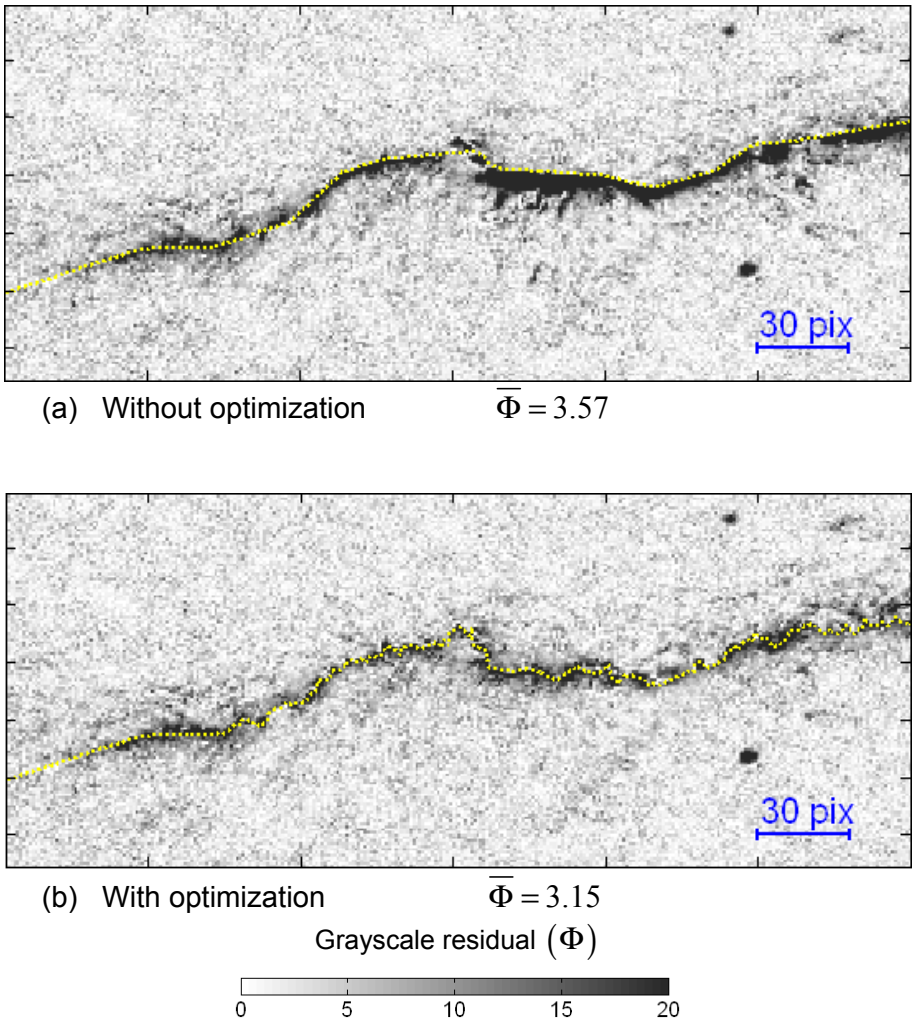

Figure 16. Grayscale residual maps (in reference configuration) from DIC analyses without (a) and with (b) crack-path optimization from a mechanical experiment of a modified Arcan specimen. The selected region corresponds to the images shown in **Figure 15**. The crack paths are plotted on top of the residual maps. The element size (30 pixels) is indicated in the figure.

7. Concluding remarks

This study has presented two different mesh adaptation techniques suitable to capture discontinuous displacement fields in a "finite element"-based DIC analysis, i.e. node splitting and a novel approach based on overlapped mesh. In the node-splitting approach, the crack path is piecewise linearized by the element boundaries, while in the overlapping mesh technique the crack path may be defined down to pixel level regardless of the chosen element size. The presented techniques have been implemented into an in-house DIC code and analyses have been carried out on both synthetic and experimental image series in order to evaluate the efficiency and accuracy of the presented approaches.

Both the node-splitting and the overlapping-mesh techniques have proven to perform well on image series with a single propagating crack. However, significant measurement uncertainties in displacements and strains close to the crack may be encountered if a combination of limited image resolution and high displacement gradients is present. Combining full-field measurements of the entire specimen with quantitative measurements of displacements and strains close to the crack path may be difficult or impractical with the particular image resolution used in this study (2048×2048 at 8-bit digitization).

It is found that the continuity criterion of the global mesh in the "finite element"-based DIC seems to have a positive effect when the measurement accuracy is challenged by grayscale noise, but may have a slightly negative effect when the correlation is compromised by high displacement gradients.

To increase robustness of the DIC analysis, a pixel-cutoff approach has been introduced, where poorly correlated pixels are filtered out of the analysis. The cutoff parameter has proven to sustain a robust correlation even for cases where a crack is propagating through the measured region. When using node-splitting in a DIC analysis, pixels inside the crack opening region of the current image may be captured by elements close to the crack, and thus degrade the correlation. In such cases, the pixel-cutoff procedure has also proved valuable.

Further, a crack-path optimization procedure is presented and evaluated. The crack-path optimization has shown to be able to locate the crack path with sub-pixel accuracy. Also, the crack-path optimization has proven to increase the robustness of the DIC analysis by reducing high grayscale residuals caused by the discontinuous displacement field.

Acknowledgement

The financial support of this work from the Structural Impact Laboratory (SIMLab), Centre for Research-based Innovation (CRI) at the Norwegian University of Science and Technology (NTNU), is gratefully acknowledged.

References

[1] M.A. Sutton, S.R. McNeill, J.D. Helm, Y.I. Chao, Advances in two-dimensional and three-dimensional computer vision, Topics Appl. Phys. 77 (2000) 323-372.

[2] B. Pan, K. Qian, H. Xie, A. Asundi, Two-dimensional digital image correlation for in-plane displacement and strain measurements: a review, Meas. Sci. Technol. 20 (2009) 062001.

[3] M.A. Sutton, M. Cheng, W.H. Peters, Y.J. Chao, S.R. McNeill, Application of an optimized digital correlation method to planar deformation analysis, Image Vis. Comput. 4 (1986) 143-150.

[4] H.A. Bruck, S.R. McNeill, M.A. Sutton, W.H. Peters III, Digital image correlation using Newton-Raphson method of partial differential correction, Exp. Mech. 29 (1989) 261-267.

[5] G. Besnard, F. Hild, S. Roux, 'Finite-element' displacement fields analysis from digital images: application to Portevin-le Châtelier bands, Exp. Mech. 46 (2006) 789-804.

[6] F. Hild, B. Raka, M. Baudequin, S. Roux, F. Cantelaube, Multiscale displacement field measurements of compressed mineral wool samples by digital image correlation, Appl. Opt. 41 (2002) 6815-6828.

[7] A. Benallal, T. Berstad, T. Børvik, O.S. Hopperstad, I. Koutin, R. Nogeira de Codes, An experimental and numerical investigation of the behaviour of AA5083 aluminium alloy in presence of the Portevin-Le Chatelier effect, Int. J. Plasticity 24 (2008) 1916-1945.

[8] J Zhang, Y. Cai, W. Ye, T.X. Yu, On the use of the digital image correlation for heterogeneous deformation measurements of porous solids, Opt. Laser Eng. 49 (2010) 200-209.

[9] J. Réthoré, F. Hild, S. Roux, Extended digital image correlation with crack shape optimization, Int. J. Numer. Meth. Engng. 73 (2007) 248-272.

[10] J. Réthoré, F. Hild, S. Roux, Shear-band capturing using a multiscale extended digital image correlation technique, Comput. Methods Appl. Mech. Engng. 196 (2007) 5016-5030.

[11] T. Belytschko, N. Moës, S. Usui, C. Parimi, Arbitrary discontinuities in finite elements, Int. J. Numer. Meth. Engng. 50 (2001) 993-1013.

[12] M. Arcan, Z. Hashin, A. Voloshin, A method to produce uniform plane stress states with applications to fibre-reinforced materials, Exp. Mech. 18 (1978) 141-146.

[13] http://openmp.org/wp/ [Cited: 15.11.2011].

[14] Kajberg J, Lindkvist G. Characterisation of materials subjected to large strains by inverse modeling based on in-plane displacement fields. Int J Solids Struct 2004 41:3439-3459.

[15] LSTC, LS-DYNA keyword user's manual, version 971. (2007) Livermore Software Technology Corporation.

[16] E. Fagerholt, C. Dørum, T. Børvik, H.I. Laukli, O.S. Hopperstad, Experimental and numerical investigation of fracture in a cast aluminium alloy, Int. J. Solids Struct. 47 (2010) 3352-3365.

[17] K. Triconnet, K. Derrien, F. Hild, D. Baptiste, Parameter choice for optimized digital image correlation, Opt. Laser Eng. 47 (2008) 728-737.

[18] B. Pan, H. Xie, Z. Wang, K. Qian, Z. Wang, Study on subset size selection in digital image correlation for speckle patterns, Opt. Express 16 (2008) 7037-7048.

[19] M. Fazzini, S. Mistou, O. Dalverny, L. Robert, Study of image characteristics on digital image correlation error assessment, Opt. Laser Eng. 48 (2010) 335-339.

DEPARTMENT OF STRUCTURAL ENGINEERING
NORWEGIAN UNIVERSITY OF SCIENCE AND TECHNOLOGY

N–7491 TRONDHEIM, NORWAY
Telephone: +47 73 59 47 00 Telefax: +47 73 59 47 01

"Reliability Analysis of Structural Systems using Nonlinear Finite Element Methods",
C. A. Holm, 1990:23, ISBN 82-7119-178-0.

"Uniform Stratified Flow Interaction with a Submerged Horizontal Cylinder",
Ø. Arntsen, 1990:32, ISBN 82-7119-188-8.

"Large Displacement Analysis of Flexible and Rigid Systems Considering Displacement-Dependent Loads and Nonlinear Constraints",
K. M. Mathisen, 1990:33, ISBN 82-7119-189-6.

"Solid Mechanics and Material Models including Large Deformations",
E. Levold, 1990:56, ISBN 82-7119-214-0, ISSN 0802-3271.

"Inelastic Deformation Capacity of Flexurally-Loaded Aluminium Alloy Structures",
T. Welo, 1990:62, ISBN 82-7119-220-5, ISSN 0802-3271.

"Visualization of Results from Mechanical Engineering Analysis",
K. Aamnes, 1990:63, ISBN 82-7119-221-3, ISSN 0802-3271.

"Object-Oriented Product Modeling for Structural Design",
S. I. Dale, 1991:6, ISBN 82-7119-258-2, ISSN 0802-3271.

"Parallel Techniques for Solving Finite Element Problems on Transputer Networks",
T. H. Hansen, 1991:19, ISBN 82-7119-273-6, ISSN 0802-3271.

"Statistical Description and Estimation of Ocean Drift Ice Environments",
R. Korsnes, 1991:24, ISBN 82-7119-278-7, ISSN 0802-3271.

“Properties of concrete related to fatigue damage: with emphasis on high strength concrete”,
G. Petkovic, 1991:35, ISBN 82-7119-290-6, ISSN 0802-3271.

"Turbidity Current Modelling",
B. Brørs, 1991:38, ISBN 82-7119-293-0, ISSN 0802-3271.

"Zero-Slump Concrete: Rheology, Degree of Compaction and Strength. Effects of Fillers as Part Cement-Replacement",
C. Sørensen, 1992:8, ISBN 82-7119-357-0, ISSN 0802-3271.

"Nonlinear Analysis of Reinforced Concrete Structures Exposed to Transient Loading",
K. V. Høiseth, 1992:15, ISBN 82-7119-364-3, ISSN 0802-3271.

"Finite Element Formulations and Solution Algorithms for Buckling and Collapse Analysis of Thin Shells",
R. O. Bjærum, 1992:30, ISBN 82-7119-380-5, ISSN 0802-3271.

"Response Statistics of Nonlinear Dynamic Systems",
J. M. Johnsen, 1992:42, ISBN 82-7119-393-7, ISSN 0802-3271.

"Digital Models in Engineering. A Study on why and how engineers build and operate digital models for decisison support",
J. Høyte, 1992:75, ISBN 82-7119-429-1, ISSN 0802-3271.

"Sparse Solution of Finite Element Equations",
A. C. Damhaug, 1992:76, ISBN 82-7119-430-5, ISSN 0802-3271.

"Some Aspects of Floating Ice Related to Sea Surface Operations in the Barents Sea",
S. Løset, 1992:95, ISBN 82-7119-452-6, ISSN 0802-3271.

"Modelling of Cyclic Plasticity with Application to Steel and Aluminium Structures",
O. S. Hopperstad, 1993:7, ISBN 82-7119-461-5, ISSN 0802-3271.

"The Free Formulation: Linear Theory and Extensions with Applications to Tetrahedral Elements with Rotational Freedoms",
G. Skeie, 1993:17, ISBN 82-7119-472-0, ISSN 0802-3271.

"Høyfast betongs motstand mot piggdekkslitasje. Analyse av resultater fra prøving i Veisliter'n",
T. Tveter, 1993:62, ISBN 82-7119-522-0, ISSN 0802-3271.

"A Nonlinear Finite Element Based on Free Formulation Theory for Analysis of Sandwich Structures",
O. Aamlid, 1993:72, ISBN 82-7119-534-4, ISSN 0802-3271.

"The Effect of Curing Temperature and Silica Fume on Chloride Migration and Pore Structure of High Strength Concrete",
C. J. Hauck, 1993:90, ISBN 82-7119-553-0, ISSN 0802-3271.

"Failure of Concrete under Compressive Strain Gradients",
G. Markeset, 1993:110, ISBN 82-7119-575-1, ISSN 0802-3271.

"An experimental study of internal tidal amphidromes in Vestfjorden",
J. H. Nilsen, 1994:39, ISBN 82-7119-640-5, ISSN 0802-3271.

"Structural analysis of oil wells with emphasis on conductor design",
H. Larsen, 1994:46, ISBN 82-7119-648-0, ISSN 0802-3271.

"Adaptive methods for non-linear finite element analysis of shell structures",
K. M. Okstad, 1994:66, ISBN 82-7119-670-7, ISSN 0802-3271.

"On constitutive modelling in nonlinear analysis of concrete structures",
O. Fyrileiv, 1994:115, ISBN 82-7119-725-8, ISSN 0802-3271.

"Fluctuating wind load and response of a line-like engineering structure with emphasis on motion-induced wind forces",
J. Bogunovic Jakobsen, 1995:62, ISBN 82-7119-809-2, ISSN 0802-3271.

"An experimental study of beam-columns subjected to combined torsion, bending and axial actions",
A. Aalberg, 1995:66, ISBN 82-7119-813-0, ISSN 0802-3271.

"Scaling and cracking in unsealed freeze/thaw testing of Portland cement and silica fume concretes",
S. Jacobsen, 1995:101, ISBN 82-7119-851-3, ISSN 0802-3271.

"Damping of water waves by submerged vegetation. A case study of laminaria hyperborea",
A. M. Dubi, 1995:108, ISBN 82-7119-859-9, ISSN 0802-3271.

"The dynamics of a slope current in the Barents Sea",
Sheng Li, 1995:109, ISBN 82-7119-860-2, ISSN 0802-3271.

"Modellering av delmaterialenes betydning for betongens konsistens",
Ernst Mørtsell, 1996:12, ISBN 82-7119-894-7, ISSN 0802-3271.

"Bending of thin-walled aluminium extrusions",
Birgit Søvik Opheim, 1996:60, ISBN 82-7119-947-1, ISSN 0802-3271.

"Material modelling of aluminium for crashworthiness analysis",
Torodd Berstad, 1996:89, ISBN 82-7119-980-3, ISSN 0802-3271.

"Estimation of structural parameters from response measurements on submerged floating tunnels",
Rolf Magne Larssen, 1996:119, ISBN 82-471-0014-2, ISSN 0802-3271.

“Numerical modelling of plain and reinforced concrete by damage mechanics”,
Mario A. Polanco-Loria, 1997:20, ISBN 82-471-0049-5, ISSN 0802-3271.

“Nonlinear random vibrations - numerical analysis by path integration methods”,
Vibeke Moe, 1997:26, ISBN 82-471-0056-8, ISSN 0802-3271.

“Numerical prediction of vortex-induced vibration by the finite element method”,
Joar Martin Dalheim, 1997:63, ISBN 82-471-0096-7, ISSN 0802-3271.

“Time domain calculations of buffeting response for wind sensitive structures”,
Ketil Aas-Jakobsen, 1997:148, ISBN 82-471-0189-0, ISSN 0802-3271.

"A numerical study of flow about fixed and flexibly mounted circular cylinders",
Trond Stokka Meling, 1998:48, ISBN 82-471-0244-7, ISSN 0802-3271.

“Estimation of chloride penetration into concrete bridges in coastal areas”,
Per Egil Steen, 1998:89, ISBN 82-471-0290-0, ISSN 0802-3271.

“Stress-resultant material models for reinforced concrete plates and shells”,
Jan Arve Øverli, 1998:95, ISBN 82-471-0297-8, ISSN 0802-3271.

“Chloride binding in concrete. Effect of surrounding environment and concrete composition”,
Claus Kenneth Larsen, 1998:101, ISBN 82-471-0337-0, ISSN 0802-3271.

“Rotational capacity of aluminium alloy beams”,
Lars A. Moen, 1999:1, ISBN 82-471-0365-6, ISSN 0802-3271.

“Stretch Bending of Aluminium Extrusions”,
Arild H. Clausen, 1999:29, ISBN 82-471-0396-6, ISSN 0802-3271.

“Aluminium and Steel Beams under Concentrated Loading”,
Tore Tryland, 1999:30, ISBN 82-471-0397-4, ISSN 0802-3271.

"Engineering Models of Elastoplasticity and Fracture for Aluminium Alloys",
Odd-Geir Lademo, 1999:39, ISBN 82-471-0406-7, ISSN 0802-3271.

"Kapasitet og duktilitet av dybelforbindelser i trekonstruksjoner",
Jan Siem, 1999:46, ISBN 82-471-0414-8, ISSN 0802-3271.

“Etablering av distribuert ingeniørarbeid; Teknologiske og organisatoriske erfaringer fra en norsk ingeniørbedrift”,
Lars Line, 1999:52, ISBN 82-471-0420-2, ISSN 0802-3271.

“Estimation of Earthquake-Induced Response”,
Símon Ólafsson, 1999:73, ISBN 82-471-0443-1, ISSN 0802-3271.

“Coastal Concrete Bridges: Moisture State, Chloride Permeability and Aging Effects”
Ragnhild Holen Relling, 1999:74, ISBN 82-471-0445-8, ISSN 0802-3271.

”Capacity Assessment of Titanium Pipes Subjected to Bending and External Pressure”,
Arve Bjørset, 1999:100, ISBN 82-471-0473-3, ISSN 0802-3271.

“Validation of Numerical Collapse Behaviour of Thin-Walled Corrugated Panels”,
Håvar Ilstad, 1999:101, ISBN 82-471-0474-1, ISSN 0802-3271.

“Strength and Ductility of Welded Structures in Aluminium Alloys”,
Miroslaw Matusiak, 1999:113, ISBN 82-471-0487-3, ISSN 0802-3271.

“Thermal Dilation and Autogenous Deformation as Driving Forces to Self-Induced Stresses in High Performance Concrete”,
Øyvind Bjøntegaard, 1999:121, ISBN 82-7984-002-8, ISSN 0802-3271.

“Some Aspects of Ski Base Sliding Friction and Ski Base Structure”,
Dag Anders Moldestad, 1999:137, ISBN 82-7984-019-2, ISSN 0802-3271.

"Electrode reactions and corrosion resistance for steel in mortar and concrete",
Roy Antonsen, 2000:10, ISBN 82-7984-030-3, ISSN 0802-3271.

"Hydro-Physical Conditions in Kelp Forests and the Effect on Wave Damping and Dune Erosion. A case study on Laminaria Hyperborea",
Stig Magnar Løvås, 2000:28, ISBN 82-7984-050-8, ISSN 0802-3271.

"Random Vibration and the Path Integral Method",
Christian Skaug, 2000:39, ISBN 82-7984-061-3, ISSN 0802-3271.

"Buckling and geometrical nonlinear beam-type analyses of timber structures",
Trond Even Eggen, 2000:56, ISBN 82-7984-081-8, ISSN 0802-3271.

”Structural Crashworthiness of Aluminium Foam-Based Components”,
Arve Grønsund Hanssen, 2000:76, ISBN 82-7984-102-4, ISSN 0809-103X.

“Measurements and simulations of the consolidation in first-year sea ice ridges, and some aspects of mechanical behaviour”,
Knut V. Høyland, 2000:94, ISBN 82-7984-121-0, ISSN 0809-103X.

”Kinematics in Regular and Irregular Waves based on a Lagrangian Formulation”,
Svein Helge Gjøsund, 2000-86, ISBN 82-7984-112-1, ISSN 0809-103X.

”Self-Induced Cracking Problems in Hardening Concrete Structures”,
Daniela Bosnjak, 2000-121, ISBN 82-7984-151-2, ISSN 0809-103X.

"Ballistic Penetration and Perforation of Steel Plates",
Tore Børvik, 2000:124, ISBN 82-7984-154-7, ISSN 0809-103X.

"Freeze-Thaw resistance of Concrete. Effect of: Curing Conditions, Moisture Exchange and Materials",
Terje Finnerup Rønning, 2001:14, ISBN 82-7984-165-2, ISSN 0809-103X

Structural behaviour of post tensioned concrete structures. Flat slab. Slabs on ground",
Steinar Trygstad, 2001:52, ISBN 82-471-5314-9, ISSN 0809-103X.

"Slipforming of Vertical Concrete Structures. Friction between concrete and slipform panel",
Kjell Tore Fosså, 2001:61, ISBN 82-471-5325-4, ISSN 0809-103X.

"Some numerical methods for the simulation of laminar and turbulent incompressible flows",
Jens Holmen, 2002:6, ISBN 82-471-5396-3, ISSN 0809-103X.

“Improved Fatigue Performance of Threaded Drillstring Connections by Cold Rolling”,
Steinar Kristoffersen, 2002:11, ISBN: 82-421-5402-1, ISSN 0809-103X.

"Deformations in Concrete Cantilever Bridges: Observations and Theoretical Modelling",
Peter F. Takâcs, 2002:23, ISBN 82-471-5415-3, ISSN 0809-103X.

"Stiffened aluminium plates subjected to impact loading",
Hilde Giæver Hildrum, 2002:69, ISBN 82-471-5467-6, ISSN 0809-103X.

"Full- and model scale study of wind effects on a medium-rise building in a built up area",
Jónas Thór Snæbjørnsson, 2002:95, ISBN82-471-5495-1, ISSN 0809-103X.

“Evaluation of Concepts for Loading of Hydrocarbons in Ice-infested water”,
Arnor Jensen, 2002:114, ISBN 82-417-5506-0, ISSN 0809-103X.

”Numerical and Physical Modelling of Oil Spreading in Broken Ice”,
Janne K. Økland Gjøsteen, 2002:130, ISBN 82-471-5523-0, ISSN 0809-103X.

”Diagnosis and protection of corroding steel in concrete”,
Franz Pruckner, 20002:140, ISBN 82-471-5555-4, ISSN 0809-103X.

“Tensile and Compressive Creep of Young Concrete: Testing and Modelling”,
Dawood Atrushi, 2003:17, ISBN 82-471-5565-6, ISSN 0809-103X.

“Rheology of Particle Suspensions. Fresh Concrete, Mortar and Cement Paste with Various Types of Lignosulfonates”,
Jon Elvar Wallevik, 2003:18, ISBN 82-471-5566-4, ISSN 0809-103X.

“Oblique Loading of Aluminium Crash Components”,
Aase Reyes, 2003:15, ISBN 82-471-5562-1, ISSN 0809-103X.

“Utilization of Ethiopian Natural Pozzolans”,
Surafel Ketema Desta, 2003:26, ISSN 82-471-5574-5, ISSN:0809-103X.

“Behaviour and strength prediction of reinforced concrete structures with discontinuity regions”,
Helge Brå, 2004:11, ISBN 82-471-6222-9, ISSN 1503-8181.

“High-strength steel plates subjected to projectile impact. An experimental and numerical study”,
Sumita Dey, 2004:38, ISBN 82-471-6282-2 (printed version), ISBN 82-471-6281-4 (electronic version), ISSN 1503-8181.

“Alkali-reactive and inert fillers in concrete. Rheology of fresh mixtures and expansive reactions.”
Bård M. Pedersen, 2004:92, ISBN 82-471-6401-9 (printed version), ISBN 82-471-6400-0 (electronic version), ISSN 1503-8181.

“On the Shear Capacity of Steel Girders with Large Web Openings”.
Nils Christian Hagen, 2005:9 ISBN 82-471-6878-2 (printed version), ISBN 82-471-6877-4 (electronic version), ISSN 1503-8181.

”Behaviour of aluminium extrusions subjected to axial loading”.
Østen Jensen, 2005:7, ISBN 82-471-6873-1 (printed version), ISBN 82-471-6872-3 (electronic version), ISSN 1503-8181.

”Thermal Aspects of corrosion of Steel in Concrete”.
Jan-Magnus Østvik, 2005:5, ISBN 82-471-6869-3 (printed version), ISBN 82-471-6868 (electronic version), ISSN 1503-8181.

”Mechanical and adaptive behaviour of bone in relation to hip replacement.” A study of bone remodelling and bone grafting.
Sébastien Muller, 2005:34, ISBN 82-471-6933-9 (printed version), ISBN 82-471-6932-0 (electronic version), ISSN 1503-8181.

“Analysis of geometrical nonlinearities with applications to timber structures”.
Lars Wollebæk, 2005:74, ISBN 82-471-7050-5 (printed version), ISBN 82-471-7019-1 (electronic version), ISSN 1503-8181.

“Pedestrian induced lateral vibrations of slender footbridges”,
Anders Rönnquist, 2005:102, ISBN 82-471-7082-5 (printed version), ISBN 82-471-7081-7 (electronic version), ISSN 1503-8181.

“Initial Strength Development of Fly Ash and Limestone Blended Cements at Various Temperatures Predicted by Ultrasonic Pulse Velocity”,
Tom Ivar Fredvik, 2005:112, ISBN 82-471-7105-8 (printed version), ISBN 82-471-7103-1 (electronic version), ISSN 1503-8181.

“Behaviour and modelling of thin-walled cast components”,
Cato Dørum, 2005:128, ISBN 82-471-7140-6 (printed version), ISBN 82-471-7139-2 (electronic version), ISSN 1503-8181.

“Behaviour and modelling of selfpiercing riveted connections”,
Raffaele Porcaro, 2005:165, ISBN 82-471-7219-4 (printed version), ISBN 82-471-7218-6 (electronic version), ISSN 1503-8181.

”Behaviour and Modelling og Aluminium Plates subjected to Compressive Load”,
Lars Rønning, 2005:154, ISBN 82-471-7169-1 (printed version), ISBN 82-471-7195-3 (electronic version), ISSN 1503-8181.

”Bumper beam-longitudinal system subjected to offset impact loading”,
Satyanarayana Kokkula, 2005:193, ISBN 82-471-7280-1 (printed version), ISBN 82-471-7279-8 (electronic version), ISSN 1503-8181.

“Control of Chloride Penetration into Concrete Structures at Early Age”,
Guofei Liu, 2006:46, ISBN 82-471-7838-9 (printed version), ISBN 82-471-7837-0 (electronic version), ISSN 1503-8181.

“Modelling of Welded Thin-Walled Aluminium Structures”,
Ting Wang, 2006:78, ISBN 82-471-7907-5 (printed version), ISBN 82-471-7906-7 (electronic version), ISSN 1503-8181.

”Time-variant reliability of dynamic systems by importance sampling and probabilistic analysis of ice loads”,
Anna Ivanova Olsen, 2006:139, ISBN 82-471-8041-3 (printed version), ISBN 82-471-8040-5 (electronic version), ISSN 1503-8181.

“Fatigue life prediction of an aluminium alloy automotive component using finite element analysis of surface topography”.
Sigmund Kyrre Ås, 2006:25, ISBN 82-471-7791-9 (printed version), ISBN 82-471-7791-9 (electronic version), ISSN 1503-8181.

”Constitutive models of elastoplasticity and fracture for aluminium alloys under strain path change”,
Dasharatha Achani, 2006:76, ISBN 82-471-7903-2 (printed version), ISBN 82-471-7902-4 (electronic version), ISSN 1503-8181.

“Simulations of 2D dynamic brittle fracture by the Element-free Galerkin method and linear fracture mechanics”,
Tommy Karlsson, 2006:125, ISBN 82-471-8011-1 (printed version), ISBN 82-471-8010-3 (electronic version), ISSN 1503-8181.

“Penetration and Perforation of Granite Targets by Hard Projectiles”,
Chong Chiang Seah, 2006:188, ISBN 82-471-8150-9 (printed version), ISBN 82-471-8149-5 (electronic version), ISSN 1503-8181.

“Deformations, strain capacity and cracking of concrete in plastic and early hardening phases”,
Tor Arne Hammer, 2007:234, ISBN 978-82-471-5191-4 (printed version), ISBN 978-82-471-5207-2 (electronic version), ISSN 1503-8181.

“Crashworthiness of dual-phase high-strength steel: Material and Component behaviour”,
Venkatapathi Tarigopula, 2007:230, ISBN 82-471-5076-4 (printed version), ISBN 82-471-5093-1 (electronic version), ISSN 1503-8181.

“Fibre reinforcement in load carrying concrete structures”,
Åse Lyslo Døssland, 2008:50, ISBN 978-82-471-6910-0 (printed version), ISBN 978-82-471-6924-7 (electronic version), ISSN 1503-8181.

“Low-velocity penetration of aluminium plates”,
Frode Grytten, 2008:46, ISBN 978-82-471-6826-4 (printed version), ISBN 978-82-471-6843-1 (electronic version), ISSN 1503-8181.

“Robustness studies of structures subjected to large deformations”,
Ørjan Fyllingen, 2008:24, ISBN 978-82-471-6339-9 (printed version), ISBN 978-82-471-6342-9 (electronic version), ISSN 1503-8181.

“Constitutive modelling of morsellised bone”,
Knut Birger Lunde, 2008:92, ISBN 978-82-471-7829-4 (printed version), ISBN 978-82-471-7832-4 (electronic version), ISSN 1503-8181.

“Experimental Investigations of Wind Loading on a Suspension Bridge Girder”,
Bjørn Isaksen, 2008:131, ISBN 978-82-471-8656-5 (printed version), ISBN 978-82-471-8673-2 (electronic version), ISSN 1503-8181.

“Cracking Risk of Concrete Structures in The Hardening Phase”,
Guomin Ji, 2008:198, ISBN 978-82-471-1079-9 (printed version), ISBN 978-82-471-1080-5 (electronic version), ISSN 1503-8181.

“Modelling and numerical analysis of the porcine and human mitral apparatus”,
Victorien Emile Prot, 2008:249, ISBN 978-82-471-1192-5 (printed version), ISBN 978-82-471-1193-2 (electronic version), ISSN 1503-8181.

“Strength analysis of net structures”,
Heidi Moe, 2009:48, ISBN 978-82-471-1468-1 (printed version), ISBN 978-82-471-1469-8 (electronic version), ISSN1503-8181.

“Numerical analysis of ductile fracture in surface cracked shells”,
Espen Berg, 2009:80, ISBN 978-82-471-1537-4 (printed version), ISBN 978-82-471-1538-1 (electronic version), ISSN 1503-8181.

“Subject specific finite element analysis of bone – for evaluation of the healing of a leg lengthening and evaluation of femoral stem design”,
Sune Hansborg Pettersen, 2009:99, ISBN 978-82-471-1579-4 (printed version), ISBN 978-82-471-1580-0 (electronic version), ISSN 1503-8181.

“Evaluation of fracture parameters for notched multi-layered structures”,
Lingyun Shang, 2009:137, ISBN 978-82-471-1662-3 (printed version), ISBN 978-82-471-1663-0 (electronic version), ISSN 1503-8181.

“Modelling of Dynamic Material Behaviour and Fracture of Aluminium Alloys for Structural Applications”
Yan Chen, 2009:69, ISBN 978-82-471-1515-2 (printed version), ISBN 978-82 471-1516-9 (electronic version), ISSN 1503-8181.

“Nanomechanics of polymer and composite particles”
Jianying He 2009:213, ISBN 978-82-471-1828-3 (printed version), ISBN 978-82-471-1829-0 (electronic version), ISSN 1503-8181.

“Mechanical properties of clear wood from Norway spruce”
Kristian Berbom Dahl 2009:250, ISBN 978-82-471-1911-2 (printed version) ISBN 978-82-471-1912-9 (electronic version), ISSN 1503-8181.

"Modeling of the degradation of TiB_2 mechanical properties by residual stresses and liquid Al penetration along grain boundaries"
Micol Pezzotta 2009:254, ISBN 978-82-471-1923-5 (printed version) ISBN 978-82-471-1924-2 (electronic version) ISSN 1503-8181.

"Effect of welding residual stress on fracture"
Xiabo Ren 2010:77, ISBN 978-82-471-2115-3 (printed version) ISBN 978-82-471-2116-0 (electronic version), ISSN 1503-8181.

"Pan-based carbon fiber as anode material in cathodic protection system for concrete structures" Mahdi Chini 2010:122, ISBN 978-82-471-2210-5 (printed version) ISBN 978-82-471-2213-6 (electronic version), ISSN 1503-8181.

"Structural Behaviour of deteriorated and retrofitted concrete structures" Irina Vasililjeva Sæther 2010:171, ISBN 978-82-471-2315-7 (printed version) ISBN 978-82-471-2316-4 (electronic version) ISSN 1503-8181.

"Prediction of local snow loads on roofs" Vivian Meløysund 2010:247, ISBN 978-82-471-2490-1 (printed version) ISBN 978-82-471-2491-8 (electronic version) ISSN 1503-8181.

"Behaviour and modelling of polymers for crash applications" Virgile Delhaye 2010:251, ISBN 978-82-471-2501-4 (printed version) ISBN 978-82-471-2502-1 (electronic version) ISSN 1503-8181.

"Blended cement with reducted CO_2 emission – Utilizing the Fly Ash-Limestone Synergy", Klaartje De Weerdt 2011:32, ISBN 978-82-471-2584-7 (printed version) ISBN 978-82-471-2584-4 (electronic version) ISSN 1503-8181.

"Chloride induced reinforcement corrosion in concrete" Concept of critical chloride content – methods and mechanisms. Ueli Angst 2011:113, ISBN 978-82-471-2769-9 (printed version) ISBN 978-82-471-2763-6 (electronic version) ISSN 1503-8181.

"A thermo-electric-Mechanical study of the carbon anode and contact interface for Energy savings in the production of aluminium". Dag Herman Andersen 2011:157, ISBN 978-82-471-2859-6 (printed version) ISBN 978-82-471-2860-2 (electronic version) ISSN 1503-8181.

"Structural Capacity of Anchorage Ties in Masonry Veneer Walls Subjected toEarthquake". The implications of Eurocode 8 and Eurocode 6 on a typical Norwegain veneer wall. Ahmed Mohamed Yousry Hamed 2011:181, ISBN 978-82-471-2911-1 (printed version) ISBN 978-82-471-2912-8 (electronic ver.) ISSN 1503-8181.

"Work-hardening behaviour in age-hardenable Al-Zn-Mg(-Cu) alloys". Ida Westermann , 2011:247, ISBN 978-82-471-3056-8 (printed ver.) ISBN 978-82-471-3057-5 (electronic ver.) ISSN 1503-8181.

"Behaviour and modelling of selfpiercing riveted connections using aluminium rivets". Nguyen-Hieu Hoang, 2011:266, ISBN 978-82-471-3097-1 (printed ver.) ISBN 978-82-471-3099-5 (electronic ver.) ISSN 1503-8181. ISSN 1503-8181.

“Fibre reinforced concrete”. Sindre Sandbakk, 2011:297, ISBN 978-82-471-3167-1 (printed ver.) ISBN 978-82-471-3168-8 (electronic ver) ISSN 1503:8181.

“Dynamic behaviour of cablesupported bridges subjected to strong natural wind”. Ole Andre Øiseth, 2011:315, ISBN 978-82-471-3209-8 (printed ver.) ISBN 978-82-471-3210-4 (electronic ver.) ISSN 1503-8181.

“Constitutive modeling of solargrade silicon materials” Julien Cochard, 2011:307, ISBN 978-82-471-3189-3 (printed ver). ISBN 978-82-471-3190-9 (electronic ver.) ISSN 1503-8181.

“Constitutive behavior and fracture of shape memory alloys” Jim Stian Olsen, 2012:57, ISBN 978-82-471-3382-8 (printed ver.) ISBN 978-82-471-3383-5 (electronic ver.) ISSN 1503-8181.